Development of Bragg coherent X-ray diffraction and ptychography methods : application to the study of semiconductor nanostructures

Gaétan Girard

Université Grenoble Alpes

THÈSE
Pour obtenir le grade de:

DOCTEUR DE L'UNIVERSITÉ GRENOBLE ALPES
Spécialité: Physique de la Matière Condensée et du Rayonnement
Arrêté ministériel: 25 mai 2016

Présentée par

GAÉTAN GIRARD

Development of Bragg coherent X-ray diffraction and Ptychography methods, application to the study of semiconductor nanostructures

- ou -

Développement des méthodes de Ptychographie et diffraction cohérente des rayons X en géométrie de Bragg, application à l'étude de nano-structures

Thèse de doctorat dirigée par:

Mr Vincent Favre-Nicolin
Scientist HDR, ESRF - The European Synchrotron — Directeur de thèse
Mr Joël Eymery
HDR, CEA-MEM, Université Grenoble Alpes — Co-directeur de thèse

préparée à Installation Européenne de Rayonnement Synchrotron (ESRF - The European Synchrotron) dans École Doctorale de Physique (n° 47).

Thèse présentée et soutenue publiquement à Grenoble, le 4 mars, 2020 devant le jury composé de :

Mr Marc De Boissieu Directeur de recherche, CNRS Délégation Alpes	Président
Mr Sylvain Ravy Directeur de recherche, CNRS Ile-de-France Gif-sur-Yvette	Rapporteur
Mr Stéphane Labat Maître de conférences HDR, Université Aix-Marseille	Rapporteur
Mme Virginie Chamard Directrice de recherche, CNRS Délégation Provence et Corse	Examinateur

Thèse de doctorat

Gaétan Girard: *Developments of Bragg coherent X-ray diffraction and ptychography methods, application to the study of semiconductor nanostructures,* PhD, © 4/03/2020

REMERCIEMENTS

Je voudrais commencer par remercier les membres de mon jury de thèse pour avoir accepté de lire d'un oeil critique et attentif ce manuscrit restituant mes travaux de thèse. Merci donc à Sylvain Ravy, Stéphane Labat, Virginie Chamard et Marc De Boissieu pour leur patience et leur attention. Je tiens à remercier particulièrement Sylvain Ravi et Stéphane Labat pour leur qualité de rapporteurs de ma thèse. J'ai été honoré d'avoir un jury aussi prestigieux.

Bien sûr, ces travaux de thèse n'auraient jamais vu le jour sans la volonté de Vincent Favre-Nicolin, mon directeur de thèse. Je souhaite ainsi exprimer toute ma gratitude à Vincent pour m'avoir mis en quelque sorte le pied à l'étrier. Les synchrotrons et les expériences de diffraction cohérente qu'il est possible d'y conduire n'ont aucun secret pour lui, ce qui était loin d'être mon cas au début de l'année 2017. Vincent m'a beaucoup appris et son appétit pour la science était contagieux.

Je souhaite aussi remercier mon co-directeur de thèse, Joël Eymery, qui a su se montrer très disponible et patient. Notamment, il a su m'expliquer d'un point de vue matériau, autant de fois que nécessaire, les tenants et aboutissants de tous les échantillons qui sont passés entre mes mains. Merci aussi à tous deux pour les longues heures que vous avez dû passer à reprendre ma rédaction!

J'exprime mes remerciements au Laboratoire d'Excellence LANEF pour avoir financé cette thèse.

Je tiens aussi à remercier Guillaume Beutier et Patrice Gergaud pour avoir accepté de constituer mon comité de suivi de thèse, et de m'avoir ainsi accompagné pour faire le point sur l'avancée de mes travaux ainsi que sur mon ressenti au long de ces trois années.

Mes remerciements vont également à l'équipe d'ID01, qui a toujours été un soutien que ce soit à travers d'innombrables discussions sur les rayons X en général, ou plus simplement grâce au déjeuner à la cantine de l'ESRF qui a toujours été synonyme de pause bien agréable au milieu des journées de travail. Merci à Tobias Schülli d'avoir accepté d'héberger mes travaux de thèse au sein de l'équipe, mais aussi merci pour les barbecue en Vercors! Merci à Steven Leake pour le temps passé à m'expliquer le fonctionnement de la beamline, les discussions à propos de la cohérence des rayons X et les problèmes de reconstruction, mais aussi d'avoir partagé son jardin à Sassenage! Merci à Peter Boesecke, dont la connaissance du musée des miniatures de Hambourg est sans faille. Merci à Marie-Ingrid Richard, pour son aide précieuse, ses conseils et surtout sa bonne humeur permanente. Merci

à Carsten Ritcher, sans qui l'analyse des données de KMAP aurait probablement ressemblé à un chemin de croix sans fin, et qui m'a fait découvrir un très bon burger à Grenoble (bizarrement juste en bas de chez lui). Merci à Jérôme Carnis, notamment pour son aide dans le post-processing des reconstructions de BCDI. Merci à Maxime Dupraz, pour les moments autour de problématiques de diffraction ou bien autour d'un verre. Merci à Hamid Djazouli, toujours disponible et avec le sourire en prime! Mes remerciements s'étendent aussi à Samuel Tardif qui m'a aidé à appréhender l'analyse de données d'expérience synchrotron. Je n'oublie pas Tao Zhou dont la capacité de travail m'a épaté, ni Longfei avec qui c'était toujours un plaisir d'échanger. Merci à Yves-Matthieu pour ses conseils quant au meilleur moyen d'approcher une rédaction scientifique !

Mention spéciale à ceux avec qui j'ai eu la chance de partager mon bureau. J'y suis resté pendant trois années mais il y a eu un peu de mouvement autour de moi. Merci à Ni et Edwin pour les derniers mois, malheureusement consacrés à la rédaction de mon côté... Merci à Lucas, qui a pu partager ma passion pour le foot. Merci à Francesco, avec qui les discussions scientifiques étaient particulièrement intéressantes. Merci à Bendix, en espérant n'avoir pas été un tuteur de stage trop exigeant. Un merci tout particulier à Tarcissius, sans qui cet été 2019 n'aurait pas eu la même saveur ! Non seulement il nous a été possible d'échanger sur les détails d'une modélisation reposant sur des éléments finis, mais en plus les trajets de retour à vélo le soir ont une pris une autre dimension. Enfin et surtout, merci à Edoardo, pour m'avoir supporté pendant deux grosses années et être devenu bien plus qu'un collègue de thèse. Si cette thèse a été une réussite, du moins sur le plan personnel, Edoardo y a joué un rôle prépondérant, merci mec !

Je voudrais également remercier ceux avec qui j'ai eu le plaisir de collaborer de près ou de loin, et grâce à qui j'ai pu mettre la main sur des échantillons remarquables. Merci à Jérémie, Mathieu et leur équipe pour les micro-disques de GeSn. Merci à Rémy et son équipe pour les échantillons de SiGe, mais surtout pour son aide précieuse sur les questions d'orientation cristalline et de son implémentation dans COMSOL ! Au passage, Rémy, les résultats sont enfin là !

Merci aux personnes qui ont constitué le meilleur groupe des Doctoriales, à savoir Sofia, Jules, Anne-Sophie, Allister, Guillaume, Anthonin et Jessica (et Marguerite) ! Bon courage à vous pour la suite de vos thèses !

Je ne peux pas non plus écrire ces remerciement sans m'adresser à ceux que j'ai rencontré dans les travées de l'ESRF et qui étaient toujours disponibles pour partager un café ou un repas. En particulier, merci à Yannick, et sa sérénité communicative, et à Alix, parce que les gens cool ça ne court pas les rues. Merci aussi à Camille, sans qui je ne serais toujours pas parti à la chasse aux champignons, quel blasphème pour un grenoblois !

Comment pourrais-je oublier Rafael ? Même s'il n'a pas partagé mon bureau, il a été tout autant présent, que ce soit pour parler de la cohérence d'un rayonnement synchrotron, simuler une ligne de lumière, partager des codes Python mais aussi de choses bien plus personnelles. Merci pour, entre autres recettes, celle des coxinhas, petit cornichon !

Enfin, la thèse, même estampillée ESRF, ne se vit pas qu'au laboratoire, et j'ai eu la chance d'être exceptionnellement bien entouré, de ma famille et mes amis. Merci donc à mes parents, qui ont toujours été disponibles pour moi, m'accueillant à bras ouverts pour n'importe quel repas de dernière minute. Merci à ma soeur Cléa, toujours réactive à mes appels et qui sait trouver les mots pour me remettre en confiance dans les étapes difficiles. Merci à mes potes de toujours, Jules, Louis, Théo, Yann et Massimo, qui ont su rester aussi proches de moi quand je prenais un chemin plus que sinueux à leurs yeux. Il faut savoir couper avec le travail de temps en temps, et il n'y avait pas mieux que leur compagnie pour y arriver ! Mention spéciale aux deux qui ont pu assister à ma soutenance, et qui ont tenu presque 3h sans sourciller !

ABSTRACT

Nanotechnologies rely on the introduction of strain engineering to enhance semiconductor devices performances. As a consequence, non-invasive characterization methods with high spatial resolution and strain sensitivity on low-amount-of-matter samples are required. This PhD work focuses on methodology of X-ray diffraction techniques performed in the Bragg geometry, which allows probing the structural properties of crystalline samples. Firstly, the Scanning X-ray Diffraction Microscopy technique, developed on a fast-timescale at the ESRF ID01 undulator beamline, is described through a thorough analysis of an experiment performed on ultra-thin strained SiGe-on-insulator patterns. Secondly, this manuscript focuses on two coherent diffraction imaging techniques, namely Bragg CDI, which yields complex density and strain map of nano-meso crystalline objects, and Ptychography, which use translational diversity to produce quantitative maps of complex transmission function of non-crystalline objects. The motivation developed in this PhD work is to combine these two techniques that both promote highly sensitive phase-contrast properties, in order to provide ultra-high resolution on complex/extended samples. Bragg Ptychography is thus introduced, along with algorithmic descriptions and considerations on the X-ray beam characterization, the latter being still a key component for successful reconstructions.

CONTENTS

LIST OF FIGURES

LIST OF TABLES

LISTINGS

ACRONYMS

AFM Atomic Force Microscopy

AP Alternating Projection

BPP Bragg Projection Ptychography

BOX Buried OXide

CDI Coherent Diffraction Imaging

CMOS Complementary Metal Oxide Semiconductor

COM Center Of Mass

DCT X-ray Diffraction Contrast Tomography

DFT Discrete Fourier Transform

DM Difference Map

FDSOI Fully Depleted Silicon On Insulator

FEM Finite Element Method

pFET p-type Field Effect Transistor

FFDXM Full-Field Diffraction X-ray Microscopy

FT Fourier Transform

FWHM Full Width at Half Maximum

FZP Fresnel Zone Plate

HIO Hybrid Input Output

KB Kirkpatrick-Baez

MOSFET Metal Oxide Semiconductor Field Effect Transistor

NBED Nano-Beam Electronic Diffraction

nMOS n-type Metal Oxide Semiconductor

pMOS p-type Metal Oxide Semiconductor

OSA Order Sorting Aperture

PIE Ptychographic Iterative Engine

PDF Probability Distribution Function

RP-CVD Reduced Pressure-Chemical Vapor Deposition

RTO Rapid Thermal Oxidation

ROI Region Of Interest

SEM Scanning Electron Microscopy

SGOI Silicon-Germanium On Insulator

SIFT Scale-Invariant Feature Transform

SOI Silicon On Insulator

sSOI Strained-SOI

sSGOI Strained-SGOI

SMT Stress Memorization Technique

STXM Scanning Transmission X-Ray Microscopy

SXDM Scanning X-Ray Diffraction Microscopy

UTBB Ultra-Thin Body and Buried oxide

UVL Ultra-Violet Litography

1

INTRODUCTION

The last decades have seen the emergence of a new parameter to tune materials properties and performance: strain. Strain engineering has expanded the development of nanosciences, when down-scaling reached its limits. Indeed, it is now possible to enhance *e. g.*, carrier mobility within transistor semiconductors, by the deliberate introduction of strain to locally modify the band structure and optimize device performances. However, the control and prediction of such modifications are difficult, as the lattice responses depend on the complete environment and processing history of the device. Precise nanoscale characterization while mitigating potential perturbations of the boundary conditions has become crucial for nanotechnologies.

X-ray coherent diffraction imaging in Bragg geometry is the perfect versatile tool that steps in to provide high spatial resolution combined with high strain sensitivity in three dimensions. Intrinsically, X-rays allow for atomic resolution and fourth generation light sources offer the prospect of pushing CDI lensless imaging to its limit, *i. e.*, wavelength limited resolution. As the Bragg geometry allows imaging strain, its combination with CDI methods was key for nanoscale strain characterization.

This PhD work is dedicated to the development and numerical test of characterization methods based on X-ray diffraction in Bragg condition. This way, it is focused on methodology and applied to samples identified as potential references in the frame of nanotechnologies which is thriving and will take advantage of the new opportunities offered by the ESRF EBS upgrade.

The first part of this manuscript is devoted to theoretical explanations on the basics of X-ray, coherence and lattice structure of crystalline material. In chapter 2, the nomenclature and symbols related to strain and elasticity are presented. A focus on the strain-stress relationship is made, with the particular case of strain in Silicon detailed.

In chapter 3, X-ray scattering theory is introduced, with a particular emphasis on Bragg diffraction. The coherence properties of X-rays produced from synchrotron radiation are discussed in order to introduce CDI techniques, along with a review of the associated phase retrieval algorithms and the recent advances in the field. A typical experimental setup is finally depicted through the example of the undulator beamline ID01 at the ESRF - the European Synchrotron.

In a second part, the manuscript focuses on the experimental works conducted throughout this Ph.D. work, including descriptions of the experiments, details on the analysis roadmaps, results and discussions.

Chapter 4 is dedicated to the case study of ultra-thin (13 to 20 nm thicknesses) strained silicon germanium layers on insulator (sSiGeOI), developed in order to be integrated as channels in Fully Depleted Silicon On Insulator p-type Field Effect Transistor. A particular attention is given to the condensation process used to grow such strained SiGe layers. The principal interrogation that remains relates to the behavior of strain when free boundary conditions are introduced by etching. Results of simulations from Finite Element Method are first presented, then characterizations performed with Raman spectroscopy from the work of R. Berthelon are recalled. Finally, a thorough description of the Scanning X-ray Diffraction Microscopy technique is given, along with point-by-point analysis. The results of the experiments carried on at ID01 are finally presented and discussed : not only a statistical characterization is extracted but also the strain relaxation length is measured.

Chapter 5 provides a description of an innovative experiment aiming to combine the large scale imaging technique of Diffraction Contrast Tomography allowing indexation of embedded grain within a Zirconia cylinder, with the nanoscale resolution and strain sensibility of Bragg Coherent Diffraction Imaging. A focus is made on the essential beam characterization, which had to be done in order to obtain a beam size of the same order than the grain. Finally, the chapter concludes with the presentation of an innovative numerical tool to assess the strain sensitivity of a Bragg CDI reconstruction.

Last but not least, Chapter 6 introduces the Ptychography method. Firstly, a short summary of the development of the technique is introduced, followed by a detailed description of the main algorithms used to recover both the illuminated object and the scanning probe. Then, the adaptation of such algorithms to the Bragg geometry is considered. This is of crucial importance for imaging strain with nanoscale spatial resolution within an extended object. Furthermore, a review of the publications related to ptychography in Bragg condition is given, from 2D Projection to multi-angle 3D Projection Bragg ptychography, providing a grasp of how to deal with the complex datasets that Bragg Ptychography experiments will inevitably provide. Finally, tests of the different approaches, as they were introduced in the ESRF's PyNX python library, are performed and the results discussed. Firstly, numerical simulations are carried on ultra-thin layers of sSiGeOI, with the implementation of displacement fields from finite element method (COMSOL) modeling. Then, experimental datasets from sSiGeOI are reconstructed, both with single-angle 3D BPP and 2D BPP. In the end, the efficiency of 2D BPP is demonstrated through the

reconstruction of the phase of a strained micro-disk of multi-graded layers of GeSn, using an isostrain approach.

Première partie

STRAIN AND X-RAYS INTERACTION WITH MATTER

2

STRAIN - DEFINITIONS

In this chapter, we introduce strain and related concepts, such as misfit and relaxation, in order to set the nomenclature and symbols that will be used consistently throughout this manuscript. Then, a particular focus on the strain-stress relationship is given through the theory of elasticity. Finally, the impact of strain on the band structure of Silicon is detailed.

2.1 INTRODUCTION

Strain is a response of a system to an applied force or system of forces over area called stress. These forces will tend to deform the material, and engineering strain is defined as the amount of deformation in the direction of the applied force on to the initial length of the material. Due to lattice mismatch, almost all thin layers of material deposited on to a substrate will experience strain, which leads to cracking, blistering or even peeling and cause eventual failure of the material. That is why for many years the main goal of crystal heteroepitaxy - the deposition of a different crystalline material onto a crystalline substrate - was to avoid strain in order to produce long-lived devices.

However, on Dec. 29, 1959, Richard Feynman gave a talk entitled "There's Plenty of a Room at the Bottom" Feynman, 1960, in which he envisioned a future in which all of the 24 volumes of the *Encyclopedia Britannica* are written and read on the head of a pin using an electron microscope. It was the founding of a field now known as nanoscience and nanotechnology, together with the related fundamental physical and mechanical challenges arising with miniaturization. At the root of better lasers, faster transistors or better catalysts, in the mechanics of materials the mantra "smaller is stronger" prevails Zhu and Li, 2010. Not only researchers found out that nanomaterials are much stronger, at low temperature at least Tian et al., 2013, but with so-called "ultra-strength materials" Zhu and Li, 2010 tuning the elastic strain directly enable s one to tailor their electronic, magnetic, optical.. properties. Therefore, heteroepitaxy is now often used to engineer strained layers. This is achieved practically via the growth of layers containing atoms of different nature, so that the lattice constants of the layer material and substrate do not match.

In the scope of this thesis, the effect of strain on the band structure of semiconductors is essentially a reduction of degeneracy at the top of the valence band,

leading to a reduction of the density of states. This results in scattering effects in the conduction mechanism in transistors, or in energy level tuning in optoelectronic devices. As an example, Patel *et al.* Patel et al., 1973 recognized very early that this would improve the efficiency of laser diodes cite, before Eliseev *et al.* Eliseev et al., 1984 gave a demonstration in 1984. Hence, the electronic properties of semiconductor nanostructures are strongly influenced by their strain state, and many examples have already shown that strain engineering was an efficient tool to boost microelectronics technologies Dunstan, 1997.

Dunstan gave an excellent review of strain ibid., that serves as a basis for the following definitions of the relevant concepts related to the strain.

2.2 DEFINITIONS

2.2.1 *Misfit strain*

When the material of a layer has a lattice parameter a_l that differs from the one of the substrate a_s, then the misfit or misfit strain is defined as :

$$\epsilon_0 = \frac{a_l - a_s}{a_s} \tag{2.1}$$

Note that this misfit strain can be anisotropic in a non-cubic material. Using Vegard's law Vegard, 1921, one can derive equation 2.1 as a function of the alloy composition. If the layer lattice parameter is larger than the one of substrate ($a_l > a_s$), the misfit is positive, as for the example of $Si_{1-x}Ge_x$ grown on Si :

$$\begin{aligned}\epsilon_0(x) =& \frac{a(x) - a_{Si}}{a_{Si}} = \frac{x a_{Ge} + (1-x)a_{Si} - a_{Si}}{a_{Si}} \\ =& \frac{x(a_{Ge} - a_{Si})}{a_{Si}} = 0.0418x\end{aligned} \tag{2.2}$$

2.2.2 *Strain tensor*

The strain tensor $\underline{\epsilon}$ is a 3×3 matrix that describe the full deformation of the unit cell from its natural shape and orientation. Usually, the tensor is symmetrized by averaging $\underline{\epsilon}_{jk}$ and $\underline{\epsilon}_{kj}$, leading to a loss of information concerning the orientation of the unit cell. Note that compressive strain has a negative sign.

2.2.3 *Strain matrix*

The strain matrix ϵ_J is reduced from the symmetrized strain tensor using the Voigt notation (*i. e.* $xx \rightarrow 1$; $yy \rightarrow 2$; $zz \rightarrow 3$; $yz \rightarrow 4$; $xz \rightarrow 5$ and $xy \rightarrow 6$). This 6×1 matrix describes the deformation but not the orientation of the unit cell. Note that the components $J \geq 4$ are twice the off-diagonal elements of the symmetrized e_{jk} :

$$\epsilon_J = \begin{pmatrix} \epsilon_{xx} \\ \epsilon_{yy} \\ \epsilon_{zz} \\ 2\epsilon_{yz} \\ 2\epsilon_{xz} \\ 2\epsilon_{xy} \end{pmatrix} \tag{2.3}$$

2.2.4 *Strain ε*

One has to emphasize the different notation used in this work. The use of ε means real strain, i.e. the deformation of the material (here SiGe) with respect to its relaxed lattice parameter. On the other hand, ϵ stands for the deformation with respect to the lattice of relaxed Silicon, which is in most cases used as a reference in strain characterization techniques. The real strain in a layer of lattice constant a_l' is the strain by which it is deformed from its natural lattice constant a_l. It is important to note that compressive strain is positive and that even in a pseudomorphic layer, *i. e.* when the layer is strictly epitaxial on its substrate with a coherent interface and is thermodynamically stable, the real strain ε differs from the misfit strain ϵ_0, as :

$$\varepsilon = \frac{a_l - a_s}{a_l} = \frac{a_s}{a_l} \cdot \epsilon_0 = \frac{1}{1+\epsilon_0}\epsilon_0 \tag{2.4}$$

In this particular case of a pseudomorphic layer, the difference between the two strains is normally insignificant. Note that the difference corresponds to the distinction drawn by Birch Birch, 1947 between the Lagrangian and the Eulerian definitions of strain, in which the strain is described respectively; with the initial or unstrained coordinates as the independent variables, or with the coordinates of the strained state being taken as independent. For infinitesimal strains, both definitions are equal to the classical linear theory.

2.3 ELASTIC STRAIN IN EPITAXIAL LAYERS TO INCREASE CARRIERS MOBILITY

In this section, the theory of elasticity will be briefly presented, with a focus made on the particular case of a silicon germanium layer grown on a silicon (110) substrate, as it will be the main sample studied in Part ii.

2.3.1 *Theory of elasticity*

Hooke's law describes the relationship between stress σ and strain ϵ :

$$\underline{\sigma} = \underline{\underline{C}} \cdot \underline{\epsilon} \Longleftrightarrow \underline{\epsilon} = \underline{\underline{S}} \cdot \underline{\sigma}, \tag{2.5}$$

where σ_{jk} and e_{jk} are the tensors of stress and strain, respectively, and $\underline{\underline{C}}$ and $\underline{\underline{S}}$ the fourth rank tensors of stiffness and compliance, respectively. By using the symmetry properties of strain and stress, Hooke's law can be derived :

$$\sigma_{ij} = C_{ijkl}\epsilon_{kl} \tag{2.6}$$

Using the Voigt notation, one can expressed Hooke's law in a matrix form, using the strain matrix introduced earlier :

$$\begin{pmatrix} \sigma_{xx} \\ \sigma_{yy} \\ \sigma_{zz} \\ \sigma_{yz} \\ \sigma_{xz} \\ \sigma_{xy} \end{pmatrix} = \begin{pmatrix} C_{11} & C_{12} & C_{13} & C_{14} & C_{15} & C_{16} \\ C_{21} & C_{22} & C_{23} & C_{24} & C_{25} & C_{26} \\ C_{31} & C_{32} & C_{33} & C_{34} & C_{35} & C_{36} \\ C_{41} & C_{42} & C_{43} & C_{44} & C_{45} & C_{46} \\ C_{51} & C_{52} & C_{53} & C_{54} & C_{55} & C_{56} \\ C_{61} & C_{62} & C_{63} & C_{64} & C_{65} & C_{66} \end{pmatrix} \cdot \begin{pmatrix} \epsilon_{xx} \\ \epsilon_{yy} \\ \epsilon_{zz} \\ 2\epsilon_{yz} \\ 2\epsilon_{xz} \\ 2\epsilon_{xy} \end{pmatrix} \tag{2.7}$$

where C_{ij} are the elastic constants, related to the material's properties. For a more detailed derivation of the theory behind strained crystal, readers are invited to look at Nye's book Nye, 1985. In the case of an isotropic material, the elasticity matrix

can be reduced and expressed with the Young's Modulus $E = C_{11}$ and the Poisson's ratio $\nu = -^{E}/_{C_{12}}$:

$$\begin{pmatrix} \epsilon_{xx} \\ \epsilon_{yy} \\ \epsilon_{zz} \\ 2\epsilon_{yz} \\ 2\epsilon_{xz} \\ 2\epsilon_{xy} \end{pmatrix} = \frac{1}{E} \begin{pmatrix} 1 & -\nu & -\nu & 0 & 0 & 0 \\ -\nu & 1 & -\nu & 0 & 0 & 0 \\ -\nu & -\nu & 1 & 0 & 0 & 0 \\ 0 & 0 & 0 & 2(1+\nu) & 0 & 0 \\ 0 & 0 & 0 & 0 & 2(1+\nu) & 0 \\ 0 & 0 & 0 & 0 & 0 & 2(1+\nu) \end{pmatrix} \cdot \begin{pmatrix} \sigma_{xx} \\ \sigma_{yy} \\ \sigma_{zz} \\ \sigma_{yz} \\ \sigma_{xz} \\ \sigma_{xy} \end{pmatrix} \tag{2.8}$$

2.3.2 *Elastic strain in epitaxial layers*

2.3.2.1 *Critical thickness*

When a crystalline material is grown by epitaxy on a crystalline substrate, the difference in lattice parameters will lead to a misfit strain 2.2.1. The strained epitaxial layer will then start to accumulate elastic energy. However, there exists a critical thickness, above which the main process minimizing the total stored elastic energy in the layer becomes the generation of dislocations, so that the lattice parameter can relax to its natural value. This critical thickness depends on the misfit strain : the higher the misfit, the smaller the thickness. The case of SiGe layers grown on a Si substrate has been widely studied, and Figure from Bruel, 1995 on Si/Ge nanostructures shows the evolution of the critical thickness for dislocation formation depending on Ge content.

2.3.2.2 *Biaxial strain*

Considering epitaxial layer grown along the <001> direction, the stress-strain relationship hence can be simplified since the boundary condition at the free surface requires σ_{zz} to vanish, and symmetry rules out the shear stresses components. The material is then experiencing biaxial strain, which can be compressive as in the case of $Si_{0.75}Ge_{0.25}$ grown on Si (see Figure 2.2). In the case of pseudomorphic structures, the in-plane strain ϵ_{xx} and ϵ_{yy} will be the same and equal to the misfit strain. If plastic relaxation occurs, through the introduction of suitable dislocation at the interface, these two in-plane strains no longer need to remain equal. In the growth direction, ϵ_{zz} directly derived from the Poisson's ratio :

$$\epsilon_{zz} = -2\frac{C_{12}}{C_{11}}\frac{\epsilon_{xx} + \epsilon_{yy}}{2} = -2\frac{\nu}{1-\nu}\epsilon_{average} \tag{2.9}$$

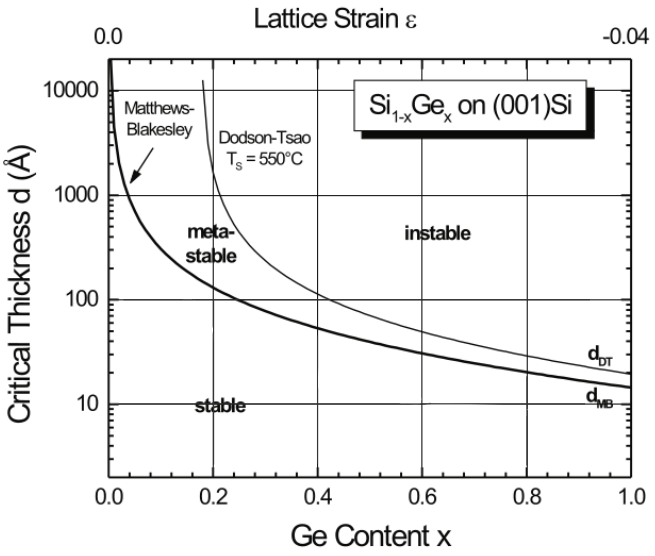

Figure 2.1 – Evolution of the critical thickness of a smooth strained SiGe layer on (001) Si, depending on the Ge content, at high and moderate substrate temperature d_{MB} and d_{DT}. According to calculations of Matthews and Blakesley Matthews and Blakeslee, 1974 or Dodson and Tsao Dodson and Tsao, 1987 respectively.

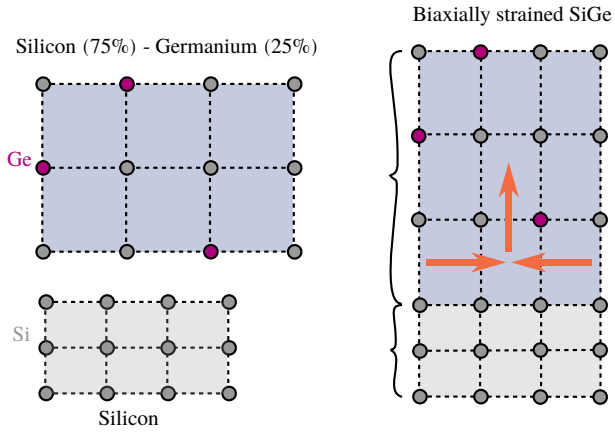

Figure 2.2 – Scheme of epitaxial formation of $Si_{0.75}Ge_{0.25}$ under biaxial strain, on top of a Si substrate. As the $Si_{0.75}Ge_{0.25}$ lattice parameter is larger than the one of Si, the epitaxial layer is under compressive biaxial strain in the epitaxial plane, and under tension in the perpendicular direction.

Material	C_{11}	C_{12}	C_{44}
Silicon (GPa)	165.7	63.9	79.6
Germanium (GPa)	129.2	47.9	67.0

Table 2.1 – Elastic constants of silicon and germanium. From Mason, 1956; Wortman and Evans, 1965

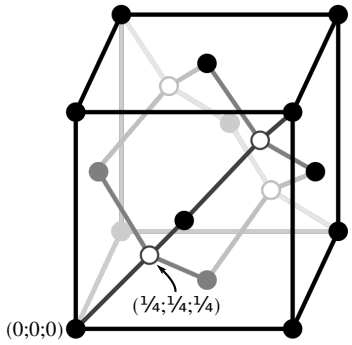

Figure 2.3 – Diamond lattice structure, as it is the case for silicon.

Now consider the particular case of silicon. Silicon is an anisotropic material and therefore cannot be described solely by the values of Young's Modulus and Poisson's ratio. Nonetheless, the silicon lattice is similar to cubic diamond (see Figure 2.3), hence its stiffness matrix can be reduced, in the reference frame (<100>,<010>,<001>), to :

$$C^{<100>} = \begin{pmatrix} C_{11} & C_{12} & C_{12} & 0 & 0 & 0 \\ C_{12} & C_{11} & C_{12} & 0 & 0 & 0 \\ C_{12} & C_{12} & C_{11} & 0 & 0 & 0 \\ 0 & 0 & 0 & C_{44} & 0 & 0 \\ 0 & 0 & 0 & 0 & C_{44} & 0 \\ 0 & 0 & 0 & 0 & 0 & C_{44} \end{pmatrix} \tag{2.10}$$

As an example, Table 2.1 gives the value of the elastic constants C_{11}, C_{12} and C_{44} for silicon and germanium. Note that Vegard's law also applies for the elastic constants, meaning that the linear variation with the alloy composition can be used as an approximation.

However, strained layers grown on orientations other than <001> present a different elasticity matrix, as the fourth rank stiffness tensor $\underline{\underline{C}}$ is rotated to the growth orientation. In the particular case of a <110> orientation of the substrate, an in-plane rotation of $\alpha = 45°$ is performed. Let R be the rotation matrix, then the stiffness coefficients read :

$$C_{ijkl}^{<110>} = R_{ig} R_{jh} C_{ghmn}^{<100>} R_{km} R_{ln} \tag{2.11}$$

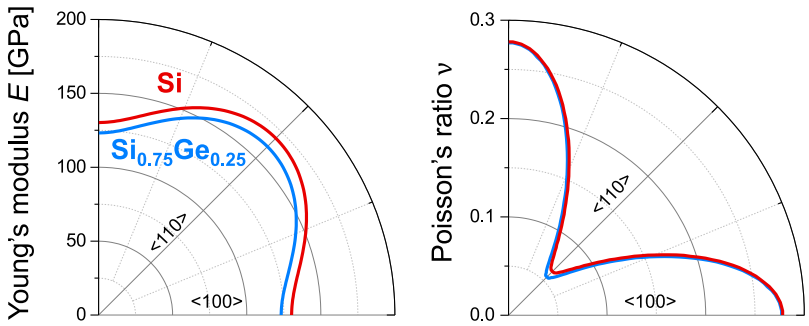

Figure 2.4 – (left) Equivalent Young's Modulus and (right) Poisson's ratio of Si and SiGe (with 25% Ge content), according to the crystal orientation.

In its new basis, the stiffness matrix derives :

$$C^{<110>} = \begin{pmatrix} C'_{11} & C'_{12} & C'_{13} & 0 & 0 & 0 \\ C'_{12} & C'_{11} & C'_{13} & 0 & 0 & 0 \\ C'_{13} & C'_{13} & C'_{33} & 0 & 0 & 0 \\ 0 & 0 & 0 & C'_{44} & 0 & 0 \\ 0 & 0 & 0 & 0 & C'_{44} & 0 \\ 0 & 0 & 0 & 0 & 0 & C'_{66} \end{pmatrix} \tag{2.12}$$

with :

$$\begin{cases} C'_{11} = \frac{C_{11}+C_{12}+2C_{44}}{2}; & C'_{12} = \frac{C_{11}+C_{12}-2C_{44}}{2}; C'_{13} = C_{12} \\ C'_{33} = C_{11}; C'_{44} = C_{44}; & C'_{66} = \frac{C_{11}-C_{12}}{2} \end{cases} \tag{2.13}$$

Rewriting the stiffness matrix in the correct orientation is crucial for the coming Finite Element Method (FEM) mechanical simulation that will be used with COMSOL AB, n.d.

The evolution of both Young's Modulus and Poisson's ratio with respect to the orientation, for a (001) plane is shown in Figure 2.4. Both the case of pure silicon and a silicon germanium alloy (25% content of germanium), are presented, as it will be of particular interest in Chapter 4.

2.3.3 *Impact of strain on silicon properties*

In solid-state physics, the band structure defines the electronic levels in crystal structures, i.e. the range of allowed energies for an electron within the crystal - energy bands - and forbidden ranges of energies - bands gap Wikipedia, n.d. By modifying the symmetries within a crystal, strain can modify band structure. The degeneracies of both valence and conduction bands may be lifted, as well as the

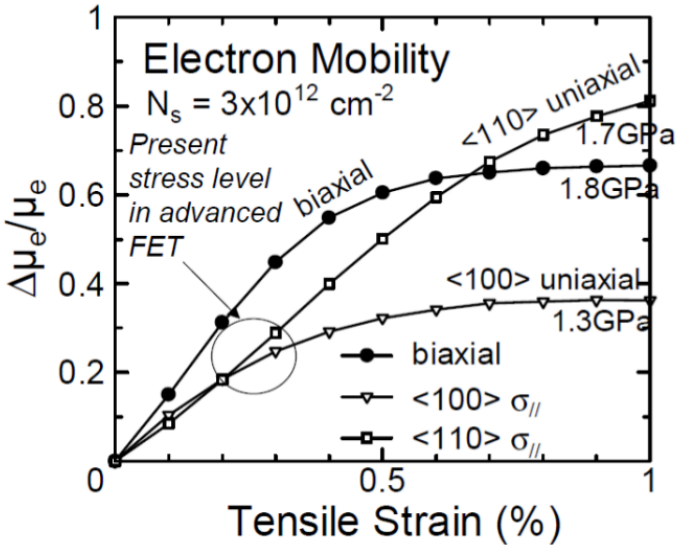

Figure 2.5 – Electron mobility enhancement with tensile strain in FET transistor. At high stress levels, a uniaxial stress along <110> is more effective than a biaxial stress because of a change in the effective mass. From Uchida et al., 2005

energy gap modified. Note that the shape of the energy isosurfaces is also affected, and the effective masses are modified. It is the deformation potential theory that accounts for band structure modification due to strain Bardeen and Shockley, 1950; Shockley and Bardeen, 1950; Herring and Vogt, 1957.

As a result, three mechanisms can occur with the introduction of strain :

— Band shift, resulting from change in the volume of the lattice,

— Band split, occuring in case of uniaxial stress.

— Band warping, that appears when the valence band curvature gets modified by the strain.

Within the effective mass assumption, the mobility of the carriers can be written as :

$$\mu_{eff} = \frac{q\tau}{m^*} \tag{2.14}$$

where q is the charge of the carriers, $1/\tau$ is the collision frequency of the carriers, and m^* is the conductivity effective mass. As the latter is inversely proportional to the band curvature, one can increase the mobility of the carriers by the introduction of strain in the structure Mohta and Thompson, 2005. Figure 2.5 shows the evolution of electron mobility within Silicon depending on the strain level of the structure. The strain integration methods in material such as silicon, in order to increase the performance of semiconductor nanostructures, will be discussed further in Chapter 4.

BIBLIOGRAPHY

Feynman, Richard P (1960). « There's plenty of room at the bottom. » In: *California Institute of Technology, Engineering and Science magazine* (cit. on p. 7).

Zhu, Ting and Ju Li (2010). « Ultra-strength materials. » In: *Progress in Materials Science* 55.7, pp. 710–757. DOI: 10.1016/j.pmatsci.2010.04.001 (cit. on p. 7).

Tian, Lin, Ju Li, Jun Sun, Evan Ma, and Zhi-Wei Shan (2013). « Visualizing size-dependent deformation mechanism transition in Sn. » In: *Scientific Reports* 3, p. 2113. DOI: 10.1038/srep02113 (cit. on p. 7).

Patel, N., J. Ripper, and P. Brosson (1973). « Behavior of threshold current and polarization of stimulated emission of GaAs injection lasers under uniaxial stress. » In: *IEEE Journal of Quantum Electronics* 9.2, pp. 338–341. DOI: 10.1109/JQE.1973.1077461 (cit. on p. 8).

Eliseev, P. G., B. N. Sverdlov, and N. Shokhudzhaev (1984). « Reduction of the threshold current of InGaAsP/lnP heterolasers by unidirectional compression. » In: *Soviet Journal of Quantum Electronics* 14.8, p. 1120. DOI: 10.1070/QE1984v014n08ABEH005386 (cit. on p. 8).

Dunstan, D. J. (1997). « Strain and strain relaxation in semiconductors. » en. In: *Journal of Materials Science: Materials in Electronics* 8.6, pp. 337–375. DOI: 10.1023/A:1018547625106 (cit. on p. 8).

Vegard, L. (1921). « Die Konstitution der Mischkristalle und die Raumfüllung der Atome. » de. In: *Zeitschrift für Physik* 5.1, pp. 17–26. DOI: 10.1007/BF01349680 (cit. on p. 8).

Birch, Francis (1947). « Finite Elastic Strain of Cubic Crystals. » In: *Physical Review* 71.11, pp. 809–824. DOI: 10.1103/PhysRev.71.809 (cit. on p. 9).

Nye, J. F. (1985). *Physical Properties of Crystals: Their Representation by Tensors and Matrices*. Clarendon Press (cit. on p. 10).

Bruel, M. (1995). « Silicon on insulator material technology. » In: *Electronics Letters* 31.14, pp. 1201–1202. DOI: 10.1049/el:19950805 (cit. on p. 11).

Matthews, J. W. and A. E. Blakeslee (1974). « Defects in epitaxial multilayers: I. Misfit dislocations. » In: *Journal of Crystal Growth* 27, pp. 118–125. DOI: 10.1016/S0022-0248(74)80055-2 (cit. on p. 12).

Dodson, Brian W. and Jeffrey Y. Tsao (1987). « Relaxation of strained layer semiconductor structures via plastic flow. » In: *Applied Physics Letters* 51.17, pp. 1325–1327. DOI: 10.1063/1.98667 (cit. on p. 12).

Mason, Warren P. (1956). « Physical Acoustics and the Properties of Solids. » In: *The Journal of the Acoustical Society of America* 28.6, pp. 1197–1206. DOI: 10.1121/1.1908593 (cit. on p. 13).

Wortman, J. J. and R. A. Evans (1965). « Young's Modulus, Shear Modulus, and Poisson's Ratio in Silicon and Germanium. » In: *Journal of Applied Physics* 36.1, pp. 153–156. DOI: 10.1063/1.1713863 (cit. on p. 13).

AB, COMSOL. *COMSOL Multiphysics® v. 5.2a* (cit. on p. 14).

Wikipedia, The Free Encyclopedia. *Electronic band structure. (2019, October 31)*. URL: https://en.wikipedia.org/w/index.php?title=Electronic_band_structure&oldid=923958859 (cit. on p. 14).

Bardeen, J. and W. Shockley (1950). « Deformation Potentials and Mobilities in Non-Polar Crystals. » In: *Physical Review* 80.1, pp. 72–80. DOI: 10.1103/PhysRev.80.72 (cit. on p. 15).

Shockley, W. and J. Bardeen (1950). « Energy Bands and Mobilities in Monatomic Semiconductors. » In: *Physical Review* 77.3, pp. 407–408. DOI: 10.1103/PhysRev.77.407 (cit. on p. 15).

Herring, Conyers and Erich Vogt (1957). « Transport and Deformation-Potential Theory for Many-Valley Semiconductors with Anisotropic Scattering. » In: *Physical Review* 105.6, pp. 1933–1933. DOI: 10.1103/PhysRev.105.1933 (cit. on p. 15).

Mohta, N. and S.E. Thompson (2005). « Mobility enhancement. » In: *IEEE Circuits and Devices Magazine* 21.5, pp. 18–23. DOI: 10.1109/MCD.2005.1517386 (cit. on p. 15).

Uchida, K., T. Krishnamohan, K.C. Saraswat, and Y. Nishi (2005). « Physical mechanisms of electron mobility enhancement in uniaxial stressed MOSFETs and impact of uniaxial stress engineering in ballistic regime. » In: *IEEE InternationalElectron Devices Meeting, 2005. IEDM Technical Digest.* Pp. 129–132. DOI: 10.1109/IEDM.2005.1609286 (cit. on p. 15).

3

COHERENT X-RAY DIFFRACTION

Considering the crystallography of three-dimensional crystal structures, the scattering of X-rays by atoms produces sharp peaks in directions determined by the orientation and the symmetry of the crystal. As these Bragg peaks originate from constructive interferences between the sets of discrete atomic parallel planes constituting the sample, they contain information about the atomic arrangement within the sample. This is also the basics of Coherent X-ray Diffraction, the central technique of the experiments presented in this manuscript. In order to understand it, this chapter defines X-rays and synchrotron radiation, then introduces some crystallographic definitions to explain the scattering from a crystal. Finally the concept of coherence is discussed, along with the basic principles of imaging regimes.

In section 3.7 Coherent X-ray Diffraction Imaging and the associated phase retrieval algorithm are presented, with details on the concept of oversampling, theoretical resolution and recent advances in the field. The particular case of the Bragg geometry is introduced, and a typical experimental setup is depicted through the description of the ESRF ID01 beamline, which has welcomed most of the experiments performed throughout this PhD.

3.1 X-RAYS

Since the discovery of "a new kind of rays" by Wilhelm Conrad Röntgen in 1895 (Röntgen, 1895), there has been tremendous progress on the understanding of what X-rays are and how they interact with matter. X-rays are electromagnetic waves with typical wavelengths ranging from 0.01 nm to 10 nm, which correspond to energies in the range of 100 keV to 100 eV. The wavelength associated with a photon is linked to its energy through the Planck constant, according to the De Broglie equation (Feynman, 2006):

$$\lambda[\text{Å}] = \frac{hc}{E} = \frac{12.398}{E[\text{keV}]} \tag{3.1}$$

where h is Planck's constant and c the speed of light. One usually distinguishes soft X-rays (6-100 Å) from hard X-rays (0.1-6 Å) as higher energies imply deeper

penetration of the radiations capable of probing the electron density of matter and determining atomic structure. [1]

Electromagnetic waves are made of synchronized oscillations of electric ($\vec{E}$) and magnetic ($\vec{H}$) fields that are perpendicular to each other but also to the direction of energy and wave propagation ($\vec{k}$). The frequency of oscillation ω defines the wave number $k = \left|\vec{k}\right| = \omega/c = 2\pi/\lambda$ and the mathematical expression of such waves at a position $\vec{R}$ in space and t in time is:

$$\begin{aligned} \vec{E}(\vec{R},t) &= \vec{E}_0 \exp i(\vec{k}\cdot\vec{R} - \omega t) \\ \vec{H}(\vec{R},t) &= \vec{H}_0 \exp i(\vec{k}\cdot\vec{R} - \omega t) \end{aligned} \tag{3.2}$$

where $\vec{E}_0$ and $\vec{H}_0$ are the two constant vectors (whose amplitudes are the electric and magnetic field magnitudes) representing the direction of polarization.

When X-rays interact with atoms, three different situations can happen. First case scenario, atoms absorb the photon which will generate electronic or phonon excitation of the atom. Secondly, the X-ray photon is inelastically scattered, with a loss of energy resulting in a scattered photon with lower frequency than the incident one. Finally, the X-ray photon is elastically scattered and the kinetic energy is conserved. To introduce the methods using third generation Synchrotron sources radiation, we make the assumption that an X-ray photon, after being scattered by an electron, cannot be scattered by another electron again, which is known as the "kinematic" approximation. We will also neglect the effects of the magnetic field and the spin of an electron as magnetic scattering is much weaker than charge scattering (Als-Nielsen and McMorrow, 2001).

3.2 SYNCHROTRON RADIATION

Since the discovery of X-rays, the main limitation has remained the X-ray source. X-rays photons generation have always relied on conversion of the kinetic energy of electrons. Before the first synchrotron radiation source was observed in 1947, the first X-ray source was achieved using the Coolidge tube that employed the principle of thermionic emission. It consists of a tungsten filament that is heated to produce electrons which are then accelerated towards a water-cooled anode by the strong tube voltage. Upon hitting the anode, the electrons decelerate quickly, and lose their excess kinetic energy mostly as heat, and partly as X-ray radiation. In order to cope with the low output intensity caused by the cooling rate, rotating anodes were introduced in the 1960's, and the liquid metal anode in 2000 (Harding et al., 2003). However the difference made by synchrotron radiation devices is still tremendous.

1. In this thesis, the experiments described use hard X-rays with a wavelength of 1.5498 Å (8 keV).

Synchrotron radiation describes radiation from charged particles accelerated to relativistic speed along curved trajectories (Elder et al., 1947). Indeed, any particle moving in a non-uniform fashion produces an electromagnetic field, and at relativistic speed the radiation produced is in the X-ray energy range. This kind of X-ray source is of exceptional intensity and spectral brightness, especially at short wavelengths. In the so-called 2nd generation synchrotron rings, the introduction of bending electromagnets allowed a shrewd exploitation of these radiations in numerous kind of experiments. As described in Figure 3.1a, the application of an uniform magnetic field perpendicularly to the orbital plane forces the relativistic electrons to travel in closed circular path, leading to radiation emission governed by the Lorentz force. In the storage ring, these bending magnets are followed by radio-frequency cavities in order to replenish the loss of energy inherent to the radiation process. The radio-frequency cavities are shaped specifically to achieve resonance and the build up in intensity of the electromagnetic waves. Hence, the charged particles that pass by this oscillating field receive an electrostatic speed boost. Compared to an X-ray tube, the emitted radiation from a bending magnet is highly collimated and covers a broad spectral range. The cone of emission is defined by its angular divergence of $1/\gamma$ where γ is the electron energy in units of the rest mass energy :

$$\gamma = \frac{E_e}{mc^2}$$

At the European Synchrotron - ESRF, the rest mass energy is of 6 GeV, leading to $\gamma = 11.8 \times 10^3$ and a radiation cone of 0.08 mrad. Note that γ can also be expressed as $\frac{1}{\sqrt{1-\frac{v^2}{c^2}}}$ where v is the particle velocity. This formulation highlights the importance of accelerating electrons as close as possible to the speed of light. This is done in a two-step process. First, high energy electrons are emitted by an electron gun and packed in bunches; then they are accelerated by a pulsed electric field : a race-track shaped booster accelerator, 300 m long, is used to make them reach the final energy of 6 GeV.

The third-generation synchrotrons have introduced a new kind of insertion device (ID) in order to deal with the main disadvantages of bending magnets, the limited coverage of hard X-rays and the relative lack of photon flux : undulators (or similarly, wigglers). As depicted in Figure 3.1b, they are magnetic multipole structures placed within the straight sections of the storage ring, and by alternating vertical polarity of magnets they force the electrons to travel in a sinusoidal manner that produces synchrotron radiation. The more periods (N) of dipole, the higher the intensity and the narrower the radiation cone, which is equal to $\frac{1}{\gamma\sqrt{N}}$. Such ID have

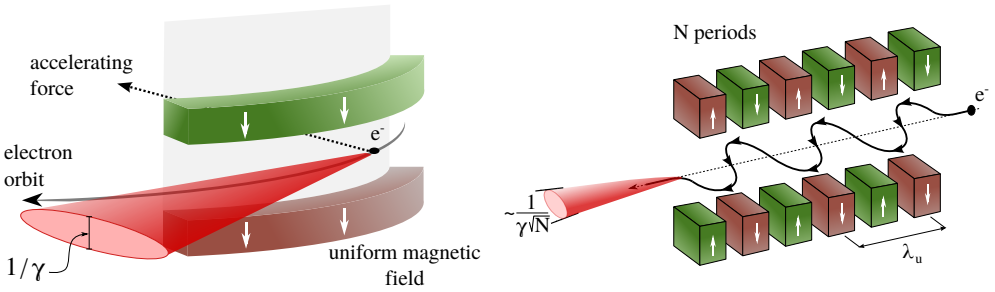

(a) (b)

Figure 3.1 – Usual synchrotron magnetic structures. Green blocks represent North magnetic polarity magnets, red ones represent South magnetic polarity magnets. The white arrows depict the direction of the magnetic field generated by the magnet. (a) Schematic of the fan radiation emitted by a bending magnet. Electrons are bent around a quasi circular path and produce a cone of radiation with an opening angle of $1/\gamma$ where $\gamma = \frac{E_e}{mc^2}$ is the electron energy. Typically, $1/\gamma \approx 0.1$ mrad. (b) Schematic of the radiation emitted by an undulator insertion device (or equivalently a wiggler). Relativistic electrons following a linear path (dashed line) enter the array of 2N dipole magnets that point alternately up and down. The alternating dipole field creates a sinusoidal wave and the electrons radiate at the Lorentz contracted wavelength $\lambda' = \frac{\lambda_u}{\gamma}$ where λ_u is the period of the magnets, also called the undulator wavelength. The cone of radiation is characterized by an opening angle of $\frac{1}{\gamma\sqrt{N}}$, which is typically around 40 µrad.

two different modes of operation that are distinguished by the deflection parameter, which depends on the magnetic field :

$$K = \frac{eB_0\lambda_u}{2\pi m_e c} \tag{3.3}$$

where B_0 is the magnetic field strength, e and m_e are the charge and mass of the electrons and λ_u is the period of the ID, also called ID wavelength. ID with $K \gg 1$ have large oscillation amplitude, wide spectrum, and are called Wigglers, whereas ID with $K \ll 1$ have small oscillation amplitude, produce sharp peaks at the harmonics of the fundamental wavelength and are called Undulators. Hence, Undulators are ideal for coherent diffraction experiments where a highly monochromatic and in-phase photon number is needed. It is the constructive interferences within the radiation cone that leads to the undulator equation (Als-Nielsen and McMorrow, 2001) :

$$\lambda_n(\theta) = \frac{\lambda_u}{2n\gamma^2}\left(1 + \frac{K^2}{2} + \gamma^2\theta^2\right) = \lambda_n(0)\left[1 + \frac{\gamma^2\theta^2}{1 + K^2/2}\right] \equiv \lambda_n(0)\left[1 + \epsilon_\theta\right] \tag{3.4}$$

Equation 3.4describes the radiation harmonic $\lambda_n(\theta)$ of order n, that is emitted under the angle θ with respect to the optical axis.

In the ESRF storage ring, which is 844 m long in circumference, a current of 200 mA circulates through 43 Bending Magnets and IDs. Most of the Coherent Diffraction Imaging experiments take place at ID01, ID10, ID13 and ID16 beamlines.

3.3 CRYSTAL DEFINITIONS

3.3.1 *Crystal lattice*

A crystal is a three-dimensional periodic structure, characterized by its unit cell. The unit cell is the minimal group of atoms representing the periodicity of the crystal, and gets repeated at each point of a regular lattice. The location of each unit cell in "direct space" is defined by a set of vectors $\vec{R_m}$ as :

$$\vec{R_m} = x_m\vec{a} + y_m\vec{b} + z_m\vec{c} \tag{3.5}$$

where x_m, y_m, z_m are integers and $\vec{a}, \vec{b}, \vec{c}$ are the primitive unit cell vectors. Each atom within the unit cell can be described as :

$$\vec{r_n} = x_n\vec{a} + y_n\vec{b} + z_n\vec{c} \tag{3.6}$$

where x_n, y_n, z_n are fractional values between 0 and 1. Then the position of an atom within the whole crystal can be expressed as :

$$\vec{R_m^n} = \vec{R_m} + \vec{r_n} \tag{3.7}$$

Lattice planes (hkl) describe a set of parallel planes whose intersections with the lattice are periodic. The integer Miller indices h, k and l are defined so that the (hkl) planes intersect the crystal principal axes at a/h, b/k and c/l as illustrated in Figure 3.2. For a cubic crystal, the interplanar distance d_{hkl} is easily calculated as :

$$d_{hkl} = \frac{a}{\sqrt{h^2 + k^2 + l^2}} \tag{3.8}$$

And one defines a "reciprocal space" lattice with reciprocal basis vectors $\vec{a^*}, \vec{b^*}$ and $\vec{c^*}$ as :

$$\begin{aligned} \vec{a^*} &= 2\pi\frac{\vec{b}\times\vec{c}}{\vec{a}\cdot(\vec{b}\times\vec{c})} \\ \vec{b^*} &= 2\pi\frac{\vec{c}\times\vec{a}}{\vec{b}\cdot(\vec{c}\times\vec{a})} \\ \vec{c^*} &= 2\pi\frac{\vec{a}\times\vec{b}}{\vec{c}\cdot(\vec{a}\times\vec{b})} \end{aligned} \tag{3.9}$$

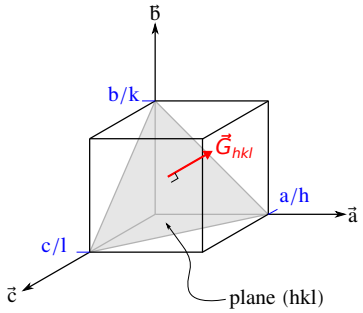

Figure 3.2 – Miller indices and reciprocal lattice vector. The (hkl) plane is defined as the plane that intercepts crystallographic axes $\vec{a}, \vec{b}$ and $\vec{c}$ at a/h, b/k and c/l respectively, where a, b and c are the lattice constants. The normal to the (hkl) plane defines the direction of the reciprocal lattice vector $\vec{G_{hkl}}$, whose norm is equal to $2\pi/d_{hkl}$.

[2]

The location of reciprocal lattice point can be defined by the reciprocal lattice vector $\vec{G_{hkl}}$:

$$\vec{G_{hkl}} = h\vec{a^*} + k\vec{b^*} + l\vec{c^*} \tag{3.10}$$

which is perpendicular to the direct space plane (hkl), and whose length is $\left|\vec{G_{hkl}}\right| = \frac{2\pi}{d_{hkl}}$.

3.3.2 *Bragg's Law*

Consider a set of parallel (hkl) planes separated by spacing d_{hkl}. Two parallel incident plane waves of X-rays are scattered from different planes with a path length difference of $2d_{hkl}\sin(\theta)$, where 2θ is the angle between the incident and the exit wave. Hence, as geometrically explained from Figure 3.3, the only way to observe constructive interferences between the two scattered spherical waves is when their phases are equal, *i.e.* when the path length difference is equal to a multiple of λ. This corresponds to Bragg's Law (Bragg, 1929):

$$\lambda = 2d_{hkl}\sin\theta \tag{3.11}$$

The 2θ angle describes the experimental geometry of constructive interference. Every 2θ angle at which interference occurs is called a Bragg peak. However, Bragg's Law expressed in equation 3.11 only contains scalar information and nothing about

2. Note that the presence of 2π in the expression of basis vectors is written in agreement with the "physicist convention", and not the "crystallographic convention".

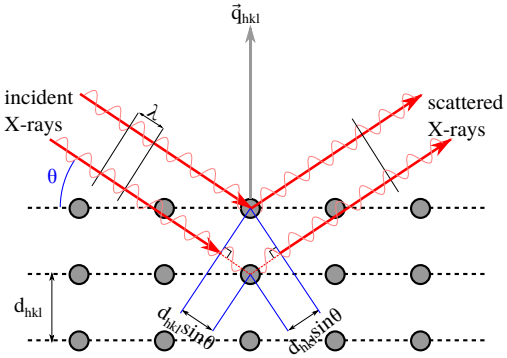

Figure 3.3 – Bragg's Law. Scheme of Bragg Scattering Geometry for a symmetric diffraction experiment. Constructive interference between X-rays incident on a set of parallel (hkl) planes only occurs when the path length difference $2d_{hkl}\sin\theta$ is equal to the incident wavelength λ, see equation 3.11.

directional components. To address this, we introduce the wavevector transfer $\vec{q_{hkl}}$ local to the Bragg peak :

$$\vec{q_{hkl}} = \vec{k_f} - \vec{k_i} \tag{3.12}$$

where $\vec{k_i}, \vec{k_f}$ are the incident and scattered wavevectors, with $\left|\vec{k_i}\right| = \left|\vec{k_f}\right| = \left|\vec{k}\right| = \frac{2\pi}{\lambda}$ from the kinetic energy conservation. Since the reciprocal lattice vector $\vec{G_{hkl}}$ is by definition perpendicular to the scattering (hkl) planes, one can write the lattice plane locations as $\vec{r} = d_{hkl}\frac{\vec{G_{hkl}}}{\left|\vec{G_{hkl}}\right|}$. From Figure 3.3, one can see that there is a path length difference between the two scattered waves, that is :

$$\frac{\vec{k_f}\cdot\vec{r}}{|k|} - \frac{\vec{k_i}\cdot\vec{r}}{|k|} = \frac{1}{\left|\vec{k}\right|}\left[(\vec{k_f} - \vec{k_i})\cdot\vec{r}\right] = \frac{1}{\left|\vec{k}\right|}(\vec{q_{hkl}}\cdot\vec{r})$$

That path length results in a phase difference, equals to $\frac{1}{\left|\vec{k}\right|}(\vec{q_{hkl}}\cdot\vec{r}) \times \frac{2\pi}{\lambda} = \vec{q_{hkl}}\cdot\vec{r}$. From Bragg's law, the phase difference must be equal to some multiple of 2π for constructive interference to occur :

$$\begin{aligned} \vec{q_{hkl}}\cdot\vec{r} = \vec{q_{hkl}}\cdot\frac{\vec{G_{hkl}}}{\left|\vec{G_{hkl}}\right|} &= 2\pi \\ \implies \vec{q_{hkl}}\cdot\frac{\vec{G_{hkl}}}{\left|\vec{G_{hkl}}\right|} &= \frac{2\pi}{d_{hkl}} \\ \implies \vec{q_{hkl}}\cdot\vec{G_{hkl}} &= 2\pi|\vec{G_{hkl}}|^2 \end{aligned} \tag{3.13}$$

Therefore, constructive interference only occurs when $\vec{q_{hkl}} = 2\pi\vec{G_{hkl}}$ which is known as the Laue condition.

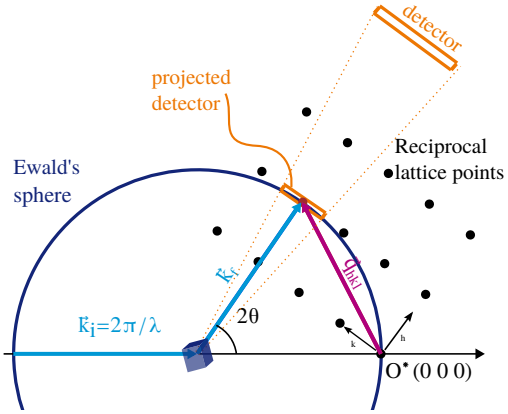

Figure 3.4 – Ewald sphere construction in 2D. The Bragg condition is satisfied for any reciprocal lattice point that lies on the circle ($\vec{q} = 2\pi\vec{G_{hkl}}$). The origin of reciprocal space is denoted as O^* and is defined as the intersection of the Ewald sphere of radius $\frac{2\pi}{\lambda} = |\vec{k_i}| = |\vec{k_f}|$, and the incident wavevector $\vec{k_i}$. The detector is place so that it is perpendicular to the scattered wavevector $\vec{k_f}$ and the intersected part of the diffraction pattern with the detector is considered flat.

3.3.3 *Ewald sphere*

In order to get a geometrical understanding of the Bragg condition in reciprocal space and its experimental consequences, the Ewald's sphere construction must be understood. As shown in Figure 3.4, Ewald's sphere is centered on the crystal, of radius $\frac{2\pi}{\lambda}$ in reciprocal space, where the incident wavevector $\vec{k_i}$, and scattered wavevector $\vec{k_f}$, are equal in norm to the radius. The origin of reciprocal space is defined as the intersection of sphere and $\vec{k_i}$. Since $\left|\vec{k_i}\right| = \left|\vec{k_f}\right| = \frac{2\pi}{\lambda}$ any point (h,k,l integers) of the discrete reciprocal lattice lying on the Ewald's sphere envelope will fulfill the Bragg condition ($\vec{q} = \vec{k_f} - \vec{k_i} = 2\pi\vec{G_{hkl}}$) and a detector located on this spot will record the corresponding diffraction pattern. With today's detector sizes and with an X-ray energy around 8 keV, the discrepancy between the Ewald's sphere and the detector plane is about one pixel at the very edges of the detector, thus the recorded cross-section through the diffraction pattern can be considered flat. Indeed, the maximal distortion Δ at the edge of the detector is defined as a function of the half solid angle of the detector Ω :

$$\Delta = \frac{2\pi}{\lambda}\left(1 - \cos(\Omega)\right)$$

at 8 keV, $\lambda = 0.155$ nm and with a 55 µm pixel size detector of 516 pixels, placed at a distance of 1.2 m from the sample, the maximal distortion is approximately 2.8×10^{-3} nm^{-1}, which corresponds to the reciprocal extent of about 1.5 pixel.

3.4 CLASSICAL SCATTERING

Readers interested in a full derivation are invited to look at texts by Warren (Warren, 1990), Als-Nielsen and McMorrow (Als-Nielsen and McMorrow, 2001), Coppens (Coppens et al., 1992) or Guinier(Guinier, 1994).

3.4.1 *Scattering from perfect crystals*

The scattering amplitude A of a crystal is described by the summation of the atomic scattering factors f_j of each atom j, which is the Fourier Transform (FT) of the electron density of an atom, multiplied by a phase factor $e^{i(\vec{q}\cdot\vec{R_m^n})}$ taking into account the phase difference introduced by the atom's location $\vec{R_m^n}$ within the crystal.

$$A(\vec{q}) = \sum_j^N f_j(\vec{q}) e^{i(\vec{q}\cdot\vec{R_m^n})} \tag{3.14}$$

By using equation 3.7, we can rewrite the scattering taking into account that the total number of atoms within the crystal N can be expressed as $N_a \times N_c$ where N_a is the number of atoms in each unit cell and N_c the number of unit cells :

$$A(\vec{q}) = \sum_m^{N_c}\sum_n^{N_a} f_n(\vec{q}) e^{i\vec{q}\cdot(\vec{R_m}+\vec{r_n})} = \underbrace{\left(\sum_m^{N_c} e^{i\vec{q}\cdot\vec{R_m}}\right)}_{Lattice}\underbrace{\left(\sum_n^{N_a} f_n(\vec{q}) e^{i\vec{q}\cdot\vec{r_n}}\right)}_{Structure} \tag{3.15}$$

Thus, the scattering amplitude is made of two components, being a form factor $L(\vec{q})$ and a structure factor F_{hkl}. The former is directly related to the envelope of the crystal, its shape, and lead the shape of the resulting intensity distribution. The latter is the FT of the electron density inside the unit cell and gives the relative intensity of the reflections. The structure factor is evaluated at Bragg condition $\vec{q_{hkl}} = 2\pi\vec{G_{hkl}}$ and thus gives information about the allowed reflections, known as the selection rules[3]. If waves scattered from the atoms in the unit cell interfere destructively, $F_{hkl} = 0$, there will be no intensity, hence the reflection is "forbidden". Space groups, or groups of symmetry, are defined from atoms arrangement within the crystal lattice, for which the selection rules are the same and independent of the chemical composition of the crystal. The knowledge of the selection rules is of fun-

3. For material with diamond structure (two identical, interpenetrating face-centered-cubic lattices - *i. e.* atoms at each corner of the cube and six atoms at each face of the cube - offset by $\frac{1}{4}[111]$) as silicon and germanium, the structure factor derives $F_{hkl} = f_{atom}\left(1 + e^{i\pi(k+l)} + e^{i\pi(h+l)} + e^{i\pi(h+k)}\right)\left(1 + e^{i\pi(h+k+l)/2}\right)$. This leads to the selection rules: for hkl all even/all odd; if $h+k+l = 4n$ then $F_{hkl} = 8f_{atom}$, if $h+k+l = 2(n+1)$ then $F_{hkl} = 0$ and if $h+k+l = 2n+1$ then $F_{hkl} = 4f_{atom}(1 \pm i)$. It results in three kind of qualitative reflection peaks: strong, medium and null. Note that at 8 KeV $f_{Si} = 14.26 + 0.32i$, $f_{Ge} = 30.9 + 0.92i$.

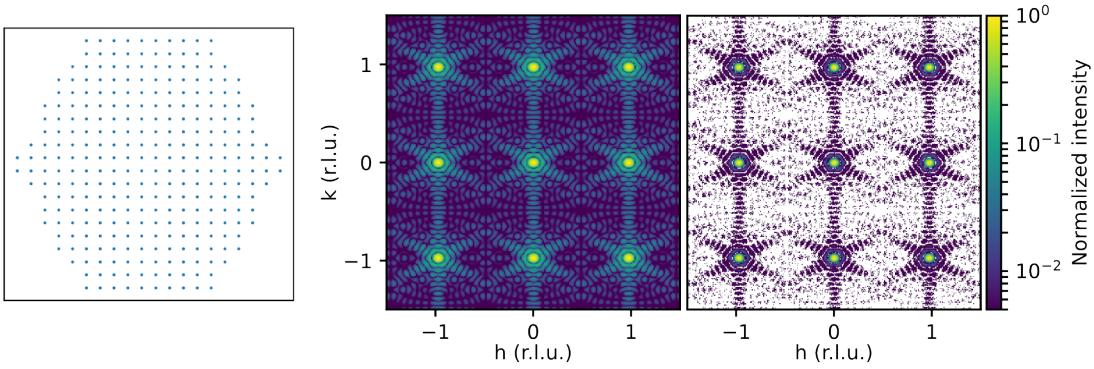

Figure 3.5 – Hexagonal crystal (left) and the results of the simulation of its normalized diffraction map, both without (middle) and with (right) Poisson noise. The diffracted intensity consists of a series of Fourier Transforms of the shape of the crystal located at finite reciprocal lattice points.

damental importance in the determination of the crystal symmetry in a diffraction experiment. (Warren, 1990; Stangl et al., 2013)

In the case where the crystal lattice can be described by a parallelepipedic envelope made of N_1, N_2 and N_3 unit cells along each direction $\vec{a_1}, \vec{a_2}$ and $\vec{a_3}$, the corresponding intensity $I(\vec{q}) = |A(\vec{q})|^2 \propto |L(\vec{q})|^2$ can be derived with the help of a geometric series approach :

$$\begin{aligned} I(\vec{q}) = F_{hkl}^2 \, |L(\vec{q})|^2 \alpha & \left| \sum_m^{N_c} e^{i\vec{q}\cdot\vec{R_m}} \right|^2 \\ \alpha & \left| \left(\sum_{m_1=0}^{N_1-1} e^{im_1\vec{q}\cdot\vec{a_1}} \right) \left(\sum_{m_2=0}^{N_2-1} e^{im_2\vec{q}\cdot\vec{a_2}} \right) \left(\sum_{m_3=0}^{N_3-1} e^{im_3\vec{q}\cdot\vec{a_3}} \right) \right|^2 \\ & = \left| \prod_{j=1}^{3} \left(\frac{\sin\left(N_j \frac{\vec{q}\cdot\vec{a_j}}{2}\right)}{\sin\left(\frac{\vec{q}\cdot\vec{a_j}}{2}\right)} \right) \right|^2 \end{aligned} \tag{3.16}$$

Note that the Laue condition is found again as the intensity is maximized when $\frac{\vec{q}\cdot\vec{a_j}}{2} = n\pi$, which is another way to find the construction of the reciprocal lattice base vectors (equation 3.9).

Let us remind that a crystal is a three-dimensional periodic structure made from the repetition of unit cells, which are the basis repeated at each point of a uniform lattice. This is basically the definition of a convolution operator, known as folding, that lays the foundations of Fourier theory. Let f and g be two functions defined in space, then their convolution is defined as :

$$(f \otimes g)(x) = \int_{\infty}^{-\infty} f(x')g(x - x')dx \tag{3.17}$$

Taking the FT of such an operation leads to the useful convolution theorem: the FT of the convolution of two functions is the point-wise product of their FTs, or equivalently, the FT of the product of two functions is equal to the convolution of their FTs :

$$\begin{aligned} \mathcal{F}(f \otimes g) &= \mathcal{F}(f)\mathcal{F}(g) \\ \mathcal{F}(f \cdot g) &= \mathcal{F}(f) \otimes \mathcal{F}(g) \end{aligned} \tag{3.18}$$

Hence, as the crystal is a convolution of a basis and an envelope function, its diffraction pattern is the product of the FT of the unit cell and the FT of the crystal's shape. The resulting periodic function exhibits local inversion symmetry at the origin of reciprocal space. Figure 3.5 shows a hexagonal crystal and its simulated diffraction map, both with and without photon noise. The streaks in the reciprocal space are clear signature of the facets of the crystal. Because the hexagonal crystal has no defects, the intensity distribution at each Bragg peak is the same and centrosymmetric.

3.4.2 *Scattering from crystals in the presence of strain*

In the case of a perfect crystal, the electron density is real[4] and its FT thus hermitian. We already showed that the scattering amplitude from a crystal is proportional to the FT of the crystal's electron density :

$$A(\vec{q}) \propto \mathcal{F}\left[\rho(\vec{r})\right] = \int \rho(\vec{r}) e^{i\vec{q}\cdot\vec{r}} dV \tag{3.19}$$

Scattering from a strained crystal can in theory be described as the FT of its electron density, but it would require a subatomic resolution which we cannot achieve. Thus, we describe the scattering by adding a complex factor which describes the displacement, either for an atom or for a group of atom (*e. g.* inside a voxel). A strained region within a crystal is basically a block of material displaced from its original location by a displacement vector $\vec{u}(\vec{r})$. As depicted in Figure 3.6, this displacement induces a phase difference between scattered X-rays, of $\vec{q_{hkl}} \cdot \vec{u}(\vec{r})$. Then the scattered amplitude of the whole crystal can be rewritten by multiplying the scattered amplitude of each atom by an additional phase factor $e^{i\vec{q_{hkl}}\cdot\vec{u}(\vec{r})}$, which is still a FT:

4. This is not strictly true : in resonant scattering, one takes into account the resonance between the photon and the bound electron that leads to an imaginary atomic scattering factor $f = f^0 + f' + if''$, where f^0 is the Thomson scattering, which is energy-independent, f' and f'' are the resonant scattering terms. Generally $|f'| \ll f^0$ and $|f''| \ll f^0$, hence the assumption of a real electron density.

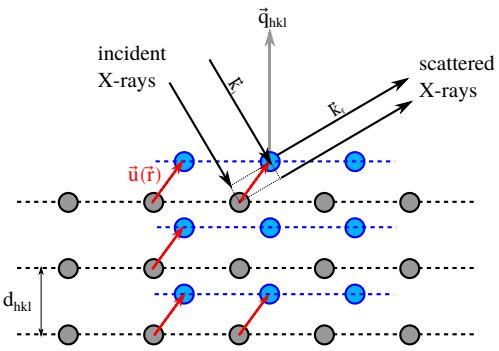

Figure 3.6 – Displacement $\vec{u}(\vec{r})$ in the crystal lattice leads to the introduction of a phase shift between the scattered X-rays. This phase shift is derived from the optical path length difference and is equal to $\vec{k_f} \cdot \vec{u}(\vec{r}) - \vec{k_i} \cdot \vec{u}(\vec{r}) = \vec{q_{hkl}} \cdot \vec{u}$. Thus, by retrieving the phase one also probes the projected displacement fields from the Bragg scattered intensity when shinning X-rays on a crystal in Bragg condition. Adapted from (Robinson and Harder, 2009)

$$A(\vec{q}) \propto \int \rho(\vec{r}) e^{i\vec{q}\cdot\vec{u}(\vec{r})} dV e^{iq\vec{_{hkl}}\cdot\vec{u}(\vec{r})} = \mathcal{F}\left[\rho(\vec{r}) e^{iq\vec{_{hkl}}\cdot\vec{u}(\vec{r})}\right]$$
$$= \mathcal{F}[\rho'(\vec{r})] \quad (3.20)$$

The complex-valued quantity $\rho'(\vec{r})$ is sometimes called the effective electron density (Stangl et al., 2013). Note that, by specifying $\vec{r} = \vec{R^n_m} + \vec{u}(\vec{r})$, the derivation above is equivalent to rewriting the phase factor of equation 3.19 as :

$$\vec{q} \cdot \vec{r} = \vec{q} \cdot (\vec{R^n_m} + \vec{u}(\vec{r})) = \vec{q} \cdot \vec{R^n_m} + q\vec{_{hkl}} \cdot \vec{u}(\vec{r}) + (\vec{q} - q\vec{_{hkl}}) \cdot \vec{u}(\vec{r}) \quad (3.21)$$

Since the scattering is measured close to a Bragg peak, $|(\vec{q} - q\vec{_{hkl}}) \cdot \vec{u}| \ll 1$, the third term of equation 3.21 can be neglected. This approximation is known as the Takagi's approximation (Takagi, 1969), which is equivalent to assuming small distortions of the lattice. Ultimately, the phase retrieved from nanobeam experiments in Bragg geometry only contains information about the projection of the displacement onto the $\vec{q}$ direction:

$$\phi_{hkl} = q\vec{_{hkl}} \cdot \vec{u}(\vec{r}) = |q\vec{_{hkl}}| \, (\hat{q_{hkl}} \cdot \vec{u}(\vec{r})) = |q\vec{_{hkl}}| \, u_{hkl} \quad (3.22)$$

Moreover, from equation 3.13 we write $|q\vec{_{hkl}}| = \frac{2\pi}{d_{hkl}}$ and finally:

$$\phi_{hkl} = 2\pi \frac{u_{hkl}}{d_{hkl}} \quad (3.23)$$

Note that there are two ways of calculating scattering maps around a Bragg reflection from strained nanostructures, either by using approximations and Discrete

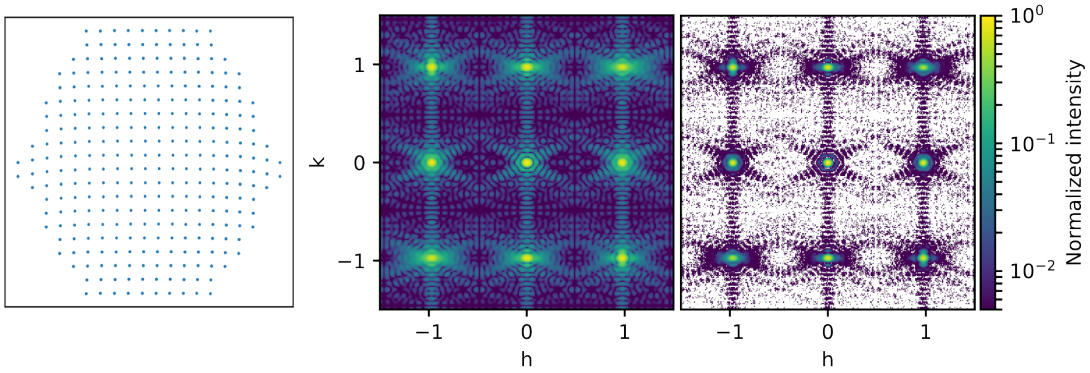

Figure 3.7 – Crystal of hexagonal shape with a displacement field - scatter plot - (left) and the results of the simulation of its normalized diffraction map, both without (middle) and with (right) Poisson noise. Note the effect of the added strain on the intensity distribution, which now depends on the Bragg reflection. All the peaks carrying apart the (00) transmission reflection are affected by the strain field inside the crystal.

Fourier Transform (DFT) or via individual atomic positions. Equation 3.20 is generally used to compute scattering near Bragg reflections (Pfeifer et al., 2006; Minkevich et al., 2007; Labat et al., 2007; Harder et al., 2007). The main advantage is that it allows the use of fast implementations of the FT, significantly increasing the computing speed of the scattering, which is in practice required for phase retrieval algorithms (Fienup, 1982; R. W. Gerchberg, 1972) due to the large number of FT these require.

Figure 3.7 shows the same hexagonal crystal as in Figure 3.5 with some displacement fields introduced on both direction. Now we see a change in the intensity : the shape of the scattered intensity changes according to the Bragg peaks and is no longer centrosymmetric. Only the (00) reflection remains the same, as it is only dependent on the shape of the crystal and not sensitive to any displacement.

3.5 COHERENCE

X-ray beams are not fully coherent because the relationship between phases of the complex field at any two points in space and time is not predictable, *i. e.* the beam does not consist simply of an "ideal" plane wave and is always coherent up to a certain degree. A general way to quantify coherence of an electromagnetic field is the mutual coherence function (Born and Wolf, 2013):

$$\Gamma(\vec{R}_1, \vec{R}_2, \tau) = \left\langle E(\vec{R}_1, t) E^*(\vec{R}_2, t+\tau) \right\rangle \tag{3.24}$$

where the brackets denote time-averaging and E^* the complex conjugate of E. Therefore, the mutual coherence is the autocorrelation in time and space of the elec-

tromagnetic field. From it, the complex degree of coherence (or mutual coherence function) is derived:

$$\gamma(\vec{R_1}, \vec{R_2}, \tau) = \frac{\Gamma(\vec{R_1}, \vec{R_2}, \tau)}{\sqrt{\left\langle I(\vec{R_1}, t)\right\rangle \left\langle I(\vec{R_2}, t)\right\rangle}} \tag{3.25}$$

where $I(\vec{R}, t)$ is the intensity, *i.e.* the square modulus of E. Then $\left\langle I(\vec{R}, t)\right\rangle$ is the expectation value of the intensity at position R. The complex degree γ has values between 0, where points R_1 and R_2 are mutually incoherent, and 1, where full coherence is achieved. However, this 7-dimensional dataset, 2×3 space coordinates and 1 time coordinate, is not easily expressed and one would rather refer to scalar quantities such as coherence lengths which are more easily calculated, for what one can consider a "nice" beam (*e.g.* Gaussian shape), as for instance the half-width at half maximum (Lin et al., 2003).

The framework of geometrical optics also provides a definition of such coherence lengths, as in Figure 3.8. In the direction of the beam propagation, the longitudinal (or temporal) coherence length is related to the monochromaticity of the X-ray beam:

$$\Lambda_L = \frac{\lambda^2}{2\delta\lambda} \tag{3.26}$$

where $\delta\lambda$ defines the spectral width and thus comes from the bandwidth of the monochromator ($\frac{\delta\lambda}{\lambda}$). The transverse coherence length is limited by the source size. Consider a source of incoherent emitters confined to a transverse area of diameter S. Two points within the sample located at a distance D from the source will see it with the same relative phase up to a separation distance Λ_T:

$$\Lambda_T = \frac{\lambda D}{2S} \tag{3.27}$$

For an undulator and $E = 8$ keV photons, using a double Silicon (111) monochromator, the longitudinal coherence length equals to $\Lambda_L = 0.5$ µm. On the ID01 ESRF beamline (Leake, G. A. Chahine, et al., 2019), the source size equals to 12 µm (V) $\times$ 120 µm (H) and is located 118 m ahead of sample, leading to transverse coherence lengths of 800 µm (V) $\times$ 80 µm (H). The consequence of these lengths is that most samples are not fully illuminated by the coherent portion of the beam. Typically, the coherent portion of the beam is selected and then focused onto a sample. Inevitably the introduction of any optical component in the beam path provides an opportunity to degrade the coherence, therefore typically optics are kept to a minimum.

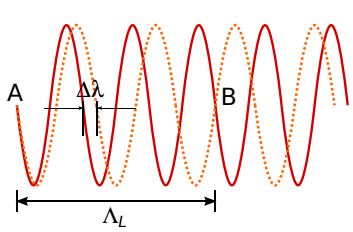

(a) Longitudinal coherence

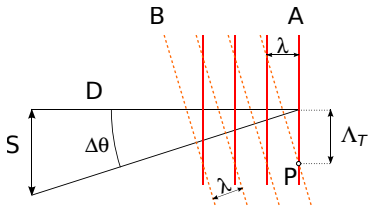

(b) Transverse coherence

Figure 3.8 – Coherence lengths. (a) Longitudinal coherence length, Λ_L is defined as the length over which two waves of wavelengths λ and $\lambda + \Delta\lambda$, propagating along the same direction, become out of phase. $\Lambda_L = AB$ as at point A, they are in phase, whereas at point B they become out of phase. Adapted from (Veen and Pfeiffer, 2004). (b) Transverse coherence is limited by the source size. Two waves A and B of equal wavelength, radiated by a source of size S, propagate in slightly different directions and coincide at the point P. The transverse coherence length is defined as the distance traveled along wavefront A from point P in both directions (vertical and outboard) at which destructive interference occurs. One can extract the geometric relationship $\tan\Delta\theta = \frac{\lambda}{2\Lambda_T} = \frac{S}{D}$. Adapted from (Als-Nielsen and McMorrow, 2001).

3.6 NOTE ON IMAGING REGIMES

3.6.1 *Propagation of a complex field*

Let a square aperture of size a be illuminated by a monochromatic plane wave of unit amplitude. The distribution of complex field immediately behind the aperture is :

$$U(\eta, \xi, z = 0) = \text{rect}\left(\frac{\eta}{a}\right) \text{rect}\left(\frac{\xi}{a}\right) \tag{3.28}$$

The Fresnel diffraction equation can be used in its convolution form (Winthrop and Worthington, 1966) to express the propagation of the complex field, yielding :

$$U(x, y, z) = \frac{e^{ikz}}{i\lambda z} \iint_{-a/2}^{a/2} \exp\left\{i\frac{\pi}{\lambda z}\left[(x-\eta)^2 + (y-\xi)^2\right]\right\} d\eta d\xi \tag{3.29}$$

The two dimensions being separable, the expression can be written as the product of two separated one-dimensional integrals :

$$U(x, y, z) = \frac{e^{ikz}}{i\lambda z} I_X(x)\, I_Y(y) \tag{3.30}$$

with :

$$\begin{aligned} I_X(x) &= \frac{1}{\sqrt{\lambda z}} \int_{-a/2}^{a/2} \exp\left[i\frac{\pi}{\lambda z}(\eta - x)^2\right] d\eta \\ I_Y(y) &= \frac{1}{\sqrt{\lambda z}} \int_{-a/2}^{a/2} \exp\left[i\frac{\pi}{\lambda z}(\xi - y)^2\right] d\xi \end{aligned} \tag{3.31}$$

These two integrals being identical, one can focus on one of them, $I_X(x)$, and make the following substitution: $\eta' = \eta/\sqrt{\lambda z}$, yielding :

$$I_X(x) = \int \exp\left[i\pi\left(\eta' - \sqrt{N_F}\frac{x}{a}\right)^2\right] d\eta' \tag{3.32}$$

where the Fresnel number has been introduced as the dimensionless quantity N_F describing the geometry of the problem :

$$N_F = \frac{(a/2)^2}{\lambda z} \tag{3.33}$$

We then define the Fresnel distance z_f for which $N_F = 1$:

$$z_F = \frac{(a/2)^2}{\lambda} \tag{3.34}$$

Note that, for fixed a and λ, as the propagation distance z increases, the Fresnel number N_F decreases and the normalized space coordinate $\sqrt{2N_F}\frac{x}{a}$ enlarges the width of the diffraction pattern.

3.6.2 *Three imaging regimes*

Let the distance between the source and the sample be D_o and the detector-to-sample distance be D. The defocusing distance is introduced as :

$$D_d = \frac{D_o D}{D_o + D} \tag{3.35}$$

The distance D_o is fixed, at a value large enough $(D_0 \gg D)$ to approximate the incident X-rays as plane waves, so that the defocussing distance is $D_d \approx D$. The different scattering elements within the sample interact with the incident X-rays acting as sources of spherical waves. Before discussing imaging using a coherent source, the different imaging regimes in which diffraction experiments can be conducted, are introduced. One discriminates three regimes : contact, Fresnel and Fraunhofer, according to the Fresnel number, or equivalently to the distance between the sample and the detector.

In the contact regime, the detector is set right behind the sample, $N_F \gg 1$ *i.e.* $D_d \ll z_f$ and the phase difference between the scattered waves is negligible. It is the absorption difference between the volume elements within the sample that creates the contrast of the recorded image which appears edge-enhanced.

In the Fresnel regime, also named near-field, the distance between detector and sample is $D_d \lesssim z_f$ and $N_F \approx 1$. Interferences between scatterers inside the sample

will build up and the intensity distribution of the recorded image will lose resemblance to the original sample. The scattered amplitude conveys the information of the spherical curvature of the emitted waves.

In the Fraunhofer regime, or far-field, the detector is placed far away from the sample $D_d \gg z_f$ and $N_F \ll 1$. In such case, the spherical curvature of the emitted waves can be neglected. Therefore the derivation of scattered amplitude above holds true, and will be used as framework for the remainder of this work.

Figure 3.9 shows a series of graphs of the intensity distribution along the x axis ($y = 0$) for various normalized distances from the aperture, as represented by different Fresnel numbers, depicting the differences between the three imaging regimes defined above.

3.7 COHERENT IMAGING PRINCIPLES

Coherent beams are especially needed for techniques relying on far-field diffraction in order to probe the atomic structure. In simple words, coherence is an ideal property of wave packets that enables stationary (*i. e.* temporally and spatially constant) interference. Thus, the notion of "coherent scattering" can sound odd as any X-ray scattering experiment relies on interferences between X-rays scattered by different parts of the studied material. Nonetheless, there are limitations to coherent X-rays scattering.

On the one hand, the finite size of the source along with monochromaticity yield finite values for the transverse and longitudinal coherence lengths (see 3.5). On the other hand, samples are not "coherent" with the dimension of the beam, as most crystals are not perfect, due to the presence of grains and mosaicity. Moreover, different micro-grains inside the same crystal can contribute to interferences, but given a large enough number of contributions, only the average scattering will remain. That is why in practice Coherent Diffraction Imaging (CDI) experiments will be performed on objects smaller than the coherent volume of the beam. However, at short wavelength the photon degeneracy D_{photon} yielding the number of photons present in the coherent volume is highly dependent on the brilliance of the source :

$$D_{photon} = (8.3 \times 10^{-25}) B \lambda^3 \tag{3.36}$$

where B is the brilliance and λ is in units of Å. Therefore, CDI requires a high brilliance and thus the technique relies on the development of undulator-based third generation synchrotron radiation sources. With the emergence of free-electron laser (FEL) sources, even higher brilliance can be obtained with the opportunity to reach photon degeneracy of approximately ten orders of magnitude higher than

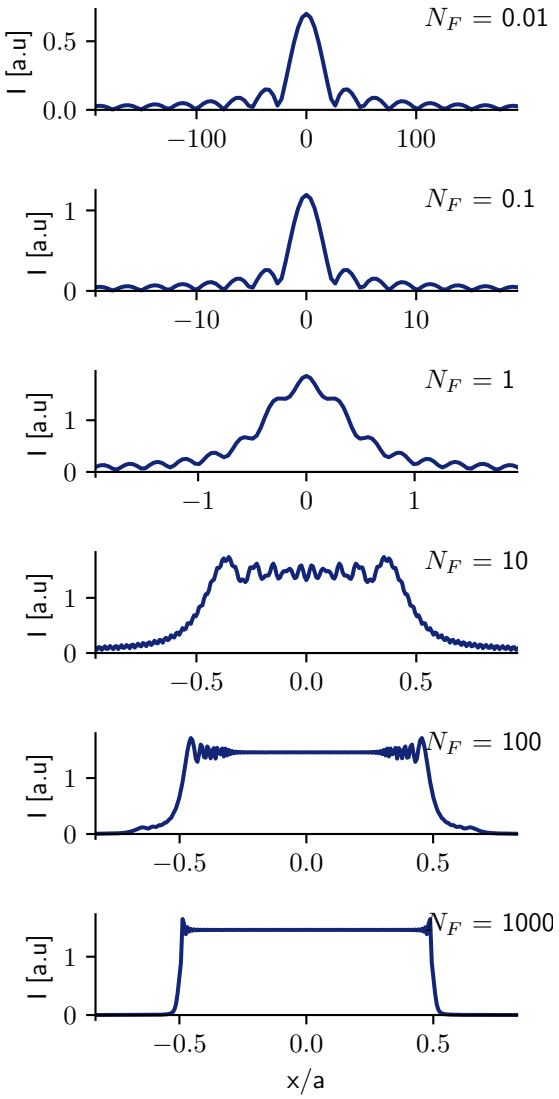

Figure 3.9 – Profiles of diffraction patterns at different distances from a square aperture of size a. The width of the diffraction pattern increases as the Fresnel number N_F shrinks. For cases where $N_F \approx 1$, the regime is the Fresnel regime or near-field. When $N_F \ll 1$, it is Fraunhofer diffraction or far-field where interference fringes from the width of the aperture are easily visible. And for $N_F \gg 1$, the propagation distance is small enough to stay in the contact regime, providing a direct image of the aperture.

undulator-based synchrotron radiation. However, FELs deliver a sufficiently high power to destroy most samples in only one shot thus the "Diffract and Destroy" technique (Spence and Hawkes, 2008; Schmidt et al., 2008). Moreover, FELs are mostly interesting for the time-resolution, not necessarily for the average flux.

CDI gathers the 3D non-destructive and lens-less probing techniques that enable structure determination of noncrystalline specimens and nanocrystals with theoretical resolution only limited by the wavelength of the X-ray beam. Experimentally, the number of scattered photons and the recorded extent of the diffraction in reciprocal space limit the resolution. Diffraction microscopy, holography and ptychography are typical examples of CDI techniques that exploit the transverse coherence properties of third-generation synchrotron X-ray to encode image information and overcome the technical limitations caused by imperfect X-ray optics. Ptychography is an extension of classical CDI where instead of recording the diffracted intensities from one sample of size smaller than the X-ray beam, multiple diffraction patterns are recorded from overlapping areas of the sample that is bigger than the X-ray beam (Hoppe, 1969; Rodenburg and Bates, 1992; Rodenburg, Hurst, et al., 2007; Thibault, Dierolf, Menzel, Bunk, David, et al., 2008). With a first successful result from by Miao et al. in 1999 on gold dots of around 500 nm diameter with resolution of approximately 75 nm (Miao, Charalambous, et al., 1999), CDI has widely benefited from the developments of X-ray focusing optics (Snigirev and Snigireva, 2008) such as compound refractive lenses (CRL)(Snigirev, Kohn, et al., 1998), Kirckpatrick-Baez mirrors (KB)(Kirkpatrick and Baez, 1948) and Fresnel-zone plate (FZP)(Baez, 1961; *High-efficiency multilevel zone plates for keV X-rays | Nature* n.d.) in order to collect the scattering of single objects with a size smaller than 100 nm, and allows reconstruction with resolution around $\sim$ 10 nm (Sakdinawat and Attwood, 2010).

3.7.1 *The phase problem*

As derived earlier, within the kinematical approximation, if we neglect the spatial variation of amplitude and phase of the X-ray wavefield at its focal point, a crystal's structural information $\rho(\vec{r})$ is directly related to its scattering amplitude $A(\vec{q})$ in the far-field via a FT :

$$A(\vec{q}) = \mathcal{F}\left[\rho(\vec{r})\right] \tag{3.37}$$

Then the intensity recorded on a detector is the square modulus of the amplitude :

$$I(\vec{q}) = |A(\vec{q})|^2 \tag{3.38}$$

which differs from the complex waveform of $A(\vec{q}) = |A(\vec{q})| e^{i\phi(\vec{q})}$ itself, and all phase information, $\phi = \vec{q} \cdot \vec{r}$ is thus lost : the inherent 'Phase Problem' of X-ray Crys-

tallography, which is a classic inverse problem. Retrieving these information then requires additional constraints and the use of iterative methods. Before presenting these methods, the fundamental notion of oversampling has to be derived.

3.7.2 *Oversampling*

Oversampling is defined by the Nyquist-Shannon theorem (Shannon, 1949) which states that in order to correctly retrieve a signal from a set of sample points, the sampling frequency must be higher than the Nyquist sampling frequency. For instance, diffraction from a slit can be described by the FT of a step function, *i. e.*, a sinc, and the associated Nyquist frequency corresponds to at least one point per sinc fringe. In order to understand how this theory can be extended to the phase problem, consider a one dimensional object with a complex-valued density $f(x) = |f(x)|\, e^{i\phi(x)}$ and its FT $F(q) = \mathcal{F}[f(x)]$. Experimentally, only the magnitude of the FT is measured :

$$|\mathcal{F}[f(x)]| = |F(q)| = \left| \int f(x) e^{iqx} dx \right| \tag{3.39}$$

where x is the real space coordinates and q the reciprocal (Fourier) space coordinates. One can sample x and q into N number of pixels from 0 to $(N-1)$. Let δx be the width of each real space pixel, the total extent of the real space is $\Delta x = N\delta x$. The pixel size in Fourier space is by definition $\delta q = \frac{2\pi}{\Delta x} = \frac{2\pi}{N\delta x}$. Equation 3.39 can thus be rewritten as its discrete Fourier transform equivalent, a set of N equations with $2N$ unknowns ($|f(x)|$ and $\phi(x)$ for each q) :

$$|F(q_i)| = \left| \sum_{j=0}^{N-1} f(x_j) e^{iq_i x_i / N} dx \right|, \forall i \in [0, N] \tag{3.40}$$

This factor of 2 follows through to 2D and 3D objects as the total number of equations will be N^2 and N^3 with a total number of unknowns of $2N^2$ and $2N^3$ respectively. Thus the problem of phase retrieval is in general underdetermined by a factor of 2 (Miao, Sayre, et al., 1998).

Following this derivation, the condition σ of oversampling is defined as the ratio between the total number of measured points and the number of unknown values. For a 2D object, the condition $\sigma > 2$ corresponds to oversample in each direction by $> 2^{1/2}$ and by $> 2^{1/3}$ for a 3D object. Though, a higher oversampling ratio is better as it leads to a more accurate reconstructed result (Veen and Pfeiffer, 2004).

3.7.3 *Field of view and pixel size*

From a defined detector pixel size and its distance from the sample, the spatial resolutions are defined both in reciprocal space and real space. To retrieve them, consider the propagation of a wave in free-space, using the Huygens-Fresnel principle. An electromagnetic wave A of wavelength λ propagating from a point P of coordinates $(x, y, 0)$ to a point M of coordinates (x_1, y_1, z) reads, discarding prefactors :

$$A_M(x_1, y_1) \propto \int A_P(x, y) e^{i\frac{2\pi}{\lambda}|PM|} dxdy \tag{3.41}$$

In the far field regime, the paraxial approximation holds : the propagation distance $|PM|$ is considered to be close enough to the optical axis, *i. e.* $z \gg \sqrt{x^2 + y^2}$ and $z \gg \sqrt{x_1^2 + y_1^2}$. Thus, the propagation distance can be rewritten in the first order as $|PM| \approx z + \frac{1}{2z}\left[(x_1 - x)^2 + (y_1 - y)^2\right]$, and leads to :

$$A_M(x_1, y_1) \propto \int A_p(x, y) e^{i\frac{2\pi}{\lambda}\frac{x^2+y^2}{2z}} e^{i\frac{2\pi}{\lambda}\frac{x_1^2+y_1^2}{2z}} e^{-i2\pi(x\frac{x_1}{\lambda z} + y\frac{y_1}{\lambda z})} dxdy \tag{3.42}$$

Let $q_x = 2\pi x_1/\lambda z$ and $q_y = 2\pi y_1/\lambda z$. Equation 3.42 derives:

$$A_M(x, y) \propto e^{i\frac{2\pi}{\lambda}\frac{x_1^2+y_1^2}{2z}} \mathcal{F}\left[A_P(\eta, \xi) e^{i\frac{2\pi}{\lambda}\frac{x^2+y^2}{2z}}\right]_{(q_x, q_y)} \tag{3.43}$$

As the detector describes a discrete set of pixels, equation 3.43 has to be discretized as well, involving a discrete FT. Given the detector pixel sizes δx_1 and δy_1, the pixel sizes in reciprocal space δq_x and δq_y are :

$$\begin{cases} \delta q_x = 2\pi \frac{\delta x_1}{\lambda z} \\ \delta q_y = 2\pi \frac{\delta y_1}{\lambda z} \end{cases} \tag{3.44}$$

Moreover, one can use the discrete FT relationship and write :

$$\begin{cases} \delta q_x = \frac{2\pi}{N_x \delta x} \\ \delta q_y = \frac{2\pi}{N_y \delta y} \end{cases} \tag{3.45}$$

Therefore, one has the equivalent representation in real-space units on the detector:

$$\begin{cases} \delta x_1 = \frac{\lambda z}{N_x \delta x} = \frac{\lambda z}{\Delta x} \\ \delta y_1 = \frac{\lambda z}{N_y \delta y} = \frac{\lambda z}{\Delta y} \end{cases} \tag{3.46}$$

In a CDI experiment, the pixel size of the detector $\delta x_1 = p_{det}$ is fixed, thus only the detector distance $z = D$ can be tweaked in order to comply with oversampling. For instance, if the maximum extent l of the sample in *e. g* the x-direction is known, then an oversampling ratio of $\sigma > 2$ leads to the necessity of having a real-space pixel size such as $N_x \delta x \geq 2l$, which derives:

$$D = \frac{p_{det}}{\lambda \delta q_x} = N \delta x \frac{p_{det}}{\lambda} \Longrightarrow D \geq 2l \frac{p_{det}}{\lambda} \tag{3.47}$$

For instance, collecting the diffraction pattern on a 516×516 pixels (55 µm in size) detector from a gold crystal ($a = 0.408$ nm) whose longest dimension is ~ 300 nm, illuminated by a 8 keV beam ($\lambda = 0.155$ nm), requires a distance to the detector of $D \geq 0.21$ m.

3.7.4 *General formalism of phase retrieval algorithms*

From an oversampled diffraction dataset together coming from an isolated sample, smaller than the coherent beam size, the phase of the sample can be in principle recovered. This is done through the use of a combination of the following algorithms.

3.7.4.1 *Error reduction*

The basic phase retrieval algorithm, known as Error reduction (ER) works by Fourier-transforming the measured intensity data back and forth between real and reciprocal space, while applying a constraint in each space. ER starts with a guess of the shape of the scattering sample, for example by calculating the auto correlation of the diffraction pattern. The first iteration consists of taking an initial guess at the scattering amplitude $A(\vec{q})$ by multiplying the square root of the recorded intensities with a random phase factor $\phi_{random}(\vec{q})$ so that $A(\vec{q}) = \sqrt{I(\vec{q})} e^{i\phi_{random}(\vec{q})}$. This way, the reciprocal space constraint is applied, by enforcing the measured diffracted amplitude while retaining the current phase. The inverse FT $\mathcal{F}^{-1}$ is then applied to obtain a guess on the electron density $\rho(\vec{r})$. This is when real space constraints are applied, consisting in setting $\rho(\vec{r})$ equals to zero everywhere outside the "support" area. This notion of support was first introduced by Fienup (Fienup, 1978) and describes the area where the object is expected to be. Let $\rho_k(\vec{r})$ be the k-th guess, then the support condition can be written as following :

$$\begin{cases} \rho_{k+1}(\vec{r}) = \rho_k(\vec{r}) & \text{if } \vec{r} \in \text{Support} \\ \rho_{k+1}(\vec{r}) = 0 & \text{if } \vec{r} \notin \text{Support} \end{cases} \tag{3.48}$$

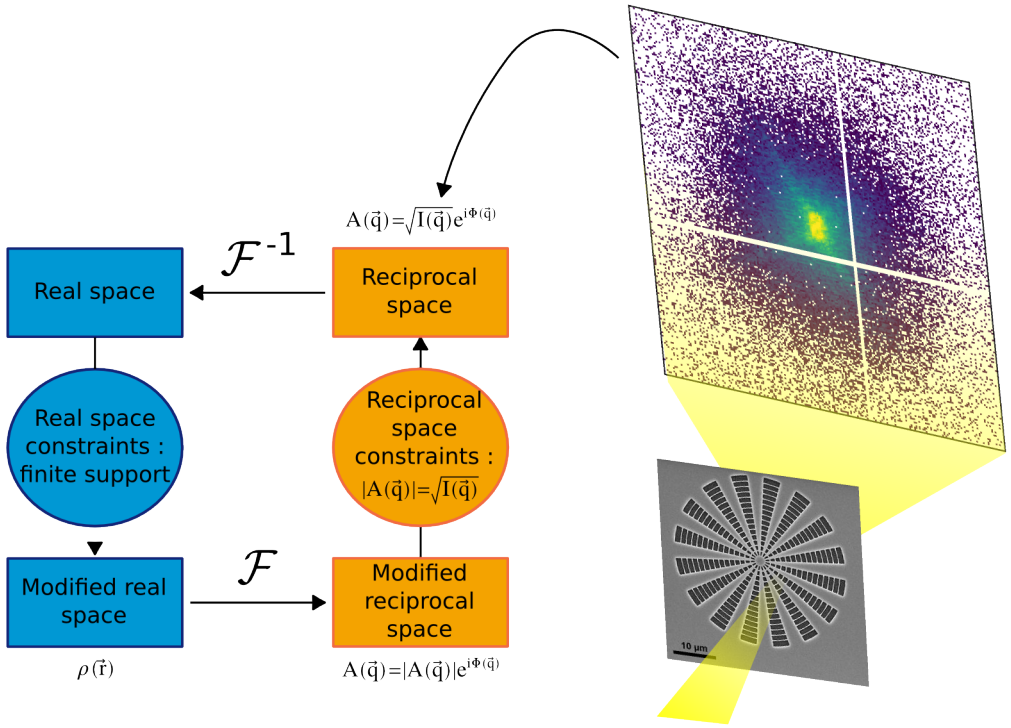

Figure 3.10 – Schematic illustrating the Error-reduction algorithm together with the finite support constraint in order to retrieve real space objects from coherent x-ray diffraction patterns. On the right, a Siemens star object is illuminated with a coherent beam and its scattered signal is recorded on a two-dimensional detector. These intensities are used during the Error-reduction algorithm to navigate using Fourier transforms back and fourth between the real and the reciprocal space, as sketched on the left. Adapted from (Yau, 2018).

The updated electron density $\rho_{k+1}(\vec{r})$ can then be FT to reciprocal space to form a new guess of the complex scattering amplitude, for which the reciprocal space constraint is applied while the updated phase information is kept. The scheme presented in Figure 3.10 charts the global process.

The likeness between the retrieved amplitude and the measured intensities can be evaluated by the simple error metric consisting in the mean squared error :

$$E_r^2 = \frac{\sum(\left|\mathcal{F}[\rho_k(\vec{r})] - \sqrt{I(\vec{q})}\right|^2)}{\sum I(\vec{q})} \tag{3.49}$$

Even though this metric can be used to monitor the convergence of the algorithm, often the error-metric will stop decreasing and the algorithm gets stuck in a local minimum. Indeed, ER is proven to be closely related to the steepest-descent method (Fienup, 1982).

3.7.4.2 *Hybrid input-output*

In order to tackle these problems of stagnation, an enhanced algorithm was introduced by Fienup (Fienup, 1982), based on a non-linear feedback control theory : the Hybrid input output (HIO). Contrary to ER, the retrieved informations outside the support are kept and substracted during the $k+1$ iteration, while being multiplied by a feedback parameter β :

$$\begin{cases} \rho_{k+1}(\vec{r}) = \rho_k(\vec{r}) & \text{if } \vec{r} \in \text{Support} \\ \rho_{k+1}(\vec{r}) = \rho_k(\vec{r}) - \beta\rho_k(\vec{r}) & \text{if } \vec{r} \notin \text{Support} \end{cases} \tag{3.50}$$

With β constant and such that $0 < \beta < 1$, with typical value around 0.9. Effectively, this modification allows faster convergence by smoothly putting the area outside the support to zero, acting as small perturbations in order to enable the algorithm to leave a local minimum. Usually, both ER and HIO are used together as their combination leads to particularly robust results (Marchesini, 2007).

Note that these iterative algorithms can be approached as a set of mathematical projections operators (Levi and Stark, 1984; Sezan and Stark, 1987), which allow to create an unify description (Marchesini, 2007). Introducing the projection onto a set as the projector $\boldsymbol{P}_S$:

$$\boldsymbol{P}_S\rho(\vec{r}) = \begin{cases} \rho(\vec{r}) & \text{if } \vec{r} \in S \\ 0 & \text{otherwise} \end{cases} \tag{3.51}$$

One can also defines a representation of the projector in reciprocal space :

$$\boldsymbol{P}_m = \mathcal{F}^{-1}\widetilde{\boldsymbol{P}}_m\mathcal{F} \tag{3.52}$$

where $\widetilde{\boldsymbol{P}}_m$ is the projection of a point in each complex plane onto the corresponding circle :

$$\widetilde{\boldsymbol{P}}_m\tilde{\rho}(\vec{q}) = \widetilde{\boldsymbol{P}}_m \left|\tilde{\rho}(\vec{q})\right| e^{i\phi(\vec{q})} = \sqrt{I(\vec{q})}e^{i\phi(\vec{q})} \tag{3.53}$$

With these notations, the $k+1$ iterations for ER and HIO can be rewritten easily :

$$\begin{array}{ll} \text{ER} & \boldsymbol{P}_s\boldsymbol{P}_m\rho_k(\vec{r}) \\ \text{HIO} & \begin{cases} \boldsymbol{P}_m\rho_k(\vec{r}) & \text{if } \vec{r} \in S \\ (\boldsymbol{I} - \beta\boldsymbol{P}_m)\rho_k(\vec{r}) & \text{otherwise} \end{cases} \end{array} \tag{3.54}$$

By introducing the reflector operator as $\boldsymbol{R} = \boldsymbol{I} + 2[\boldsymbol{P} - \boldsymbol{I}] = 2\boldsymbol{P} - \boldsymbol{I}$, with $\boldsymbol{I}$ being the identity operator, these notations also allow us to introduce the Relaxed Averaged Alternating Reflectors (RAAR) algorithm (Luke, 2005) :

$$\text{RAAR} \quad \left[\tfrac{1}{2}\beta(\boldsymbol{R}_s\boldsymbol{R}_m + \boldsymbol{I}) + (1-\beta)\boldsymbol{P}_m\right]\rho_k \tag{3.55}$$

It behaves somewhere in between ER and HIO for similar β, but reaching the solution much earlier.

3.7.4.3 *Difference Map*

Elser (Elser, 2003) introduced the Difference map (DM) algorithm which takes two instances of the Fourier modulus update, in order to avoid traps, *i. e.* regions of the search space where the distance between the two constraint spaces is a local minimum (Thibault, 2007). With the projection operators formalism, one can write the DM algorithm as :

$$\text{DM} \quad \left[\boldsymbol{I} + (1+\beta)\boldsymbol{P}_s\boldsymbol{P}_m - \boldsymbol{P}_s - \beta\boldsymbol{P}_m\right]\rho_k \tag{3.56}$$

This algorithm, which is also a variant from HIO, has been successfully adapted to ptychography (Menzel et al., 2008; Thibault, Dierolf, Menzel, Bunk, and Pfeiffer, 2009; Hruszkewycz et al., 2012), where the constraints become the Fourier projections and the overlap projections.

3.7.4.4 *Support determination and shrink wrap algorithm*

In order to estimate the support of the object, either one uses other techniques (such as Scanning Electron Microscopy (SEM) or Atomic Force Microscopy (AFM) for instance) that give the knowledge of the shape and dimensions of the sample, or, in case of complete lack of information, one uses the autocorrelation function (Marchesini et al., 2003) on the diffraction signal which leads to a rough estimate of the support. The latter is based on the Patterson function, the inverse FT of the recorded intensities, which is equivalent to the electron density convolved with its inverse :

$$\begin{aligned}
\text{Patterson}(\vec{r}) &= \mathcal{F}^{-1}\left[I(\vec{q})\right] \\
&= \mathcal{F}^{-1}\left[A(\vec{q})A^*(\vec{q})\right] \\
&= \mathcal{F}^{-1}\left[\mathcal{F}\left[\rho(\vec{r})\right]\mathcal{F}\left[\rho(-\vec{r})\right]\right] \\
&= \rho(\vec{r}) \otimes \rho(-\vec{r})
\end{aligned} \tag{3.57}$$

From equation 3.57, it is clear that the Patterson function contains information about the shape of the object. However, while most CDI experiments deal with weakly strained objects, there are systems with so much inhomogeneous strain that the shape has no obvious impact on the diffraction pattern (Beutier et al., 2013), *e. g.* loss of symmetry and interference streaks disappearing. Furthermore, the Patterson function overestimates the size by a factor of 2, thus most algorithms use a thresholding around 2% to 4% of the maximum (Marchesini et al., 2003).

In order to cope with the unknown shape of the object, Marchesini *et al.* (ibid.) introduced a novel algorithm to be used in combination with *e. g* HIO + ER, the shrink-wrap (SW) algorithm which is now routinely used in CDI. It allows to update the support during the object reconstruction, by smoothing it with a Gaussian convolution at certain iterations and then applying a threshold of a typical 10% of the maximum value of the amplitude.

3.7.5 *Recent advances in phase retrieval*

Even though the combination of Hybrid input-output, Error reduction and Shrink wrap has proven to converge, there is no guarantee of a successful reconstruction, especially in the case of highly strained sample (Beutier et al., 2013; Diaz et al., 2010). Moreover, the noise level, diffuse scattering, substrate scattering and positioning errors can also be the source of phase retrieval stagnation in non-global minimum. Here we introduce some improvements that have been recently proposed in order to improve the convergence of the phase retrieval procedure.

3.7.5.1 *Guided phase retrieval*

Introduced with the traditional HIO method by Chen *et al.* (Chen et al., 2007) in 2007, the guiding algorithm uses the concept of optimization by guiding searching direction to locate the global minimum. As explained deeper by Ulvestad *et al.* (Ulvestad, Nashed, et al., 2017) and Colombo *et al.* (Colombo et al., 2017), the procedure relies on the generation of several initial random guesses as starting points that will enable to select a set of solutions, designed as the best one according to a specific criteria such as the error metric. These solutions will then guide the next round of iteration. Thanks to the breeding in successive generations, the algorithm will converge regardless of the initial starts. This procedure leave the algorithms unmodified, and have produced consistent experimental results (Clark, Ihli, et al., 2015; Ulvestad, Singer, et al., 2015; Ulvestad, Welland, et al., 2017; Liu et al., 2017) since 2015.

3.7.5.2 *Taking into account partial coherence*

The classical methods for phase retrieval in CDI are limited to a either complete or partial *a priori* knowledge of the coherence properties of the illumination. Clark *et al.* (Clark, Huang, et al., 2012) demonstrated in 2012 the successful inversion of three-dimensional partially coherent diffraction patterns. Actually, as described by the Schell model (Schell, 1967), the recorded intensity patterns are partially coherent as they are the result of a blurring of the coherent intensity by a convolution with the Fourier transform of the normalized mutual coherence function (introduced in section 3.5, see equation 3.25). Hence, the recorded partially coherent intensity reads :

$$I_{pc}(\vec{q}) = I_c(\vec{q}) \otimes \tilde{\gamma}(\vec{q}) \tag{3.58}$$

In order to accommodate partial coherence, the modulus constraint is modified by introducing modal techniques (Thibault and Menzel, 2013), relying on the fact that the recorded diffraction pattern is effectively made up of the incoherent sum of a given number of modes. Moreover, the iterative Richardson-Lucy algorithm (Richardson, 1972; Lucy, 1974) is employed to get numerical update of $\tilde{\gamma}^k(\vec{q})$, using the measured partially coherent intensity $I_{pc}(\vec{q})$ and a linear combination of the current and the previous iterates estimate of the coherent intensity, $I^{\Delta k}(\vec{q}) = 2I^k(\vec{q}) - I^{k-1}(\vec{q})$:

$$\tilde{\gamma}^{k,i+1}(\vec{q}) = \tilde{\gamma}^{k,i}(\vec{q}) \left(I^{\Delta k}(-\vec{q}) \otimes \frac{I_{pc}(\vec{q})}{I^{\Delta k}(\vec{q}) \otimes \tilde{\gamma}^{k,i}(\vec{q})} \right), \tag{3.59}$$

where i is the sub iteration number relating to the coherence function determination.

3.7.5.3 *Metrics*

As described earlier, the use of the conventional χ error-metric (mean squared error between the measured and the retrieved amplitude) sometimes does not correspond to a successful reconstruction. In order to promote desirable features in the final image, different fitness metrics have been introduced and tested. For instance, as the width of a diffraction peak of a crystal depends on both the size of the crystal and on the level of strain, a large strained crystal and a smaller unstrained crystal can lead to the same Bragg peak width. That way, a solution with underestimated crystal dimensions could originate from a local minimum of the phase retrieval algorithm. Promoting larger real space extent can be done through a fitness metric that promotes more uniformity of diffracted amplitudes, the Sharp metric :

$$E_s = \sum_r |\rho(\vec{r})|^4 \tag{3.60}$$

Moreover, in (Ulvestad, Nashed, et al., 2017), the Sharp norm metric $E_{sn} = \left(\sum_r |\rho(\vec{r})|^{1/4}\right)^4$ which is based on the Sharp metric while preserving the units of ρ is performing best when the signal-to-noise ratio of the data is low. In the same study, they introduced the Max Volume metric in order to favor "anti-sparsity" directly by choosing the largest crystal. The Max Volume metric is defined as following :

$$E_{MV} = \sum_r |\rho(\vec{r})| \,/ \max |\rho(\vec{r})| \quad \text{with} \begin{cases} |\rho(\vec{r})| = 0 & \text{if } |\rho(\vec{r})| < 0.2 \\ |\rho(\vec{r})| = 1 & \text{if } |\rho(\vec{r})| \geq 0.2 \end{cases} \tag{3.61}$$

In this metric, the maximum is selected as best solution. The aim of using this metric is to counterweight the effect of the shrink wrap algorithm that usually decreases the total volume of the reconstructed object.

3.7.5.4 *Maximum-likelihood*

All CDI techniques rely on experimental data that are by nature probabilistic because of noise and measurement uncertainties. From a broader perspective, reconstruction from noisy data is a classic problem in experimental sciences, and standard tools have been developed in order to solve it. Among them, likelihood maximization is one of the most general and robust. Maximum-likelihood (ML) concepts were evoked for CDI methods and introduced in ptychography by Thibault and Guizar-Sicairos (Thibault and Guizar-Sicairos, 2012) as a refinement step after a reconstruction that is close to a solution. ML has been particularly demonstrated on ptychography as it has been shown in (Guizar-Sicairos and Fienup, 2009) that ptychography can be stated as a phase retrieval problem with transverse translation diversity, a case for which gradient-based minimization approaches are particularly well adapted.

However, ML can be extended to any CDI technique, and we will derive the related equations within the frame of classical CDI, where the diffraction patterns come from one crystalline sample illuminated by a wider X-ray beam. As described in equation 3.38, in the absence of noise or any other experimental errors, each of the N intensity in the far-field plane is :

$$I_j^{calc} = \left|\mathcal{F}\left[\rho(r_j)\right]\right|^2 \tag{3.62}$$

However, in a realistic experimental dataset, the presence of photon noise results in degradation of the measured data set. Depending on the assumption made on the noise model, the criterion that links the unknown object to the measured data will change. The detector collects only a finite number of photons instead of the real-numbered far-field intensity quantity. The integer photon counts per pixels can

be considered as a random variable which Probability Distribution Function (PDF) is the Poisson probability law. Assuming N independent measurements I_j^{obs}, the probability that the entire data set I^{obs} is collected reads :

$$p(I^{obs}, \rho) = \prod_{j=1}^{N} \frac{(I_j^{calc})^{I_j^{obs}}}{I_j^{obs}!} e^{-I_j^{calc}} \tag{3.63}$$

The negative log-likelihood function associated with this PDF is then :

$$\mathcal{L}_p = -\log p(I^{obs}, \rho) = -\frac{1}{N} \sum_{j=1}^{N} \log \frac{(I_j^{calc})^{I_j^{obs}}}{I_j^{obs}!} e^{-I_j^{calc}} \tag{3.64}$$

Then, the maximisation of the likelihood, equivalent to the minimization of $\mathcal{L}$, passes by the calculation of its gradient, which can be written analytically and efficient minimization procedures such as conjugate gradient descent (Nocedal and Wright, 2006; Shewchuk et al., 1994) are readily available (Jones et al., 2001–). Note that another noise model can be used, by considering that the detector data are corrupted by an additive Gaussian thermal noise (Godard et al., 2012). Such a model can be built the following way :

$$(I_j^{obs})^{1/2} = (I_j^{calc})^{1/2} + \mathcal{G}_j, \quad \forall j \tag{3.65}$$

where $\mathcal{G}_j$ is an independent centered fluctuation from a Gaussian distribution of variance σ_j^2. The PDF of the transformed data set $\left\{\sqrt{I_j^{obs}}\right\}$ is also Gaussian and now reads :

$$g(I^{obs}, \rho) = \prod_j (2\pi\sigma^2)^{-1/2} e^{-\frac{1}{2}\left[\frac{\left(I_j^{obs}\right)^{1/2} - \left(I_j^{calc}\right)^{1/2}}{\sigma}\right]^2} \tag{3.66}$$

The corresponding negative log-likelihood is, up to an additive constant :

$$\mathcal{L}_g \approx \sum_j \frac{1}{2\sigma} \left[\frac{\left(I_j^{obs}\right)^{1/2} - \left(I_j^{calc}\right)^{1/2}}{\sigma}\right]^2 \tag{3.67}$$

It appears to be identical to the cost function formulated as a Euclidean metric in the reciprocal space. In the case where the number of expected counts $\left\{I_j^{calc}\right\}$ is large enough, the Central Limit Theorem states that the Gaussian PDF is a good approximation of the Poissonian PDF derived earlier. The difference between the two models is hence significantly higher for low photon counts in the pixel detector (less than 10 counts), where the Poissonian approach should be adopted (ibid.).

3.8 COHERENT BRAGG IMAGING

3.8.1 *Definition*

CDI in the Bragg geometry allows one to probe displacement fields inside crystals, which, as derived in section 3.4.2, corresponds to the phase of the complex electron density. It is useful to remember that (from eq 3.20), at a given Bragg reflection with its diffraction vector $\vec{q_{hkl}}$, the scattered amplitude of the crystal derives :

$$A(\vec{q}) = \mathcal{F}\left[\rho(\vec{r})e^{i\vec{q_{hkl}}\cdot\vec{u}(\vec{r})}\right] \tag{3.68}$$

One should emphasize once again that a single BCDI measurement is limited to the direction parallel to the scattering vector: a successful object reconstruction will yield $\vec{q}\cdot\vec{u}$ as the phase of the reconstructed density.

Even if the basics of CDI measurements is pretty simple, the case of Bragg geometry is delicate, especially since it involves small (from nano-size to micron-size) crystals with specific experimental setups that are to be handled with care. As shown in Figure 3.11, the sample and the detector are oriented in order to fulfill the Bragg conditions, requiring to rotate the two dimensional detector, sometimes to angles above 60 degrees. Bragg geometry allows directly a 3D investigation of reciprocal space.

3.8.2 *From detection to direct space*

As only a slice of the three-dimensional diffraction pattern is recorded by the two dimensional detector, one efficient manner to obtain the full 3D intensity is to rotate the sample, with $\Delta\theta \lessapprox 1^\circ$ total angle rotation, which is actually transformed into a linear scan along q_3 (see Figure 3.11). Hence, the 3D intensity is obtained from consecutive 2D acquisitions at different $\delta\theta$ positions. This is known as the rocking curve method. As the 3D matrix obtained is sampled homogeneously along the 3 axis of the detector basis, fast Fourier transform (FFT) routine can be directly applied on the raw data, allowing a large gain of computational time. In addition, the use of FFT goes along with some relations between the resulting direct space and the reciprocal - Fourier - space, including the notions of sampling and extent. These have been discussed earlier (see section 3.7.3), but can be derived using vectorial conjugation relations. Considering that the components of the scanned $\vec{q}$ vectors are

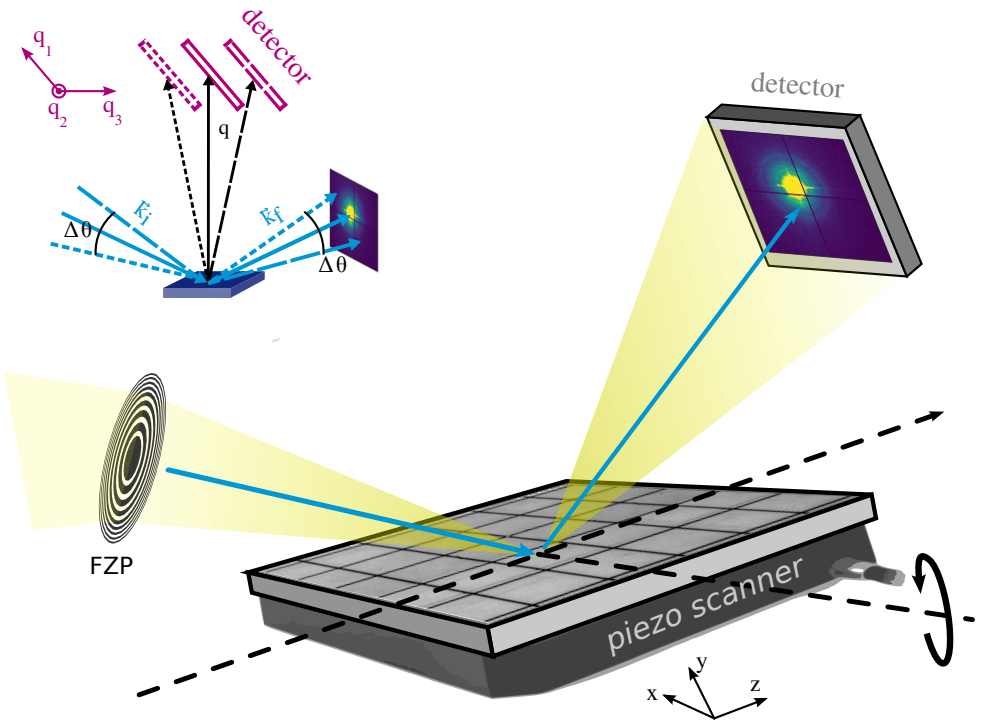

Figure 3.11 – Bragg Coherent Diffraction Imaging setup. The inset shows the 3D exploration of Fourier space with angular scanning $\Delta\theta$. The convention for space orientation definition in both real and reciprocal space is shown as well. Adapted from (Stangl et al., 2013).

noted $\vec{q_1}, \vec{q_2}$ in the detector plane and $\vec{q_3}$ perpendicular to $\vec{q_{hkl}}$, then the unit vectors of the direct space $\vec{r_1}, \vec{r_2}$ and $\vec{r_3}$ are obtained using Fourier conjugation relation :

$$\vec{r_i} = 2\pi \frac{\vec{q_j} \times \vec{q_k}}{V} \tag{3.69}$$

where V is the volume defined by $\vec{q_i} \cdot \vec{q_j} \times \vec{q_k}$ and where the $\{i, j, k\}$ indexes are given by the circular permutation of the {1,2,3} indexes. In the case where $(\vec{q_i}, \vec{q_j}, \vec{q_k})$ represents an orthogonal basis, the smallest spatial element $\delta\vec{r_i}$ along the i direction is given by :

$$\delta\vec{r_i} = \frac{2\pi}{\vec{q_{\max,i}}} \tag{3.70}$$

where $\vec{q_{\max,i}}$ is the maximal recorded frequency, or reciprocal space maximum exploration, along the i direction. The extent of the direct space $\Delta\vec{r_i}$ along the i direction is hence defined by :

$$\Delta\vec{r_i} = N_i \frac{2\pi}{\vec{q_{\max,i}}} = \frac{2\pi}{\delta\vec{q_i}} \tag{3.71}$$

where N_i is the number of detector pixels along the i direction and $\delta\vec{q_i}$ is the reciprocal space resolution. It is worth noting that all these expressions can be simplified using the geometrical distances of an experimental setup, *i.e.*,follows introducing the detector-to-sample distance D and the detector pixel size $p_{det,i}$ along the i direction $(i = \{1, 2\})$, as we have the relation :

$$\begin{aligned} D|\vec{q_{\max,i}}| &= N_i p_{det,i} |\vec{k_f}| \\ \iff |\vec{q_{\max,i}}| &= 2\pi \frac{N_i p_{det,i}}{\lambda D} \end{aligned} \tag{3.72}$$

It derives that in the plane of the detector $(i = \{1, 2\})$, the smallest element in direct space is given by :

$$|\delta\vec{r_i}| = \frac{\lambda D}{N_i p_{det,i}} \tag{3.73}$$

Moreover, one can note that in the third dimension of reciprocal space, along the scanning direction $\vec{q_3}$, the resolution is defined by the angular step $\delta\theta = \frac{\Delta\theta}{N_3}$ where N_3 is the number of sample rotation. Hence, the smallest element in direct space is given by :

$$\delta r_3 = \frac{\lambda}{N_3 \delta\theta} \tag{3.74}$$

Note that the effective spatial resolution of the reconstruction is in general larger than the size of the pixel elements, which can in principle always be reduced as they are inversely proportional to the extent of the reciprocal space. Indeed, the imaging

process is very likely to be degraded by uncertainties in the dataset, level of photon noise, or even data analysis itself.

3.9 ESRF ID01 BEAMLINE SET-UP

The ID01 beamline of the ESRF is dedicated to three kinds of experiments : Bragg Coherent Diffraction Imaging (Fernández et al., 2019), Scanning X-ray Diffraction Microscopy (KMAP) (G. Chahine et al., 2015) and Full-Field Diffraction X-ray Microscopy (FFDXM) (Hilhorst et al., 2014). That way, ID01 combines the lattice parameter resolution supplied by X-ray diffraction with the resolution in direct space facilitated by current imaging techniques using the most advanced X-ray optics technology. Recently, Schülli et al. published a review thoroughly describing the nanodiffraction beamline, from the X-ray source to the sample stage and its applications (Leake, G. A. Chahine, et al., 2019). ID01 presents the special feature of being adapted to *operando* experiments on functional devices, being particularly flexible while offering high beam stability.

Due to its total length of 118 m, ID01 is among the five longest beamline of the ESRF and is optimized to produce highly focused micro- to nano- size X-ray beams. The X-ray source itself is made from up to three undulators, a single 27 mm period (U27), a single 35 mm period (U35) and a revolver which offers either of the aforementioned periods. The fundamental harmonic of the U27 yields a first brilliance maximum in the energy regime from 6.5 to 11 keV, while the third harmonic produces a second brilliance maximum in the energy from 19.5 to 22 keV. The U35 provides the possibility to tune the energy in between the gap represented by the first and third harmonic of the U27. The main operating regime is at 8 keV, where the Full Width at Half Maximum (FWHM) of the source amounts to 12 µm (V)$\times$120 µm (H) at a beam divergence of 20 µrad (V) $\times$170 µrad (H) (FWHM).

3.9.1 *Optics*

Before reaching the endstation inside the experimental hutch, the X-ray photons pass through three optics hutch:

— The first optic hutch contains the main beam-conditioning components such as monochromators and mirrors. In the first optic hutch, high-power slits are introduced to shape the white beam as a function of required illumination of the optics. Then, the primary optics are made of 900 mm long reflective mirrors chosen to reflect in the horizontal plane as there is higher tolerance of the horizontal source size. Two monochromators are available: a channel-cut silicon crystal monochromator in order to get the most stable incident beam and

a double-crystal monochromator to work with wavefront-sensitive techniques. In horizontal geometry, the two are superimposed on an in-vacuum rotation table with vertical axis, a translation in height enabling to interchange between systems. The bandpass of the resulting Si(111) monochromator is of the order of 10^{-4}, however a multilayer monochromator with 10^{-3} bandwidth is also available for samples that are thin enough to tolerate a broader bandwidth, hence a gain in incident intensity (two order of magnitude compared to the Si(111) monochromator). This multilayer will be used in Chapter 4 in order to reach a maximum flux on ultra-thin semiconductor nanostructures. Typical beam longitudinal coherence length is of 800 nm, set by the monochromator (Leake, Newton, et al., 2009).

— The second and third optic hutches serve as secondary optical elements, hosting respectively a transfocator device and a virtual source. The transfocator, located at 55 m from the source, is made of two sets of Be lenses and is used to either condense a significant fraction of the beam, or pre-focusing the incident beam. A virtual secondary source can also be used to tune the compromise between beam spot size and beam flux on the sample.

— The experimental endstation contains the focusing optics.

3.9.2 *Nanofocusing endstation*

The endstation is designed to deliver nanofocused beams with high stability on a sample stage with high accuracy and precision relative to the reference laboratory frame (see Figure 3.12). It contains a large granite table physically supporting both the focusing optic and sample environment. Two main focusing optics are available, on the one hand Fresnel zone plates (FZPs) (Baez, 1961; Fabrizio et al., 1999) and on the other hand Kirkpatrick-Baez (KB) mirrors (Kirkpatrick and Baez, 1948).

FZP is a diffractive focusing device that needs small working distances (below 20 mm) at 8 keV to focus the beam below 200 nm in both horizontal and vertical direction. The available FZPs have 300/200/120 µm diameter with 70/60 nm outer zone width or 200 µm diameter with 45 nm outer zone width (Leake, Favre-Nicolin, et al., 2017). The KB mirror has a 200 µm × 176 µm clear aperture, and at a working distance of 70 mm can focus the beam to a few hundred nm. Combined with the multilayer, this KB will be used to get the brightest 200 x 200 nm^2 beam to illuminate ultra-thin semiconductor nanostructures in chapter 4. FZP will also be used with proper defocus in order to maximize the size of the beam and shine on microsized Zirconia grains in chapter 5.

Note that in order to control the beam size and its coherence properties, an additional set of slits is used right before the focusing optics. The aperture of these

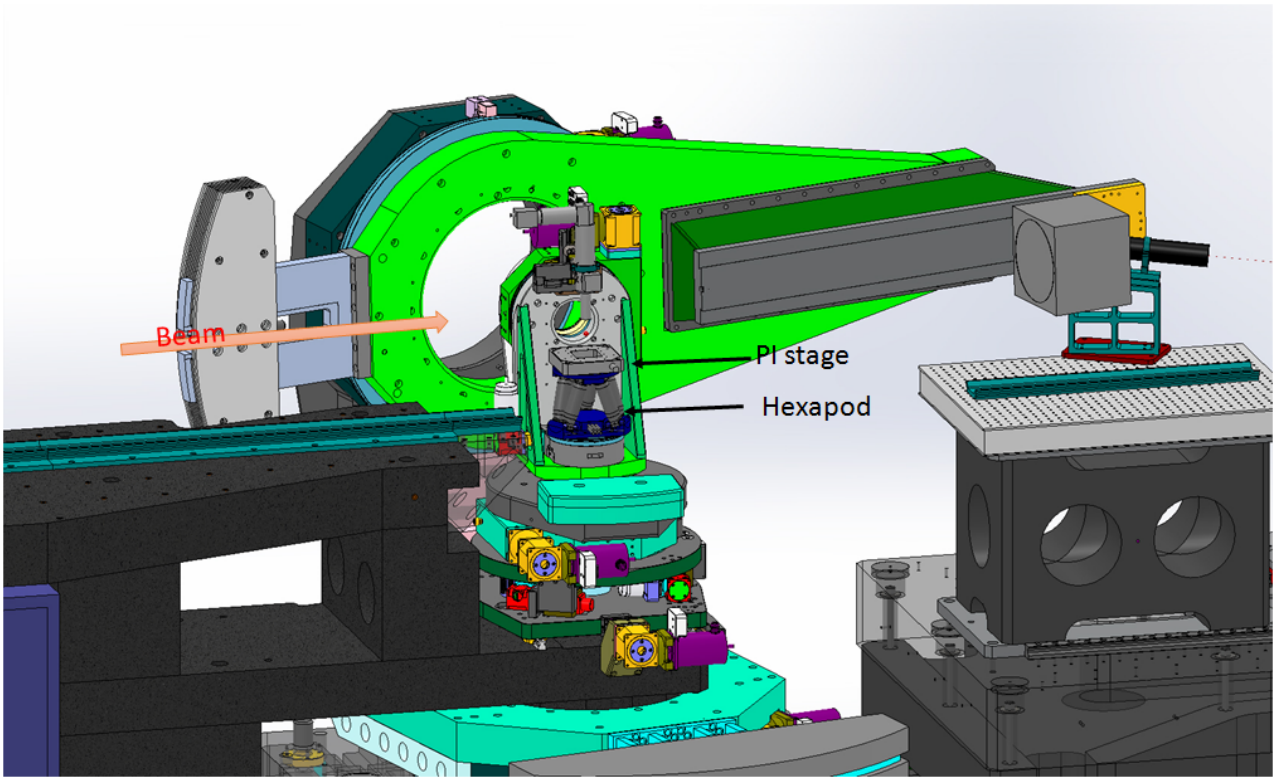

Figure 3.12 – Solid work sketch of the experimental hutch of the ID01 ESRF beamline. The PI-Mars piezo stage, providing a few nanometer resolution, sits on top of a BORA Hexapod.

slits defines both the transverse dimensions of the focal spot and the focal depth, but also impacts the flux inversely to the coherent fraction of the beam. In order to increase the size of the focal spot, the opening of the slits has to be decreased but it will also lead to a decrease of the flux (Mastropietro et al., 2011).

The sample stage is made of a heavy load 3+2-circles diffractometer together with a tripod of motors controlling a z-translation and a y-translation, a Symmetric BORA hexapod with three axes of translation with right-handed rotation for each axis, and finally a PI-Mars three axis piezo. The three Huber circles of rotation, all left-handed rotation, give rise to a sphere of confusion of less than 10 µm, while the sphere of confusion of the hexapod is less than 50 µm, thus being the limiting factor for alignment. The detector arm is uncoupled from the sample, with two left-handed rotation axes around z (denoted ν) and y (denoted δ). A Maxipix detector (Ponchut et al., 2011) is available on the arm, with a 55 µm pixel size and limits of up to 2.36 m and to δ 68°, and 1.76 m to δ 120°.

BIBLIOGRAPHY

Röntgen, WC (1895). « Über eine neue Art von Strahlen. Sitzungsberichte der Physik.-Med. » In: *Gesellschaft zu Würzburg* 137, pp. 132–141 (cit. on p. 19).

Feynman, Richard Phillips (2006). *QED: The strange theory of light and matter*. Princeton University Press (cit. on p. 19).

Als-Nielsen, J. and D. McMorrow (2001). *Elements of Modern X-ray Physics*. en. John Wiley & Sons (cit. on pp. 20, 22, 27, 33).

Harding, Geoffrey, A Thran, and Bernd David (2003). « Liquid metal anode X-ray tubes and their potential for high continuous power operation. » In: *Radiation Physics and Chemistry* 67, pp. 7–14. DOI: 10.1016/S0969-806X(03)00007-0 (cit. on p. 20).

Elder, FR, AM Gurewitsch, RV Langmuir, and HC Pollock (1947). « Radiation from electrons in a synchrotron. » In: *Physical Review* 71.11, p. 829 (cit. on p. 21).

Bragg, W. L. (1929). « The Diffraction of Short Electromagnetic Waves by a Crystal. » In: *Scientia* 23.45, p. 153 (cit. on p. 24).

Warren, BE (1990). *X-ray Diffraction*. en. Dover (cit. on pp. 27, 28).

Coppens, Philip, David Cox, Elias Vlieg, and Ian K Robinson (1992). *Synchrotron radiation crystallography*. Academic Pr (cit. on p. 27).

Guinier, André (1994). *X-ray Diffraction in Crystals, Imperfect Crystals, and Amorphous Bodies*. en. Courier Corporation (cit. on p. 27).

Stangl, Julian, Cristian Mocuta, Virginie Chamard, and Dina Carbone (2013). *Nanobeam X-ray Scattering: Probing matter at the nanoscale*. John Wiley & Sons (cit. on pp. 28, 30, 49).

Robinson, Ian and Ross Harder (2009). « Coherent X-ray diffraction imaging of strain at the nanoscale. » In: *Nature materials* 8.4, p. 291 (cit. on p. 30).

Takagi, Satio (1969). « A dynamical theory of diffraction for a distorted crystal. » In: *Journal of the Physical Society of Japan* 26.5, pp. 1239–1253 (cit. on p. 30).

Pfeifer, Mark A., Garth J. Williams, Ivan A. Vartanyants, Ross Harder, and Ian K. Robinson (2006). « Three-dimensional mapping of a deformation field inside a nanocrystal. » In: *Nature* 442.7098, pp. 63–66. DOI: 10.1038/nature04867 (cit. on p. 31).

Minkevich, A. A., M. Gailhanou, J.-S. Micha, B. Charlet, V. Chamard, and O. Thomas (2007). « Inversion of the diffraction pattern from an inhomogeneously strained crystal using an iterative algorithm. » In: *Physical Review B* 76.10, p. 104106. DOI: 10.1103/PhysRevB.76.104106 (cit. on p. 31).

Labat, S., V. Chamard, and O. Thomas (2007). « Local strain in a 3D nano-crystal revealed by 2D coherent X-ray diffraction imaging. » In: *Thin Solid Films*. The Ninth International Conference on Surface X-Ray and Neutron Scattering 515.14, pp. 5557–5562. DOI: 10.1016/j.tsf.2006.12.031 (cit. on p. 31).

Harder, R., M. A. Pfeifer, G. J. Williams, I. A. Vartaniants, and I. K. Robinson (2007). « Orientation variation of surface strain. » In: *Physical Review B* 76.11, p. 115425. DOI: 10.1103/PhysRevB.76.115425 (cit. on p. 31).

Fienup, James R (1982). « Phase retrieval algorithms: a comparison. » In: *Applied optics* 21.15, pp. 2758–2769 (cit. on pp. 31, 41, 42).

R. W. Gerchberg, W. O. Saxton (1972). « A practical algorithm for the determination of phase from image and diffraction plane pictures. » In: *Optik* 35 (cit. on p. 31).

Born, Max and Emil Wolf (2013). *Principles of Optics: Electromagnetic Theory of Propagation, Interference and Diffraction of Light*. en. Elsevier (cit. on p. 31).

Lin, J. J. A. et al. (2003). « Measurement of the Spatial Coherence Function of Undulator Radiation using a Phase Mask. » In: *Physical Review Letters* 90.7, p. 074801. DOI: 10.1103/PhysRevLett.90.074801 (cit. on p. 32).

Veen, Friso van der and Franz Pfeiffer (2004). « Coherent x-ray scattering. » en. In: *Journal of Physics: Condensed Matter* 16.28, pp. 5003–5030. DOI: 10.1088/0953-8984/16/28/020 (cit. on pp. 33, 38).

Leake, S. J., G. A. Chahine, et al. (2019). « The Nanodiffraction beamline ID01/ESRF: a microscope for imaging strain and structure. » en. In: *Journal of Synchrotron Radiation* 26.2, pp. 571–584. DOI: 10.1107/S160057751900078X (cit. on pp. 32, 51).

Winthrop, John T. and C. R. Worthington (1966). « Convolution Formulation of Fresnel Diffraction. » In: *JOSA* 56.5, pp. 588–591. DOI: 10.1364/JOSA.56.000588 (cit. on p. 33).

Spence, John C. H. and P. W. Hawkes (2008). « Diffract-and-destroy: Can X-ray lasers "solve" the radiation damage problem? » In: *Ultramicroscopy* 108.12, pp. 1502–1503. DOI: 10.1016/j.ultramic.2008.05.003 (cit. on p. 37).

Schmidt, K. E., J. C. H. Spence, U. Weierstall, R. Kirian, X. Wang, D. Starodub, H. N. Chapman, M. R. Howells, and R. B. Doak (2008). « Tomographic Femtosecond X-Ray Diffractive Imaging. » In: *Physical Review Letters* 101.11, p. 115507. DOI: 10.1103/PhysRevLett.101.115507 (cit. on p. 37).

Hoppe, Walter (1969). « Beugung im inhomogenen primärstrahlwellenfeld. i. prinzip einer phasenmessung von elektronenbeungungsinterferenzen. » In: *Acta Crystallographica Section A: Crystal Physics, Diffraction, Theoretical and General Crystallography* 25.4, pp. 495–501 (cit. on p. 37).

Rodenburg, J. M. and R. H. T. Bates (1992). « The theory of super-resolution electron microscopy via Wigner-distribution deconvolution. » In: *Philosophical Transactions*

of the Royal Society of London. Series A: Physical and Engineering Sciences 339.1655, pp. 521–553. DOI: 10.1098/rsta.1992.0050 (cit. on p. 37).

Rodenburg, J. M., A. C. Hurst, A. G. Cullis, B. R. Dobson, F. Pfeiffer, O. Bunk, C. David, K. Jefimovs, and I. Johnson (2007). « Hard-X-Ray Lensless Imaging of Extended Objects. » In: *Physical Review Letters* 98.3, p. 034801. DOI: 10.1103/PhysRevLett.98.034801 (cit. on p. 37).

Thibault, Pierre, Martin Dierolf, Andreas Menzel, Oliver Bunk, Christian David, and Franz Pfeiffer (2008). « High-Resolution Scanning X-ray Diffraction Microscopy. » In: *Science* 321.5887, pp. 379–382. DOI: 10.1126/science.1158573 (cit. on p. 37).

Miao, Jianwei, Pambos Charalambous, Janos Kirz, and David Sayre (1999). « Extending the methodology of X-ray crystallography to allow imaging of micrometre-sized non-crystalline specimens. » En. In: *Nature* 400.6742, p. 342. DOI: 10.1038/22498 (cit. on p. 37).

Snigirev, Anatoly and Irina Snigireva (2008). « High energy X-ray micro-optics. » In: *Comptes Rendus Physique*. Synchrotron x-rays and condensed matter 9.5, pp. 507–516. DOI: 10.1016/j.crhy.2008.02.003 (cit. on p. 37).

Snigirev, A., V. Kohn, I. Snigireva, A. Souvorov, and B. Lengeler (1998). « Focusing high-energy x rays by compound refractive lenses. » EN. In: *Applied Optics* 37.4, pp. 653–662. DOI: 10.1364/AO.37.000653 (cit. on p. 37).

Kirkpatrick, Paul and A. V. Baez (1948). « Formation of Optical Images by X-Rays. » EN. In: *JOSA* 38.9, pp. 766–774. DOI: 10.1364/JOSA.38.000766 (cit. on pp. 37, 52).

Baez, Albert V. (1961). « Fresnel Zone Plate for Optical Image Formation Using Extreme Ultraviolet and Soft X Radiation. » EN. In: *JOSA* 51.4, pp. 405–412. DOI: 10.1364/JOSA.51.000405 (cit. on pp. 37, 52).

High-efficiency multilevel zone plates for keV X-rays | Nature (cit. on p. 37).

Sakdinawat, Anne and David Attwood (2010). « Nanoscale X-ray imaging. » en. In: *Nature Photonics* 4.12, pp. 840–848. DOI: 10.1038/nphoton.2010.267 (cit. on p. 37).

Shannon, Claude Elwood (1949). « Communication in the presence of noise. » In: *Proceedings of the IRE* 37.1, pp. 10–21 (cit. on p. 38).

Miao, Jianwei, David Sayre, and HN Chapman (1998). « Phase retrieval from the magnitude of the Fourier transforms of nonperiodic objects. » In: *JOSA A* 15.6, pp. 1662–1669 (cit. on p. 38).

Fienup, James R (1978). « Reconstruction of an object from the modulus of its Fourier transform. » In: *Optics letters* 3.1, pp. 27–29 (cit. on p. 40).

Yau, A. (2018). « Bragg coherent diffractive imaging of defects dynamics in individual nanoparticles and thin film grains. » In: (cit. on p. 41).

Marchesini, Stefano (2007). « Invited article: A unified evaluation of iterative projection algorithms for phase retrieval. » In: *Review of scientific instruments* 78.1, p. 011301 (cit. on p. 42).

Levi, Aharon and Henry Stark (1984). « Image restoration by the method of generalized projections with application to restoration from magnitude. » In: *JOSA A* 1.9, pp. 932–943 (cit. on p. 42).

Sezan, M Ibrahim and Henry Stark (1987). « Applications of convex projection theory to image recovery in tomography and related areas. » In: *Image Recovery: Theory and Application*, pp. 155–270 (cit. on p. 42).

Luke, D Russell (2005). « Relaxed averaged alternating reflections for diffraction imaging. » In: *Inverse problems* 21.1, pp. 37–50 (cit. on p. 43).

Elser, Veit (2003). « Phase retrieval by iterated projections. » In: *JOSA A* 20.1, pp. 40–55 (cit. on p. 43).

Thibault, Pierre (2007). *Algorithmic methods in diffraction microscopy*. Cornell University Ithaca (cit. on p. 43).

Menzel, Andreas, Pierre Thibault, Martin Dierolf, Cameron M. Kewish, Oliver Bunk, Christian David, Wolfram Leitenberger, and Franz Pfeiffer (2008). « Advances in ptychographical coherent diffractive imaging. » In: 7076, p. 707609. DOI: 10.1117/12.794186 (cit. on p. 43).

Thibault, P., M. Dierolf, A. Menzel, O. Bunk, and F. Pfeiffer (2009). « High-resolution scanning coherent X-ray diffraction microscopy. » In: pp. 145–149. DOI: 10.1051/uvx/2009023 (cit. on p. 43).

Hruszkewycz, S. O., M. V. Holt, C. E. Murray, J. Bruley, J. Holt, A. Tripathi, O. G. Shpyrko, I. McNulty, M. J. Highland, and P. H. Fuoss (2012). « Quantitative Nanoscale Imaging of Lattice Distortions in Epitaxial Semiconductor Heterostructures Using Nanofocused X-ray Bragg Projection Ptychography. » In: *Nano Letters* 12.10, pp. 5148–5154. DOI: 10.1021/nl303201w (cit. on p. 43).

Marchesini, S., H. He, H.N. Chapman, S.P. Hau-Riege, A. Noy, M.R. Howells, U. Weierstall, and J.CH. Spence (2003). « X-ray image reconstruction from a diffraction pattern alone. » In: *Physical Review B* 68.14, p. 140101 (cit. on pp. 43, 44).

Beutier, G., M. Verdier, G. Parry, B. Gilles, S. Labat, MI. Richard, T. Cornelius, PF. Lory, S.V. Hoang, and F. Livet (2013). « Strain inhomogeneity in copper islands probed by coherent X-ray diffraction. » In: *Thin Solid Films* 530, pp. 120–124 (cit. on p. 44).

Diaz, A., V. Chamard, C. Mocuta, R. Magalhães-Paniago, J. Stangl, D. Carbone, T.H. Metzger, and G. Bauer (2010). « Imaging the displacement field within epitaxial nanostructures by coherent diffraction: a feasibility study. » In: *New Journal of Physics* 12.3, p. 035006. DOI: 10.1088/1367-2630/12/3/035006 (cit. on p. 44).

Chen, CC., J. Miao, C. W. Wang, and T. K. Lee (2007). « Application of optimization technique to noncrystalline x-ray diffraction microscopy: Guided hybrid input-output method. » In: *Phys. Rev. B* 76 (6), p. 064113. DOI: 10.1103/PhysRevB.76.064113 (cit. on p. 44).

Ulvestad, A., Y. Nashed, G. Beutier, M. Verdier, S. O. Hruszkewycz, and M. Dupraz (2017). « Identifying Defects with Guided Algorithms in Bragg Coherent Diffractive Imaging. » In: *Scientific Reports* 7.1, pp. 1–9. DOI: 10.1038/s41598-017-09582-7 (cit. on pp. 44, 46).

Colombo, A., D.E. Galli, L. De Caro, F. Scattarella, and E. Carlino (2017). « Facing the phase problem in Coherent Diffractive Imaging via Memetic Algorithms. » In: *Scientific Reports* 7, p. 42236. DOI: 10.1038/srep42236 (cit. on p. 44).

Clark, JN, J Ihli, AS Schenk, Y Kim, AN Kulak, JM Campbell, G Nisbet, FC Meldrum, and IK Robinson (2015). « Three-dimensional imaging of dislocation propagation during crystal growth and dissolution. » In: *Nature materials* 14.8, p. 780 (cit. on p. 44).

Ulvestad, A, A Singer, JN Clark, HM Cho, JW Kim, R Harder, J Maser, YS Meng, and OG Shpyrko (2015). « Topological defect dynamics in operando battery nanoparticles. » In: *Science* 348.6241, pp. 1344–1347 (cit. on p. 44).

Ulvestad, A, MJ Welland, W Cha, Y Liu, JW Kim, R Harder, E Maxey, JN Clark, MJ Highland, and H You (2017). « Three-dimensional imaging of dislocation dynamics during the hydriding phase transformation. » In: *Nature materials* 16.5, p. 565 (cit. on p. 44).

Liu, Y, PP Lopes, W Cha, R Harder, J Maser, E Maxey, MJ Highland, NM Markovic, SO Hruszkewycz, and GB Stephenson (2017). « Stability limits and defect dynamics in Ag nanoparticles probed by bragg coherent diffractive imaging. » In: *Nano letters* 17.3, pp. 1595–1601 (cit. on p. 44).

Clark, JN, X Huang, R Harder, and IK Robinson (2012). « High-resolution three-dimensional partially coherent diffraction imaging. » In: *Nature communications* 3, p. 993 (cit. on p. 45).

Schell, A (1967). « A technique for the determination of the radiation pattern of a partially coherent aperture. » In: *IEEE Transactions on Antennas and Propagation* 15.1, pp. 187–188 (cit. on p. 45).

Thibault, P. and A. Menzel (2013). « Reconstructing state mixtures from diffraction measurements. » In: *Nature* 494.7435, pp. 68–71. DOI: 10.1038/nature11806 (cit. on p. 45).

Richardson, W.H. (1972). « Bayesian-based iterative method of image restoration. » In: *JoSA* 62.1, pp. 55–59 (cit. on p. 45).

Lucy, L.B. (1974). « An iterative technique for the rectification of observed distributions. » In: *The astronomical journal* 79, p. 745 (cit. on p. 45).

Thibault, P. and M. Guizar-Sicairos (2012). « Maximum-likelihood refinement for coherent diffractive imaging. » In: *New Journal of Physics* 14.6, p. 063004. DOI: 10.1088/1367-2630/14/6/063004 (cit. on p. 46).

Guizar-Sicairos, Manuel and James R. Fienup (2009). « Measurement of coherent x-ray focused beams by phase retrieval with transverse translation diversity. » In: *Optics Express* 17.4, pp. 2670–2685. DOI: 10.1364/OE.17.002670 (cit. on p. 46).

Nocedal, Jorge and Stephen J Wright (2006). *Numerical optimization second edition*, pp. 497–528 (cit. on p. 47).

Shewchuk, Jonathan Richard et al. (1994). *An introduction to the conjugate gradient method without the agonizing pain* (cit. on p. 47).

Jones, Eric, Travis Oliphant, Pearu Peterson, et al. (2001–). *SciPy: Open source scientific tools for Python*. [Online; accessed <today>] (cit. on p. 47).

Godard, Pierre, Marc Allain, Virginie Chamard, and John Rodenburg (2012). « Noise models for low counting rate coherent diffraction imaging. » In: *Optics Express* 20.23, pp. 25914–25934. DOI: 10.1364/OE.20.025914 (cit. on p. 47).

Fernández, Sara et al. (2019). « In situ structural evolution of single particle model catalysts under ambient pressure reaction conditions. » en. In: *Nanoscale* 11.1, pp. 331–338. DOI: 10.1039/C8NR08414A (cit. on p. 51).

Chahine, GA, MH Zoellner, M-I Richard, S Guha, C Reich, P Zaumseil, G Capellini, T Schroeder, and TU Schülli (2015). « Strain and lattice orientation distribution in SiN/Ge complementary metal–oxide–semiconductor compatible light emitting microstructures by quick x-ray nano-diffraction microscopy. » In: *Applied Physics Letters* 106.7, p. 071902 (cit. on p. 51).

Hilhorst, J., F. Marschall, T. N. Tran Thi, A. Last, and T. U. Schülli (2014). « Full-field X-ray diffraction microscopy using polymeric compound refractive lenses. » en. In: *Journal of Applied Crystallography* 47.6, pp. 1882–1888. DOI: 10.1107/S1600576714021256 (cit. on p. 51).

Leake, Steven J., Marcus C. Newton, Ross Harder, and Ian K. Robinson (2009). « Longitudinal coherence function in X-ray imaging of crystals. » EN. In: *Optics Express* 17.18, pp. 15853–15859. DOI: 10.1364/OE.17.015853 (cit. on p. 52).

Fabrizio, E. Di, F. Romanato, M. Gentili, S. Cabrini, B. Kaulich, J. Susini, and R. Barrett (1999). « High-efficiency multilevel zone plates for keV X-rays. » en. In: *Nature* 401.6756, pp. 895–898. DOI: 10.1038/44791 (cit. on p. 52).

Leake, S. J., V. Favre-Nicolin, E. Zatterin, M-I. Richard, S. Fernandez, G. Chahine, T. Zhou, P. Boesecke, H. Djazouli, and T. U. Schülli (2017). « Coherent nanoscale X-ray probe for crystal interrogation at ID01, ESRF - The European Synchrotron. » In: *Materials & Design* 119, pp. 470–471. DOI: 10.1016/j.matdes.2017.01.092 (cit. on p. 52).

Mastropietro, F., D. Carbone, A. Diaz, J. Eymery, A. Sentenac, T. H. Metzger, V. Chamard, and V. Favre-Nicolin (2011). « Coherent X-ray wavefront reconstruction of a partially illuminated Fresnel zone plate. » In: *Optics Express* 19.20, pp. 19223–19232. DOI: 10.1364/OE.19.019223 (cit. on p. 54).

Ponchut, C., J. M. Rigal, J. Clément, E. Papillon, A. Homs, and S. Petitdemange (2011). « MAXIPIX, a fast readout photon-counting X-ray area detector for synchrotron applications. » en. In: *Journal of Instrumentation* 6.01, pp. C01069–C01069. DOI: 10.1088/1748-0221/6/01/C01069 (cit. on p. 54).

Deuxième partie

EXPERIMENTAL WORKS

4

SCANNING X-RAY DIFFRACTION MICROSCOPY TO IMAGE STRAIN FLUCTUATIONS IN ULTRA-THIN SIGE-ON-INSULATOR NANOSTRUCTURES FOR ELECTRONICS

This chapter provides an introduction to the historical development of strain engineering in Complementary Metal Oxide Semiconductor (CMOS) channels to boost the materials performance. A particular attention is drawn to the condensation process, which is used to grow silicon germanium ultra thin (below 20 nm thickness) layers to be integrated as channels in Fully Depleted Silicon On Insulator (FDSOI) p-type Field Effect Transistor (pFET). The Scanning X-Ray Diffraction Microscopy (SXDM) method is presented and used in order to assess the level and relaxation of strain in patterned SiGe directly on insulator. Finally, the empirical model proposed by R. Berthelon Berthelon, 2018 is adjusted so that it fits better with the measured relaxation lengths.

4.1 INTRODUCTION

4.1.1 *Strained SiGe on Silicon-Oxide Insulator*

Electronic properties of semiconductor nanostructures are strongly influenced by their strain state, and many examples have already shown that strain engineering is an efficient tool to boost microelectronics technologies, in particular to improve carrier transport. In order to maintain Moore's law, stating in 1965 that the number of transistors per Silicon area would double every two years, the microelectronics industry had to introduce new ways to boost performance. Thus, enhancement of CMOS circuits has become an important issue, and with it much attention has been paid to MOS channel materials. Down-scaling of devices was replaced by the introduction of strain in materials, as tensile strain increases the electron mobility, while compression of the lattice improves the hole mobility Sun et al., 2007.

Different technologies have been tested and developed to locally modify the mechanical strain during the fabrication of transistors. In a general way, the mechanical loading of the transistor channel can be performed by four methods. Firstly, via the integration of tensile (respectively compressive) contact etch stop layers for n- (p-) Metal Oxide Semiconductor Field Effect Transistor (MOSFET)s Pidin et al., 2004, e.g

an amorphous layer typically made of Silicon nitride. Secondly, with the use of Stress Memorization Technique (SMT), depositing a high tensile stressed SiN layer on top of the source and drain, the whole structure is then recrystallized and finally the SiN removed. A similar technique, known as "Buried OXide (BOX) creep", based on the creep of a BOX at high temperature in order to transfer the strain from a SiN layer, has been assessed recently Berthelon, Andrieu, Mathieu, et al., 2017. Thirdly, by Pseudomorphic Epitaxy of the source and drain in a material with different lattice parameter than the Silicon substrate Yeo, 2006. Ultimately, Substrate Engineering aims to use a modified substrate by epitaxy or bonding transfer of a set of non-matching materials, such as the Silicon-Germanium On Insulator (SGOI), which will be studied in this section.

The latter prestrained semiconductor substrates have been adopted, in particular for the formation of high mobility channels for the ultrathin FDSOI technology Weber et al., 2015. FDSOI forms a new substrate made of an ultra thin body of buried Silicon oxide, lowering losses and reducing parasitic currents. On the one hand, the Silicon On Insulator (SOI) substrate, fabricated by the smart-cut technique which relies on direct bonding Bruel, 1995, has to be thin enough to be fully depleted. In the other hand, in order to mitigate the coupling effect between the drain and the channel through the BOX Ernst et al., 2007, the very same BOX has to be as thin as possible Gallon et al., 2006. Thus, the electrostatic control is maximized for thin Silicon film and BOX, hence the Ultra-Thin Body and Buried oxide (UTBB)-FDSOI Schwarzenbach et al., 2016. The FDSOI technology has been developed at the 28 nm node Planes et al., 2012 and 14 nm node Weber et al., 2015 by STMicroelectronics/CEA-LETI/SOITEC, and heavily relies on a strained channel Berthelon, Andrieu, Ortolland, et al., 2017.

Silicon has long been the first choice material for CMOS technology, due to the high-quality of low-cost Si substrates and the stability of its associated oxide SiO_2. Nowadays, to increase the mobility of carriers, Germanium and III-V materials are considered Kuhn, 2012. However, as the CMOS technology relies on the concomitant use of p-type Metal Oxide Semiconductor (pMOS) and n-type Metal Oxide Semiconductor (nMOS) transistors featuring similar performances, III-V materials low hole mobilities struggle to compete with the well-balanced carrier mobility of Germanium (see Table 4.1).

	Si	Ge	C	GaAs	InAs	InP
Electron mobility ($cm^2.V^{-1}.s^{-1}$)	1600	3900	2800	9200	40000	5400
Hole mobility ($cm^2.V^{-1}.s^{-1}$)	430	1900	1500	400	400	200

Table 4.1 – Carrier mobility at 300K for crystalline structures of Si, Ge, C, GaAs, InAs and InP. D.W.Palmer, 2019

Then, Silicon Germanium alloy has appeared as a first choice to build the new pMOSFET transistors. Thanks to the development of deposition processes on Silicon substrates, industries have adopted the binary alloy Si_xGe_{1-x} to be introduced in pMOSFET. SiGe presents a diamond-like crystalline structure, made of two face-centered cubic lattices, shifted by a quarter of the diagonal of one lattice. A 4.2% lattice mismatch between Si and Ge occurs from the difference in lattice parameters, being 5.431 Å and 5.658 Å respectively. The lattice parameter of a virtual Si_xGe_{1-x} crystal can be approximated by Vegard's law Vegard, 1921 :

$$a_{SiGe}(x) = (1-x)a^0_{si} + xa^0_{Ge} \tag{4.1}$$

Or more precisely thanks to the empirical parabolic law J.P.Dismukes, 1964, describing the bowing effect :

$$a_{SiGe}(x) = 5.431 + 0.20x + 0.027x^2 \tag{4.2}$$

By tweaking the stoichiometry, one can modify the properties of the current carriers while varying continuously the electronic and crystalline properties of the material. The FDSOI specifications target a 20% to 30% range of Germanium content within the SiGe channel. Strained SiGe channels enable a significant increase of electron and hole mobility, as it was proposed by calculations and also demonstrated by experimental measurements DeSalvo et al., 2014. For instance, the effective hole mobility for SiGe channel with 34% Germanium is twice that of SOI Berthelon, 2018; Andrieu et al., 2005, p. 53.

4.1.2 *Condensation process*

In comparison to the other growth techniques, the condensation method exhibits three main assets: firstly, it allows integration of compressively strained SiGe in p-type channels, secondly, it enables the manufacture of highly crystalline and strained SiGe films directly on insulator (Strained-SGOI (sSGOI)) with a Germanium concentration up to 50%, and finally, it presents the possibility of using only conventional manufacturing processes.

From an original idea of Tezuka et al. Tezuka, Sugiyama, et al., 2001, from the Toshiba-MIRAI group, in 2001, to produce high-quality Germanium-On-Insulator (GeOI) or SGOI buffer layers for the growth of tensely strained Si channels, the condensation technique has since been studied by numerous research groups, such

as CEA-LETI Vincent, J. F. Damlencourt, et al., 2008, IBM Bedell et al., 2006, Stanford University Gunji et al., 2011... The first publication on the use of condensation in order to form a defect-free and compressively strained SiGe channel on insulator saw the light of day in 2003 Nakaharai et al., 2003. One can note that the name "condensation" can be misleading, as it refers not to a phase change from gaseous to liquid, but to the fact that the final SiGe layer can be "enriched" in Ge, i.e., a final Ge concentration higher than the one of the initial epitaxial layer.

The condensation technique is described in Figure 4.1. Starting from a Silicon-On-Insulator, a 5 nm to 20 nm-thick fully strained SiGe layer is epitaxially grown on Si. Then, thermal oxidation is performed. Si-selective oxidation occurs and Ge atoms are rejected into the underlying SiGe film. Thanks to the interdiffusion of Si and Ge in the underlying film and the presence of the BOX as a diffusion barrier, the Ge concentration is homogenized. During the last step, the sSGOI layer tends to shrink because some Si is incorporated into the growing oxide during the oxidation process. This technique results in a naturally strained and highly crystalline SiGe layer, whose thickness and Ge content can be precisely controlled within 7 to 20 nm and from 0% to 50% respectively Boureau, Benoit, et al., 2016.

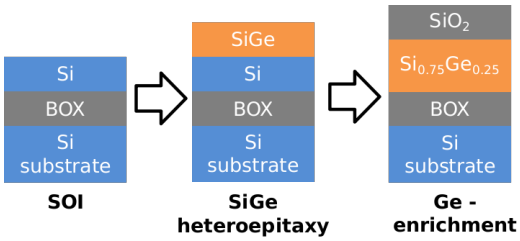

Figure 4.1 – SiGe condensation process.

This process remains difficult to control, hence leaving a number of open questions. We will try to address the issues of crystalline quality, in-depth homogeneity and particularly the accuracy and behavior of strain with respect to the initial target.

4.2 SAMPLE DESIGN AND FABRICATION

4.2.1 *Sample design*

As described in Remy Berthelon's PhD thesis Berthelon, 2018, the reference process is as follows : starting from a SOI substrate (SOITEC supplier) with a 20 nm-thick BOX, the SiGe layer is grown by heteroepitaxy by Reduced Pressure-Chemical Vapor Deposition (RP-CVD). The thickness of the deposited SiGe is 20 nm with a targeted Ge-concentration of 24 atomic %. Then, the SiGe layer on insulator is obtained by the condensation process at 1050 °C (Rapid Thermal Oxidation (RTO)),

taking advantage of the preferential oxidation of Silicon over Germanium [1]. The upper SiO_2 oxide (designed as padox) is then removed by wet etching. To perform the lithography process, a hard mask has to be deposited first by Plasma Enhanced CVD with TEOS (TetraEthylOrthoSilicate). To protect the surface, a 4 nm-thick oxide pad is deposited before a 55 nm-thick SiN hard mask by Low Pressure-CVD. In order to achieve a uniform SiGe layer directly on insulator, an anneal of 30 min at 1050 °C under N_2 is performed to allow Silicon-Germanium atom interdiffusion. The SiGe is then patterned by Ultra-Violet Litography (UVL) and a deep etching step. The SiN hard mask is then removed by selective H_3PO_4 assisted etching. This reference sample (Figure 4.2, SGOI) is compared with samples of different integration schemes. In order to study the role of the SiN hard mask, a sample is studied prior to the SiN removal (Figure 4.2, SiN/SGOI). Another sample did not undergo the condensation process neither the annealing, yielding a SiGe/Si bilayer.

The samples are then patterned with a special mask. As the SiGe layer thicknesses are well below the critical thickness, there is no plastic relaxation People and Bean, 1985; Tezuka, Nakaharai, et al., 2006. However this patterning will enable elastic relaxation of the SiGe layers. What drives us to characterize these samples is the need for a strain control and the evaluation of the strain relaxation. The use of an X-ray nanobeam will allow us to study a large number of structures in a given sample and thus get statistical information on the growth process used.

The four different kind of samples depicted in Figure 4.2, and studied in the following, are labeled as follow:

— Sample A - SGOI with nitride on top, 20 nm-thick SiGe layer,
— Sample B - SGOI without nitride on top, 20 nm-thick SiGe layer,
— Sample C - SGOI without nitride on top, 13 nm-thick SiGe layer,
— Sample D - Bilayer: SiGe/Si/BOX without nitride on top, 20 nm thick SiGe layer.

1. This high temperature favors the oxidation mechanisms with respect to atomic diffusion.

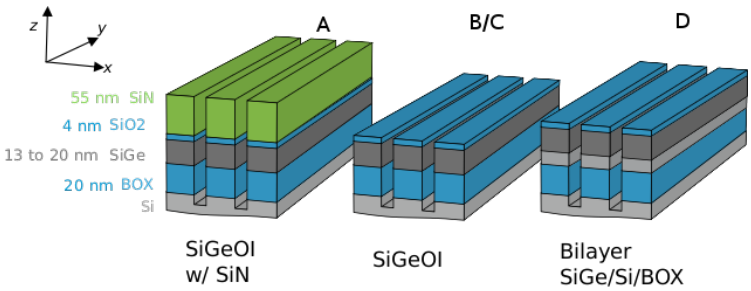

Figure 4.2 – Sketches of the three kinds of samples investigated. Light gray stands for Si, blue for oxide, dark gray for SiGe and green for nitride. From left to right : first appears the condensed SiGe directly on insulator before SiN hard mask removal (sample A), then the same SGOI after the SiN removal (sample B & C) and finally the SiGe/Si bilayer case, i.e. without condensation (sample D). The X direction is along the [110] direction, and the vertical Z direction is oriented along the [001] direction.

4.2.2 *DIVA mask*

The special mask for patterning developed at CEA-LETI to investigate geometry effects, contains 103 structures, each of 2 mm x 2 mm (see Figure 4.3). 102 structures are grid patterns of either lines, squares or rectangles.

		1	2	3	4	5	6	7	8	9	10
lignes hor.	A	A1	*A2*	*A3*	*A4*	A5	A6	*A7*	*A8*	*A9*	A10
lignes hor.	B	*B1*	*B2*	B3	*B4*	*B5*	*B6*	B7	*B8*	B9	*B10*
lignes hor.	C	C1	C2	C3	C4	C5	C6				
carrés	D	*D1*	D2	*D3*	D4	*D5*	D6	*D7*	D8	*D9*	D10
carrés	E	E1	*E2*	*E3*	*E4*	E5	E6				
double-carrés	F	*F1*	*F2*	*F3*	F4	F5	*F6*	*F7*	F8	*F9*	F10
double-carrés	G	*G1*	*G2*	G3	*G4*		*G6*				
triple-carrés	H	*H1*	*H2*	*H3*	H4	H5	*H6*	*H7*	H8	*H9*	H10
triple-carrés	I	*I1*	*I2*	I3	*I4*		*I6*				
quadruple-carrés	J	J1	J2	J3	J4	J5	J6	J7	J8	J9	J10
quadruple-carrés	K	K1	K2	K3	K4	K5	K6	K7	K8		
triple-carrés (c=0.5d)	L	*L1*	*L2*	*L3*	*L4*	L5	*L6*	*L7*	*L8*	L9	
triple-carrés (c=2d)	M	M1	*M2*	M3	M4		M6		*M8*		M10

A6	: DUV cas1
A8	: DUV *cas 2*
A5	: Ebeam cas 1
A7	: Ebeam *cas 2*

Figure 4.3 – Scheme of the DIVA mask and the different structures it holds (coordinates system from A to M and 1 to 10 enables precise location). Blue areas are ebeam lithographed and yellow areas are deep uv (DUV) lithographed. Each structure is 2 x 2 mm^2 and the studied ones are enlighten by a red circle.

The presence of a strip above each structure, containing information about coordinates and characteristic sizes of the grid pattern, enables a clear and efficient location with a microscope (see Figure 4.4). Note that these labels will be very useful for the next experiments carried out at synchrotron sources.

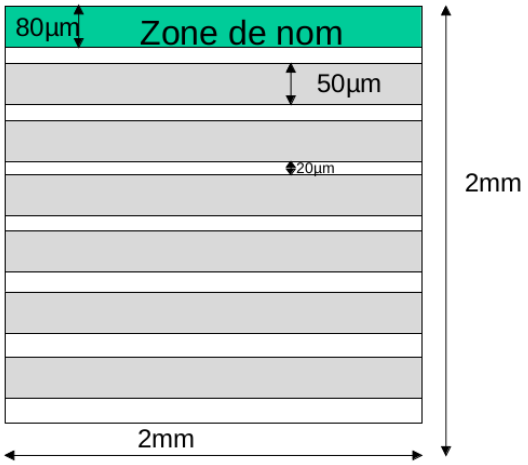

Figure 4.4 – Scheme of one particular DIVA structure.

Thanks to e-beam lithography, some structures can reach characteristic lateral size as small as 45 nm. On this study, we focused on a limited set of structures with a square-based geometry :

— D2 : squares of 500 nm x 500 nm, spaced by 500 nm,
— D4 : squares of 2 µm x 2 µm, spaced by 2 µm,
— D6 : squares of 5 µm x 5 µm, spaced by 5 µm.

And a line-based structure was also selected in order to have a quasi-bulk reference :

— C6 : horizontal lines of 50 µm width, spaced by 20 µm, which can be seen as a full sheet layer relative to the size of the nanobeam of our experiments.

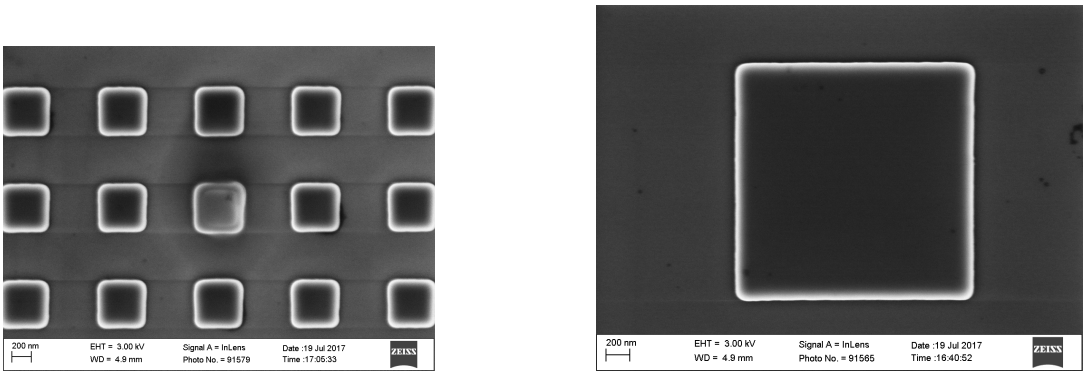

(a) (b)

Figure 4.5 – SEM image of patterns from different structures. (a) D2 structure - squared pattern of 500 nm x 500 nm. On this caption, taken after the experiment described in the following section, one can notice the deposition of carbon on the central pattern, due to beam exposition; (b) D4 structure - squared pattern of 2 µm x 2 µm. Note also the rounded shape of the corner due to the etching process.

4.3 STRAIN MEASUREMENT AND SIMULATION

4.3.1 *Comsol modeling*

Finite Element Method (FEM) mechanical simulations using COMSOL AB, n.d. were performed in order to have the theoretical evolution of the strain inside the SiGe layer, according to the channel's length. The "structural mechanics" module was used to model a 3D structure, under stationary study.

The growth direction is along z, and the (x, y) plane defines the epitaxial plane. As the calculation were not specially computationally intense, we decided not to reduce the system although a quarter of the structure could have been considered given the symmetry of the model. The SiGe layer, containing 24% of Ge, is centered on the geometrical frame so that the point of coordinate $(0, 0, 0)$ is at the center of the SiGe/BOX interface plane. Figure 4.6 shows the refined mesh, along with the complete geometry of the model.

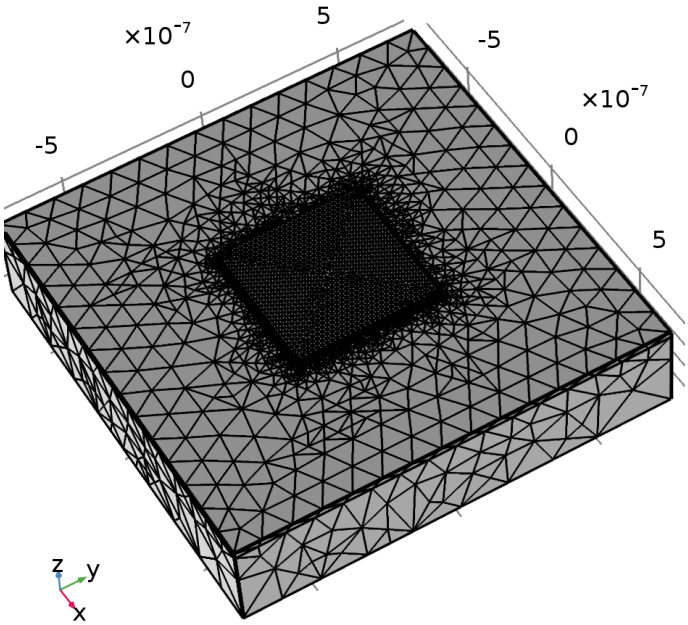

Figure 4.6 – Geometrical model and COMSOL mesh. Si substrate is 300 nm thick and 3 times the width of the SiGe island. A 20 nm-thick oxide layer is present in-between the substrate and the island. Units are in meter.

At $x, y = L_{act}/2$, a free boundary condition is introduced to account for the etching process. The latter is performed at low temperature, therefore the elastic domain assumption is valid [2]. Table 4.2 gives a review of the material mechanical properties used within the scope of the simulations.

2. SiO_2 creeping does not happen below ≈960°C EerNisse, 1977

MATERIAL	YOUNG'S MODULUS	POISSON'S RATIO
$Si_{0.75}Ge_{0.25}$	Anisotropic material: $C_{ij}^{<110>}$ [GPa] $\begin{pmatrix} 184.6 & 31.8 & 60 & 0 & 0 & 0 \\ 31.8 & 184.6 & 60 & 0 & 0 & 0 \\ 60 & 60 & 156.5 & 0 & 0 & 0 \\ 0 & 0 & 0 & 76.4 & 0 & 0 \\ 0 & 0 & 0 & 0 & 76.4 & 0 \\ 0 & 0 & 0 & 0 & 0 & 48.2 \end{pmatrix}$	
Si	Anisotropic material: $C_{ij}^{<110>}$ [GPa] $\begin{pmatrix} 194.5 & 35.3 & 63.9 & 0 & 0 & 0 \\ 35.3 & 194.5 & 63.9 & 0 & 0 & 0 \\ 63.9 & 63.9 & 165.8 & 0 & 0 & 0 \\ 0 & 0 & 0 & 79.6 & 0 & 0 \\ 0 & 0 & 0 & 0 & 79.6 & 0 \\ 0 & 0 & 0 & 0 & 0 & 51 \end{pmatrix}$	
Oxide	70 GPa	0.17

Table 4.2 – Material mechanical properties used for FEM simulations.

The proper way to simulate a pseudomorphic SiGe layer with COMSOL is to introduce an "initial stress and strain" for the SiGe "linear elastic material". As a result, the initial stress is set to zero, while the initial strain in all 3 directions (x, y and z) must be set to $\varepsilon_{\parallel}(x_{Ge}) = 0.94\%$, the true misfit strain. This can be considered as an initial force coming from the lattice mismatch between SiGe and Si, driving the SiGe to expand. During the epitaxy, at least far from the edges of the wafer, the epitaxial SiGe layer is free to expand only in the z direction. Therefore, the pseudomorphic SiGe experience a compressive in-plane strain.

First, we investigate the scenario when no SiN layer is present. Figure 4.7 shows a 3D visualization of the resulting out-of-plane strain ϵ_{zz} of the SiGe layer, with a 10 times magnification of the deformation in oder to visualize the impact of the strain on the bending of the island. Note that the values of strain extracted from COMSOL are relative to the silicon substrate lattice parameter, hence not "real strain" as defined in section 2.2.

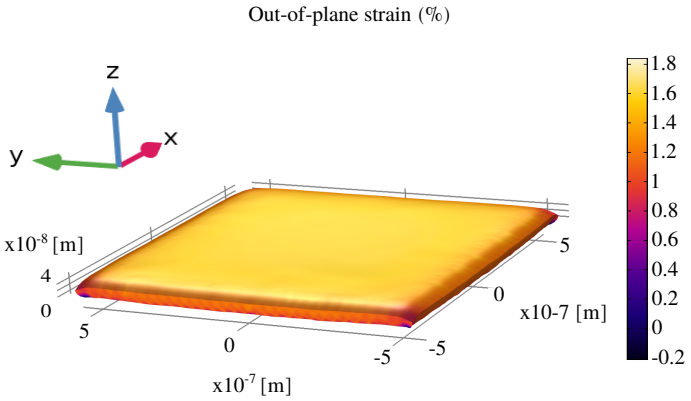

Figure 4.7 – 3D representation of out-of-plane strain of the SiGe epitaxial layer, with the corresponding deformation of the layer, displayed with a 10 fold magnification. From this, one can clearly see the bending of the layer at its edge, and the relative uniform strain at its center. On this figure, the island of width L_{act} =1 µm reaches an out-of-plane strain of 1.6% at its center.

In order to understand the evolution of the relative strain with respect to the width of the channel, we investigated three different active widths : 250, 500 and 1000 nm. For the three different widths, profiles of strain have been extracted at three different depths of the layer, namely at the interface between the SiGe and the BOX, at halfway up the SiGe and at its last atomic plane, *i. e.* in contact with the padox. Figure 4.8 shows these profiles of both (a) out-of-plane ϵ_{zz} and (b) in-plane strain ϵ_{xx}. A few comments have to be made on these results. Firstly, the behavior of both strains at the SiGe/BOX interface is not accurate as the software constrains the strain to be equal to zero at the very edges of the channel. This is most likely due to the mesh and may lead to the creation of "bounces" just before the edges, as a result these profiles at the substrate interface will not be further analysed. Secondly, the mirror behavior of out-of-plane strain and in-plane strain that respectively decreases and increases at the edges of the channel, demonstrates the lattice relaxation of the layer at the edges, thanks to the free-boundary conditions introduced by the etching step of the process : the lattice tends to the one of SiGe, larger than the one of the Si substrate. Finally, the maximum (respectively minimum) of the out-of-plane strain (respectively in-plane strain) is reached at the center ($x = 0$) of the channel, and decreases (respectively increases) while the active width decreases. Therefore, the SiGe layer is no longer in fully-constrained when its width is smaller than 500 nm. This gives us a hint concerning the relaxation length, that has to be around 250 nm (*i. e.* half of the 500 nm-wide channel).

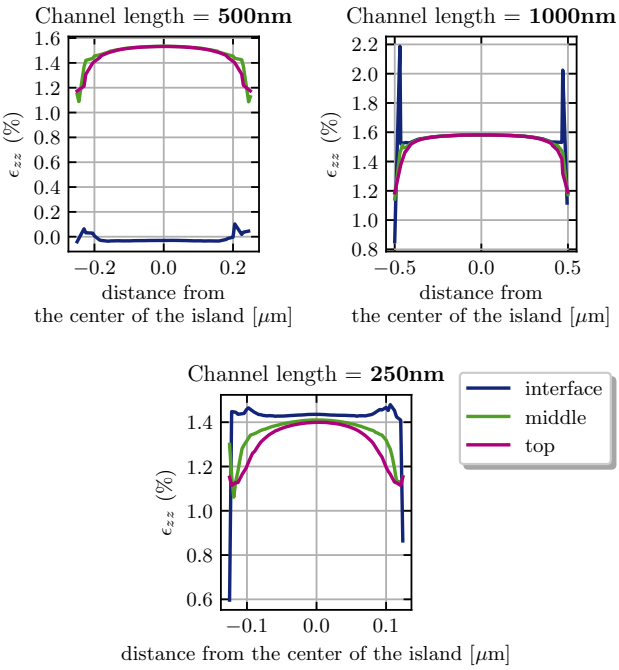

(a) Evolution of out-of-plane strain

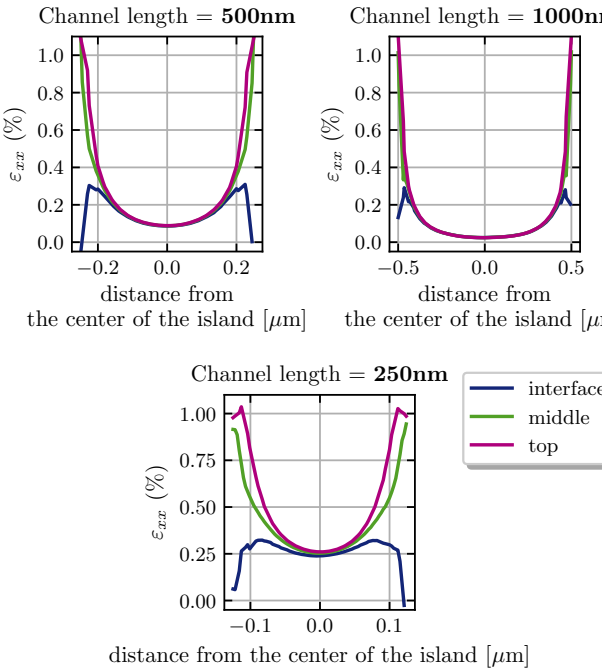

(b) Evolution of in-plane strain

Figure 4.8 – Profiles of (a) the out-of-plane strain ε_{zz} and (b) the in-plane strain ε_{xx}, at three different thicknesses of the SiGe layer, and for three different widths L_{act} = 250, 500 and 1000 nm. The profiles are extracted along the width of the pseudomorphic layer, at either the SiGe/BOX interface (blue curves), the middle of the SiGe layer (green curves) or at the top of the SiGe layer (magenta curves). One should notice the difference between the wider island and the narrower one : the out-of-plane strain no longer reach its fully-strained value of 1.6% when the island is narrow. This indicates that the relaxation length of such SiGe should be at least larger than the half width, *i. e.* larger than 125 nm. Note that the interface is disturbed most likely because of the mesh, which may not be fine enough for such an ultra-thin layer. However, this does not affect the behavior of strains at higher z profiles.

Then, the impact of a tensely stressed SiN layer on top of the SiGeOI was assessed on a 1 µm wide SiGe layer. The role of the SiN is to conserve the strain of the underlying SiGe by preventing it to expand its in-plane lattice and thus relax its strain[3]. Figure 4.9 shows the evolution of both the in-plane strain and the out-of-plane strain, with respect to the Si substrate lattice parameter, for three different conditions : without any SiN layer, with an unstressed SiN layer and with a tensely stressed SiN layer at σ =1.2 GPa. The strains are extracted at the mid-height of the SiGe layer, and its profile is displayed from the center to one edge of the channel. Concerning the in-plane strain, the SiN layer allows to maintain it at 0% until 200 nm

3. The relaxation of the full stacking can be obtained by the "BOX-creep" technique, introduced in section 4.1.1.

from the edge (150 nm when the SiN is tensely stressed at 1.2 GPa), and to halve it at the very edge.

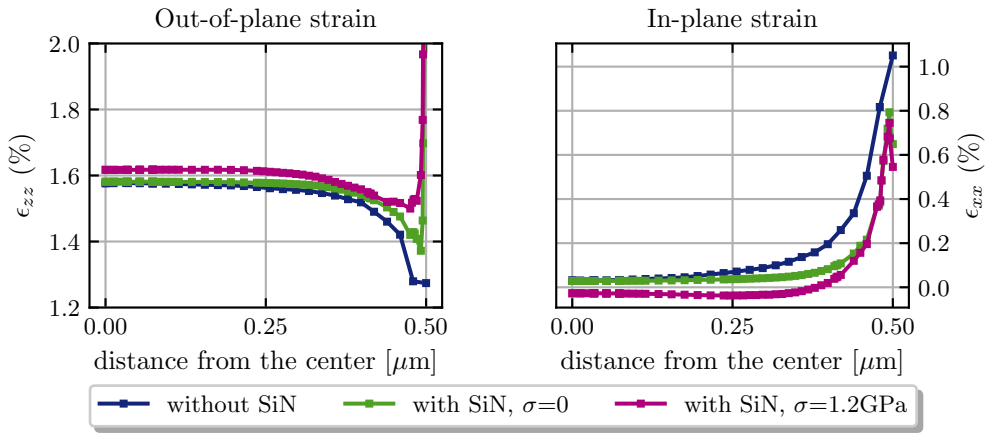

Figure 4.9 – Impact of a SiN layer on top of a 1 µm-wide sSiGeOI. Profiles of out-of-plane and in-plane strains, for three different case : without any SiN layer, with an unstressed SiN layer and with a tensely stressed SiN layer at σ =1.2 GPa.

In conclusion, the FEM simulations give an insight on the relaxation process of the sSiGeOI, and demonstrate the impact of adding a SiN layer to prevent this relaxation. However, the elastic simulation is probably lacking a physical mechanism as the relaxation lengths seem to be underestimated compared with the results of the experimental measurements described later.

4.3.2 *µRaman measurements*

The patterning-induced strain relaxation of these samples has been assessed by means of µRaman spectroscopy in the work of R. Berthelon Berthelon, 2018. The monochromatic laser source used during the measurement reached a spatial resolution of around 500 nm, and the analysis assumed a biaxially strained pseudomorphic SiGe film. Within these assumptions, the measured Raman shift only depends on the Ge-concentration x Anastassakis et al., 1990; Wong et al., 2005; Wolf, 1999:

$$\Delta\omega^{\mathrm{Si-Si}} = \frac{p}{2\omega_0}\left[\left(1 - 2\frac{C_{12}(x)}{C_{11}(x)}\varepsilon_{/\!/}(x)\right)\frac{a_{SiGe}(x)}{a_{Si}} - 1\right] \tag{4.3}$$

where $\varepsilon_{/\!/}(x) = \frac{a^{/\!/}_{SiGe} - a_{SiGe}(x)}{a_{SiGe}(x)}$ is the in-plane strain for growth along the (001) direction, $a_{SiGe}(x)$ is derived from 4.2, the $C_{ij}(x)$ are the elastic constants of $Si_{1-x}Ge_x$, ω_0 is the peak position of Silicon and p is the deformation potential ($p = -1.85\omega_0^2$)

As a result, the Raman measurement of wide (50 µm) stripes provides quantitative evaluation of the Ge-concentration. This is made possible through the assumption

that the stripes are made of pseudomorphic SiGe, *i. e.*, $a^{/\!/}_{SiGe} = a_{Si}$. Furthermore the Ge-concentration is presumed to be the same for all the structures within a same sample (see Figure 4.2). As a result, the Ge-content is found to be equal to 22.2% for all samples but the bilayer sample; the latter features a slightly higher concentration of 23.7%. The most likely explanation of this difference is the spatial fluctuation of Ge-concentration during the epitaxy of SiGe. Indeed, on the one hand, all the samples with a 20 nm-thick SiGe layer are grown on the same Si wafer and on the other hand, Ge-enrichment is only possible when the (at least quasi-) totality of Si in the starting SOI substrate has been consumed by oxidization. That way, the bilayer stack with SOI remaining in-between the SiGe layer and the BOX is less likely to experience an increase of the Ge-concentration.

However, these assumptions do not take into account process variability (*e. g.* completion of the condensation process) or any other dependence on the thickness or strain. That way, it is likely that slight in-depth inhomogeneities or sliding at the SiGe/BOX interface arise, leading to a deviation of the SiGe in-plane lattice parameter from the Si substrate lattice parameter. For instance, one should note that a 0.1% error in the assumed in-plane lattice parameter (*i. e.* $a^{/\!/}_{SiGe} = 1.001 \times a_{Si}$ in equation 4.3) of the pseudomorphic SiGe leads to a 1.1% difference in the Ge-concentration. In addition, it is assumed that the error on peak position is $\pm 0.1 \text{cm}^{-1}$ which leads to an uncertainty on the Ge-concentration calculation of $\pm 0.3\%$. The case of perfectly matching interface sets a conservative lower bound of the Ge-concentration, of $22.2\% \pm 0.3\%$, whereas the case of slight mismatch at the interface, with the same error coming from the Raman measurement, sets a conservative upper bound of $23.3\% \pm 0.3\%$. All in all, if one the Ge-concentration of the SGOI sample of reference can safely be said to be between 21.9% and 23.6%.

Then, when the SiGe layer is patterned in one direction (x-axis from Figure 4.2), a free boundary condition is introduced and allows unidirectional strain relaxation, breaking the biaxial configuration. Studying 2 mm-long SiGe stripes makes it possible to extract the partially relaxed strain in the transverse direction. With the knowledge of the Ge-concentration, the fully-relaxed SiGe lattice parameter is known, as well as the elastic constants of $Si_{1-x}Ge_x$ (interpolated using Vegard's law Vegard, 1921) and the initial strain before patterning $\varepsilon_{/\!/}$. As a result, the Raman shift only depends on the strain in the transverse direction ε_{XX}. On 5 and 2 µm wide stripes, µRaman scans of 200 nm step size (with a 500 nm spot size) have been performed. The results are showing an increase of the Raman shift towards the negative values, which means a compressive strain reduction. However, the measurements at the edge of the stripes still exhibit a high ε_{XX} strain, whereas it should theoretically tend to zero for very small width (note that one deals with real strain, i.e. deforma-

tion of the material with respect to its relaxed lattice parameter). This is attributed to the spot size being too large to give sufficient resolution.

In order to get more sensitivity to the strain relaxation, it has been decided to perform μRaman measurements on arrays of stripes. This way, the spot covers several stripes, the frequency shift is thus related to the mean strain in the stripes. Stripes of width 100 nm, 250 nm and 500 nm have been measured. The narrower the SiGe stripe, the lower the value of SiGe Raman frequency peak i.e., the lower the ε_{XX} strain. This is expected as a finer stripe should be made of more relaxed lattices than a wider one.

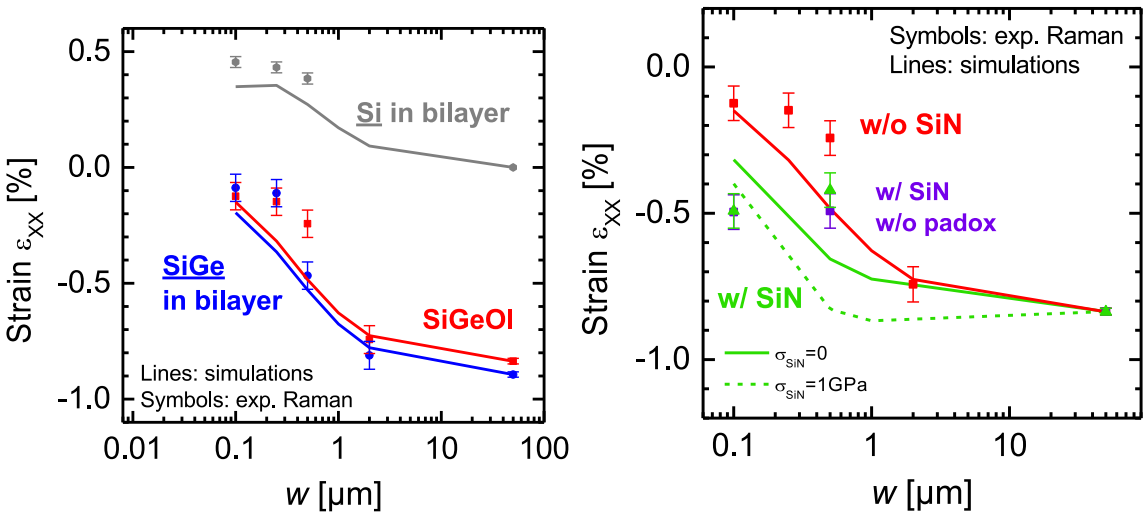

Figure 4.10 – From R.Berthelon Berthelon, 2018. Extracted mean strain ε_{XX} according to the stripe width w for SGOI with and without SiN, and for SiGe/Si bilayer. The lines correspond to FEM mechanical simulations. The SiGe compressive strain decreases when the stripe width is reduced for both samples because of the relaxation on edges. The SOI of the bilayer shows an increased uniaxial tensile strain for reduced stripe widths. The SiN layer enables to maintain the compressive strain in the SiGe layer, especially for w=100 nm.

Figure 4.10 shows the mean strain ε_{XX} deduced from Raman analysis for all samples compared with FEM simulations. One can derive two conclusions from the two subplots. Firstly, the impact of the SiN: the compressive strain in the SiGe layer remains even for stripes of width 100 nm, which matches with the simulation since the SiN mechanically prevents the SiGe from relaxing. Secondly, the strain extracted experimentally for stripes of width 500 nm is lower than expected from simulations: the relaxation length is higher than expected, and should reach at least 250 nm as a 500 nm-wide stripe exhibits the same averaged strain as a 100 nm-wide, that is fully-relaxed.

4.3.3 *NBED measurements and modeling*

The patterning-induced strain relaxation of the samples has also been assessed by means of NBED in the work of R. Berthelon Berthelon, 2018. NBED measurements give the relative deformation of the SiGe with respect to the lattice of relaxed Silicon, by comparing the SiGe diffraction pattern with the one of the bulk Silicon lying underneath.

Furthermore, as the self-consistent force-distributed model of Hu Hu, 1979, 1991 failed to be consistent with the observations [4], they propose an empirical description of the stress relaxation occurring in patterned SGOI. Starting from a simple exponential decay with only one parameter, the typical relaxation length λ, and taking into account the impact of two edges plus the fact that this function must cancel at both edges, the relaxation can finally be written as ::

$$f_{\text{relax}} = 1 - \exp\left(\frac{x}{\lambda}\right) - \exp\left(-\frac{L_{act} - x}{\lambda}\right) + \exp\left(-\frac{L_{act}}{\lambda}\right)$$

where L_{act} is the active area length. One just needs to integrate $\sigma_0(x_{Ge}) \times f_{\text{relax}}(x, L_{act})$ to derive the mean stress $\langle\sigma\rangle$.

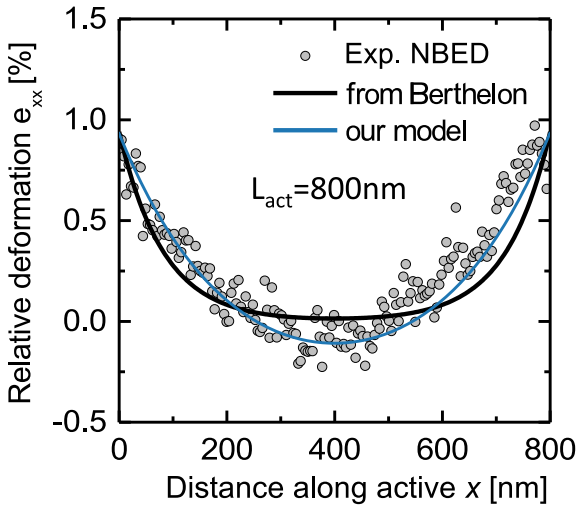

Figure 4.11 – From R. Berthelon Berthelon, 2018. Relative deformation after etching from NBED measurement and analytical model for an active length of 800 nm. The model from Berthelon, 2018 assumes a typical relaxation length $\lambda = 84$ nm (black line) while our model is using a typical relaxation length of $\lambda = 220$ nm (blue line)

4. The Hu's model neglects the strain variation of the film along the surface normal (very thin film approximation) and considers a distributed force in the film resulting from the coupling of the film relaxation with the substrate. For the model to be valid, the substrate and the film should also be perfectly adherent.

Figure 4.11 shows the relative deformation profile on a SGOI of active length $L_{act} = 800$ nm. The profile is confronted with the empirical model, translated into relative deformation assuming a Ge-concentration of $x_{Ge} = 25\%$ and with a typical relaxation length $\lambda = 84$ nm. One could note that the slope of the model looks sharper than the slope of the actual dataset, and the model's plateau is 400 nm-long while the plateau of the dataset is less than 200 nm-long. This would indicate that the typical relaxation length used is underestimated. As seen in Figure 4.11, a model using a relaxation length $\lambda = 220$ nm, depicted by the blue line, looks far more consistent with the dataset.

4.4 SCANNING X-RAY DIFFRACTION MICROSCOPY

4.4.1 *Principle*

The technique of SXDM is a powerful method to characterize small features combining the lattice parameter resolution supplied by hard X-ray diffraction with the beam size available in real space. Scanning X-ray diffraction microscopy is a scanning probe technique that allows the study of individual nanostructures, giving access to qualitative and quantitative characterization of the structural properties, e.g. lattice parameters and orientations Mocuta et al., 2008; Hanke et al., 2008. Contrary to transmission electron microscopy, SXDM needs no a priori preparation of the sample and can be used for both embedded structures or in situ experiments. As a result, SXDM can be sometimes called "non-destructive", although care should be taken with the number of photons interacting with the sample as they may impact it.

However, the technique is limited by two main experimental difficulties. Firstly, the nanoscopic size of the sample makes its localization very difficult. Secondly, scanning a structure with a nano-focused beam and steps of a few hundred nanometers may take a long time.

4.4.2 *Quick mapping*

The beamline control program at the ESRF, SPEC, allows performing step scans : each step requires an amount of time which is determined in the one hand by the exposure time, intrinsically related to the diffraction power of the sample and limited by the least necessary counting statistics, and on the other hand by a fixed holding and settling time, which includes data transfer and connection between program and motors/detector. At the ID01 beamline, this latter time is of the order of 1 s per frame when using a 2D detector, and represents the lower limit of the

total time required for each step. With exposure time of the order of milliseconds for samples such as nanomaterial thin-films and photon counting pixel detectors enabling exposure time shorter than a millisecond, it is clear that the weakness of step scans is the positioning time of the hardware and software.

These difficulties were overcome thanks to the development of a continuous quick mapping scanning mode (Kmap) Chahine et al., 2014. The development and integration of a multipurpose unit for synchronization sequencing and triggering card provided the means to combine high-speed continuous motion with precise and continuous readout, together with high-frequency image recording. In other terms, it enables reducing the overhead and parallelizing positioning, exposure, and data handling.

Thanks to this fast-continuous two-dimensional mapping, a 100 x 100 μm^2 space map with 500 nm step size (40 000 frames) with 10 ms exposure time went from 10 hours of measurement down to 7 minutes. The benefits are two-fold. Firstly, this makes possible precise and fast localization of the target sample by mapping real space at only a few angles. Secondly, reciprocal space maps can now be obtained within a few hours of beamtime instead of days. For example, a spatial map at each angle of a 20-points rocking curve that would require approximatively nine days of measurement in a basic step-scan mode is now feasible in less than 2.5 hours. A full dataset $I(x, y, Q_x, Q_y, Q_z)$, which is then five-dimensional, often represents approximately 0.3TB of uncompressed data (and few tens of GB once compressed). These features will be still improved by the extremely brilliant source project presently under way at the ESRF, that will increase the brilliance by a factor of about 40 and the coherence of the beam by two orders of magnitude.

4.4.3 *Experimental protocols*

In this subsection, the general principle of SXDM is described, followed by the definition of key parameters and typical applications. The experimental setup is then detailed carefully, with a point-by-point "how to" of a SXDM experiment at the ID01 beamline.

The general principle of SXDM is to record, on each position of a scanned sample, three-dimensional Bragg peaks by rotating the sample and recording frames on a two-dimensional detector. By adding a third dimension to the 2D detector data, a precise location of the center of mass of the Bragg peak is achievable and thus gives access to the local structure variations.

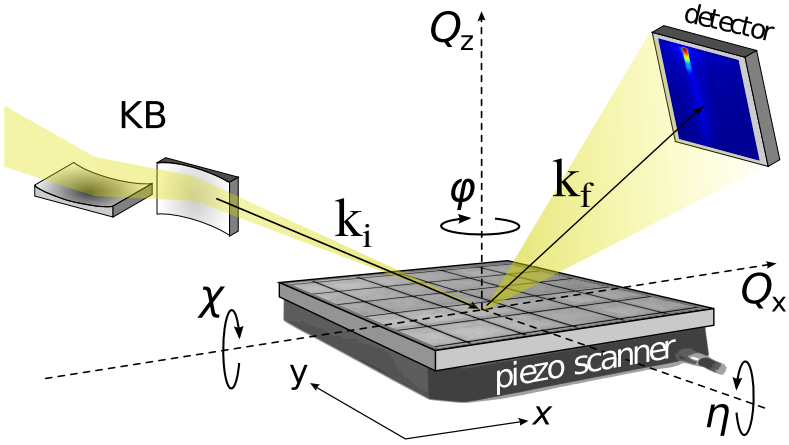

Figure 4.12 – Sketch of the experimental setup of a SXDM experiment. KB mirrors focus a beam on a sample that is raster scanned on a piezo stage, at a certain Bragg angle in order to record the corresponding diffraction on a 2D detector. Both real space (x,y) and reciprocal space (Qx,Qz) axes are depicted to understand the coordinate systems that are used during SXDM. The figure also depicts the incident and exit wavevectors (k_i, k_f) and all the angular motor to set the sample in Bragg condition (η, ϕ, χ).

That way, SXDM yields information on tilt and strain at each position of a 2D sample by generating 5D dataset that can be represented by two map, one in real space with a resolution limited by the size of the X-ray beam on the sample, and one in reciprocal space, formed by slices of 2D diffraction pattern from each illuminated spot, whose resolution is then limited by the beam divergence. The typical setup of a SXDM experiment with KB mirrors is depicted in Figure 4.12. In theory, Abbe's diffraction limit sets the relation between the focal spot size S and the beam convergence angle 2α to be $S = \lambda/(2\sin\alpha)$ which indicates that the wavelength λ should be the fundamental resolution limit. However, the achievable spot size in real-life experiment is most of the time limited by the source size combined with the working distance which defines the maximum demagnification ratio that can be reached.

The photon yield of the X-ray source combined with the scattering power of the sample are key parameters to define the working regime of the technique. Penetration depth and robustness of the sample usually define the X-ray energy regime and maximum counting time of illumination.

Some typical applications are:

— orientation/strain/composition mapping in semiconductor devices,
— imaging of ferroelectric/ ferromagnetic domains,
— imaging of phase coexistence,
— tracing crystallization paths in *e. g.* phase change memories.

A fast readout two-dimensional Maxipix photon counting, mounted at 96 cm from the sample, with 516 x 516 pixels of 55 µm size, was used to record the diffracted intensities. The sample (Figure 4.2) was mounted on a fast scanning piezoelectric stage with a 2 nm resolution and a 200 µm range.

To be able to get reasonable counting statistics from the ultra thin SiGe layers along with high lateral resolution, a specific setup has been used with no monochromator but a 0.4% bandwidth pink beam illumination at 8 keV. The X-ray beam was then focused down to a 380 nm (horizontal) x 170 nm (vertical) spot size using KB mirrors, with coherent slits opened at 200 µm x 60 µm, in order to reach $3.5x10^6$ photons/sec/nm^2. This flux density was possible thanks to the use of a pink-beam.

After aligning the beam on the center of rotation of the diffractometer [5], the incident beam was characterized using two methods. The first one consists in scanning a Silicon wedge on the sample stage vertically, while the beam is aligned with the horizontal direction of the sample stage, so as to go from a state where the beam is fully illuminating the detector to a state where no photon reaches it. This enables to get a grazing incidence onto the sample stage and one can then move the sample rotation to 0.2° and the detector arm to 0.4° in order to get the reflected beam on the detector. Another vertical scan of the Silicon wedge gives a good estimation of the beam profile of around 220 nm (see Figure 4.13). The second method is more complete. Using direct ptychography on a reference sample (Siemens Star [6]), the incident beam is fully characterized in amplitude and phase, within a few tens of minutes - alignment, scan and data analysis Leake et al., 2019. This task is performed using a python library developed at the ESRF Favre-Nicolin, 2019; Mandula et al., 2016. From this second method, one can derive the beam size at the focal plane to be 385 nm in the horizontal and 170 nm in the vertical directions (see Figure 4.13). After a first series of alignment scans, the coherent slits of the KB mirrors were opened to their maximum (i.e. 200 µm x 200 µm) in order to get even more flux, and reducing the horizontal size to 220 nm.

5. The COR of the diffractometer is done using image registration of a feature registered with the beamline microscope Diffractometer COR alignment on the intranet of the ESRF (accessible to ESRF users).

6. Siemens star sample, on the intranet of the ESRF (accessible to ESRF users)

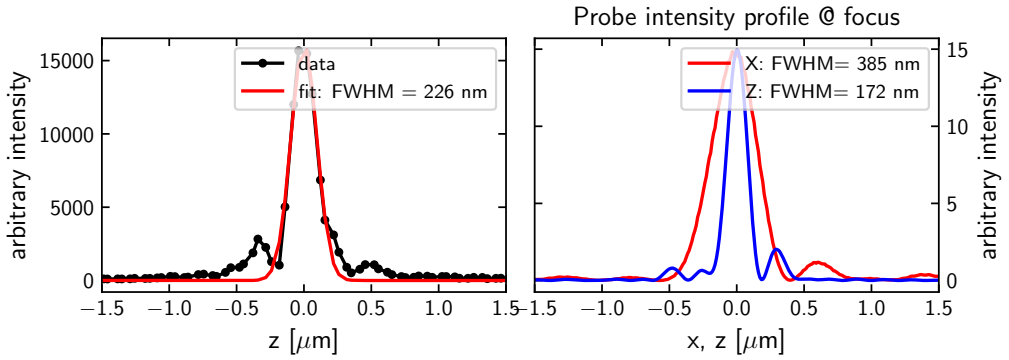

Figure 4.13 – KB incident beam (probe) profiles. On the left-hand side, the dotted black line represents a scan of the beam in the vertical direction, and the red line is the associated Gaussian fit that leads a 226 nm FWHM. On the right-hand side, both vertical (blue line) and horizontal (red line) profiles from the reconstructed beam via ptychographic scan of a reference pattern (Siemens Star) are depicted, leading to a beam size of 385 nm (horizontal) x 172 nm (vertical).

Once the beam is aligned and characterized, one needs to find out the structure of interest on the sample. Thanks to the DIVA lithography mask, the different areas of one sample are easily identifiable with the beamline optical microscope, at the time mounted vertically on top of the sample. Then, a finer alignment is helped by the fast continuous mapping at a Bragg angle: once the sample is put in diffraction condition, a raster scanning of a zone with just a detector integrated intensity map gives clear location of the features of interest.

The next important step is to optimize the Bragg diffraction angles for both the substrate, so that a clear reference can be used, and the SiGe layer, by radial scans at each reflection of interest. For instance, the (004) reflection of the buried bulk Si provides an absolute reference for the further calculated lattice parameters. From Figure 4.14, the center of mass of the Si peak on the detector, at the incident angle giving rise to the maximum of intensity can be estimated to be at $(X = 220, Y = 266)$ in pixels. This, combined with the known position of the direct beam and the angles of the diffractometer, provides $a_{Si}^{\text{measured}} = 4\lambda/(2\sin\theta) = 5.441\,\text{Å}$. This value corresponds to a 0.19% absolute error relative to the tabulated Silicon bulk lattice parameter at room temperature ($a_{Si} = 5.431\,\text{Å}$ for an incidence angle of 34.8°), which gives rise to a normalization factor that will be applied throughout the entire analysis of the data. Note that the approximation made by rounding on the pixel corresponds to around 0.005% of the absolute error relative to the tabulated Silicon lattice parameter.

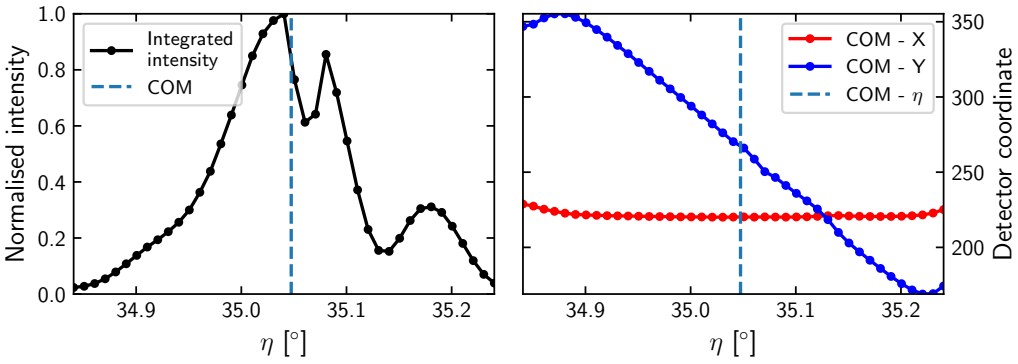

Figure 4.14 – (Left) Rocking curve on the (004) reflection of the Silicon substrate with a 0.01° angular step. The drop around the middle of the curve is due to the gaps of the Maxipix detector (see 4.5.2.2 for more insights) that were not properly corrected, but has no influence in the estimation of the center of mass of the rocking curve, displayed as a vertical dotted blue line. One can note that the COM in η (the incidence angle) does not corresponds with the theoretical value for the tabulated (004) reflection of Silicon bulk (34.8°). The cause is the absence of numerical correction of the η offset for this scan, but also it also indicates that the measured Silicon lattice parameter is going to differ and will have to be corrected for all future calculations. (Right) Position on the detector of the center of mass of the Silicon Bragg peak for each frame of the rocking curve, in the horizontal (red dotted curve) and vertical (blue dotted curve) direction. The vertical dotted blue line indicates the position of the center of mass of the rocking curve.

The (004) SiGe reflection, as Germanium has a larger lattice parameter than Silicon ($a_{Ge} = 5.658$Å), will appear at a lower incident angle, thus at a lower scattering vector ($Q = 4.589$Å^{-1}). Each detector frame corresponds to a two-dimensional slice of the reciprocal space, defined by the wavelength and the direction of the incident and scattered X-ray beam. Once this Bragg peak is found on the detector, one can start performing two-dimensional scans of the sample while rocking it in order to record the 3D reciprocal space of the scattered intensity from the (004) SiGe crystalline planes. Thanks to the spectral divergence of the pink beam, this is achieved by a 0.4° rotation of incident angles between 34.28° and 34.68°with a 0.01° angular step.

The same method was used to analyse the asymmetric (113) reflection, which is quite well separated from the contribution of the Si substrate and has also the advantage to be almost tangential to the Ewald's sphere at 8 keV. In order to acquire strain and tilt information from the (113) reflection, 3D scanning is performed for incident angles varying between 53.99° and 54.39° with a 0.01° angular step, collecting the diffracted beam at $2\theta = 55.7°$. This reflection thus also presents the advantage of being closer to a normal incidence on the sample, hence providing a smaller footprint yielding a higher spatial resolution.

One can note that the 0.4% energy bandwidth of the pink beam can be transcribed into an angular bandwidth thanks to Bragg's law :

$$2d \sin\theta = \lambda \Rightarrow \frac{\Delta\lambda}{\lambda} = \frac{\Delta\theta}{\tan\theta} \Leftrightarrow \Delta\theta = \tan\theta \frac{\Delta\lambda}{\lambda} \tag{4.4}$$

From equation 4.4, it derives a 0.45% angular bandwidth, i.e 0.12° for $\theta = 28°$ (004) and 0.16° for $\theta = 34.8°$ (113). This shows that the angular bandwidth of the incident beam is larger than the angular step of the rocking curves, meaning that the data is oversampled.

More information about the strain tensor can be retrieved on samples which have been measured at the two (004) and (113) reflections. It could also be extrapolated for the thinner samples assuming that the out-of-plane strain, deduced from the (004) reflection measurement, would not change from one sample to the other.

4.5 SXDM ANALYSIS

4.5.1 *Introduction*

When dealing with SXDM, some problems come into play, both for the measurement step and the analysis step. Part of them are linked to the acquisition of diffracted data, which is necessarily limited by the scan ranges but also deeply linked to the quality and calibration of the detector: gaps, flatfield, hot pixels have to be corrected. Then another unavoidable uncertainty comes from the parasitic motion of the sample due to misalignment. Last but not least, the shape of the reciprocal space can be very misleading, and one has to distinguish peak overlapping and background noise for instance. Often, the signal coming from the substrate of an epitaxial layer is the main issue.

4.5.2 *Assessing and addressing issues*

Before going into more details about the typical analysis procedure, the following elucidates the problems that have been listed above.

4.5.2.1 *Scan ranges*

Finite scan ranges create virtual boundaries in each of the 5 dimensions. This means that both the real space, i.e. the scanned area of the sample, and the reciprocal space, i.e. the intensity distribution of scattered radiation, have limited extents.

In order to cope with the limited field of view in real space, an optical microscope is used. For samples with patterns of few microns in size, the microscope is suffi-

cient to localize the region of interest. By the time of the experiment, this optical microscope was mounted on top of the sample stage and had to be removed after alignment, as it was impeding the rocking movement of the diffractometer for high δ angle. Hence, a precise map of the sample was first built from microscope images, using the patterns of the DIVA mask as references (see Figures 4.4 and 4.3).

However, in reciprocal space, a rocking curve at one particular point of the sample is not enough to know the extent of the diffracted intensity and as soon as strong tilt is present, the beam may leave the detector window. Correctly assessing the center of mass of a partially known intensity distribution requires a thorough measurement with wide ranges and many points in rocking scan.

4.5.2.2 *Detector gaps, flatfield, hot pixels*

Gaps in the detector will distort the center of mass analysis if not considered (as seen in Figure 4.14). For ID01's Maxipix detector, gaps between the four modules can be filled, and hence intensity redistributed (see Figure 4.15). The same is true for dead pixels, which should not be set to zero but either interpolated or masked.

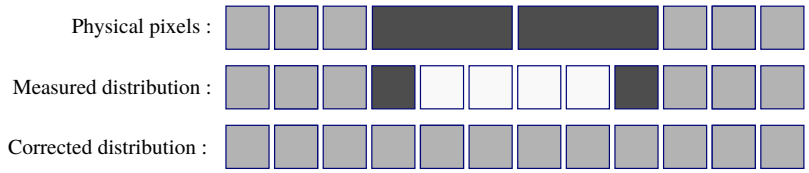

Figure 4.15 – Pixels redistribution for Maxipix. First line represents the physical repartition of the pixels, with two being three times bigger than their neighbor to compensate the physical gap separating two modules. Second line is the actually measured distribution, with three virtual pixels taking the place of the big physical one: the first contains all the intensity, whereas the two next are empty. Third line shows the corrected distribution, involving a redistribution from the first virtual pixel towards the two after.

4.5.2.3 *Parasitic motions*

There are three different and independent source of parasitic motions. Firstly, the confusion sphere of the motors limits the precision of the displacements, and even after good optical alignment from the start of an experiment, a 1 µm per degree shift is the minimum. Indeed, due to the confusion sphere, it is not possible to make simultaneously the focus of the beam, the surface of the sample and the center of rotation of the stage coincide on a same spot. Secondly, noise in mechanical stability is coming from *e. g.* temperature fluctuations and mainly from gravity nduced drifts. As we work at Bragg angles, the stage has to stay rotated at high angles during several hours, leading to a slow "sinking" of the sample as a function

of time. Last but not least, systematic drift will always be present and the only way to get rid of it is by applying Bond method requiring to redo several time the same acquisition. This is in practice difficult, hence parasitic motions will be present. Hence, the problem becomes how to assess the actual amount of drift induced by this misalignment.

Drifts evaluation is usually not possible without looking at the full 5D SXDM dataset, and the challenge is complicated by the fact that sample waviness will produce apparent drift in diffraction which is not related to the physical drift. In other words, natural tilt of the sample will make it diffract at a large range of angle, thus there might not be any clear extinction of the diffraction while rocking the sample.

There are two methods to assess drift in an efficient way. On the one hand, one may look at the sum of intensity over η (the rocking angle) - over a certain Region Of Interest (ROI) of the detector to eliminate parasitic diffraction - and vary the shift per angle. If the sample presents a sharp interface in the scanning plane, the minimization of the sum of all discrete differences along the axis of the given interface, with respect to the shift per angle, will give a good estimation of the real drift. On the other hand, if the sample presents a strongly scattering feature, one would rather try to identify manually this feature at all the different angles from the rocking curve. The latter will be more robust in situations where the beam size is similar to the size of the pattern of interest, or if the tails of the beam are too extended. Once the drift is retrieved, a subpixel correction is used. This is done with a linear shift and not higher polynomial interpolation, because even if it would preserve resolution, it would mainly produce negative intensity values and make the future fit impossible. Finally, we were able to determine that during our experiment on SGOI layers, drift has varied up to a maximum of 2 µm per degree.

4.5.2.4 *Diffractometer misalignment*

In a general case, for a thorough and complete evaluation of strain and composition, absolute values are required from SXDM. Indeed, the δ angle (detector arm) and the energy define the d-spacing. However, in a case where we are not interested in getting the full strain tensor the solution for absolute values assessment is eased. First, one has to measure a reference reflection for a known component (e.g. the substrate). Then compare macroscopic measurements (e.g. powder diffraction in a lab) with the sample-average of SXDM : a simple tweaking of the δ offset for each measurement in order to meet reference values is enough. Note that from the growth condition of the SGOI layers, shear strain is not expected in our sample configuration hence this simple method based on a reference measurement is enough.

4.5.2.5 *Peak overlap, background issue*

When dealing with epitaxial films, the presence of a substrate with a lattice parameter close to the one of the film leads to the generation of two Bragg peaks in reciprocal space close to each other, and often overlapping.

In the best case scenario, there is only a slight overlap and maxima of both peaks are still separated. Then it is possible to use only a ROI on the detector to virtually cut off the substrate peak and calculate the center of mass of the selected distribution. But often this center of mass will be distorted and not really representative of the actual lattice parameter of the probed layer. To tackle this issue, one can calculate the center of mass using a threshold or instead perform a peak fit with background removal, i.e., assessing the signal coming from the substrate alone, on an area of the real space with no epitaxial layer.

In the worst case scenario, when the overlap is strong enough that the ROI boundaries need to be adapted for each point of the SXDM map, a realistic fitting of the whole distribution is required and this has no general recipe. The best way is then to fit projections of reciprocal space, using non-linear least-square minimization associated to a Gaussian function. Indeed, a 3D fit is not robust enough, particularly as it demands interpolation which becomes probelematic with small intensities.

4.5.2.6 *Full strain tensor*

Retrieving the full strain tensor is possible only if three non-coplanar Bragg reflections are scanned in order to disentangle tilt and strain. A further complicating factor for that is the correct matching of the surface coordinates of the three different datasets. This can be done by correlating either real space features clearly visible or reciprocal space angular components as each reflection contains partially redundant information about tilts of unit cells Hofmann et al., 2017. Then, the general equation relating the diffraction vector $\mathbf{Q}$ from a certain reflection $[hkl]$ with the crystal parameters is :

$$\begin{pmatrix} Q_x \\ Q_y \\ Q_z \end{pmatrix} = \mathbf{U}(\phi, \chi, \eta) \cdot \mathbf{B}(a, b, c, \alpha, \beta, \gamma) \cdot \begin{pmatrix} h \\ k \\ l \end{pmatrix}. \tag{4.5}$$

In which the $\mathbf{U}$ matrix is the orthogonal matrix that defines the crystal orientation with respect to the diffractometer coordinate system and the $\mathbf{B}$ matrix is the reciprocal metric tensor, determined uniquely by the unit cell of the crystal. The $\mathbf{U}$ and $\mathbf{B}$ matrices are often combined into a single matrix $\mathbf{UB}$, sometimes referred to as the "orientation matrix". With three non-coplanar reflections, the nine unknowns from eq 4.5 can be solved for each position on the sample locally.

4.5.3 *Typical analysis road-map*

4.5.3.1 *Introduction*

In an ideal experiment, with all necessary references and measurements, the workflow of analysis could follow this:

— Correct whatever is possible to correct (detector, motion, background...);
— Get an overview of the 5D data: merge, convert, visualize (with the correct choice of coordinate system);
— Reduce the dataset to three 2D dataset $\mathbf{Q}(x, y)$ from the extraction of the average peak position for each point;
— Combine data from 2 to 3 reflections to obtain the complete crystallographic metric $(a, b, c, \alpha, \beta, \gamma)$
— Interpret the obtained results

4.5.3.2 *Example on the (113) Bragg reflection for 13 nm-thick SGOI*

MERGING AND FIRST VISUALIZATION

The first step of the analysis is to merge all the real space scan from each angle into the full 5D dataset, and correct and convert the raw detector images to reciprocal-space slices. Then, one has to take a closer view of the data, by looking at detector-average, surface projections and average Q-space. The detector average enables to determine ROI of scattering coming from the target sample (in our case, to distinguish the SiGe scattering from the Silicon substrate scattering). For instance, Figure 4.16 shows the averaged reciprocal space along the Q_x direction, i.e. normal to the detector. The Silicon substrate scatters more than the 13 nm-thick SiGe, generating a strong peak on the top part of the detector, combined with diffuse scattering and a truncation rod all along Q_z. A first correction is made by masking the pixels of the detector receiving the most flux from Si scattering, and Figure 4.16b makes the SiGe scattering visible.

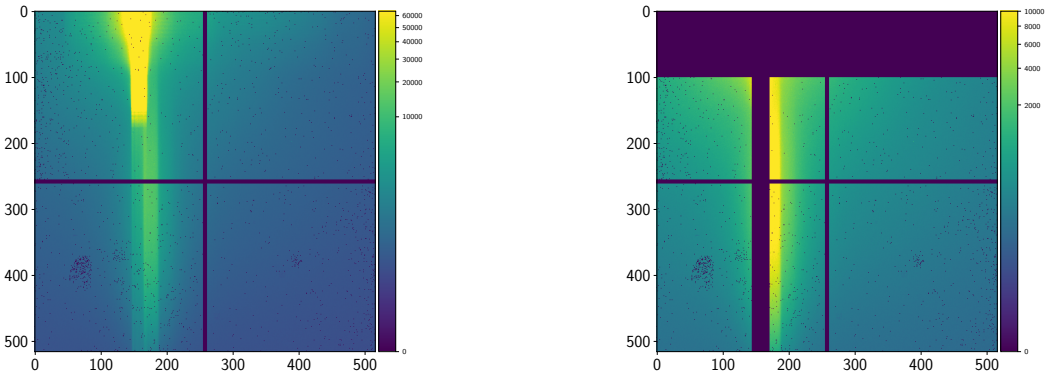

(a) (b)

Figure 4.16 – (113) Reciprocal space averaged along the direction normal to the detector (Q_x) from all positions on the sample (C, D4) : (a) without any mask applied on the detector, the strongest signal at $Q_z \simeq 3.43\text{Å}^{-1}$comes from the Si substrate and is convoluted with the beam. (b) After masking on each detector pictures the same areas, i.e. Si peak, and its truncation rod (vertical stripe around 160), the signal coming from the SiGe is finally visible, spreading along Q_z because of the thickness of the sample.

Surface projections at each rocking angle will make it possible to identify drift of the sample during the η-rocking.

To visualize the reciprocal space projections, one has the choice between Cartesian coordinates that is suitable for fully strained, pseudomorphic layers, and spherical coordinates that is efficient for relaxed layers, as the Q-modulus will directly be the inter-planar spacing ($|\mathrm{Q}| = 2\pi/d$) and the angles will account for tilts in two orthogonal planes (ϕ the azimuthal tilt and θ the planar tilt).

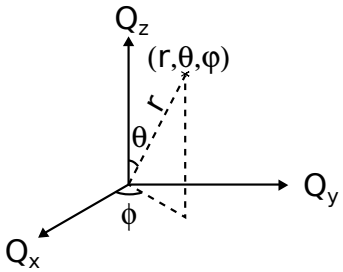

Figure 4.17 – From Cartesian to spherical coordinate system.

Q-SPACE PROJECTIONS

In order to reach the (113) Bragg peak, Q_z has been aligned close to the $[00l]$ reciprocal lattice vector (i.e. along the sample normal) and Q_x to the $[110]$ reciprocal lattice vector, as the SGOI pattern is <110> oriented.

Figure 4.18 shows the reciprocal space intensity projected along the spherical axes, summed over the full scanned area. Here, Two different maxima can be distin-

guished, one coming from the Si substrate at higher $|\mathbf{Q}|$ and giving rise to a silicon truncation rod, and the other one, extended in $|\mathbf{Q}|$, coming from the strained SGOI.

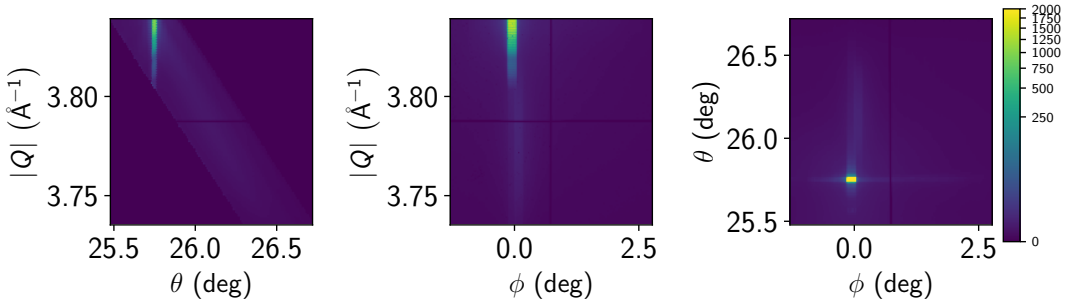

(a)

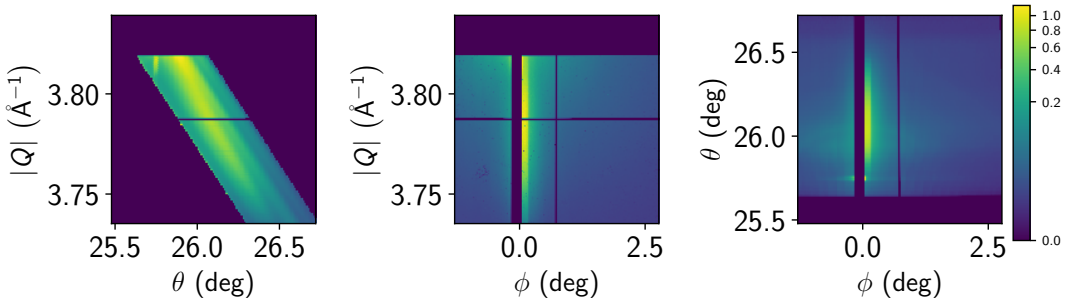

(b)

Figure 4.18 – Projections of 3D reciprocal space map intensity from the (113) asymmetric reflection of SiGe (sample C), for the sample average ("large-beam" equivalent). Intensities are in arbitrary units, spherical coordinate system, (a) without any mask on the detector, (b) with masking of the Si substrate scattering. Mosaicity clearly appears from the elongated shape along θ, synonym of planar tilt, and from the spread in ϕ, related to azimuthal tilt. Note however that the planar tilt measurement is limited to $\pm 0.5°$ due to the limited angular scan range, and that the azimuthal tilt measurement is restricted to the spanning of the detector. Once again, the finite thickness of the sample is reflected in the stretching along the radial component$|\mathbf{Q}|$: $\sim 0.5\text{Å}^{-1}$ translates into 125 Å, which fits with the 13 nm thickness of sample C.

On Figure 4.18b, one can see the same projections of Q-space calculated from the masked detector images, i.e. with a mask applied on the pixels recording mainly scattering from the Si substrate, and hence the SiGe scattering appears more clearly, with an adapted colorbar. In the (ϕ, θ) plane, two streaks originating from the central diffraction peak of SiGe are visible and are the signature of high tilt of the crystal lattice at the edges of the square patterns. In the $(\phi, |\mathbf{Q}|)$ plane, the diffraction width reflects the finite thickness of the sample, which thus can be retrieved: a $\sim 0.5\text{Å}^{-1}$ reciprocal spanning translates into 125 Å in real space, which is in accordance with the 13nm thickness of the probed layer.

Note however that this serves only visualization purpose, as it has been observed that masking Si scattering prior to Q-space conversion impairs fitting of SiGe peak, as some pixels were also recording SiGe scattering, possibly at a different η angle.

In order to cope with the issue of substrate scattering, background estimation is necessary. It is possible to do this by monitoring positions on the sample where no SGOI is present. The signal from a significant number of SiGe-free positions can be averaged and then subtracted. Another way to eliminate substrate scattering from the analysis is to set a ROI in reciprocal space. For certain samples with high background noise, both methods have been used. After removing Si signal and cropping, Q-space can be integrated in order to get local peak positions, for each location of the sample.

Figure 4.19 shows an example of the fitting of the projections for three different locations on a 2 x 2 μm^2 SiGe pattern. The locations are depicted with red, green and blue crosses on the intensity map on the bottom right. In order to highlight the edge-effect on the analysis and on the strain, these three locations have been chosen at borders of the square, one only along the direction of the beam (Y) as the symmetry along this direction might be broken due to the rocking of the sample, and two on the (X) border for clarity, as the symmetry along the horizontal axis is respected. On the left side of Figure 4.19, from left to right, appear projections along each of the three principal Cartesian axes (Q_x, Q_y, Q_z) along with the position of the center of mass (COM, plain vertical line) and the center of the Gaussian fit (dotted vertical line). These give us insight about the accuracy of the analysis, and a first glance at the behavior of strain and tilts from different locations on the sample. For instance, the variations in Q_x^{cen} and Q_y^{cen} from one location to an other show us that the azimuthal tilt ($\phi = \arctan\left(\frac{Q_y}{Q_x}\right) \approx \frac{Q_y}{Q_x}$ as $\frac{Q_y}{Q_x} \to 0$) varies from $\pm 0.01^\circ$.

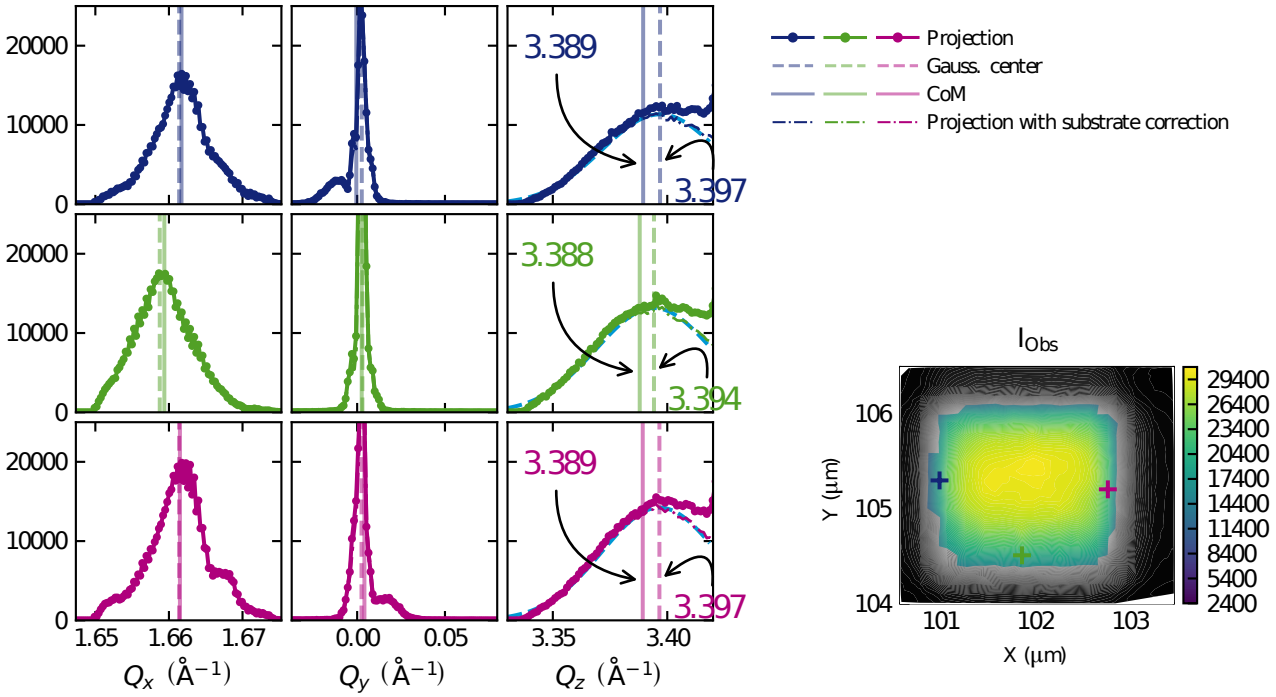

Figure 4.19 – Example of projection fits for three different locations on a 2 x 2 µm^2 square pattern. The three locations are depicted with colored cross on the intensity map (red, blue, green) to show the differences in the intensity projections along Cartesian axes for typical area of the sample. Each column represents projection onto one axis (Q_x, Q_y, Q_z) for the three locations : bullet marked line are coming from data, straight vertical line depicts the position of the COM, dotted vertical line the position of the center of a Gaussian fit (and for the third column, an other point dotted line depicting the data after correction of the substrate scattering). Note that the effect of substrate scattering is 10 times more important for Q_z higher than the right-most abscissa, hence the choice of plotting a limited range. A difference between COM and Gaussian fits is clearly visible for the Q_z axis, with a shift on lower Q_z values for COM, hence the Gaussian fit is preferred for this axis. Note also the variations of the COM on Q_x according to the position on the sample, as Q_x is aligned with the <110> sample direction and is also parallel to the direction of the scattering beam: the COM varies accordingly to the bending of the sample.

4.6 RESULTS AND DISCUSSION

4.6.1 *Comparison between samples obtained by condensation and by standard smart-cut process*

As described earlier, the specificity of the samples studied lies in the particular process of condensation. This technique has to be compared with the traditional smart-cut molecular bonding technique that is conventionally used to obtain strained Silicon-On-Insulator layers. An experiment conducted in 2015 at the ESRF gave us indications about the homogeneity of samples made by molecular bonding,

which can now be compared with the results of the SXDM on SGOI (sample A), on a structure which can be assimilated to a full sheet layer (C6).

Figure 4.20 depicts the comparison between these two approaches. The first row is made up of results from the condensation process, while the second row shows the results from the process of smart-cut and transfer of a strained Si layer. Each row presents the deviation from the Bragg angle (at the symmetrical (004) reflection), the azimuthal tilt and the planar tilt.

Figure 4.20a & a' give information on the homogeneity of the crystalline layer, which is comparable for the two techniques, except that clear gradual undulations along both directions appear on the bottom row. This so-called "cross-hatch" pattern, attributed to the graded structure which results from the relaxation process of two orthogonal non regular networks (oriented along the <110> directions) coming from the epitaxy of strained Si on SiGe before the transfer Hartmann et al., 2007; Kimura et al., 2006; Kutsukake et al., 2004. The existence of "cross-hatch" pattern is long known Kishinû et al., 1972 and has been quantitatively studied with e.g. scanning force microscopy Hsu et al., 1992, and SXDM Zoellner et al., 2015Richard et al., 2015.

Tilt maps depicted in Figure 4.20b,c & b',c' refer to the angular deviation of the diffracted beam in the direction either perpendicular or parallel to the scattering plane. Thus, they relate how locally bent the structure is. Once again, the cross-hatch pattern is visible on the second row, whereas the scale for the first row is an order of magnitude lower, and clearly demonstrates the absence of underlying inhomogeneities. Indeed, the mosaicity is about 0.1° and the standard deviation of both azimuthal and in-plane tilt is $\sigma = 0.08^\circ$ for the second row, against $\sigma = 0.004^\circ$ for the first row. Note that the ranges are not identical between the two rows. Furthermore, one can distinguish on Figure 4.20b' a clear vertical defect on the sample made by traditional molecular bonding, at $X = 80$ µm.

All in all, the effectiveness of the condensation method to lower tilt fluctuations and defect is well shown. Nonetheless, it can be stressed that the map of the Ge enriched structure only covers a 8 x 8 μm^2 area, compared with 100 x 100 μm^2 for the other structure.

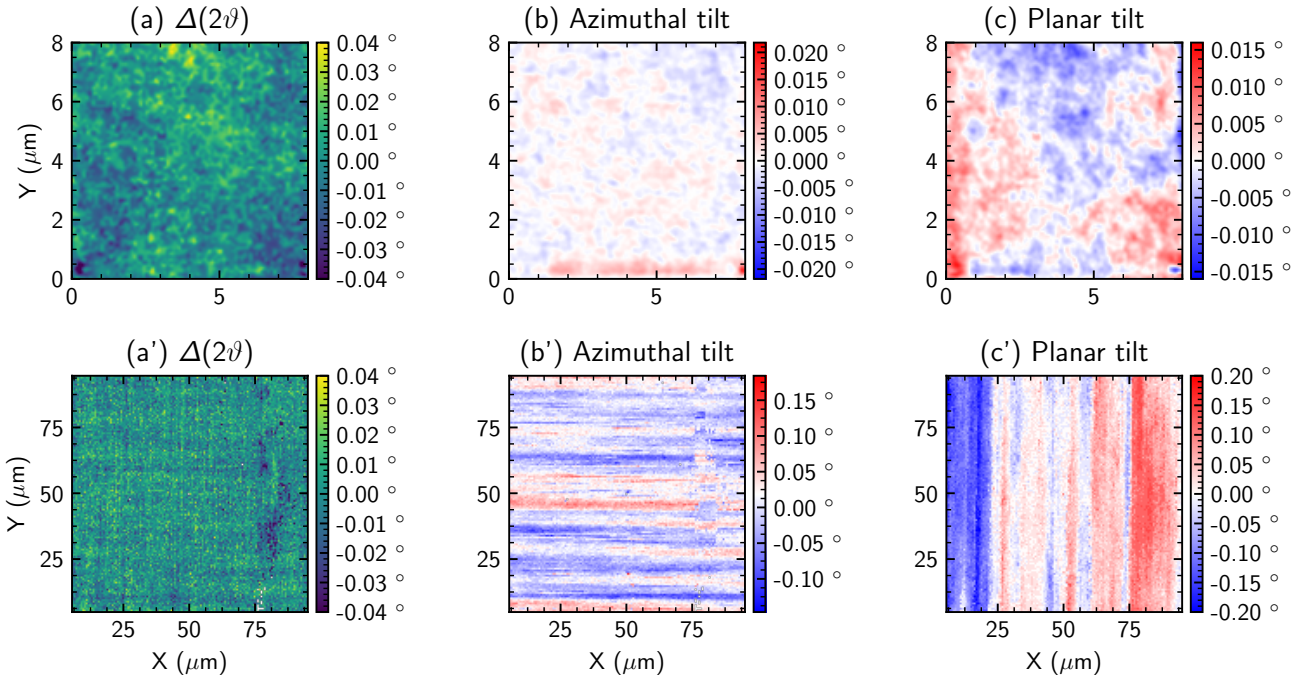

Figure 4.20 – Comparison of the diffraction maps recorded on a 13 nm-thick SiGe layer obtained by the condensation Tezuka, Sugiyama, et al., 2001; Nakaharai et al., 2003; Gourhant et al., 2014; Vincent, J.-F. Damlencourt, et al., 2007; Glowacki et al., 2014; Morin et al., 2015 method (a,b,c) and on a 70 nm-thick sSOI layer obtained by the traditional smart-cut and molecular bonding Bruel, 1995 (a',b',c'): (a-a') measured Bragg angle 2ϑ. (b-b') (resp. (c-c')) angular deviation of the diffracted beam in the direction perpendicular (resp. parallel) to the scattering plane. The sSOI sample (second line) shows a vertical defect positioned at about X=80 µm and the vertical and horizontal stripes appearing on the tilt maps are related to the cross-hatch pattern Kishinû et al., 1972. These stripes are not present in the condensation sample (note the different color scales for (b-b') and (c-c')), demonstrating the effectiveness of the condensation method to lower tilt fluctuations.

4.6.2 *2 x 2 µm² Silicon-Germanium On Insulator (SGOI) squares (D4)*

The 2 x 2 µm² structures have been scanned on samples A, B and C. Map of 12 x 12 µm² or 6 x 6 µm² have been performed with a 100 nm step size in each direction of the piezo motors.

4.6.2.1 *20 nm-thick layer with SiN (Sample A)*

Concerning sample A, the role of the silicon nitride layer on top as a protective layer was checked, by observing a long-lasting stability under the X-rays: no significant evolution of the diffracted intensity during the measurement was observed below 250 s of continuous exposure. This sample has also been probed for both

the (004) and the (113) Bragg reflections, in order to determine a part of the strain tensor.

Figure 4.21 shows the maps for these two reflections. The first map of both Figure 4.21a and 4.21b depicts the 2D integrated intensity over the detector frame that corresponds to the most intense slice of the SiGe Bragg peak. This gives a clear indication of the square SGOI patterns and is used as reference to determine a threshold that enables us to separate the square islands from the substrate underneath. In practice, it is used to generate the white mask of the other maps.

Note that the squares appear less straight for the (004) measurements than for the (113), because for this reflection: (i) the Silicon substrate peak is closer to the SiGe one (i.e. the overlap is higher) and (ii) the projected beam onto the sample is wider, causing a blurring effect. Indeed, as the incident angle for the (004) (respectively (113)) reflection is 34.5° (resp. 53.2°), the vertical beam footprint on the sample is 300 nm (resp. 212 nm).

It is also important to stress out that the quality of the results is poorer in the vertical (Y) direction due, not to the asymmetry of the incoming beam, but to the artifacts induced by the movement of the sample which sinks over time. Hence, the expected four-fold symmetry of strain and tilt is reduced to a two-fold symmetry, in the direction of the highest spatial resolution (X). Note that the four-fold symmetry is due to the crystallographic symmetry, as the boundaries are parallel to the in-plane $\langle 110 \rangle$ crystallographic directions, within $\approx 1°$.

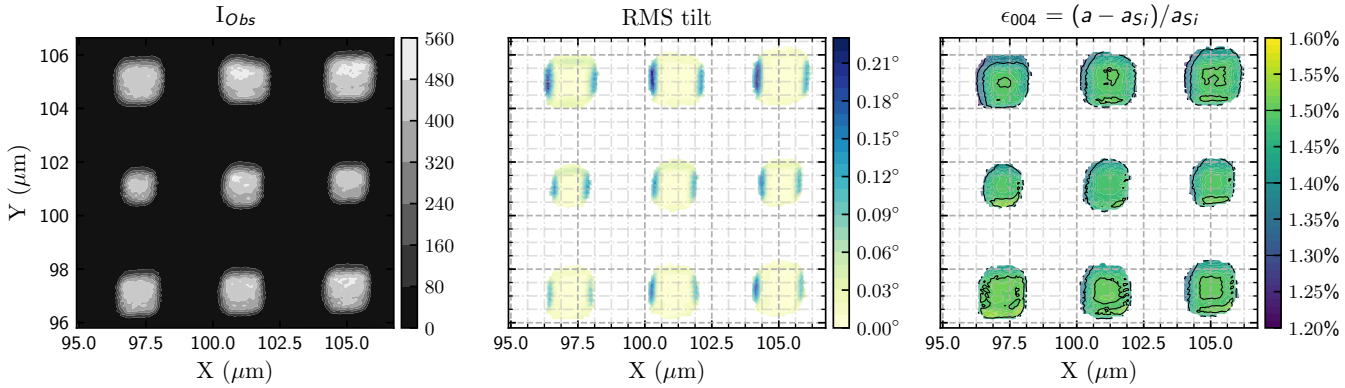

(a)

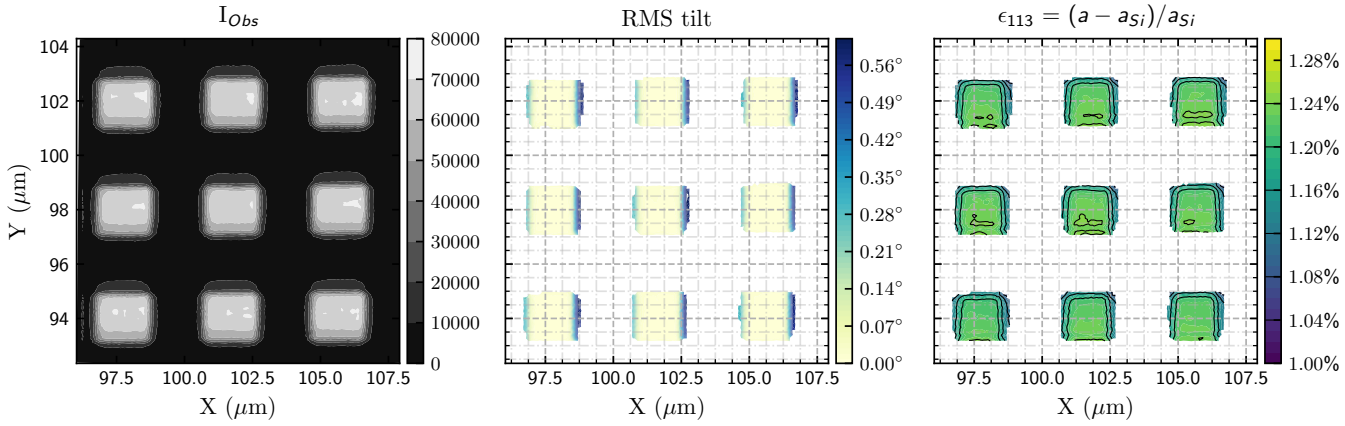

(b)

Figure 4.21 – Map of a 12 x 12 µm^2 area of sSiGe-on-insulator layer of thickness 20 nm (sample A), for both 4.21a the (004) and 4.21b the (113) Bragg reflection. (Left) Maximum of intensity integrated on the whole detector for each pixel. (Center) RMS tilt angle, taking into account both the perpendicular and parallel angular deviation with respect to the scattering plane. (Right) (above) Out-of-plane strain ϵ_{zz} distribution, (below) strain ϵ_{113} distribution, both calculated with respect to the bulk Si lattice parameter. High tilt (up to 0.5°) and strain variations on the edges of the patterns are clear evidence of the side relaxation of the islands.

The center maps of Figure 4.21 show the square-root of the sum of the squared azimuthal and planar tilts (Root Mean Square, RMS). These clearly demonstrate the bending of the squares at the edges, intrinsically linked to the relaxation of the lattice parameter. The latter mentioned relaxation is exhibited in the last column of maps through strain distribution. Suppose that we focus on the out-of-plane strain (Figure 4.21a) which is the most intelligible as it is just the expression of the expansion of the cubic lattice in the growth direction. As the in-plane lattice parameter at the interface between the Silicon substrate and the SiGe layer is fixed

at the Silicon lattice parameter, the SiGe tends to expand in the growth direction in order to get back to the relaxed SiGe lattice parameter. When looking at the edge, the SiGe has the possibility to expand in the plane perpendicular to the growth direction, hence its normal lattice parameter will shrink. This is observed as the mean out-of-plane strain $\epsilon_{004} = \epsilon_{zz} \backsimeq 1.52\%$ at the center of each square whereas at the edge, the lowest value measured is $\epsilon_{004} = \epsilon_{zz} \backsimeq 1.48\%$.

As it can be seen from the above results, the footprint of the beam on the sample was too large to allow precise analysis of the relaxation at the edges, only an average value can be extracted. However, interesting statistical information can be drawn from the fact that nine squares are probed within one scan. By defining an area of 300 x 300 nm^2 at the center of each square, one can assess the homogeneity inside one square and from one square to another. Figure 4.22 depicts the strain distribution at the center of each square for both the (004) and (113) Bragg reflections. On a subset of nine squares, one can observe that the strain distribution is fairly homogeneous, ϵ_{004} spanning from 1.5% to 1.53% (2% fluctuation) and ϵ_{113} from 1.218% to 1.233% (1.2% fluctuation) average. Furthermore, within one square the quadratic mean of the strain distribution is smaller than 0.01%, indicating that each square pattern is homogeneous.

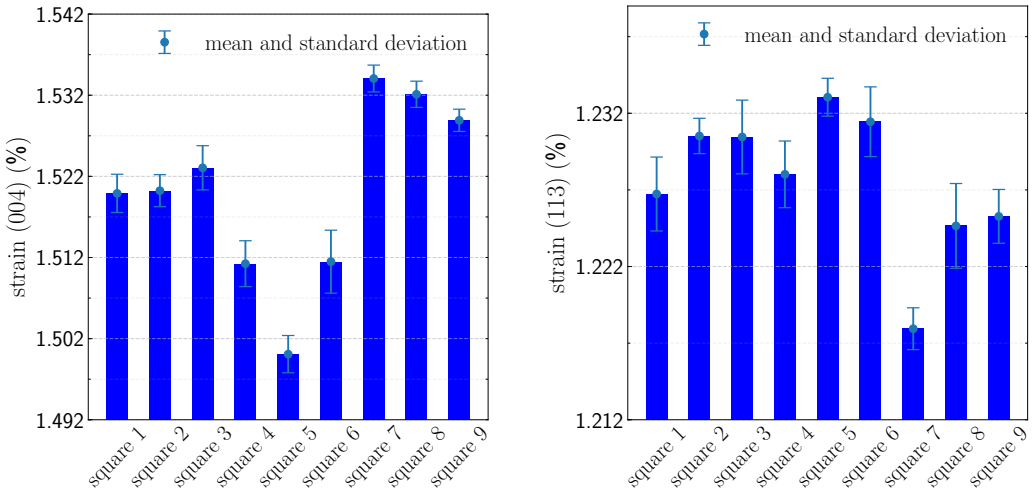

(a) (b)

Figure 4.22 – Statistical repartition of strain at the center of the 2 x 2 µm^2 squares of 20 nm-thick sSGOI w\ nitride. (a) Out-of-plane strain from the (004) Bragg reflection, which averages across all squares to 1.52%. (b) Strain from the (113) Bragg reflection, whose average is of 1.227%. Each column regroups all the points within the 300 nm x 300 nm area at the center of a square. The light blue error bars span from the average strain to $\pm\sigma_\epsilon$, the root mean square of the strain distribution within a square, found to be lower than 0.01% each time.

Combining information from the two reflections, one can retrieve the in-plane strain at the center of the squares. Indeed, the inter-planar spacing d_{113} is directly linked to the dimensions of the unit cell:

$$d_{113}^2 = \left(\frac{1}{a^2} + \frac{1}{b^2} + \frac{9}{c^2} \right)^{-1} \tag{4.6}$$

Hence, assuming that the symmetry of the system leads to $a = b = a_{/\!/}$, measurements of d_{113} and $d_{004} = c/4$ allow calculation of the in-plane lattice parameter:

$$a_{/\!/} = \sqrt{2 \left(\frac{1}{d_{113}^2} - \frac{9}{(4d_{004})^2} \right)^{-1}} \tag{4.7}$$

This result should hold at least at the center of the squares, where the biaxial stress is maintained even after etching.

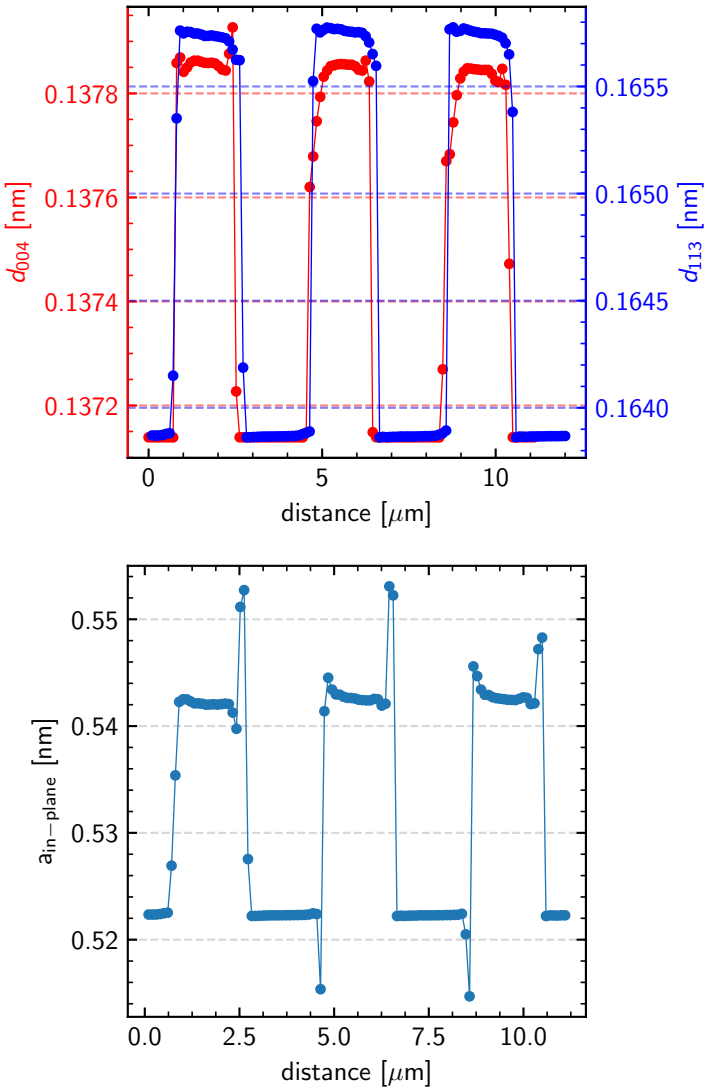

Figure 4.23 – (Top) Interplanar distances extracted from a horizontal profile on three squares (from the (113) reflection in blue, from the (004) reflection in red). (Bottom) In-plane lattice parameter extracted from the measurements. Note that the border and void regions (corresponding to $d_{004} < 0.1378$ nm) are invalid due to either low intensity, higher tilt than covered by the reciprocal scan range or simply because it is an area without any SiGe structure. Moreover, one should keep in mind the horizontal footprint of the beam of 220 nm, which limits the spatial resolution. Nonetheless, on the in-plane lattice parameter profile, a slight increasing trend at the edges is noticeable, the marker for side relaxation.

Figure 4.23 shows an example of profile plots over three different squares. The bottom row is obtained by feeding Equation 4.7 with the two measured interplanar distances, whose behaviour is depicted on the top row. Obviously, the data are invalid as soon as they are no longer measured on a SiGe square, whose edges are well visible on the first row. The corresponding in-plane lattice parameter calculated

in the center of the squares oscillates around 5.435 Å, i.e. a 0.08% strain with respect to the Silicon substrate. It is important to note that 0.08% strain falls within the assumption made in 4.3.2 about defects at the back interface, modifying the expected Si/SiGe in-plane lattice matching.

One can also observe that the layer geometry leads necessarily to the absence of stress in the out-of-plane direction :

$$\sigma_{zz} = 0 = C_{31}\varepsilon_{xx} + C_{32}\varepsilon_{yy} + C_{33}\varepsilon_{zz} \tag{4.8}$$

Since $C_{31} = C_{32} = C_{12}$ in an isotropic and cubic material like SiGe, and taking into account that the distortions are assumed to be biaxial, Equation 4.8 can be reduced to:

$$\varepsilon_{zz} = -\frac{2C_{12}}{C_{11}}\varepsilon_{average} = -\frac{2\nu}{(1-\nu)}\varepsilon_{average} \tag{4.9}$$

where $\varepsilon_{average} = \frac{(\varepsilon_{xx}+\varepsilon_{yy})}{2}$ and ν is the Poisson's ratio of the SiGe, which depends on the Ge content x in $Si_{1-x}Ge_x$. For a given content, the Poisson's ratio can be derived by linear interpolation of Silicon and Germanium's known Poisson ratio. The same goes for $a_0(x) = b_0(x) = c_0(x)$ the crystal lattice constants for zero strain. Once again, by assuming the local symmetry of the cubic crystal bearing biaxial stress, one can write $\varepsilon_{average} = \frac{a-a_o(x)}{a_0(x)} = \frac{b-b_o(x)}{b_0(x)} = \frac{a_{/\!/}-a_{/\!/,o}(x)}{a_{/\!/,0}(x)}$. Hence, Equations 4.7 & 4.9 can be combined in order to recover the Ge-content x inside the layer: $x_{\text{Ge}}^{\text{mean}} = 21.98\%$ averaged on the nine probed squares. This is in good agreement with the target Ge-content of the process, but nonetheless valid only for the homogeneous central part of the pattern.

Note however that this result can be further analysed by taking into account the propagation of the uncertainties on the calculated interplanar distances. The precision of the calculations from the projections fitting reaching approximatively 10^{-5}, one can estimate that the variations from the variety of strain will mostly impact the precision of the Ge-concentration. By probing several patterns over one map, and by acquiring many points within a central area on each of these patterns, a statistical standard deviation can be evaluated: $\epsilon_{004}^{\text{mean}} = 1.52\% \pm 0.01\%$ and $\epsilon_{113}^{\text{mean}} = 1.227\% \pm 0.004\%$. This leads to mean Ge-concentration ranging between 21.41% and 22.55%.

4.6.2.2 *20 nm-thick layer without SiN (Sample B)*

For this sample, we perform a map of 8 x 8 μm^2 with a 100 nm step size in each direction of the piezo motors and only the (113) reflection has been probed. The same analysis as for sample A is used and Figure 4.24 shows the intensity, RMS tilt and strain maps. The (Y) direction is less reliable than the horizontal (X)

one, and the same method of masking from intensity thresholding is applied. The RMS tilt denotes a four-fold symmetry with up to 0.1°of inclination on the very borders while the upper part of each square's strain breaks this symmetry. This can be explained again by the continuous drift induced by the sinking of the sample during the measurement time.

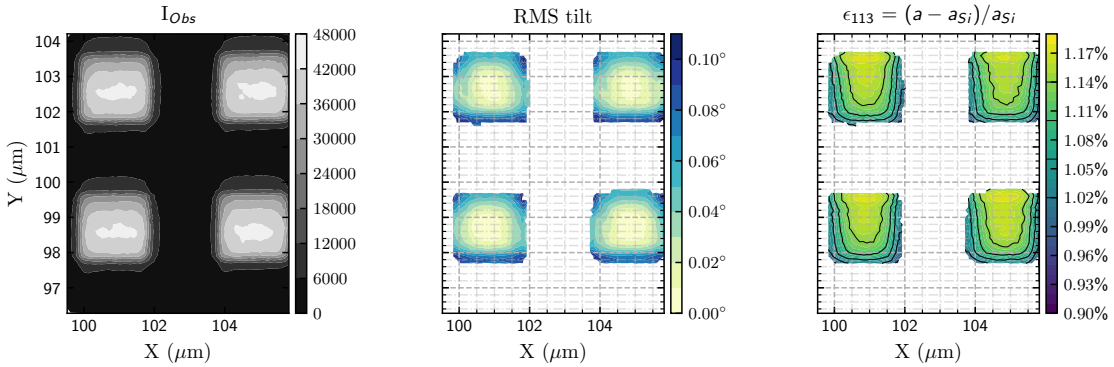

Figure 4.24 – Map of a 8 x 8 µm^2 area of strained SiGe-on-insulator layer of thickness 20 nm without nitride on top (sample B), for the (113) Bragg reflection. (Left) Maximum of intensity integrated on the whole detector for each pixel. (Center) RMS tilt angle, taking into account both the perpendicular and parallel angular deviation with respect to the scattering plane. (Right) strain ϵ_{113} distribution, calculated with respect to the bulk Si lattice parameter. Drift in the (Y) direction, along the beam propagation, is visible from the strain map. In the transverse (X) direction, the decrease of the strain towards the edges of the patterns indicates relaxation.

The substrate's contribution for this sample is very high, as fifty times more summed counts (over the forty-one points of the rocking curve) are coming from the Si than from the SiGe, on a central part of a square. This number jumps to a few hundred on the borders of the square, where the quantity of SiGe matter lit by the beam drops quickly. Analysis on the edges is thus made difficult as the signal is largely disturbed and substrate subtraction imprecise. Nonetheless, one can still rely on the analysis at centers, where the (113) averaged strain is found to be around $1.125\% \pm 0.007\%$.

Fig 4.25 shows the statistical repartition of strain across the four scanned squares, highlighting the fact that there is less than 0.02% variation on the area, with a standard deviation smaller than 0.007%. Note that the average strain of 1.125% is 0.1% lower than the one found on the same kind of 2 x 2 µm^2 structure grown on sample A. In order to check if the out-of-plane value at the center of the square is homogeneous from one sample to another, we first use the average out-of-plane lattice parameter found for the sample A to calculate the Ge-content of sample B, leading to $x^{\text{mean}}_{\text{Ge,B}} = 15.96\% \pm 0.4\%$. Compared to the Ge-concentration found for sample A, this value is less in accordance with the target Ge-content of the process,

demonstrating that the value of the out-of-plane lattice parameter measured on sample A cannot be extended to other samples.

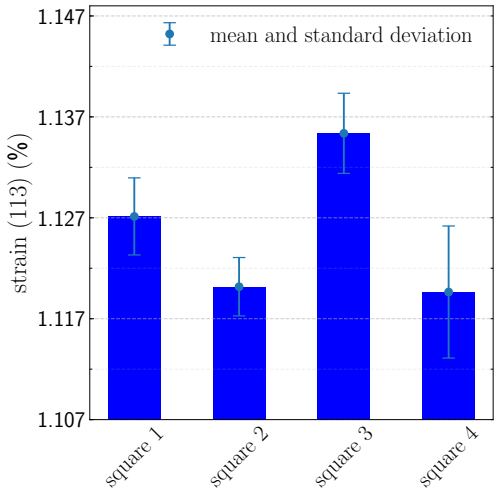

Figure 4.25 – Statistical repartition of ϵ_{113} strain at the center of the D4 squares of 20 nm-thick sSGOI w\o nitride. Each column regroups all the points within the 300 nm x 300 nm area at the center of a square. The light blue error bars span from the average strain to $\pm\sigma_\epsilon$, the root mean square of the strain distribution within a square. The average strain over all squares is found to be 1.125%, with a RMS error of 0.007%, illustrating the accuracy of the measurements.

Yet, to determine the Ge-concentration of the SiGe layer, one can start from another assumption: the rigidity of the back SiGe/Si interface fixes the SiGe lattice in the in-plane direction, hence $a^{/\!/}_{SiGe} = a_{Si}$. Equation 4.7 can then be used to express d_{004} as a function of $a^{/\!/}_{SiGe}$ and the measured d_{113}. Finally, equation 4.9 is inverted to retrieve the x content of Germanium inside the SiGe biaxially strained layer, the result holding only for the central part of a square: $x_{\text{Ge}}^{\text{mean}} = 20.6\%$. The latter is then in accordance with the specifications of the growth process. Moreover, note that the variations of $\epsilon_{113}^{\text{mean}}$ over the centers of the patterns lead to a standard deviation of 0.139%. In addition, the impact of sliding or in-depth inhomogeneities can be evaluated. Indeed, the assumption of a defect at the back interface results in up to a 0.1% increase of the in plane lattice parameter $a^{/\!/}_{SiGe}$ from Bulk Silicon and hence modifies the Ge-concentration. This way, replacing $a^{/\!/}_{SiGe} = a_{Si}$ by $a^{/\!/}_{SiGe} = 1.001 \times a_{Si}$ leads to a new Ge-concentration of $x_{\text{Ge}}^{\text{mean}} = 21.39\% \pm 0.139\%$ (note that the standard deviation of the measurements is not impacted by this new assumption, as the latter mainly derives into a translation of the mean).

4.6.2.3 *13 nm-thick layer without SiN (Sample C)*

For this sample, we perform a map of 8 x 8 μm^2 area with a 100 nm step size in each direction of the piezo-motors. This sample is made of a lower quantity

of matter than the previous ones, as the SiGe layer is only thirteen nanometers thick. This translates into a small number of counts from the SiGe scattering (mean counting of 7 photons/pixel/0.1s) as compared to Si substrate scattering (mean counting of 1.8 x 10^3 photons/pixel/0.1s), as it is depicted in Figure 4.26, and makes the analysis more challenging.

These measurements correspond to state-of-the-art nanobeam diffraction on Si - with quite low Z number - at this ultra-low thickness. Figure 4.27, in which the squares appear in a visible way from the contrast of the intensity map, shows that with the chosen optics (KB mirrors, with coherent slits opened at 200 µm x 200 µm to optimize the flux) we can still obtain accurate results.

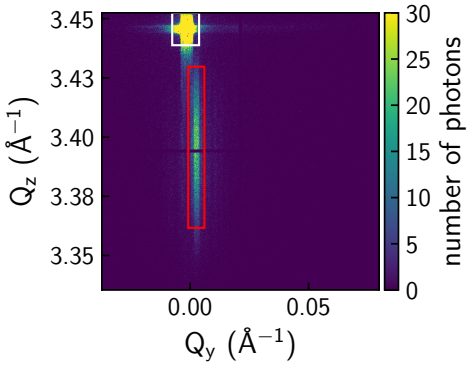

Figure 4.26 – Detector frame from a rocking curve with 0.1 second exposure on the SiGe (113) reflection of the full sheet 13 nm-thick SGOI SGOI (sample C). Two ROI have been drawn, one in red centered on the SiGe peak, and one in white centered on the Si scattering, in order to estimate the mean counting value of the two scattering layers caught by the detector. With that, one founds the SiGe to scatter a mean value of 7 photons/pixel/0.1s, when Si scatters a mean value of 1800 photons/pixel/0.1s. Note that the colorbar depicting the number of photons per 0.1s has been intentionally capped to 30 in order to make the SiGe scattering visible.

Both tilt and strain denote a four-fold symmetry that was not clearly evidenced in sample B, possibly a sign of better alignment of the sample with respect to the center of rotation of the experimental stage. Tilt increases uniformly from the center to edges, where it does not exceed 0.14°. The strain of the (113) crystalline planes looks homogeneous on the center part of each of the four square, where it reaches an average value of $\epsilon_{113} = 1.391\% \pm 0.01\%$. Calculated with the same method of averaging a set of around fifteen points located at the center of a square, the standard deviation of the strain is below 0.01%, proving good homogeneity of the measurement. Fig 4.28 shows the repartition of strain over the scanned area, with an averaged value over the center of one square oscillating between 1.382% and 1.407%.

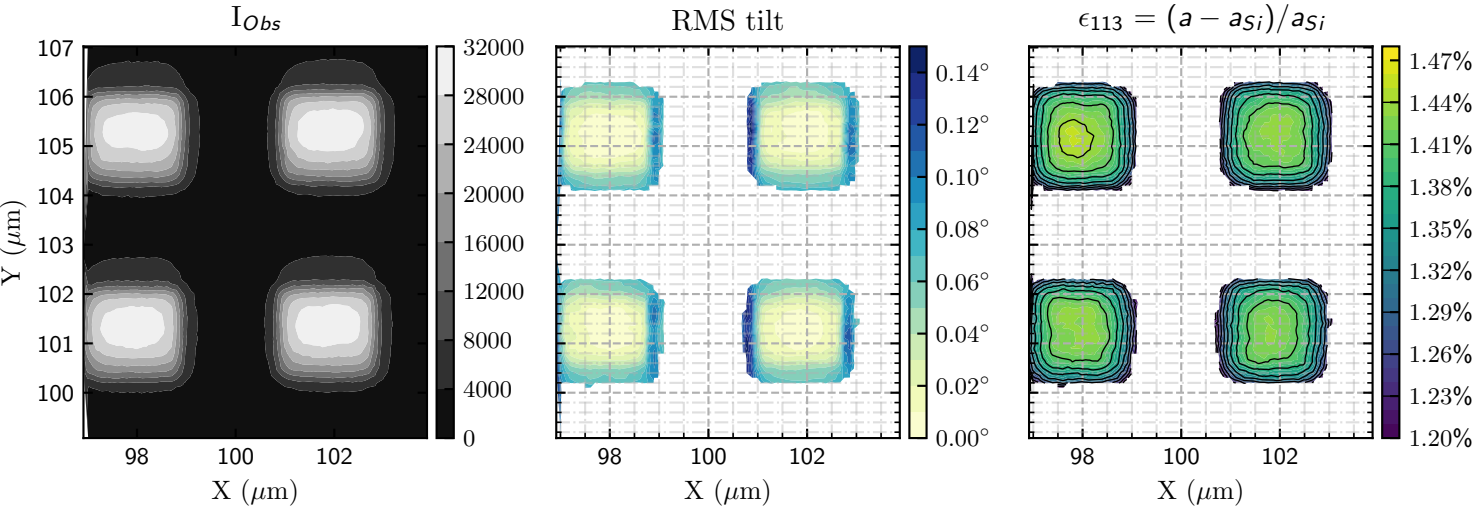

Figure 4.27 – Map of a 8 x 8 µm^2 area of strained SGOI layer of thickness 13 nm without nitride on top (sample C), for the (113) Bragg reflection. (Left) Maximum of intensity integrated on the whole detector for each pixel. (Center) RMS tilt angle, taking into account both the perpendicular and parallel angular deviation with respect to the scattering plane. (Right) strain ϵ_{113} distribution, calculated with respect to the bulk Si lattice parameter. The behaviour of both strain and RMS tilt demonstrates the side relaxation of the islands.

The 1.391% strain of the (113) direction is slightly higher than the one measured on samples A & B. From the back interface rigidity assumption (see 4.6.2.2) a higher ϵ_{113} induces a higher out-of-plane lattice parameter and thus necessarily results into a higher concentration in Germanium. By following the same method, inversion of equation 4.9 allows extracting $x_{Ge}^{mean} = 25.35\% \pm 0.158\%$.[7]

Besides, one could note that a 0.1% relaxation at the back interface leads to $x_{Ge}^{mean} = 26.11\% \pm 0.177\%$.

7. Note that the method consisting in reusing the out-of-plane lattice parameter measured on sample A to calculate the Ge-concentration leads in this case to a mean value of 32.35%, consolidating the idea of leaving this method on the side for further analysis.

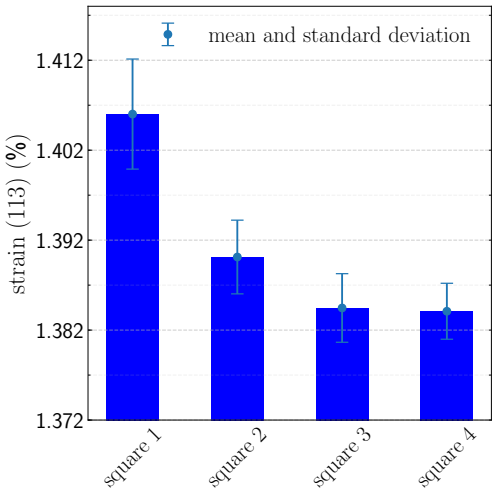

Figure 4.28 – Statistical repartition of ϵ_{113} strain at the center of the D4 squares of 13 nm-thick SGOI without nitride on top (sample C). Each column regroups all the points within the 300 nm x 300 nm area at the center of a square. The light blue error bars span from the average strain to $\pm\sigma_\epsilon$, the root mean square of the strain distribution within a square. The average strain is of 1.391% with a 0.01% root mean square error.

On this sample, it is of interest to notice that strain profiles can be extracted along the squares, thanks to the good quality of the diffracted data and the lack of drift during the scanning. Figure 4.29 shows horizontal and vertical strain profiles, along the four scanned squares. The impact of the edges is clear, with a diminution of strain which is synonym of tensile strain reduction.

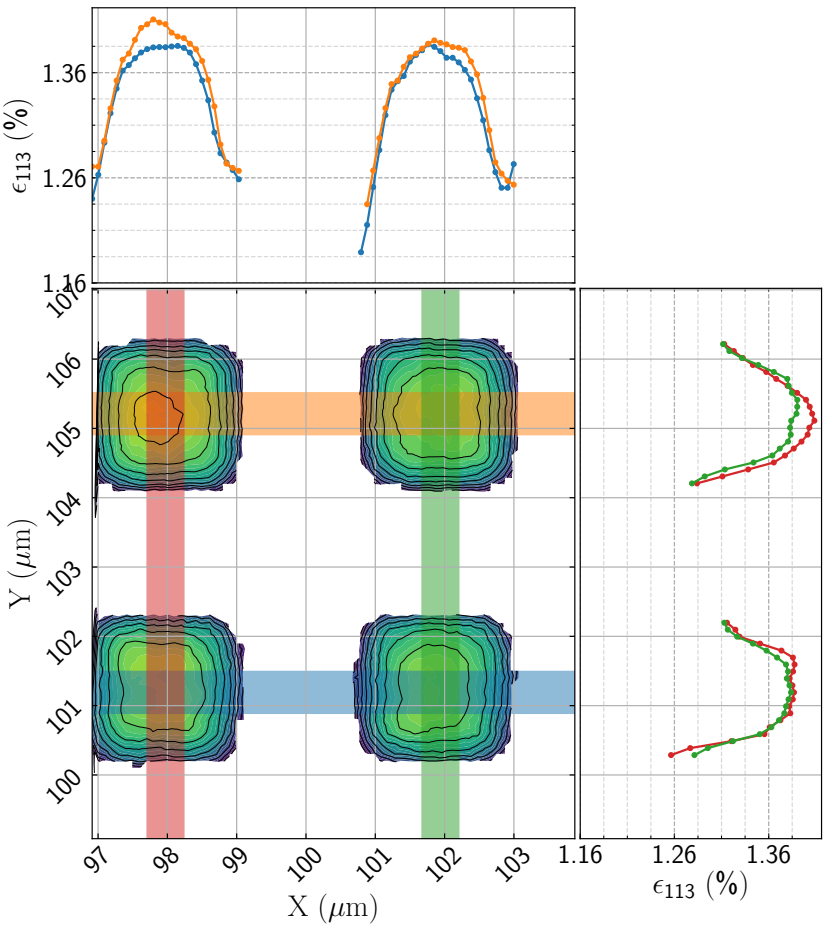

Figure 4.29 – (113) strain map and profiles of 2 x 2 µm^2 pattern of 13 nm-thick sSGOI, without nitride on top. The colored stripes on the strain map depict the area of integration for respective profile. On the right-hand side sits vertical strain profiles from the four squares (red and green lines), and on the top side sits horizontal strain profiles from the four squares (orange and blue lines).

Finally, the highly similar strain profiles from one square to the other, both horizontally and vertically, and together with similar average strain values from the center of each square, show the high accuracy and reproducibility of the measurements and also the good homogeneity of the SGOI and its strain relaxation.

4.6.2.4 *Bilayer: 20 nm-thick-SiGe/Si/BOX without nitride on top (sample D)*

For this sample, a map of a 4 x 8 µm^2 area was performed with a 100 nm spacing in each direction with the piezo motors. The Si layer in between the SiGe and the BOX is not of concern for the experiment, as it has been found to diffract at the same position as the Si substrate. Indeed, the diffraction pattern of the SiGe did not look

as if it was polluted by a signal coming from the Si underneath. Hence the same analysis method has been employed. Figure 4.30 depicts the repartition of tilt and strain over two squared patterns. Note that the (Y) direction suffers this time from the drifts hence provides results of lower quality than in the (X) direction.

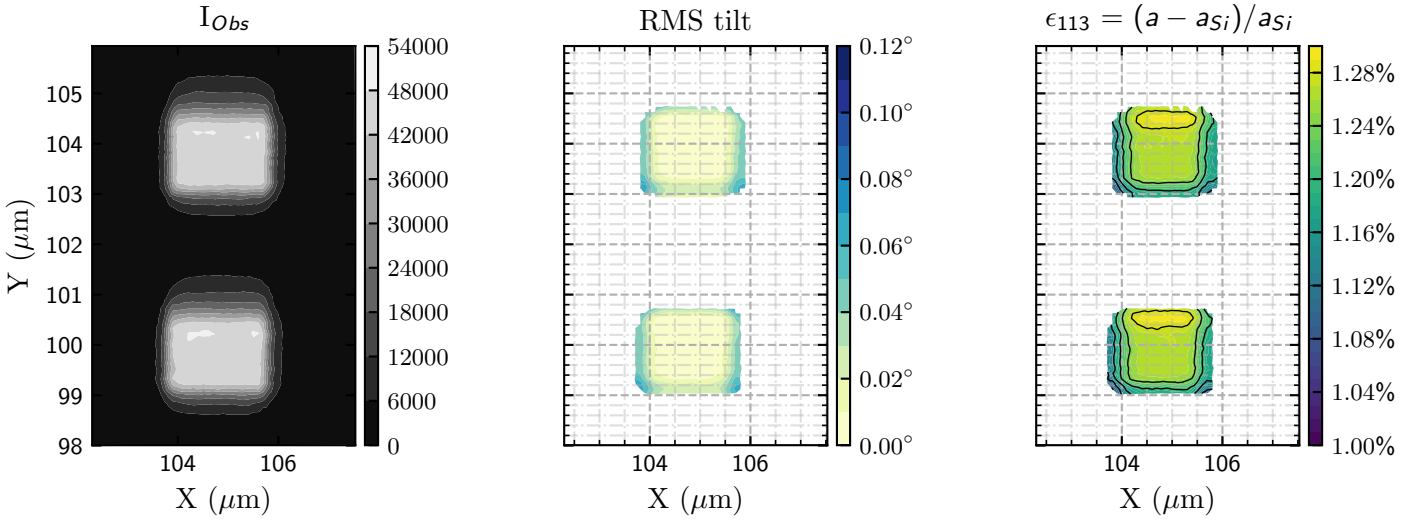

Figure 4.30 – Map of a 4 x 8 µm^2 area of the bilayer 20 nm-thick-SiGe/Si/BOX (sample D) from the (113) Bragg reflection. (Left) Maximum of intensity integrated on the whole detector for each pixel. (Center) RMS tilt angle, taking into account both the perpendicular and parallel angular deviation with respect to the scattering plane. (Right) strain ϵ_{113} distribution, calculated with respect to the bulk Si lattice parameter. The (Y) direction is clearly impacted by drifts issues hence providing results of lower quality than in the (X) direction, along which the strain evidences relaxation on the edges of the pattern, at the same time as the RMS tilt increases.

In the (X) direction, the decrease of the ϵ_{113} strain from the center to the edges of the squares proves relaxation of both the tensile out-of-plain and compressive in-plane strain. Strain relaxation is paralleled by an increase of tilts on the very edges, up to 0.1°. A finer analysis comparing the repartition of strain, comparing the trend over both squares and the trend over the central area of both squares is presented in Figure 4.31. Areas of 300 x 300 nm^2 centered on each square has been used to draw the red histogram, which results in a mean value of deformation of $1.247\% \pm 0.002\%$. Note that this standard deviation error results only from the statistical collection, and not from the accuracy of the measurement method.

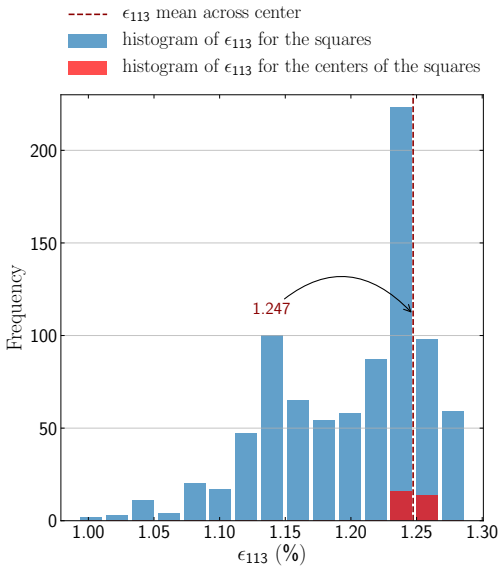

Figure 4.31 – Histogram of 20 nm-thick-SiGe/Si/BOX with respect to bulk Silicon lattice for the (113) reflection. Blue histogram presents the repartition over the entire square. Red histogram depicts the repartition over a portion centered on the square, made of approximately 15 points which correspond to an area of 300 x 300 nm^2. The average strain from the latter distribution is shown by a dotted dark red line. The behaviour of the histogram follows the expected trend: the higher frequency is around the center-pattern-mean value of 1.247%, and as the strain decreases, the frequency decreases as well, showing the homogeneity of the layer at the same time as the tensile out-of-plane strain relaxation and compressive in-plane strain relaxation.

Associating this mean value with the biaxial strain hypothesis and the back interface rigidity assumption, one can retrieve the Germanium of the 20 nm-thick SiGe layer to be $x_{Ge}^{mean} = 22.78\% \pm 0.04\%$. This value can rise up to $23.56\% \pm 0.04\%$ if one assumes a 0.1% mismatch between SiGe and Si at the interface. However, one should emphasize that this bilayer sample has undergo nor the condensation process neither the annealing. Thus, the perfect rigidity of the back interface is even more likely than for the other samples.

4.6.3 *5 x 5 μm^2 SGOI squares (D6)*

The 5 x 5 μm^2 structures have been scanned on the samples A and C. Maps of $\sim$10 x 10 μm^2 have been performed with a 100 nm step size in each direction of the piezo motors, again performing a rocking curve made of 40 η angles with a 0.01° step, around the same angles as described in section 4.4.3.

4.6.3.1 *20 nm-thick layer with SiN (Sample A)*

Both (004) and (113) Bragg reflections have been scanned over sample A, allowing precise measurement of out-of-plane lattice parameter and interpolation of Ge-content. The intensity maps observed in Figure 4.32 evidence clear localization of the square pattern from both reflections, even though a small gradient is noticeable in the (Y) direction, due to sample drift. This causes blurring in the (Y) direction and discards the edge analysis.

Concerning the analysis from the (004) reflection, one can focus on what happens along the (X) direction, with a clear sharp tilt increase on the edges, i. e., a bending of the layer at this location. Nonetheless, the behaviour of the out-of-plane strain is not as expected while going from the center to the borders. Indeed, progressive relaxation of the SGOI layer is expected, from a fully strained state up to 300 nm close to the edge, to a relaxed state on the edge, i.e. an increase of the in-plane strain which is exactly a decrease of the out-of-plane strain. On the other hand, the trend of the out-of-plane strain is to increase on the (X) borders.

One of the argument for choosing the (113) Bragg reflection during the experiment is the possibility to reach it by a simple η displacement, i.e. by rotating only one motor and staying within the same scattering plane since all the SiGe layers are <110> oriented. A drawback is that the analysis for the (113) Bragg reflection suffers from the same issue of sample drift, along the same direction as the other samples. Figure 4.32b still evidences a 0.1° tilt on the (X) borders and high homogeneity of the strain at the center of the 5 x 5 μm^2 square.

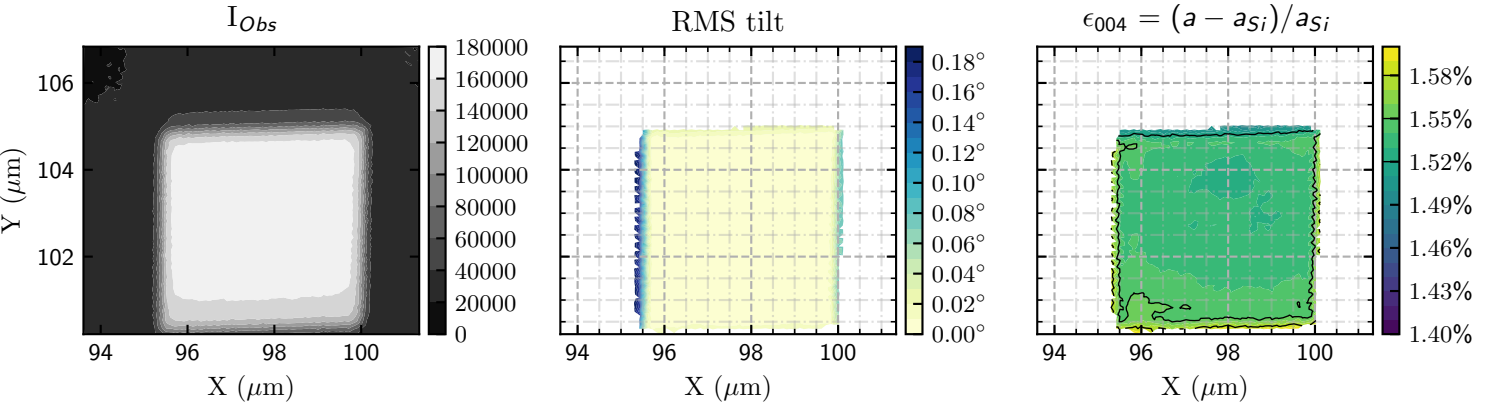

(a)

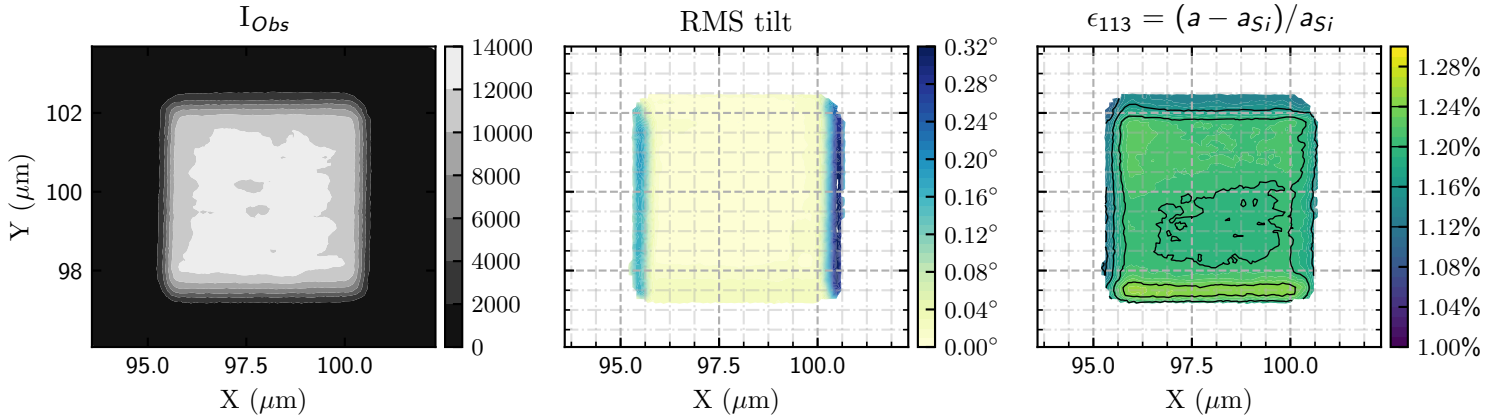

(b)

Figure 4.32 – Map of strained SGOI, 20nm thickness, with nitride on top (sample A). The pattern is a 5 x 5 μm^2 square. From left to right, intensity map from detector integrated images with a ROI (region of interest) centered on the SiGe Bragg peak, RMS tilt map and map of strain with respect to the lattice of bulk Silicon. The top row (a) comes from the analysis of the data collected during the (004) Bragg reflection probing, giving insight to the out-of-plane behaviour of the layer, whereas the bottom row (b) is obtained from the (113) Bragg reflection. The striking information is the very high uniformity of both tilt and strain a few hundred nanometers from the edges, sign of homogeneity and defect-free aspect of the crystalline layer.

Furthermore, as the pattern is wider than the ones from the previous section (4.6.2), a more detailed analysis of the strain distribution around the center of the square pattern can be led. Figure 4.33 depicts this distribution for the two Bragg

reflections. When looking at the distribution throughout the entire square (blue histogram), one can notice that the strain spreads over 0.2%, from 1.4% to 1.6% and from 1% to 1.2% for (004) planes and (113) planes respectively. This large spread is attributable to the specific behaviour at the edges, thus one can discard it to focus on the repartition of strain within a smaller portion of the square, i.e., from a set of around 400 probed points, covering an area of approximately 2 x 2 μm^2 centered on the square pattern. Then, the homogeneous distribution is evidenced by the red histograms of figure 4.33 which highlights a 0.02% spread of the strain, around a mean value of 1.5% for the out-of-plane strain and 1.15% for the (113) strain.

As both the (004) and the (113) Bragg reflections are measured for this sample, it is possible to combine the results of strain analysis with equation 4.7 to evaluate the in-plane lattice parameter. Then, the measured out-of-plane strain is combined with the extracted in-plane strain, assuming biaxial strain as in equation 4.9 in order to get access to an averaged Ge-content: $x_{\mathrm{Ge}}^{\mathrm{mean}} = 18.13\% \pm 0.393\%$. Note that with the assumption of the rigidity of the back interface (*i. e.* $a_{SiGe}^{/\!/} = a_{Si}$), the use of only d_{004} leads to a Ge-concentration of $23.45\% \pm 0.05\%$, whereas the use of only d_{113} leads to $21.06\% \pm 0.12\%$. These discrepancies probably indicate either that the SiGe/Si back interface of the sample suffers from inhomogeneities and sliding, or that the condensation process has not been homogeneous throughout the depth of the sample.

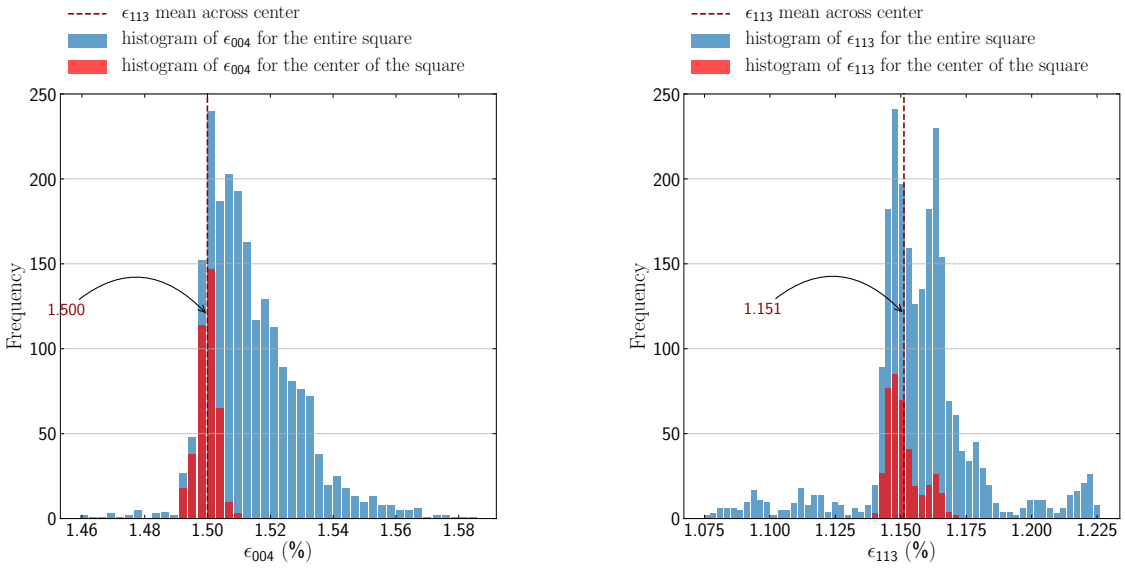

(a) (b)

Figure 4.33 – Histograms of SGOI strain with respect to bulk Silicon lattice, for (a) the (004) and (b) the (113) Bragg reflections. Blue histogram presents the repartition over the entire square (more than 2000 points are taken into consideration). Red histogram depicts the repartition over a portion centered on the square, made of approximately 400 points which corresponds to an area of 2 x 2 μm^2. The average strain from the latter distribution is shown by a dotted dark red line.

4.6.3.2 *13 nm-thick layer without SiN (Sample C)*

On this sample, only the (113) Bragg reflection has been probed. Even though the sample C contains less matter than the other, due to it being ultra thin - 13 nm thick - the analysis gives better results. From Figure 4.34, on the one hand, the square's corners appear less right-angled (but this can be real, as it can be seen in some TEM images, see Figure 4.5) and on the other hand, the dimensions are well respected. More importantly, the four-fold symmetry of both the RMS tilt and the strain is clearly visible in this pattern. Homogeneous tilt, up to 0.09% on the very edges, evidences the good uniformity of the layer, the absence of defects and the relaxation on the borders. Same goes for the (113) strain, which is fairly homogeneous in the center.

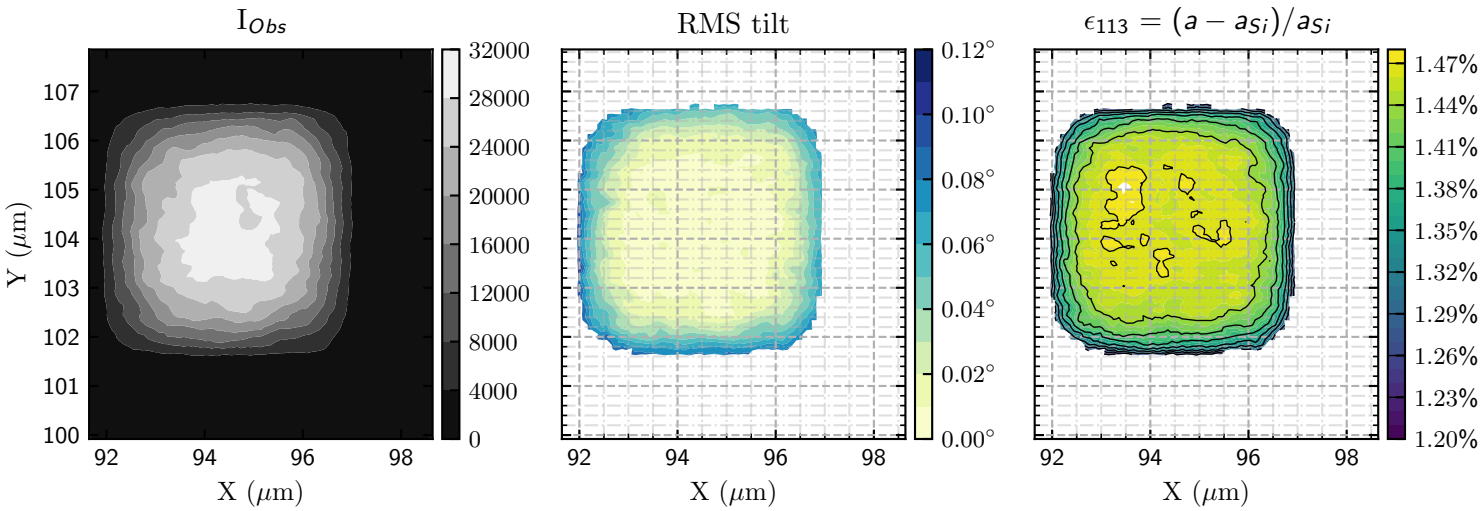

Figure 4.34 – Map of strained SiGe-on-insulator, 13 nm thickness, without nitride on top. The pattern is a 5 x 5 μm^2 square probed with (113) reflection. From left to right, intensity map from detector integrated images with a ROI centered on the SiGe Bragg peak, RMS tilt map and map of strain with respect to the lattice of bulk Silicon. A few hundred nanometers from the edges both tilt and strain present very high uniformity, sign of homogeneity and defect-free aspect of the crystalline layer. The RMS tilt reaches almost 0.1° on each of the very edges, while the strain decreases from 1.39% at the center down to 1.20% at the edges, showing tensile out-of-plane strain relaxation.

In terms of statistics, Figure 4.35 depicts the distribution of the (113) strain over the square. Considering a set of approximately 400 points taken at the center of the square, an averaged value of $1.392\% \pm 0.008\%$ is found. This, combined with the back interface rigidity and equation 4.9, enables one more time to estimate the Ge-concentration of the layer: $x_{Ge}^{mean} = 25.36\% \pm 0.153\%$, which is 3% higher than the target of the process. Note that this Ge-concentration is in agreement with the one measured on the same sample but different patterns (see section 4.6.2.3), providing assurance towards the measurements on this sample.

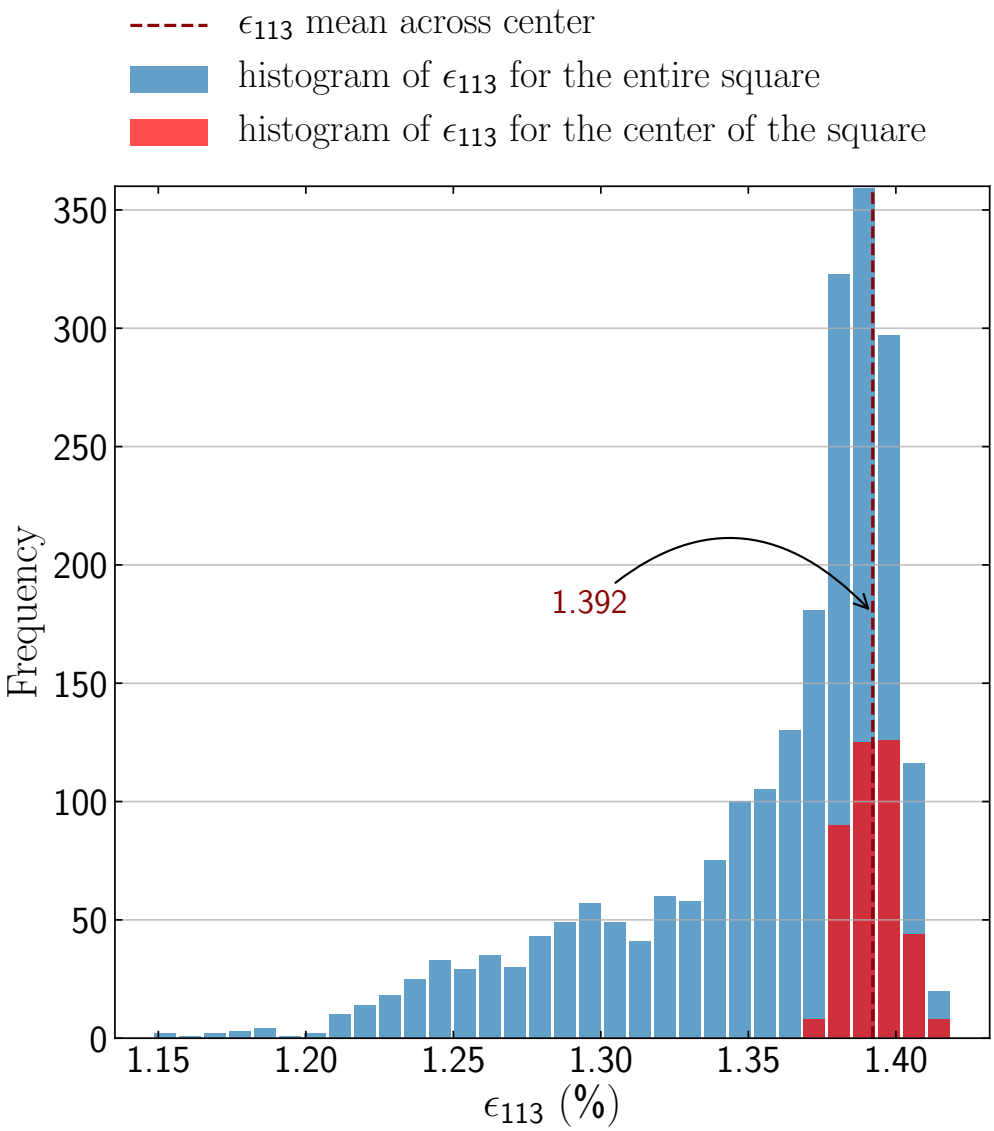

Figure 4.35 – Histogram of SGOI strain with respect to bulk Silicon lattice from the (113) reflection. Blue histogram presents the repartition over the entire square (more than 2000 points are taken into consideration). Red histogram depicts the repartition over a portion centered on the square, made of approximately 400 points which correspond to an area of 2 x 2 μm^2. The average strain from the latter distribution is shown by a dotted dark red line. The behaviour of the histogram follows the expected trend: the higher frequency is around the center-pattern-mean value of 1.392%, and as the strain decreases, the frequency decreases as well, showing the homogeneity of the layer at the same time as the tensile out-of-plane strain relaxation and compressive in-plane strain relaxation.

The same goes for this sSGOI sample as in section 4.6.2.3, the good analysis quality allows for an extraction of the strain profile. Figure 4.36 shows such strain profiles

in both parallel-beam direction and orthogonal-beam direction. On the edges, the tendency for a decrease of the strain is clear, meaning diminution of the tensile out-of-strain as expected due to the free-boundary conditions introduced by the etching of SGOI around the square.

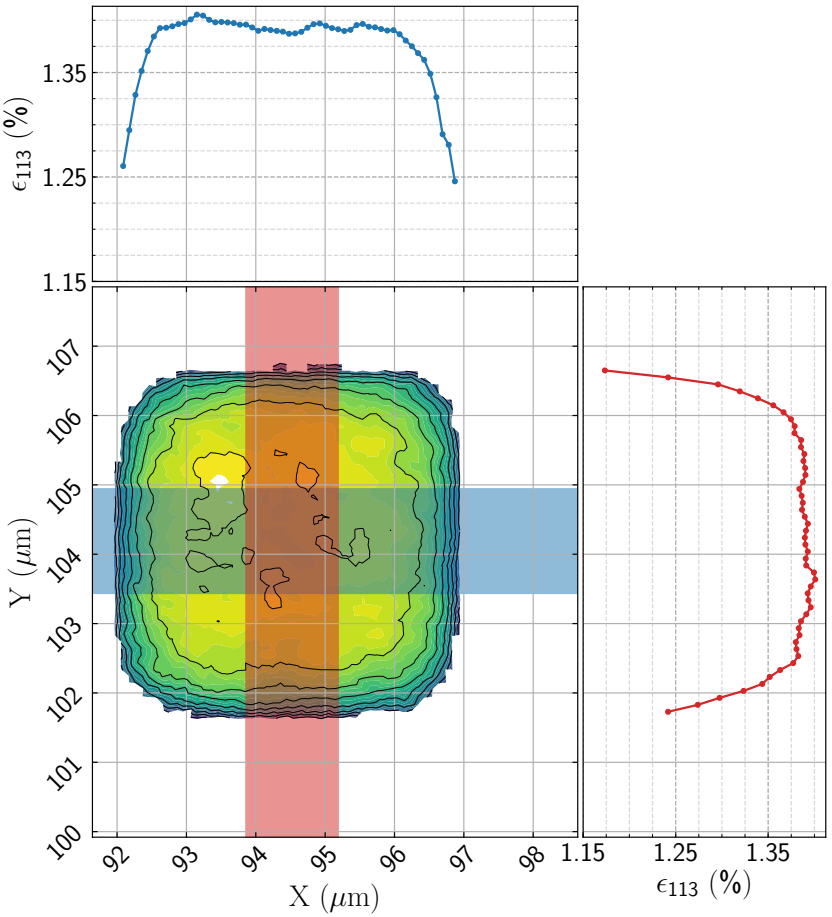

Figure 4.36 – Strain map and profiles. The two colored stripes on the strain map depict the area of integration for respective profile. On the right-hand side sits the vertical strain profile (red line), and on the top side sits the horizontal strain profile (blue line). Integrations have been performed on wide enough stripes to average small variations of strain and minimize errors from the step-by-step scanning method. The strain relaxation is then evidenced: the strain remains around a plateau of 1.39% from the center of the square until a few hundred of nanometers from the edges, where its value drops in a qualitative way. The quantitative value of strain at the very borders is not reliable as their location is approximative and because of the decrease of the signal. Nonetheless, we can still claim that there is at least a 0.1% decrease in strain.

4.6.4 *500 x 500 nm^2 SGOI squares (D2)*

For these 500 x 500 nm^2 patterns, the beam size becomes almost similar to the size of the pattern, hence the spatial resolution decreases. In order to get statistical information of the average strain & Ge-concentration, scans of 8 x 8 µm^2 have been performed on samples A and B.

4.6.4.1 *20 nm-thick layer with SiN (Sample A)*

Information from the reference 20 nm-thick SiGe sample has been gathered for the (004), the (113) and the $(1\bar{1}3)$ reflections. Figure 4.37 depicts the intensity, RMS tilt and strain maps from both the (004) and the (113) reflections. One should note that the lack of intensity from the (004) reflection in a wide area of the scan may be attributed to the degradation of the layer after multiple scans (the (113) Bragg peak has been scanned first, then the $(1\bar{1}3)$ and finally the (004)). Even if this affects the quality and quantity of information from the (004) reflection, two dozen patterns still provide compelling information.

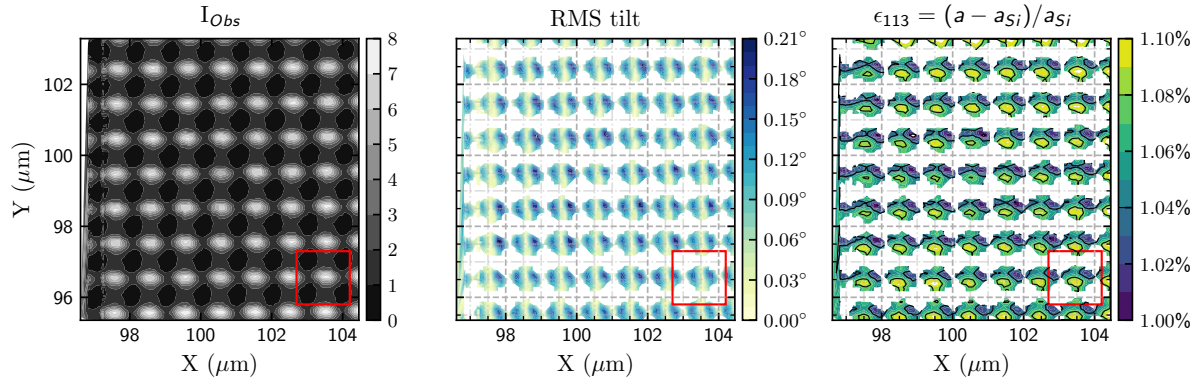

(a)

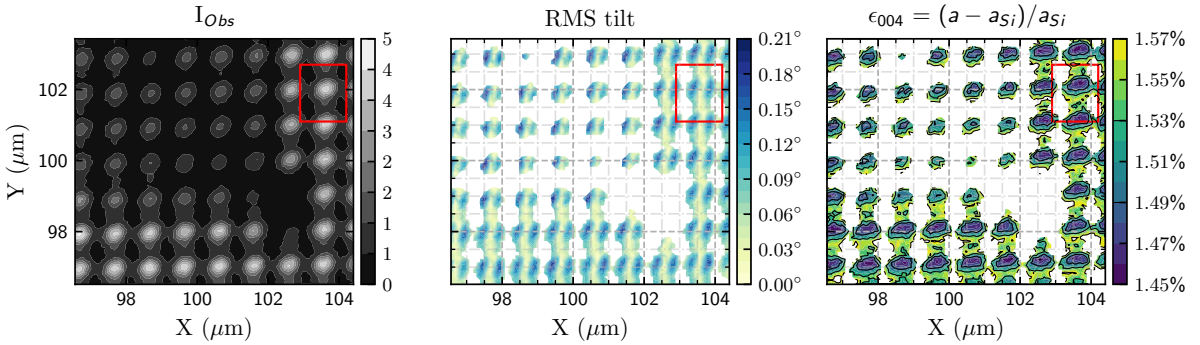

(b)

Figure 4.37 – Map of two 8 x 8 μm^2 areas of strained SiGe-on-insulator layer of thickness 20 nm (sample A), from both (113) (a) and (004) (b) Bragg reflections. The two rows depicts the same information: (Left) Maximum of intensity integrated on the whole detector for each pixel. (Center) RMS tilt angle, taking into account both the perpendicular and parallel angular deviation with respect to the scattering plane. (Right) (a) strain ϵ_{113} distribution, both calculated with respect to the bulk Si lattice parameter, (b) Out-of-plane strain ϵ_{zz} distribution. The (004) reflection (b) evidences clear drops of scattering, hence the patterns located in areas associated with the lowest intensities are discarded from the analysis. The red insets show the location of the pattern that is used for detailed analysis (see Figures 4.38 & 4.40).

In order to show the behaviour of the strain over a pattern, in the direction transverse to the propagation of the beam, i.e. along (X), the Q-space projections from the (004) reflection (respectively from the (113) reflection) along Q_z (respectively Q_x and Q_z) are displayed in Figure 4.39 (respectively Figure 4.41), for the positions depicted in Figure 4.38 (respectively Figure 4.40). Projections appear both with and without the Silicon substrate scattering correction, and are displayed along with the center value from the associated fit function (Center of mass or Gaussian).

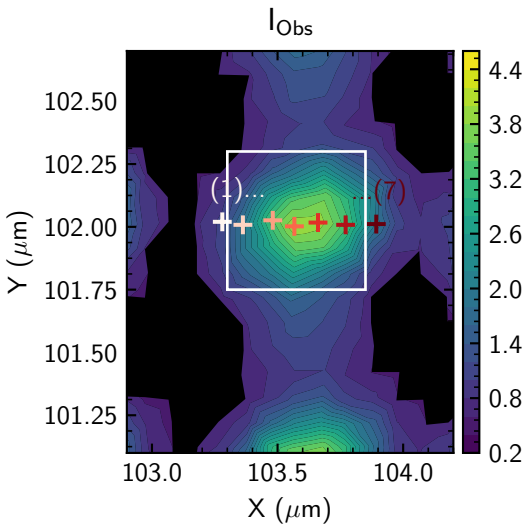

Figure 4.38 – Intensity map from (004) Bragg reflection of sample A, centered on a pattern. The crosses are related to the projections of Figure 4.39, and the white frame gives a reference of a 500 nm square. Note that the black mask has been set to values below the 65^{th} percentile of the intensity.

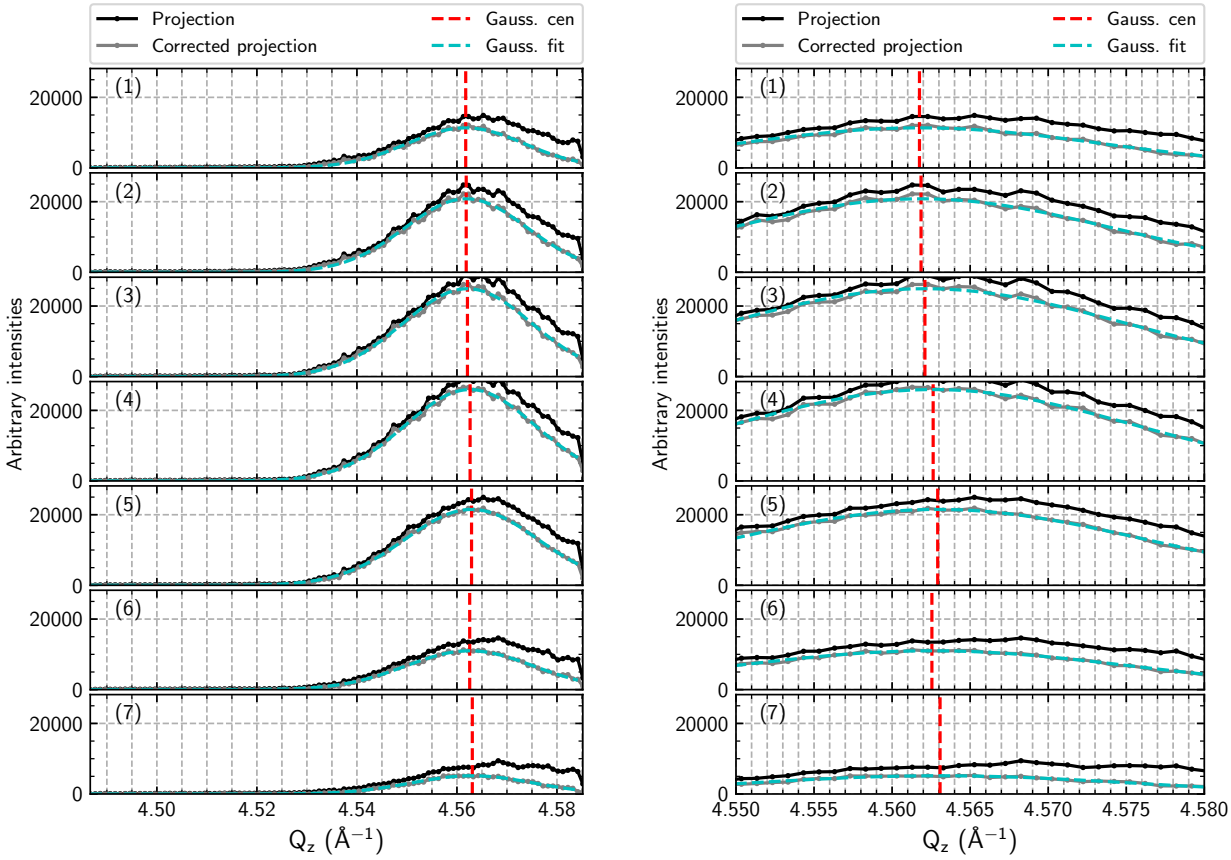

(a) (b)

Figure 4.39 – (004) Q_z projections from 7 locations extracted along a given squared pattern (see Figure 4.38 for locations (1) to (7)). On the right-hand side sits a zoomed view of the left hand-side. Black lines depict the scattering integrated over the detector for a full rocking curve on one point of the scan, while gray lines depict the same scattering freed from the Silicon substrate part. Cyan lines show the Gaussian fit of the associated corrected projection and red vertical dotted lines signal the center of the Gaussian fit. From the left-hand side, one can note that the substrate scattering removal enables to smooth the projections for $Q_z \geq 4.56$ Å^{-1}, while the zoom-in view shows that the variations of the center of the Q_z Gaussian fit are within 0.001 Å^{-1} but their trend do not match the expected trend for relaxation. Indeed, the out-of-plane strain being inversely proportional to Q_z^{center}, we expect to have minimum Q_z^{center}-value from diffraction at the center of the square [*i. e.* positions (3-4)] and maximum Q_z^{center}-value at the edges [*i. e.* positions (1) and (7)].

For the (004) reflection, only the Q_z projections are meaningful as $Q_x \backsimeq Q_y \backsimeq 0$. As the out-of-plane strain is inversely proportional to the norm of the Q vector, we have:

$$\epsilon_{004} \propto 1/\left|\mathrm{Q}\right| \simeq 1/Q_z^{\text{center}}$$

Hence, the position of the center of the Gaussian peak, Q_z^{center}, directly gives us insight about strain. In order to assess the evolution of strain across the width

of a pattern, we extracted the Q_z projections of the diffraction coming from seven points located from left to right on a pattern, as depicted on Figure 4.38. Figure 4.39 shows that through all the locations on the pattern, the variations of the norm of the Q vector are within 0.001 $Å^{-1}$. This amplitude translates into a 0.02% strain variation. Moreover, the behaviour of the strain across the square does not appear as expected. In the center of the square the out-of-plane strain is expected to be maximum whereas at the borders it should decrease due to relaxation from etching. Hence, one should expect minimum Q_z^{center}-values at positions (3)-(5) and maximum Q_z^{center}-values at position (1) & (7). From Figure 4.39b, it is clear that the center of the Gaussian fit from position (1) to (7) does not follow the trend of strain relaxation. This can be explained either by the method or by the material. On the one hand, the size of the incident beam probe is about half the the size of the pattern, making it difficult to measure reliable strain information without averaging. On the other hand, if the typical relaxation length of the SiGe layer is around 250 nm, *i. e.* half the pattern size, it is likely that most of the pattern experiences the same strain state. One possible conclusion is that no supplementary strain relaxation at the edges happens, as most of the SiGe layer is in the same strain state and is very likely to reach its maximally relaxed lattice parameter. One should note that this maximally relaxed lattice parameter is likely to differ from the fully relaxed lattice parameter of the SiGe as the presence of the SiN layer prevent the SiGe from fully relaxing.

For the (113) reflection, $|\mathrm{Q}| \simeq \sqrt{Q_x^2 + Q_z^2}$. Figure 4.41 shows that the variations of Q_x are within 0.001 $Å^{-1}$ while the variations of Q_z are within 0.002 $Å^{-1}$ for eight points located from left to right on a pattern (depicted on Figure 4.40). This translates into strain varying between 1.11% and 1.06%. Thus, as for the (004) Bragg reflection analysis, it is very likely that most of the SiGe layer is in the same strain state and is at its maximally relaxed lattice parameter. Thus, it is fully relaxed.

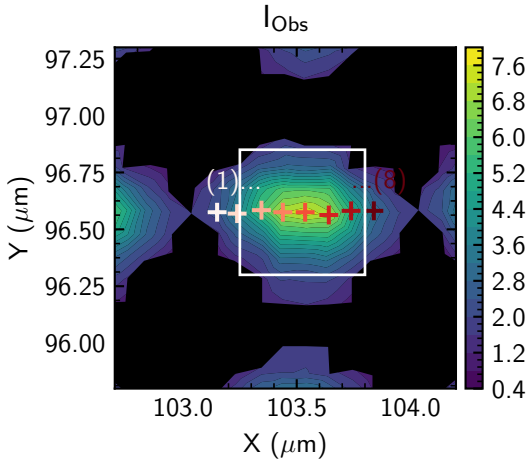

Figure 4.40 – Intensity map from (113) Bragg reflection of sample A, centered on a pattern. The crosses are related to the projections of 4.41, and the white frame shows the allegedly position of the squared pattern according to the intensity repartition. Note that the black mask has been set to values below the 65^{th} percentile of the intensity.

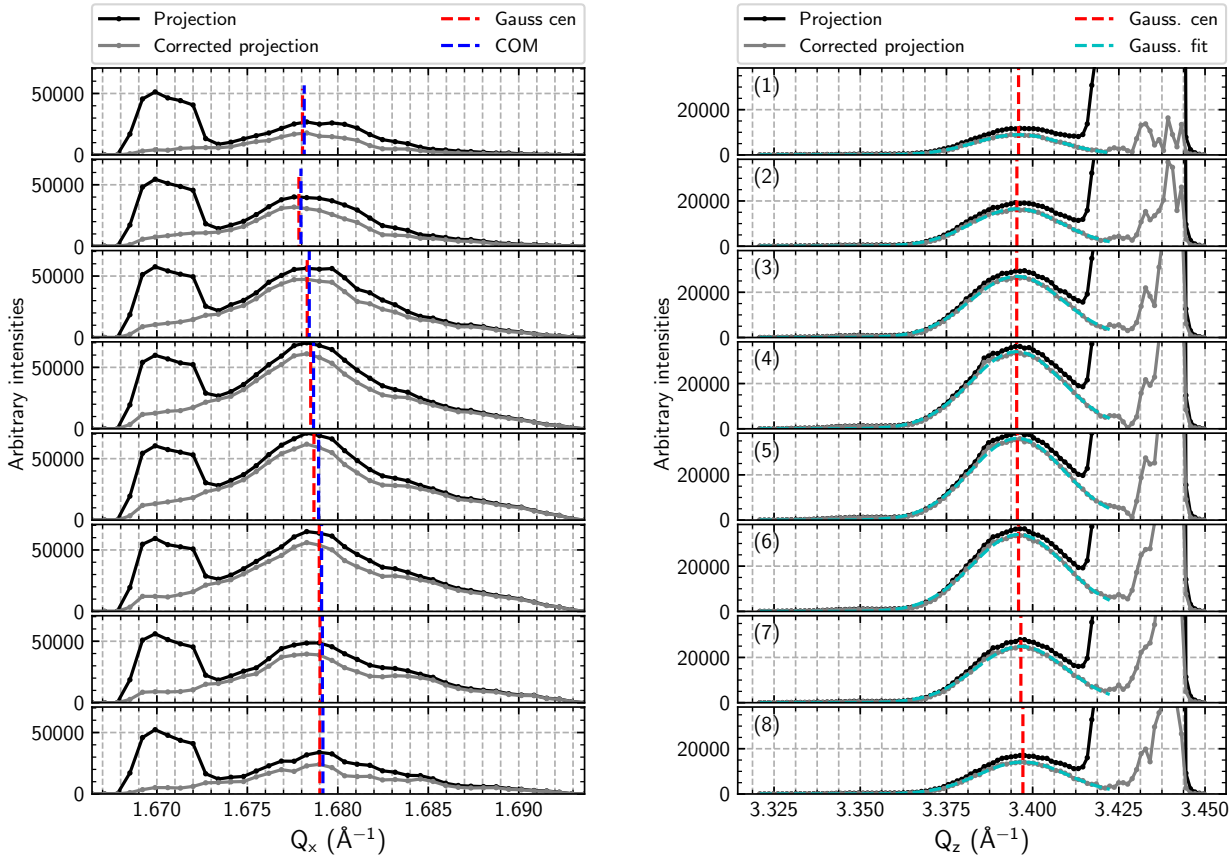

Figure 4.41 – (113) (a) Q_x and (b) Q_z projections from 8 locations extracted along a given squared pattern (see Figure 4.40 for locations (1) to (8)). Black lines depict the scattering integrated over the detector for a full rocking curve on one point of the scan, while gray lines depict the same scattering freed from the Silicon substrate part. Cyan lines show the Gaussian fit of the associated corrected projection and red vertical dotted lines signal the center of the Gaussian fit. Vertical dotted blue lines signal the center of mass of the corrected projections. Firstly, one can note that the substrate scattering removal enables to smooth the projections (for $Q_z \geq 3.42$ Å^{-1} and $Q_x \leq 1.673$ Å^{-1}) as the Si and SiGe peaks are slightly shifted one to each other. Then, from (1) to (8), the Q_z center moves within 0.002 Å^{-1} and the center of mass of Q_x varies within 0.001 Å^{-1}, accounting for a total variation of strain of 0.05%.

By taking an average over 5 points centered on each pattern, the repartition of strain through the entire scanned area can be evaluated. Figure 4.42 depicts the repartition for the (004) and the (113) reflections. As mentioned above, the strain over one pattern does not vary more than 0.05% thus the variations of the histograms must be related to variations of SiGe properties from a pattern to another, for instance slight changes of Ge-concentration. The mean value of the out-of-plane strain is $\epsilon_{004} \simeq 1.430 \pm 0.067\%$ and for the (113) planes the mean strain is $\epsilon_{113} \simeq 1.101\% \pm 0.027\%$. Note that independent measurements from the $(1\bar{1}3)$ re-

flection give the same strain $\epsilon_{1\bar{1}3} \simeq 1.101\% \pm 0.043\%$, confirming the biaxial assumption. It is worth pointing out that the measured variations, of both ϵ_{113} and ϵ_{004}, are very small. This denotes the performance levels achieved by the SXDM method with optimized beam, and demonstrates the accuracy of this method of measurement.

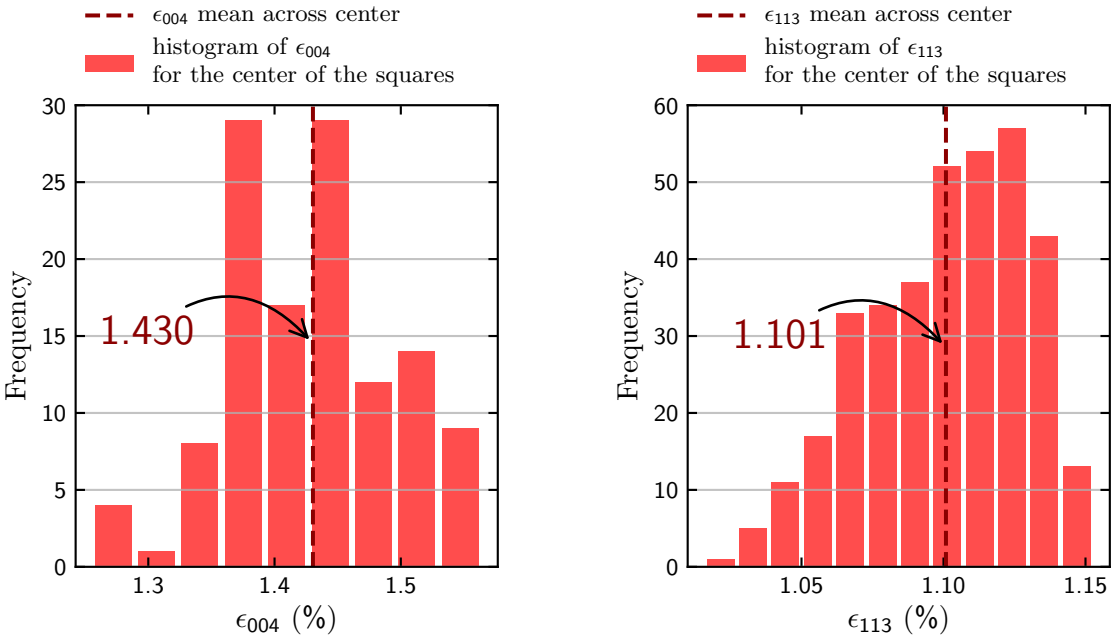

(a) (b)

Figure 4.42 – Strain distribution from (004) Bragg reflection (a) and (113) Bragg reflection (b). Values are taken from a selection of 5 points from the center of every squared pattern appearing on the map. The dotted red lines depict the average value of the distribution. The 13% variations over ϵ_{004} are due to the poorer quality of the scan, on an area that already spent 4 hours under the X-ray beam.

Finally, with the knowledge of both ϵ_{113} and ϵ_{004}, Equations 4.7 & 4.9 can be combined in order to recover the Ge-content x inside the layer: $x_{\text{Ge}}^{\text{mean}} = 17.47\% \pm 1.65\%$. This value is lower than the ones found previously on sample A, but one should note that a 0.05% increase of the ϵ_{113} values leads to $x_{\text{Ge}}^{\text{mean}} = 20.44\% \pm 1.64\%$ thus the Ge-concentration is very sensitive to the strain measurements precision. Moreover, one could notice that by assuming the back interface rigidity hypothesis, and considering the ϵ_{113} measurements, the Ge-concentration becomes $x_{\text{Ge}}^{\text{mean}} = 20.16\% \pm 0.5\%$ or $x_{\text{Ge}}^{\text{mean}} = 20.94\% \pm 0.5\%$ for a slight mismatch at the interface ($a_{\text{SiGe}} = 1.001 \times a_{\text{Si}}$). One can suppose that the variation of the Ge-composition induced by the gas phase growth process can also be in the 1-2% range at the wafer scale. This result provides again a good indicator about the quality of the measurements.

4.6.4.2 *13 nm-thick SiGe without SiN (sample C)*

For these 500 x 500 nm^2 pattern, map of 8 x 8 µm^2 area has been performed for the (113) reflection. Figure 4.43 shows the intensity, RMS tilt and strain maps. On this sample, the patterns are easily discernible but the spatial resolution is limiting the analysis. One can still note a RMS tilt of 0.07° on the edges of the pattern and especially an homogeneous strain across the area, with variations smaller than 0.05%.

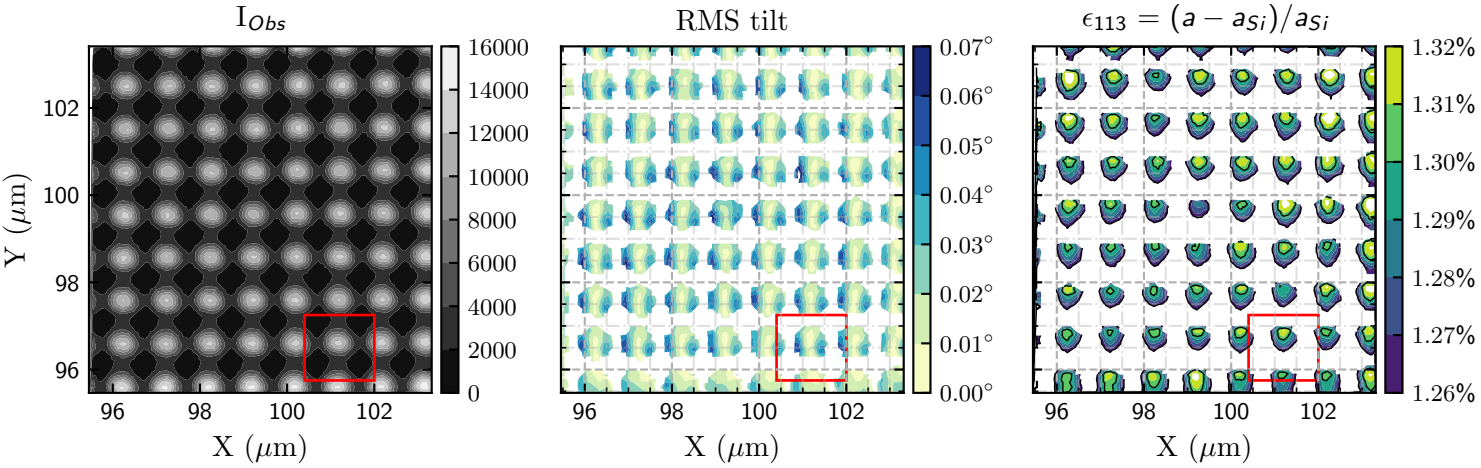

Figure 4.43 – Map of 8 x 8 µm^2 areas of strained SiGe-on-insulator layer of thickness 13 nm (sample C), from the (113) Bragg reflection. (Left) Maximum of intensity integrated on the whole detector for each pixel. (Center) RMS tilt angle, taking into account both the perpendicular and parallel angular deviation with respect to the scattering plane. (Right) strain ϵ_{113} distribution, both calculated with respect to the bulk Si lattice parameter. As both tilt and strain present restricted variations, the patterns are probably in their fully relaxed state. Detailed analysis of the square located inside the red inset is given in the Appendix A.

By performing the same analysis as for the preceding sample, the strain along a pattern is found to vary less than 0.03%, and the mean (113) strain averaged over a small area centered on each pattern is found to be 1.224%. Taking into account the order of magnitude of the strain variations and the fact that the strain does not exhibit significant decrease when reaching the edges of a pattern, one concludes that the area is made of patterns that have also reached their maximally relaxed state. This statement is in accordance with the small characteristic size and the absence of SiN. Figure 4.44 depicts the aforementioned strain repartition.

From the mean strain value, using the back interface rigidity assumption, one finds the Ge-concentration of this area to be $x_{Ge}^{mean} = 22.36\% \pm 0.55\%$ for perfect lattice matching, or $x_{Ge}^{mean} = 23.14\% \pm 0.55\%$ for a 0.1% mismatch. Note that this value

does not match the one found on wider patterns (2 x 2 μm^2, see section 4.6.2.3 and 5 x 5 μm^2, see section 4.6.3.2) from the same sample. This difference in Ge-content within a sample, at the wafer scale, can be explained either by intrinsic growth fluctuations (around 1%), but as the pattern are separated by a maximum of 8 mm (see Figure 4.3) it is more likely that the difference in Ge-content implies the center of the 500 x 500 nm^2 patterns is already relaxing and the pseudomorphic assumption does not hold anymore: the in-plane lattice parameter can not be considered equal to the one of Silicon. Thus, one could use the Ge-concentration calculated for wider patterns (25.3%), along with the (113) interplanar spacing, to derive the in-plane and out-of-plane strain of the relaxed SiGe layer. Therefore $a_{001}^{mean} = 5.5078$ Åand $a_{100}^{mean} = 5.4520$ Åthat translate into $\varepsilon_{XX} = -0.57\%$ and $\varepsilon_{ZZ} = 0.44\%$. Note that these are the "real deformation" i.e., with respect to the lattice parameter of a fully relaxed $Si_{0.75}Ge_{0.25}$, meaning that the center of the patterns still exhibits a compressive in-plane strain.

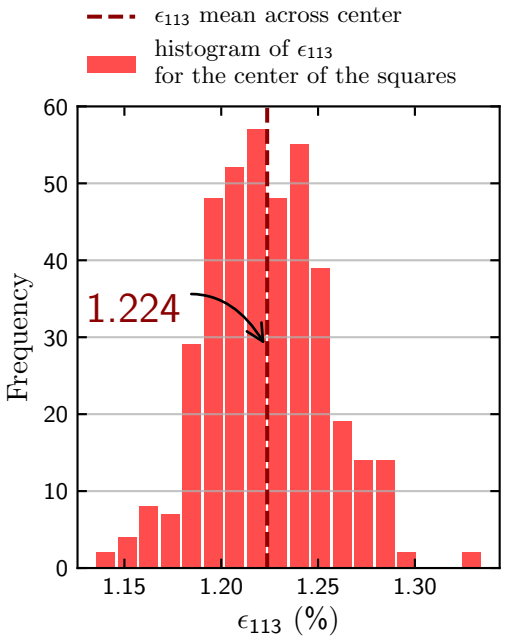

Figure 4.44 – Strain distribution from (113) Bragg reflection. Values are taken from a selection of 5 points from the center of every squared pattern appearing on the map. The dotted red lines depict the average value of the distribution.

4.6.5 *Discussion*

Firstly, a quantitative analysis can be carried on the center of the patterns, as they have a homogeneous area in contrary to the edges, where the introduction of free

boundaries modifies the strain state. The (113) strain of the samples, measured at the center of each of the characteristic patterns, is gathered in Table 4.3. This gives us an insight into the role of the nitride layer, the impact of thickness and the width of a pattern.

The tensor role of the nitride cap is evidenced by comparing sample A and sample B. For the same 2 x 2 μm^2 pattern, the (113) strain is lower in the absence of SiN (1.125% without, 1.227% with). The SiN layer hence maintains compressive in-plane strain.

Compared to the reference 20 nm-thick SGOI (sample A), thinner material (sample C) appears to undergo more strain (+0.16%).

A first understanding of the relaxation length is given by comparing the 2 x 2 μm^2 and 5 x 5 μm^2 patterns to the 500 x 500 nm^2 ones. Indeed, the 2 x 2 μm^2 and 5 x 5 μm^2 patterns experience higher strain than 500 x 500 nm^2 patterns, which hence are already in some relaxed state. This suggests that, as we are only considering the center area of the patterns, the relaxation length is close to half the width of the smallest patterns. Finally, the probing of the (004) Bragg reflection from the reference 20 nm-thick SGOI (sample A) gives us confidence about our interpretations as ϵ_{004} =1.43% for the 500 x 500 nm^2 patterns, ϵ_{004} =1.52% for the 2 x 2 μm^2 patterns and ϵ_{004} =1.51% for the 5 x 5 μm^2 patterns. However, the (113) strain from the wider patterns of sample A does not fit with our expectations.

SAMPLE/ PATTERN SIZE	A: 20 nm-thick w\ SiN	B: 20 nm-thick w\o SiN	C: 13 nm-thick w\o SiN	D: Bilayer SiGe/Si
500 x 500 nm^2	1.101±0.027%	X	1.224±0.03%	X
2 x 2 μm^2	1.227±0.004%	1.125±0.007%	1.391±0.01%	1.247±0.002%
5 x 5 μm^2	1.151±0.02%	X	1.392±0.008%	X

Table 4.3 – Table summarizing the (113) strain (in percent) extracted from the (113) Bragg reflections, averaged over the center of the different scanned patterns for each sample. The precision represents the root mean square from the statistical distribution of extracted strain.

Secondly, the Ge-concentration calculated from the (113) strain assuming back interface rigidity, *i.e.* $a^{/\!/}_{SiGe} = a_{Si}$, is presented in Table 4.4. The Ge-content values enable to get a different perspective on the strain differences observed in Table 4.3. From this sight, it looks like epitaxial growth control can be an issue for an ultra-thin layer. Indeed, with the assumption of perfect lattice matching at the SiGe/Si interface, higher (113) strain of the SiGe layer leads to higher Ge-concentration. That way, the 13 nm-thick SGOI contains more germanium (25.35%) than the reference

20 nm-thick SGOI (≈22%). Note that Ge-enrichment is only possible when the (at least quasi-) totality of Si in the starting SOI substrate has been consumed by oxidization. Hence the Ge-content that arises from the heteroepitaxial growth of SiGe prior to condensation is very likely higher for the 13 nm-thick sample than for the 20 nm-thick. Of course, these conclusions rely on the back interface rigidity assumption and any defect, or gliding, at this interface would break the assumption. In case of total oxidation of the Si layer, the final stack is made of an interface between a strained SiGe crystal and an amorphous SiO_2 material. Thus, it is very likely that the in-plane lattice parameter of SiGe is free from being different than that of initial Si lattice on which the SiGe grown.

SAMPLE→ ↓PATTERN SIZE	A: 20 nm-thick w\ SiN	B: 20 nm-thick w\o SiN	C: 13 nm-thick w\o SiN	D: Bilayer SiGe/Si
500 x 500 nm^2	20.16±0.5%	X	22.36±0.55%	X
2 x 2 µm^2	22.42±0.09%	20.6±0.14%	25.35±0.16%	22.78±0.042%
5 x 5 µm^2	21.06±0.12%	X	25.36±0.15%	X

Table 4.4 – Table summarizing the Ge-content (in percent) averaged over the center of the different scanned patterns for each sample. The Ge-content is extracted from the (113) strain (see Table 4.3) together with two assumptions: biaxial approximation and back interface rigidity. The precision represents the root mean square.

Nonetheless, another way to extract the Ge-content from the reference 20 nm-thick SGOI is available since both the (004) and the (113) Bragg reflections have been probed, leading to the knowledge of the in-plane SiGe lattice parameter without rigidity assumption. Though, the biaxial assumption, confirmed as the additional probing of the $(1\bar{1}3)$ reflection of the 500 x 500 nm^2 patterns gave $\epsilon_{113} = \epsilon_{1\bar{1}3}$, is still necessary to derive the Ge-content from equation 4.9. It results in Ge-content of 17.5% for the 500 x 500 nm^2 patterns, 21.98% for the 2 x 2 µm^2 patterns and 18.13% for the 5 x 5 µm^2 patterns. These variations are attributed to the intrinsic fluctuations of each step of the process, from epitaxial growth to condensation.

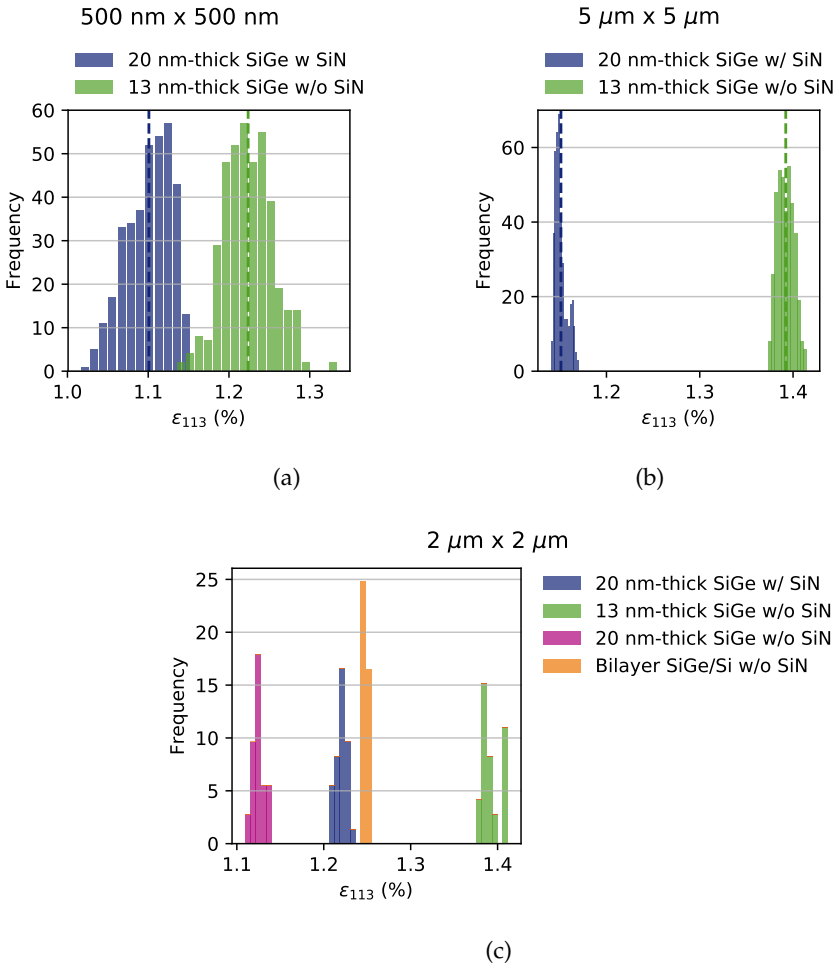

Figure 4.45 – Distribution of (113) strain from the center of all the probed patterns on each sample. The dotted lines depict the average strain over the entire distribution. (a) 500 x 500 nm^2 patterns, probed on sample A (20 nm-thick SGOI with nitride cap) and C (13 nm-thick SGOI without nitride cap). (b) 5 x 5 µm^2 patterns, probed on sample A (20 nm-thick SGOI with nitride cap) and C (13 nm-thick SGOI without nitride cap). (c) 2 x 2 µm^2 patterns, probed on sample A (20 nm-thick SGOI with nitride cap), sample B (20 nm-thick SGOI without nitride cap), C (13 nm-thick SGOI without nitride cap) and sample D (bilayer SiGe/Si/BOX).

Figure 4.45 summarises the behaviour of the (113) strain throughout the four different samples and the probed patterns. Histograms of strain are presented by pattern size.

In a second part, the strain measurement by SXDM on patterned SGOI has evidenced side strain relaxation. In order to assess the strain relaxation at the edges, we compared the extracted strain profiles of the 13 nm-thick SGOI. The choice of sample was driven by the fact that the mean value of ϵ_{113} did not change from the 5 x 5 µm^2 patterns and the 2 x 2 µm^2 patterns, plus the fact that less parasitic drift

occurred. Figure 4.46 presents strain profiles along both (X) and (Y) directions, together with an empirical model adapted from Berthelon, 2018 in order to derive a typical relaxation length consistent with what have been observed so far; the relaxation is expanding until 300 nm from the edges. The relaxation function we used allows both the edges and the center of the active zone to behave freely:

$$f_{\text{relax}} = f_{min} + (f_{max} - f_{min}) \left[\left(1 - \exp\left(-\frac{x}{\lambda}\right)\right) - \left(\exp\left(-\frac{(L_{act} - x)}{\lambda}\right)\right) \right] \quad (4.10)$$

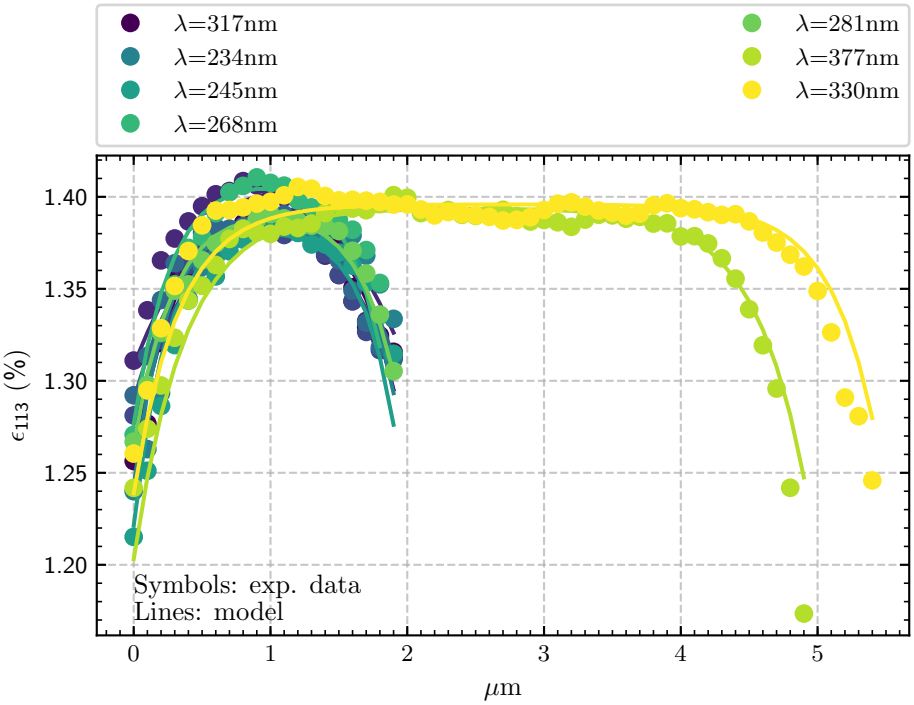

Figure 4.46 – (113) strain profiles from 5 x 5 μm² and 2 x 2 μm² paterns of 13 nm-thick SGOI (sample C) and corresponding curves from the analytical model (see equation 4.10). The typical relaxation lengths obtained with the analytical model (lines) are in good agreement with the data (dots) and are between 234 nm and 377 nm.

This model reproduces faithfully the relaxation occurring on both edges, with typical relaxation lengths between 234 nm and 377 nm. Such relaxation is not consistent with elasticity simulations ibid. As the precision of the SXDM measurement is high enough, the intrinsic fluctuations of the two main steps of the reference process can be incriminated : heteroepitaxy of SiGe on a SOI substrate and condensation by RTO. The condensation being a kinetic process, doubts on depth homogeneity and defects/sliding at the SiGe/Si interface have to be tackled once more.

Recent electron holography measurements tend to validate the interface gliding assumption Boureau, Reboh, et al., 2019. To analyse these data, a "thin elastic interface" is defined as a boundary in-between the SiGe and the BOX. A relative displacement between them is added, and normal and tangential stiffnesses of this layer are used to model the in-plane displacement fields. FEM calculations with this model (adding three parameters) are in quantitative agreement with the holographic measurements. The maximal relaxation of the edge of the SiGe layer is about 3.8 nm and is not attributed to extended defects (such as dislocations), but rather to the propagation of defects from the edges (e.g. punctual) that are driven by the stress at the interface.

4.7 CONCLUSION

In this chapter, details on the evolution of strain engineering for a performance boost of CMOS transistor have been provided, with a focus on the condensation technique developed in order to integrate strain in FDSOI. The step of patterning in order to define active area is key in the appearance of strain relaxation at the edges of the SiGeOI pattern.

The SXDM technique has been described thoroughly, with a point-by-point protocol detailing the important steps of both the experimental data collection and its advanced analysis. From this, the most accurate and precise quantitative results have been achieved. Advantages and limitations of the technique have also been given throughout the chapter. In order to gather a complete statistical analysis, different epitaxial systems have been studied, with different characteristic sizes of patterns. As a result, the limits of strain sensitivity, or of the equivalent composition sensitivity, were investigated.

This relaxation has been observed and qualitatively assessed by means of SXDM, a powerful method giving access to high resolution strain fluctuations (up to 10^{-5}) with X-ray beam size limited spatial resolution (around 100 nm). Fluctuations in Ge-content have also been evidenced, suggesting that intrinsic fluctuations of hetero-epitaxy and likely of the condensation process are to blame. The strong relaxation measured have to come from a specific behavior of the interface between the strained SiGe layer and the underlying amorphous BOX. Lastly, the typical relaxation length over which the SiGe is not fully constrained has revealed to be higher than expected by standard elasticity calculations (below 100 nm Berthelon, 2018), reaching values comprised between 200 and 300 nm. These measurements are in agreement with the modeling of electron holography experiments based on an interface gliding at the edge of the patterns Boureau, Reboh, et al., 2019.

BIBLIOGRAPHY

Berthelon, Remy (2018). « Strain integration and performance optimization in sub-20nm FDSOI CMOS technology. » PhD. Université Paul Sabatier - Toulouse III (cit. on pp. 65, 67, 68, 77, 79, 80, 132, 133).

Sun, Y., S. E. Thompson, and T. Nishida (2007). « Physics of strain effects in semiconductors and metal-oxide-semiconductor field-effect transistors. » In: *Journal of Applied Physics* 101.10, p. 104503. DOI: 10.1063/1.2730561 (cit. on p. 65).

Pidin, S. et al. (2004). « A novel strain enhanced CMOS architecture using selectively deposited high tensile and high compressive silicon nitride films. » In: *IEDM Technical Digest. IEEE International Electron Devices Meeting, 2004.* Pp. 213–216. DOI: 10.1109/IEDM.2004.1419112 (cit. on p. 65).

Berthelon, R., F. Andrieu, B. Mathieu, D. Dutartre, C. Le Royer, M. Vinet, and A. Claverie (2017). « Mechanical simulations of BOX creep for strained FDSOI. » In: *2017 Joint International EUROSOI Workshop and International Conference on Ultimate Integration on Silicon (EUROSOI-ULIS).* Athens, Greece: IEEE, pp. 91–94. DOI: 10.1109/ULIS.2017.7962609 (cit. on p. 66).

Yeo, Yee-Chia (2006). « Enhancing CMOS transistor performance using lattice-mismatched materials in source/drain regions. » en. In: *Semiconductor Science and Technology* 22.1, S177–S182. DOI: 10.1088/0268-1242/22/1/S42 (cit. on p. 66).

Weber, O., E. Josse, J. Mazurier, N. Degors, S. Chhun, P. Maury, S. Lagrasta, D. Barge, J.- Manceau, and M. Haond (2015). « 14nm FDSOI upgraded device performance for ultra-low voltage operation. » In: *2015 Symposium on VLSI Technology (VLSI Technology)*, T168–T169. DOI: 10.1109/VLSIT.2015.7223664 (cit. on p. 66).

Bruel, M. (1995). « Silicon on insulator material technology. » In: *Electronics Letters* 31.14, pp. 1201–1202. DOI: 10.1049/el:19950805 (cit. on pp. 66, 97).

Ernst, T., R. Ritzenthaler, O. Faynot, and S. Cristoloveanu (2007). « A Model of Fringing Fields in Short-Channel Planar and Triple-Gate SOI MOSFETs. » In: *IEEE Transactions on Electron Devices* 54.6, pp. 1366–1375. DOI: 10.1109/TED.2007.895241 (cit. on p. 66).

Gallon, C. et al. (2006). « Ultra-Thin Fully Depleted SOI Devices with Thin BOX, Ground Plane and Strained Liner Booster. » In: *2006 IEEE international SOI Conferencee Proceedings*, pp. 17–18. DOI: 10.1109/SOI.2006.284410 (cit. on p. 66).

Schwarzenbach, Walter, Bich-Yen Nguyen, Frederic Allibert, Christophe Girard, and Christophe Maleville (2016). « Ultra-thin body and buried oxide SOI substrate development and qualification for Fully Depleted SOI device with back bias capa-

bility. » In: *Solid-State Electronics* 117, pp. 2–9. DOI: 10.1016/j.sse.2015.11.008 (cit. on p. 66).

Planes, N. et al. (2012). « 28nm FDSOI technology platform for high-speed low-voltage digital applications. » In: *2012 Symposium on VLSI Technology (VLSIT)*, pp. 133–134. DOI: 10.1109/VLSIT.2012.6242497 (cit. on p. 66).

Berthelon, R., F. Andrieu, S. Ortolland, R. Nicolas, T. Poiroux, E. Baylac, D. Dutartre, E. Josse, A. Claverie, and M. Haond (2017). « Characterization and modelling of layout effects in SiGe channel pMOSFETs from 14nm UTBB FDSOI technology. » In: *Solid-State Electronics*. Extended papers selected from EUROSOI-ULIS 2016 128, pp. 72–79. DOI: 10.1016/j.sse.2016.10.011 (cit. on p. 66).

Kuhn, Karl Josef (2012). « Considerations for Ultimate CMOS Scaling. » In: *IEEE Transactions on Electron Devices* 59, pp. 1813–1828 (cit. on p. 66).

D.W.Palmer (2019). *http://www.semiconductors.co.uk/* (cit. on p. 66).

Vegard, L. (1921). « Die Konstitution der Mischkristalle und die Raumfüllung der Atome. » de. In: *Zeitschrift für Physik* 5.1, pp. 17–26. DOI: 10.1007/BF01349680 (cit. on pp. 67, 78).

J.P.Dismukes (1964). « Lattice parameter and Density in Germanium-Silicon Alloy. » In: *The Journal of Physical Chemistry* (cit. on p. 67).

DeSalvo, B. et al. (2014). « A mobility enhancement strategy for sub-14nm power-efficient FDSOI technologies. » In: *2014 IEEE International Electron Devices Meeting*, pp. 7.2.1–7.2.4. DOI: 10.1109/IEDM.2014.7047002 (cit. on p. 67).

Andrieu, F. et al. (2005). « Co-integrated dual strained channels on fully depleted sSDOI CMOSFETs with HfO/sub 2//TiN gate stack down to 15nm gate length. » In: pp. 223–225. DOI: 10.1109/SOI.2005.1563596 (cit. on p. 67).

Tezuka, Tsutomu, Naoharu Sugiyama, Tomohisa Mizuno, Masamichi Suzuki, and Shin-ichi Takagi (2001). « A Novel Fabrication Technique of Ultrathin and Relaxed SiGe Buffer Layers with High Ge Fraction for Sub-100 nm Strained Silicon-on-Insulator MOSFETs. » en. In: *Japanese Journal of Applied Physics* 40.4S, p. 2866. DOI: 10.1143/JJAP.40.2866 (cit. on pp. 67, 97).

Vincent, B., J. F. Damlencourt, et al. (2008). « The Ge condensation technique: A solution for planar SOI/GeOI co-integration for advanced CMOS technologies? » In: *Materials Science in Semiconductor Processing*. E-MRS 2008 Spring Conference Symposium J: Beyond Silicon Technology: Materials and Devices for Post-Si CMOS 11.5, pp. 205–213. DOI: 10.1016/j.mssp.2008.10.005 (cit. on p. 68).

Bedell, S. W., A. Reznicek, K. Fogel, J. Ott, and D. K. Sadana (2006). « Strain and lattice engineering for Ge FET devices. » In: *Materials Science in Semiconductor Processing*. Proceedings of Symposium T E-MRS 2006 Spring Meeting on Germanium based semiconductors from materials to devices 9.4, pp. 423–436. DOI: 10.1016/j.mssp.2006.08.001 (cit. on p. 68).

Gunji, Marika, Ann F. Marshall, and Paul C. McIntyre (2011). « Strain relaxation mechanisms in compressively strained thin SiGe-on-insulator films grown by selective Si oxidation. » In: *Journal of Applied Physics* 109.1, p. 014324. DOI: 10.1063/1.3506420 (cit. on p. 68).

Nakaharai, Shu, Tsutomu Tezuka, Naoharu Sugiyama, Yoshihiko Moriyama, and Shin-ichi Takagi (2003). « Characterization of 7-nm-thick strained Ge-on-insulator layer fabricated by Ge-condensation technique. » In: *Applied Physics Letters* 83.17, pp. 3516–3518. DOI: 10.1063/1.1622442 (cit. on pp. 68, 97).

Boureau, Victor, Daniel Benoit, Benedicte Warot, Martin Hÿtch, and Alain Claverie (2016). « Strain/composition interplay in thin SiGe layers on insulator processed by Ge condensation. » In: *Materials Science in Semiconductor Processing*. E-MRS Spring Meeting 2015 Symposium Z: Nanomaterials and processes for advanced semiconductor CMOS devices 42, pp. 251–254. DOI: 10.1016/j.mssp.2015.07.034 (cit. on p. 68).

People, R. and J. C. Bean (1985). « Calculation of critical layer thickness versus lattice mismatch for Ge_xSi_{1-x}/Si strained-layer heterostructures. » In: *Applied Physics Letters* 47.3, pp. 322–324. DOI: 10.1063/1.96206 (cit. on p. 69).

Tezuka, Tsutomu, Shu Nakaharai, et al. (2006). « Strained SOI/SGOI dual-channel CMOS technology based on the Ge condensation technique. » en. In: *Semiconductor Science and Technology* 22.1, S93–S98. DOI: 10.1088/0268-1242/22/1/S22 (cit. on p. 69).

AB, COMSOL. *COMSOL Multiphysics® v. 5.2a* (cit. on p. 72).

EerNisse, E. P. (1977). « Viscous flow of thermal SiO2. » In: *Applied Physics Letters* 30.6, pp. 290–293. DOI: 10.1063/1.89372 (cit. on p. 73).

Anastassakis, E., A. Cantarero, and M. Cardona (1990). « Piezo-Raman measurements and anharmonic parameters in silicon and diamond. » In: *Physical Review B* 41.11, pp. 7529–7535. DOI: 10.1103/PhysRevB.41.7529 (cit. on p. 77).

Wong, L. H., C. C. Wong, J. P. Liu, D. K. Sohn, L. Chan, L. C. Hsia, H. Zang, Z. H. Ni, and Z. X. Shen (2005). « Determination of Raman Phonon Strain Shift Coefficient of Strained Silicon and Strained SiGe. » In: *Japanese Journal of Applied Physics* 44.11R, p. 7922. DOI: 10.1143/JJAP.44.7922 (cit. on p. 77).

Wolf, Ingrid De (1999). « Stress measurements in Si microelectronics devices using Raman spectroscopy. » In: *Journal of Raman Spectroscopy* 30.10, pp. 877–883. DOI: 10.1002/(SICI)1097-4555(199910)30:10<877::AID-JRS464>3.0.CO;2-5 (cit. on p. 77).

Hu, S. M. (1979). « Film-Edge-Induced stress in substrates. » In: *Journal of Applied Physics* 50.7, pp. 4661–4666. DOI: 10.1063/1.326575 (cit. on p. 80).

– (1991). « Stress-Related problems in silicon technology. » In: *Journal of Applied Physics* 70.6, R53–R80. DOI: 10.1063/1.349282 (cit. on p. 80).

Mocuta, C., J. Stangl, K. Mundboth, T. H. Metzger, G. Bauer, I. A. Vartanyants, M. Schmidbauer, and T. Boeck (2008). « Beyond the ensemble average: X-ray microdiffraction analysis of single SiGe islands. » In: *Phys. Rev. B* 77 (24), p. 245425. DOI: 10.1103/PhysRevB.77.245425 (cit. on p. 81).

Hanke, M., M. Dubslaff, M. Schmidbauer, T. Boeck, S. Schöder, M. Burghammer, C. Riekel, J. Patommel, and C. G. Schroer (2008). « Scanning x-ray diffraction with 200nm spatial resolution. » In: *Applied Physics Letters* 92.19, p. 193109. DOI: 10.1063/1.2929374 (cit. on p. 81).

Chahine, G. A. et al. (2014). « Imaging of strain and lattice orientation by quick scanning X-ray microscopy combined with three-dimensional reciprocal space mapping. » en. In: *Journal of Applied Crystallography* 47.2, pp. 762–769. DOI: 10.1107/S1600576714004506 (cit. on p. 82).

Leake, S. J. et al. (2019). « The Nanodiffraction beamline ID01/ESRF: a microscope for imaging strain and structure. » en. In: *Journal of Synchrotron Radiation* 26.2, pp. 571–584. DOI: 10.1107/S160057751900078X (cit. on p. 84).

Favre-Nicolin, V. (2019). *PyNX Python Library*. URL: http://ftp.esrf.fr/pub/scisoft/PyNX/ (visited on 08/2019) (cit. on p. 84).

Mandula, O., M. Elzo Aizarna, J. Eymery, M. Burghammer, and V. Favre-Nicolin (2016). « PyNX.Ptycho: a computing library for X-ray coherent diffraction imaging of nanostructures. » en. In: *Journal of Applied Crystallography* 49.5, pp. 1842–1848. DOI: 10.1107/S1600576716012279 (cit. on p. 84).

Hofmann, Felix, Edmund Tarleton, Ross J. Harder, Nicholas W. Phillips, Pui-Wai Ma, Jesse N. Clark, Ian K. Robinson, Brian Abbey, Wenjun Liu, and Christian E. Beck (2017). « 3D lattice distortions and defect structures in ion-implanted nanocrystals. » In: *Scientific Reports* 7, p. 45993. DOI: 10.1038/srep45993 (cit. on p. 90).

Hartmann, J. M., A. Abbadie, D. Rouchon, M. Mermoux, and T. Billon (2007). « Tensile-strained Si layers grown on Si0.6Ge0.4and Si0.5Ge0.5virtual substrates: II. Strain and defects. » In: *Semiconductor Science and Technology* 22.4, pp. 362–368. DOI: 10.1088/0268-1242/22/4/011 (cit. on p. 96).

Kimura, Y., N. Sugii, S. Kimura, K. Inui, and W. Hirasawa (2006). « Generation of misfit dislocations and stacking faults in supercritical thickness strained-Si/SiGe heterostructures. » In: *Applied Physics Letters* 88.3, p. 031912. DOI: 10.1063/1.2167391 (cit. on p. 96).

Kutsukake, Kentaro, Noritaka Usami, Toru Ujihara, Kozo Fujiwara, Gen Sazaki, and Kazuo Nakajima (2004). « On the origin of strain fluctuation in strained-Si grown on SiGe-on-insulator and SiGe virtual substrates. » In: *Applied Physics Letters* 85.8, pp. 1335–1337. DOI: 10.1063/1.1784036 (cit. on p. 96).

Kishinû, Seigo, Masahiko Ogirima, and Kazuhiro Kurata (1972). « A Cross - Hatch Pattern in $GaAs_{1-x}$ P_x Epitaxially Grown on GaAs Substrate. » en. In: *Journal of*

The Electrochemical Society 119.5, pp. 617–622. DOI: 10.1149/1.2404273 (cit. on pp. 96, 97).

Hsu, J. W. P., E. A. Fitzgerald, Y. H. Xie, P. J. Silverman, and M. J. Cardillo (1992). « Surface morphology of related Ge_xSi_{1-x} films. » In: *Applied Physics Letters* 61.11, pp. 1293–1295. DOI: 10.1063/1.107569 (cit. on p. 96).

Zoellner, Marvin H. et al. (2015). « Imaging Structure and Composition Homogeneity of 300 mm SiGe Virtual Substrates for Advanced CMOS Applications by Scanning X-ray Diffraction Microscopy. » In: *ACS Applied Materials & Interfaces* 7.17. PMID: 25871429, pp. 9031–9037. DOI: 10.1021/am508968b. eprint: https://doi.org/10.1021/am508968b (cit. on p. 96).

Richard, Marie-Ingrid, Marvin H. Zoellner, Gilbert A. Chahine, Peter Zaumseil, Giovanni Capellini, Maik Häberlen, Peter Storck, Tobias U. Schüli, and Thomas Schroeder (2015). « Structural Mapping of Functional Ge Layers Grown on Graded SiGe Buffers for sub-10 nm CMOS Applications Using Advanced X-ray Nanodiffraction. » In: *ACS Applied Materials & Interfaces* 7.48. PMID: 26541318, pp. 26696–26700. DOI: 10.1021/acsami.5b08645. eprint: https://doi.org/10.1021/acsami.5b08645 (cit. on p. 96).

Gourhant, Olivier et al. (2014). « Ge Condensation Using Rapid Thermal Oxidation for SGOI Substrate Preparation. » en. In: *ECS Transactions* 64.6, pp. 469–478. DOI: 10.1149/06406.0469ecst (cit. on p. 97).

Vincent, B., J.-F. Damlencourt, P. Rivallin, E. Nolot, C. Licitra, Y. Morand, and L. Clavelier (2007). « Fabrication of SiGe-on-insulator substrates by a condensation technique: an experimental and modelling study. » en. In: *Semiconductor Science and Technology* 22.3, pp. 237–244. DOI: 10.1088/0268-1242/22/3/011 (cit. on p. 97).

Glowacki, F. et al. (2014). « Ultrathin (5nm) SiGe-On-Insulator with high compressive strain : From fabrication (Ge enrichment process) to in-depth characterizations. » In: *Solid-State Electronics*. Selected papers from EuroSOI 2013 97, pp. 82–87. DOI: 10.1016/j.sse.2014.04.026 (cit. on p. 97).

Morin, Pierre Francois et al. (2015). « Mechanical Analyses of Extended and Localized UTBB Stressors Formed with Ge Enrichment Techniques. » en. In: *ECS Transactions* 66.4, pp. 57–65. DOI: 10.1149/06604.0057ecst (cit. on p. 97).

Boureau, Victor, Shay Reboh, Daniel Benoit, Martin Hÿtch, and Alain Claverie (2019). « Strain evolution of SiGe-on-insulator obtained by the Ge-condensation technique. » In: *APL Materials* 7.4, p. 041120. DOI: 10.1063/1.5088441 (cit. on p. 133).

5

BRAGG COHERENT DIFFRACTION IMAGING, APPLICATION ON EMBEDDED GRAINS IN ZIRCONIA USING DIFFRACTION CONTRAST TOMOGRAPHY

This chapter provides a description of an experiment aiming to combine Diffraction Contrast Tomography and Bragg Coherent Diffraction Imaging on Zirconia embedded grains.

After stressing the gain of the combination of both technique applied to the described sample, Diffraction Contrast Tomography, a non-coherent imaging technique that allows for indexing sample volumes of several micrometers, containing hundreds up to a few thousand grains and gives access to their crystallographic orientation, position, and average elastic strain tensor, is explained and the experimental conditions detailed.

Then, a focus is made on the Bragg Coherent Diffraction Imaging experiment, with a review of the experimental setup and the essential beam characterization. Results of the phase retrieval procedure are presented, together with statistical information on average strain.

Finally, the question of the strain precision of Bragg Coherent Diffraction Imaging dataset is tackled, with the introduction of a new tool to assess the strain precision.

5.1 INTRODUCTION

5.1.1 *A matter of scale*

Residual stresses and strains resulting from differences and anisotropy of thermal expansion coefficients have a large impact on the mechanical properties of ceramic materials, affecting their ultimate strength and fatigue properties. However, although the macroscopic and microscopic relationship between stress and strain has long been studied, the study of strain fields at the micrometer grain level with nanoscale strain resolution is still being developed. By combining 3D location of embedded grains in a polycrystalline sample volume trough a non-coherent imaging technique known as Diffraction Contrast Tomography (DCT) with Bragg Coherent Diffraction Imaging (BCDI), the complete determination of the 3D strain tensor in a single grain can be achieved.

During the last 15 years, several techniques have been developed for grain and strain mapping: polycrystal indexing routines used in 3D X-ray Diffraction, also called Diffraction Contrast Tomography (3DXRD/DCT), allow indexing sample volumes containing hundreds up to a few thousand grains and give access to their crystallographic orientation, position and average elastic strain tensor. Reischig et al., 2013; Lyckegaard et al., 2011 On the other hand, BCDI allows recovering the 3D strain in an isolated grain with spatial resolution down to 20 nm but the technique has proved its worth mainly on isolated objects of size smaller than the beamRobinson et al., 2001, while recent improvements in Bragg Ptychography paved the way for extended objects, such as grains/domains at a sample surfaceMastropietro et al., 2017.

The ability to link information concerning the 3D grain neighborhood (position, orientation and average strain tensor of all grains from 3DXRD) and the elastic strain distribution inside a (subset of selected) grain(s) can be considered a prerequisite for future investigations on the complex interplay of local texture and residual strain on processes like phase transformations and nucleation of damage in this important class of functional materials.

5.1.2 *Sample details*

Ceramics are solid materials comprising an inorganic compound of metal, nonmetal or metalloid atoms primarily held in ionic and covalent bonds. Residual micro-stresses are generally very high in ceramics, as their Young's modulus is larger than that of metals and because they can hardly accommodate thermal expansion mismatches between grains by plasticity. Therefore, residual stresses play a pivotal role on ceramics mechanical behavior, especially their fracture and their long-term behavior. It has been shown in some Zirconia ceramics that they can reach about 1 GPa Gremillard et al., 2000 around triple junctions between grains. In the particular case of Zirconia, they can also trigger the tetragonal to monoclinic phase transformation Deville et al., 2006 and are even more crucial than applied external stress fields. Thus, a detailed 3D knowledge of strain at the grain level would prove highly useful.

The project of combining DCT and BCDI on embedded ceramic grains was conducted in collaboration between Dr. Wolfgang Ludwig (INSA Lyon/ESRF), visiting scientist at the ID11 ESRF beamline, Dr. Jerome Chevalier (INSA Lyon) and Dr. Vincent Favre-Nicolin (ESRF).

A cylindrical sample with 10 µm diameter and 80 µm height has been FIB machined from Yttrium stabilized Zirconia ($YZrO_2$, 8% of Yttrium). The grain size in the material ranges from 500 nm to 5 µm and the miniature sample has then been

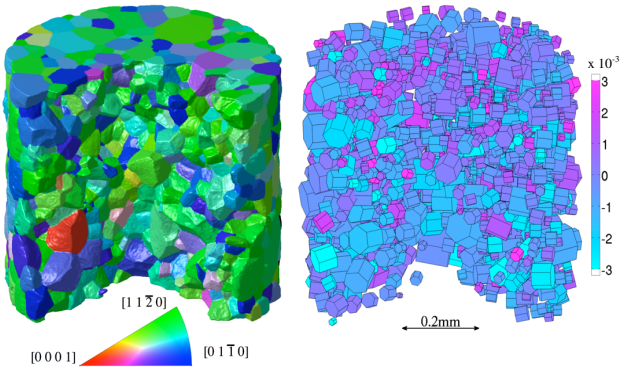

Figure 5.1 – From Reischig et al., 2013. Example of 3D grain map in a large grained (50-100 µm) sample of Ti alloy. The sample exhibits a strong texture and is loaded in compression. The 3D grain map is colored according to the orientations in the inverse pole figure (left). The same grain locations, orientations and sizes are represented by heaxagonal unit cells and colour coded according to the normal strain along the rotation axis and loading direction (right). Applied to small-grained ceramic materials, it is not be possible to resolve 3D grain shapes. Nevertheless, the center of mass, orientation and average elastic strain information is still accessible and can be compiled into schematic 3D sample representations as shown in this figure.

mounted on a thin steel pin (200 µm diameter) such that it could be positioned at less than 1 mm distance from the scintillation screen of a high-resolution imaging detector.

5.2 DIFFRACTION CONTRAST TOMOGRAPHY

5.2.1 *Principle*

X-ray Diffraction Contrast Tomography (DCT) is part of the three-dimensional X-ray diffraction microscopy techniques allowing fast and non-destructive structural characterization of crystalline element, as grains or subgrains, of millimeter-sized polycrystalline specimens. By combining the principle of projections reconstruction (tomography) and X-ray diffraction imaging (topography), DCT provides high-resolution grain maps along with orientation and average elastic strain tensor of the individual grains with an accuracy of 10^{-4}.

First introduced as a variant of the 3D XRD methodology Poulsen, 2004, DCT aims to simultaneously reconstruct the absorption and crystalline orientation of a material. As described by Ludwig et al. Ludwig, Schmidt, et al., 2008, during acquisition of an optimized tomographic scan, undeformed grains embedded in the bulk of a polycrystalline sample give rise to distinct diffraction contrasts which can be observed in the transmitted beam each time a grain fulfills the Bragg diffraction condition. By extracting and sorting these contrasts into groups belonging to individual

grains, one is able to reconstruct the three-dimensional grain shapes by means of parallel beam, and algebraic reconstruction techniques (ARTs; Gordon et al., 1970).

The development of an innovative Friedel pair method for analyzing diffraction data Ludwig, Reischig, et al., 2009 enabled the indexing and reconstruction procedures to be solely based on the analysis of diffracted beams. The logic of the processing route can be summarized as demonstrated by Reischig et al Reischig et al., 2013: Friedel pairs are used as a basis for finding grain positions and orientation by indexing diffraction spots. The grains are then reconstructed individually in three dimensions and assembled to create a space-filling grain map under a mask found from the absorption reconstruction. The DCT processing route can be summarized with the following steps:

1. Preprocessing of the image stack
2. Segmentation of diffraction spots
3. Matching of Friedel pairs
4. Indexing of grains from Friedel pairs; alternatively fitting strain tensors
5. Selection of diffraction spots for grain reconstruction
6. Reconstruction of grain shapes
7. Assembly of the grain map

5.2.2 *Setup geometry*

As the needs for DCT are similar to those of standard synchrotron microtomography, any beamline dedicated to imaging and diffraction can be considered for the experiments. The sample lies on a rotation stage and is illuminated by a parallel monochromatic X-ray beam. The 1.6 µm pixel size high-resolution detector is located closely behind the sample and records the absorption contrast radiograph while the sample is being continuously rotated through 360° (with typically 0.05°angular increments) around an axis perpendicular to the incident beam. During this rotation, grains will find themselves in a Bragg diffraction condition and will cause part of the direct beam intensity to be diffracted and recorded on the detector.

Figure 5.2 depicts a scheme of the setup, and introduces the notion of Friedel pair of a specific grain. They are at the basis of the efficiency and the accuracy of the processing route. A specific crystal plane will find itself in diffraction condition a maximum four times during a full 360° rotation, which make up two pairs, each separated by a 180° rotation of the sample. As the two spots of a single Friedel pair define the optical path of the diffracted beam which must pass through the grain,

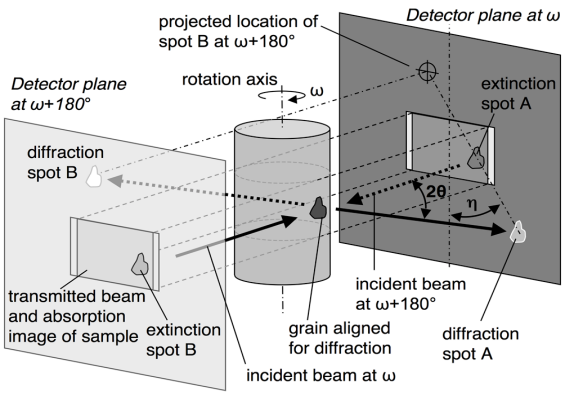

Figure 5.2 – From Ludwig, Reischig, et al., 2009. Schematic of the DCT setup, also representing a Friedel pair in the reference fixed to the sample: diffraction spot A appears at ω and its pair, spot B, is shown on the opposite imaginary detector plane at $\omega + 180°$. The diffraction path connecting both diffraction spots passes through the corresponding grain.

they allow for the retrieval of the diffraction angle related to the (hkl) and $\overline{(hkl)}$ lattice planes and lead to the knowledge of the associated scattering vector.

5.2.3 *Implementation on ID01 and results*

This setup has been used on the Zirconia cylinder in order to get a map of as many grains as possible, together with their individual orientation. On the ESRF ID01 beamline, the transfocator, made of one 2D Be lens of radius 500 µm located 56.4 m from the X-ray source, was used to focus the beam to 28 µm×48 µm. Then, a 20x objective was inserted in-between the sample and the high-resolution detector in order to perform phase-contrast tomography on the sample.

As a large rotation of the sample is needed to get a complete orientation matrix of as many grains as possible, the precision of the rotation stage was carefully examined. In order to create a precise lookup table for the φ-angle, we used the microscope's camera, looking at the sample stage from above. Firstly, we calibrated the microscope's camera images by translating a Si wedge sample by 100 µm in both in-plane directions with the Hexapod. The correct orientation of the camera images with the right scaling factor of the pixel size were retrieved from Scale-Invariant Feature Transform (SIFT) registration Lowe, 2004 between the translated images [1], represented in Figure 5.3.

Then, the studied sample, a Zirconia cylinder of 20 µm diameter, was used to monitor a ∼300° rotation around φ (around the vertical axis of the diffractometer)

1. The registration was performed using the dedicated toolkit of the SILX library VINCENT et al., 2019; al., n.d.

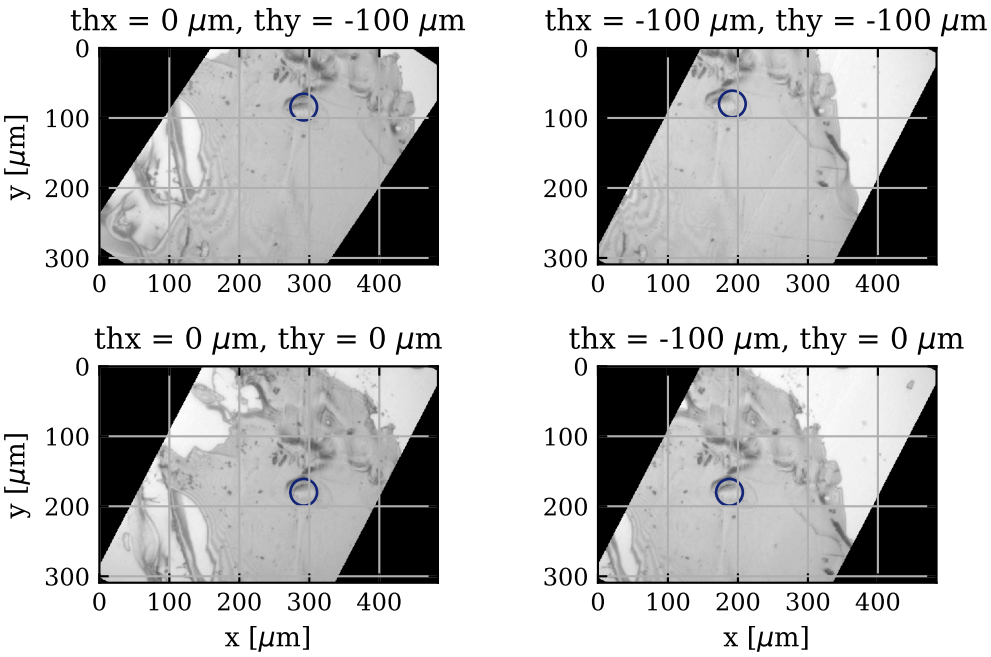

Figure 5.3 – Calibration of the microscope's camera images on a Si wedge sample. The Hexapod motors thx and thy were used to translate the sample by 100 µm in orthogonal directions. From SIFT registration Lowe, 2004, the micorscope was found to be titled with respect to the Hexapod in-plane orientation and the pixel size of the images were calibrated.

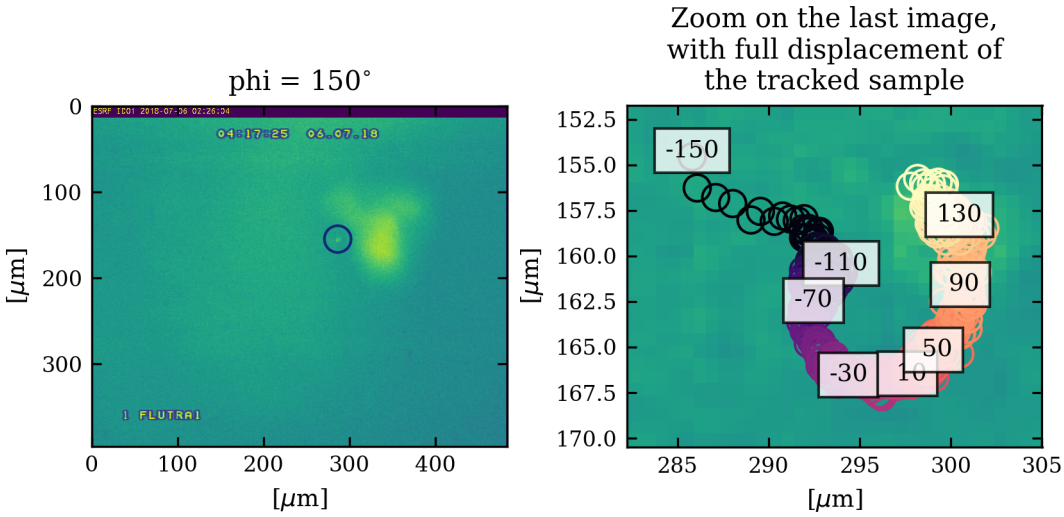

Figure 5.4 – Microscope's camera images of the sample stage while the φ-angle is rotated in order to create a lookup table. Note that only the tip of the cylinder is visible, as a single point on the left image, and as a few pixels on the right image. On the left hand side is represented the first image at $\varphi = -150°$ with a blue circle around the location of the ZrO_2 cylinder. The right hand side shows a zoom on the last image at $\varphi = 150°$. The scatter plot depicts the complete evolution of the position of the cylinder during the φ-scan.

with a 0.05° angular step. The microscope was focused on the tip of the Zirconia cylinder, and this position was tracked during the 6000 positions of the angular scan. Figure 5.4 shows the microscope's camera image of the sample at both start and end of the scan. As the tip of the cylinder is a few microns in diameter and the field of view of the microscope of few hundred micrometers, the sample appears as a single point in the first image. On the image recorded at the end of the ϕ-scan, a zoom into a 20 × 20 μm^2area is displayed, in which the motion of the tracked cylinder throughout the scan is represented. It results that the sample has moved during the scan because of the confusion circle of the diffractometer, preventing one from having the sample exactly aligned with the center of rotation.

A cleaner plot of the confusion circle around the φ-axis, from -150° to 150° is shown in Figure 5.5. The δx and δy offset values were used to correct the sample position during the experimental DCT scan.

From the DCT analysis, the orientation matrix information of a number of grains have been retrieved. This is detailed in table 5.1: the orientation of seven grains is given, with the detail of the Bragg reflection, the Bragg angle, the φ-angle of the sample, and the ν and δ angles of the detector. This table only displays part of the relevant information extracted from the DCT scan.

GRAIN	BRAGG REFLECTION	BRAGG ANGLE (°)	PHI (°)	NU (°)	DELTA (°)
#6	(111)	15.08	36.18	30.14	-0.9
	(200)	17.48	10.53	25.97	24.27
	(220)	25.14	68.79	45.6	24.01
#18	(111)	15.08	30.29	20.26	24.06
	(200)	17.48	109.37	28.39	23.03
	(220)	25.14	63.69	48.12	20.47
#22	(111)	15.07	69.59	30.44	1.09
	(200)	17.48	41.25	25.59	25.27
	(220)	25.13	44.42	50.56	0.07
#42	(111)	15.08	34.37	31.15	0.52
	(200)	17.48	2.04	28.0	23.51
	(220)	25.14	64.88	45.14	27.46
#51	(111)	15.08	77.08	22.93	21.63
	(200)	17.48	31.66	35.90	2.49
	(220)	25.14	43.59	35.76	39.33
#102	(111)	15.08	99.74	17.45	24.99
	(200)	17.48	10.53	25.97	24.27
	(220)	25.14	68.79	45.60	24.01
#141	(111)	15.08	18.38	31.06	2.90
	(200)	17.48	67.08	23.11	28.20
	(220)	25.14	63.94	51.09	5.43

Table 5.1 – DCT-indexed Zirconia grains, with different Bragg reflections along with the corresponding angular orientation. Phi is the in-plane angle of the sample, nu and delta are the in-plane and out-of-plane detector angles.

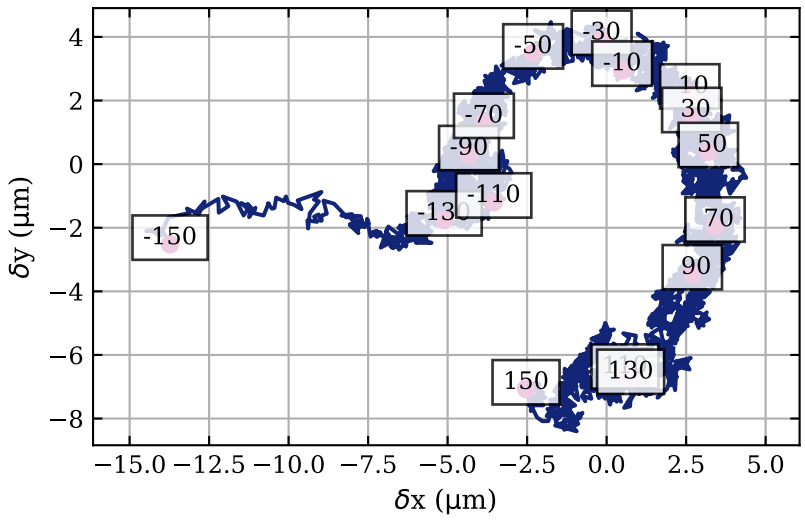

Figure 5.5 – Confusion circle of the diffractometer at the ID01 beamline, for its rotation around the vertical axis, from -150° to 150°. The white boxes indicate the φ angle. The displacements in the x- and y- axis were used as a look-up-table during DCT analysis to recenter the sample.

Then, we switched to a Bragg Coherent Diffraction Imaging setup, with the newly acquired ability to travel from one grain to another and reach any Bragg diffraction spot. This is detailed in the following section.

5.3 BRAGG COHERENT DIFFRACTION IMAGING

As CDI and its specificities in the Bragg geometry were presented in sections 3.7 and 3.8, Bragg Coherent Diffraction Imaging was conducted in order to retrieve the 3D strain map in a single grain. This part describes the setup used at ID01, the way we carried the second part of the experiment, how we handle the analysis and the hurdles we encountered.

Thanks to the previous DCT, we were able to orient the sample and the detector to specific angles and immediately reach a Bragg peak associated with one embedded gain of the ZrO_2 volume, and then assess its visibility and its eligibility for a full rocking curve scan.

5.3.1 *Experimental setup and probe measurements*

The general layout of ID01 is described in section 3.9. We used a Maxipix detector Ponchut et al., 2011, mounted at 1.2 m and a Fresnel Zone Plate to focus a 7.938 keV beam. As depicted in Figure 5.6, the diffractometer stage enabled rotation of the

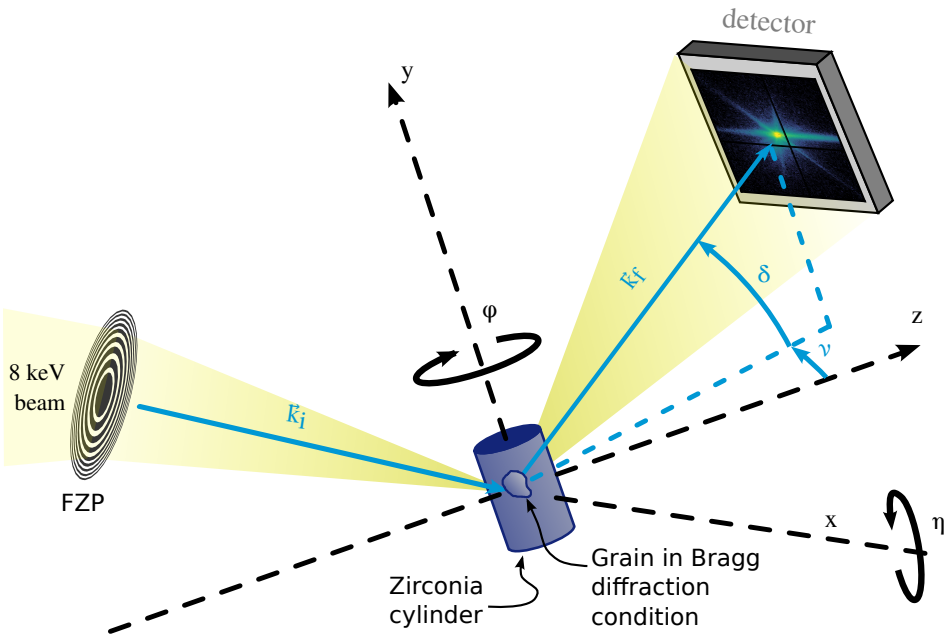

Figure 5.6 – Scheme of the experimental setup for BCDI on a Zirconia cylinder. The three main components of the experiment are present, namely the Fresnel Zone plate focusing the beam onto a Zirconia cylinder of 80 micrometers in height, containing a grain in Bragg condition which scatters light onto a Maxipix detector located about 1.2 m away from the sample. During the experiment, in order to avoid any gravity-related drifts, the η-angle was kept to zero, and the φ-angle rotation was used to perform angular scans while the detector ν and δ-angles were used to orient the selected Bragg reflection from a grain in diffraction condition.

sample in the vertical diffraction plane (η-angle rotation) and horizontal diffraction plane (φ-angle rotation), while the detector arm's rotations δ and ν allow to reach a particular reciprocal space area.

5.3.1.1 *Ptychography for beam characterization*

Prior to moving to Bragg geometry, the tip of the Zirconia cylinder was used as a reference object to characterize the beam in forward scattering, $\delta = \nu = 0$. By performing spiral scan in the plane normal to the beam propagation, the complex wavefront of the beam could be retrieved using ptychographic algorithms implemented in the PyNX library Favre-Nicolin, 2019; Mandula et al., 2016. Available as a python script already parametrized to match the ID01 geometrical parameters, forward ptychography with PyNX leads to quick and robust results.

The key aspect of the beam calibration was to find the right combination of Fresnel Zone Plate (FZP) coherent slits sizes and defocus distance in order to make the beam size fit with the grain size. Starting with "coherent slits" of 200 $\times$ 60 μm^2 (VxH) placed right before the FZP, we performed spiral scans on the sample while varying its location along the beam propagation. Defocusing enables increasing the beam

size, but it also allow retrieving the radius of curvature of the beam wavefront hence the possibility to find the focus position, where the beam size is minimal.

As an example, Figure 5.7 shows the reconstruction of both the 2D object and the probe, obtained with a sequence of 40 iterations of Difference Map, followed by setting the probe as the multi-modal object to update, followed by 200 iterations of Difference Map and 100 iterations of Maximum Likelihood (see 6.2.2 and 3.7.5.4). It is important to stress out that only a few iterations are needed with update performed only on the sample in order to get a first good estimate. Then, both the sample and the probe are being updated at each iteration, with the particularity that the probe is considered as a multi-modal array. The following line gives an example of the use of the PyNX script to perform this kind of rectonstruction:

$$\begin{gathered} pynx - id01pty.py\, specfile = siemens.spec\, scan = 57\, detectordistance = 1.3 \\ ptychomotors = pix, piz, -x, y\, probe = 60e-6x200e-6, 0.09 \\ algorithm = analysis, ML**100, DM**200, nbprobe = 3, probe = 1, DM**40 \\ loadmask = maxipix\, verbose = 10\, save = all\, saveplot\, liveplot \end{gathered} \tag{5.1}$$

In the command-line, one has to set an initial probe, that is in 5.1 implemented as a focused wavefront from given slits size of 200 $\times$ 60 μm^2 (V$\times$H) at a focal distance of 9 cm. The key chain after "algorithm =" sets the algorithm sequence for the optimization, from right to left. By setting probe = 1, the probe gets updated and nbprobe = 3 adds two mode to the initial probe. On Figure 5.7, the shape of the cylinder is clearly visible and consistent with its expected shape. The beam displayed on the right hand side is the probe retrieved at the object position, *i .e.*, approximately 1800 µm away from the focus position.

Note that in order to confirm our probe's reconstruction from the tip of the Zirconia cylinder, we also performed the same kind of ptychographic scan on a reference object, a Siemens star Pfeiffer, 2018 with a very fine structure. Figure 5.8 shows both the reference object and probe reconstructions using ptychography for slits of 30 $\times$ 30 μm^2, performed at the focus position.

All in all, the beam was retrieved from several combinations of coherent slits size and defocus distances, and a selection is presented in Figure 5.9. One can note that the FWHM extracted from the peak intensity of each retrieved wavefront is given, with a maximum of 567 $\times$ 500 nm^2 (VxH) obtained from a focused beam with slits closed down to 30 $\times$ 30 μm^2 (VxH). This will be the configuration used to perform BCDI angular scans on the embedded grains. Indeed, large grain size requires the largest illumination. It is interesting to note that this retrieved beam (bottom right subplot of Figure 5.9) exhibits some variation with respect to the one retrieved from ptychography on a Siemens star with the same configuration (Figure 5.8). This is

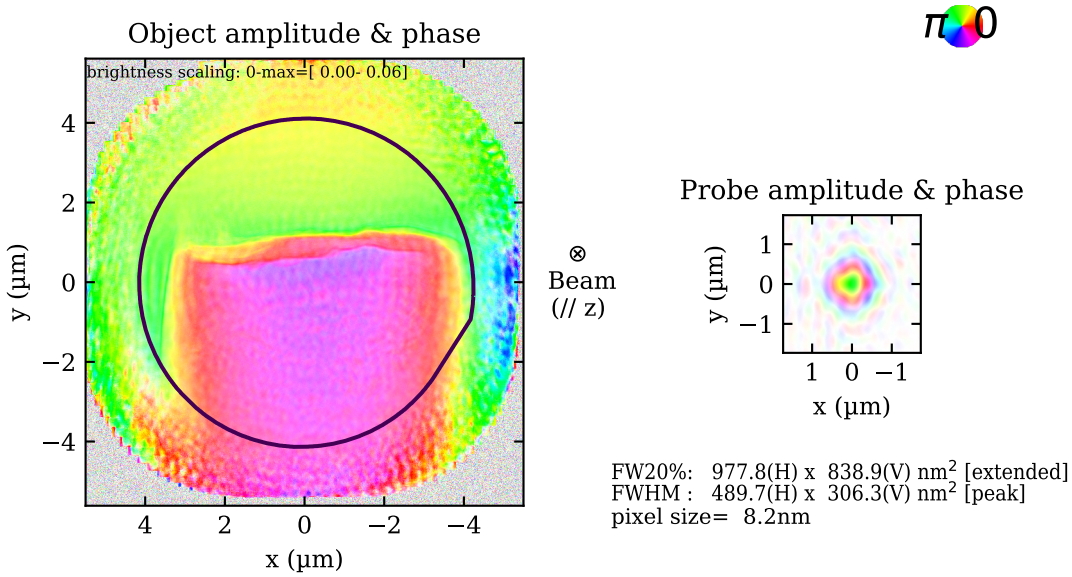

Figure 5.7 – Reconstructions of object (2D cut of a Zirconia cylinder) and probe at sample position, from a forward ptychographic scan. The coherent slits before the FZP focusing optics are opened at $60 \times 60\ \mu m^2$ and the cylinder was moved 1800 µm away from the known focal position. The forward ptychography analysis was performed with the PyNX python library. The spiral scan performed on the plane perpendicular to the beam propagation is made of 513 frames and the reconstructed pixel size is 8.2 nm. The area covered by the spiral scan is described by the black circle. The spatial scale for both subplots are identical, and they use the same colorbar, described by the HSV colorwheel on the top right. Therefore, brightness represents the amplitude and colour the phase of the image. Once the complex wavefront of the probe is retrieved, it can be back-propagated up to the FZP focus position, where it shape is of $219 \times 273\ nm^2$ (FWHM). On the figure, both the width at 20% of the maximum intensity (FW20%) and the width at half of the maximum intensity (FWHM) are given for the beam wavefront at the sample position.

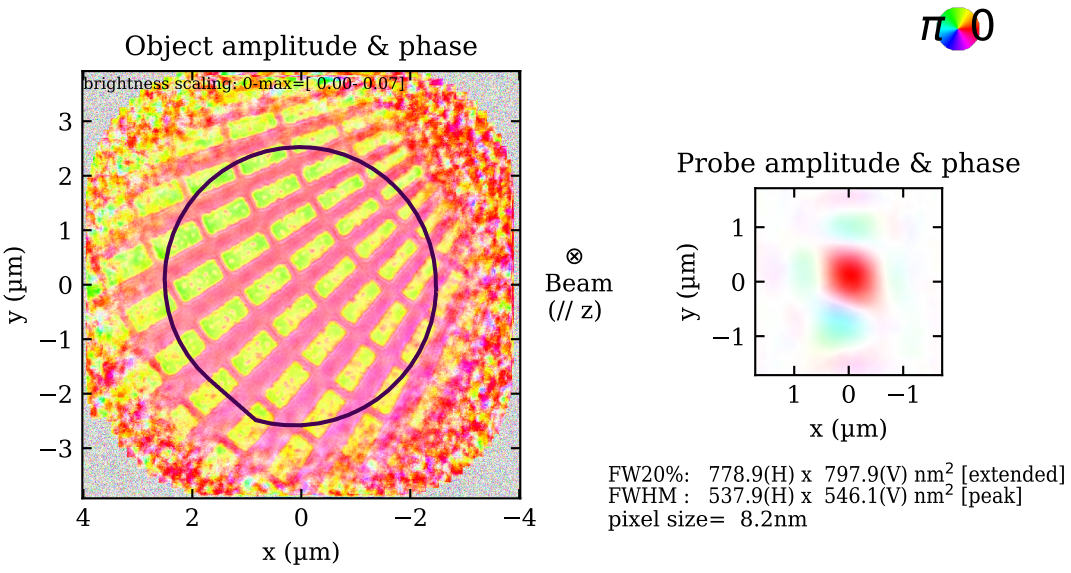

Figure 5.8 – Reconstruction of the probe used to illuminate the ZrO2 grain, from ptychographic reconstruction of a reference Siemens Star pattern. The spatial scales are the same for both plots. (Left) Siemens star reconstruction, (right) probe reconstruction. The black circle on the object depicts the limits of the area covered by the spiral scan performed on the sample. The pixel size is 8.2 nm on both reconstructions.

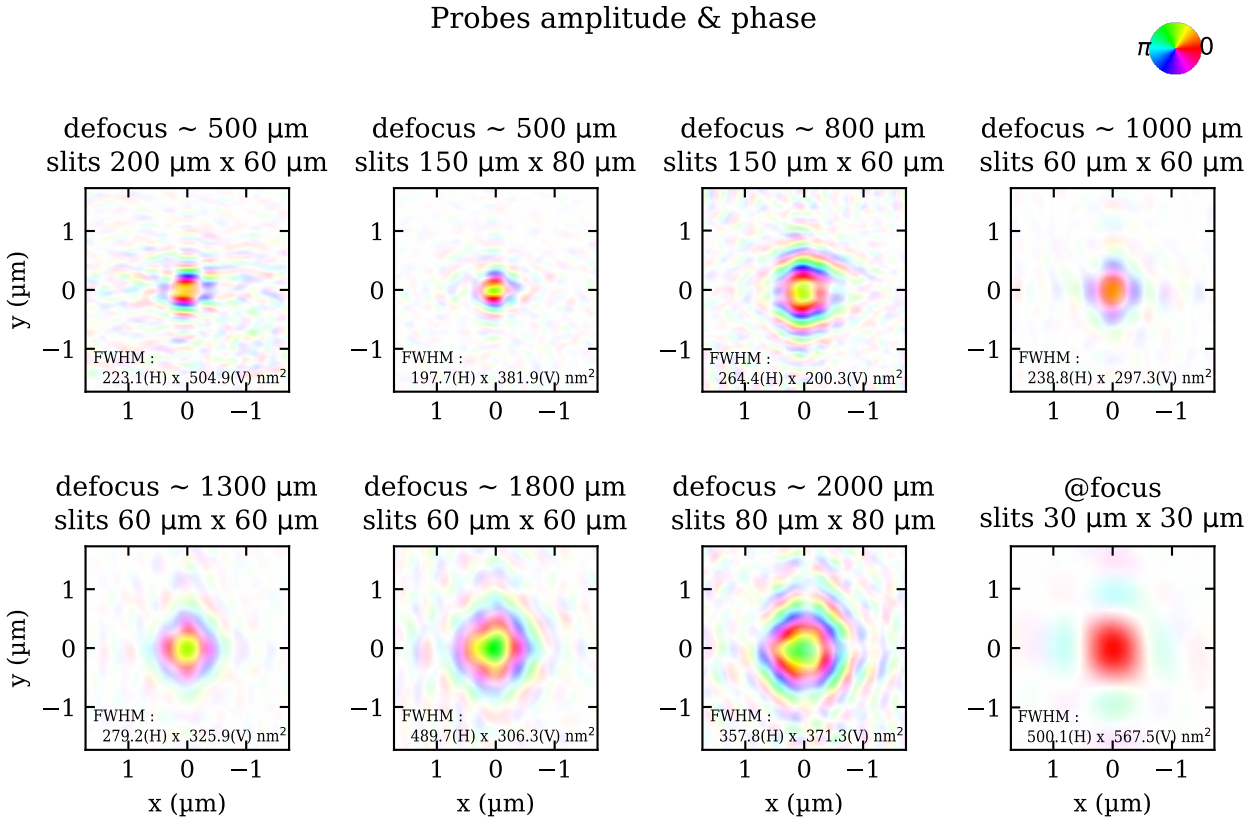

Figure 5.9 – Effect on the optical configuration (coherent slits size, defocus distance) on the beam wavefront. Reducing the slits size as well as increasing the defocus distance of the sample enable to increase the beam FWHM. This is demonstrated through several beam reconstructions. All the probe wavefronts have been retrieved from ptychographic scans performed on either the tip of the ZrO_2 sample or a reference Siemens star (the strength of Ptychography being to retrieve both the object and the probe, the only difference between these two kinds of scan is that the reconstructions from the Siemens star should in principle be slightly better as this reference object introduces more diversity in the diffraction).

actually explained by the fact that the latter pytchographic scan has been performed with the presence of a transfocator lens (one 2D Be lens of 500 µm, 56.4 m away from the source): the effect is a slight defocusing, estimated to be of 800 µm from simulation achieved with the SRW package Chubar and Elleaume, 1998.

5.3.1.2 *Beam propagation*

As mentioned above, there is another interest for retrieving the probe from a defocus position, that is retrieving the radius of curvature of the beam's wavefront. Indeed, although the change in beam radius is often regarded as the actual end-function of a lens, its first action is to change the curvature of the transmitted wavefront: between the lens and the beam focus, the light converges because of the

wavefront curvature, whereas after the focus, the light diverges due to the wavefront being curved in the opposite direction. Measuring the beam out-of-focus allows one to retrieve the curvature, which can be seen from the phase gradient. Figure 5.10 shows two retrieved wavefront, one from a scan at a defocus position and the second from a scan at the focus. In the first row, the unwrapped phase of each wavefront is shown, and the second row presents horizontal profiles of both the amplitude and the unwrapped phase. The green vertical spans locate the "center" of the wavefront, from a FWHM estimation, and serve as a reference: within this vertical span, the unwrapped phase is parabolic on the left hand side and flat on the right hand side.

From this, a wavefront retrieved at a defocus position holds its curvature information and can be propagated in order to find the focus position, where the radius of curvature is null and the size of the wavefront (FWHM) is minimal. This is depicted in Figure 5.11, a beam from slits opened at 60 x 60 μm^2 has been retrieved at a defocus position of approximately 1800 µm upstream and then propagated over a 2 mm range. The left hand side of Figure 5.11 represents the caustics both in horizontal and vertical direction, with the marker of the focus position, while the right hand side depicts the evolution along the propagation range of either the FWHM at 20% of the peak intensity or the statistical FWHM (evaluated from the standard deviation assuming Gaussian distribution of the probe FWHM $= 2\sqrt{2\ln(2)}\sigma \simeq 2.35\frac{\sqrt{\sum|P|^2}}{2\pi|P|^2_{max}}$). A clear minimum of the FWHM is obtained at a propagation of $z \simeq 1700$ µm. At this position, the FWHM of the beam is found to be of approximatively 220 x 272 nm^2 (HxV).

5.3.1.3 *Probe modes*

During the ptychographic reconstruction, the probe can be decomposed in an arbitrary number of coherent modes. Indeed, the only requirement is that the incoherent sum of the contribution of each of the multiple probe mode has to be compliant with the recorded diffraction data :

$$I_j(\vec{q}) = \sum_n \left| \int P_n(\vec{r}) O(\vec{r} + \vec{r}_j) e^{i\vec{q}\cdot\vec{r}} \mathrm{d}r \right|^2 \tag{5.2}$$

Where $O(\vec{r})$ is the diffracting object, $P_n(\vec{r})$ the multiple probe modes and $I_j(\vec{q})$ the recorded diffraction pattern at he j^{th} scanning position. Thibault and Menzel Thibault and Menzel, 2013 showed that the redundancy in a ptychographic dataset can be high enough in order to solve for this mixture of modes without additional *a priori* knowledge.

That way, the weight of the first mode conveys information about the coherent fraction of the beam. When the first mode represents 80% or more of the total

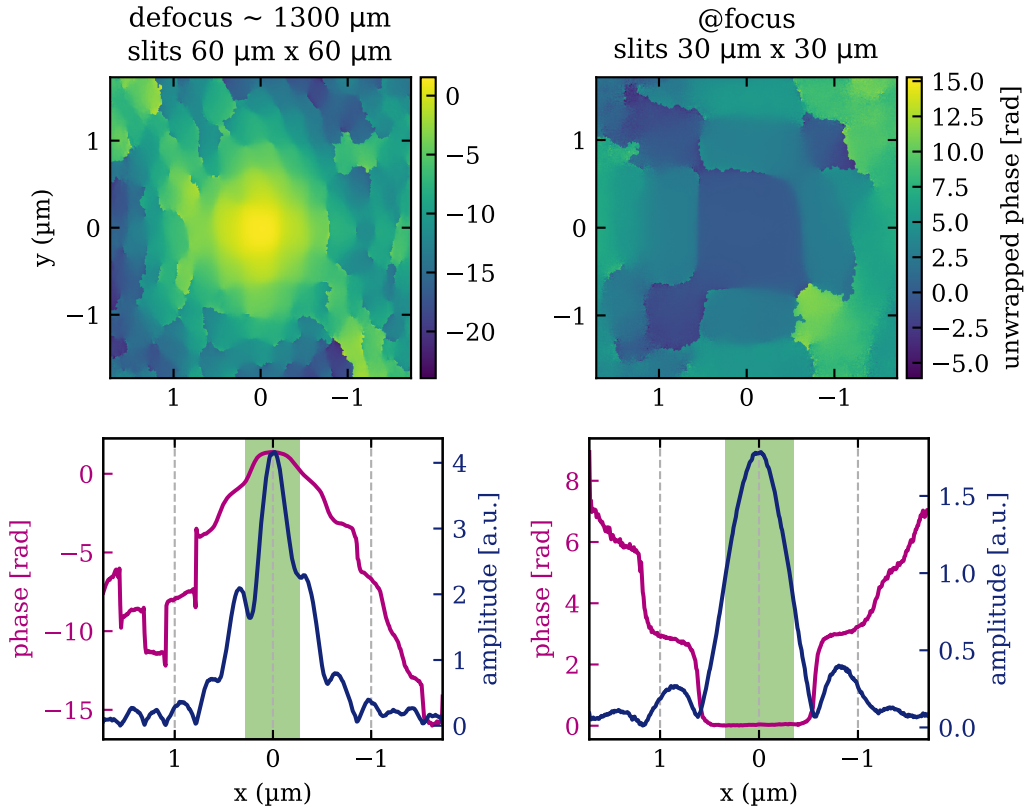

Figure 5.10 – Comparison between probe reconstructions obtained from object with defocus and at focus. The figure depicts both the (top row) unwrapped phase of the retrieved beam wavefront, with the same amplitude in phase, and (bottom row) horizontal profiles of phase and amplitude at $y = 0$. The green vertical spans on the bottom row are visual markers delimiting the FWHM of the Gaussian-like amplitude shape. On the left hand side, the wavefront has been retrieved at a defocused position and exhibits a parabolic phase within the intensity peak, whereas on the right hand side, the wavefront has been retrieved at the focus, and its corresponding unwrapped phase is flat within the peak intensity. This shows that the radius of curvature of the wavefront is retrieved when the ptychographic scan is performed at a defocus position.

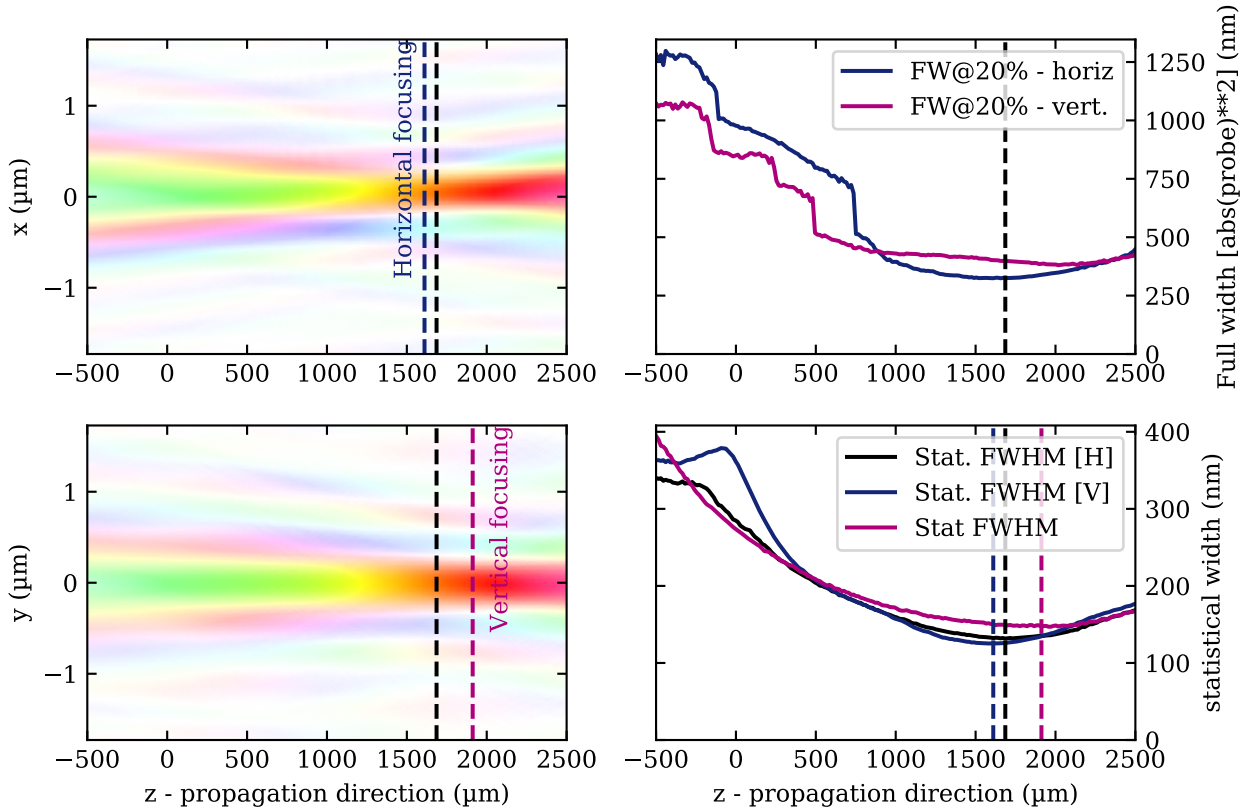

Figure 5.11 – On the left hand side, beam caustic retrieved from the ptychographic reconstruction, in each horizontal (top) and vertical (bottom) direction. On the right hand side, evolution of either the FWHM at 20% of the peak intensity (top) or the statistical FWHM, evaluated from a Gaussian approximation of the beam shape. The dashed lines indicate the focal plane position, at which the FWHM is minimum .

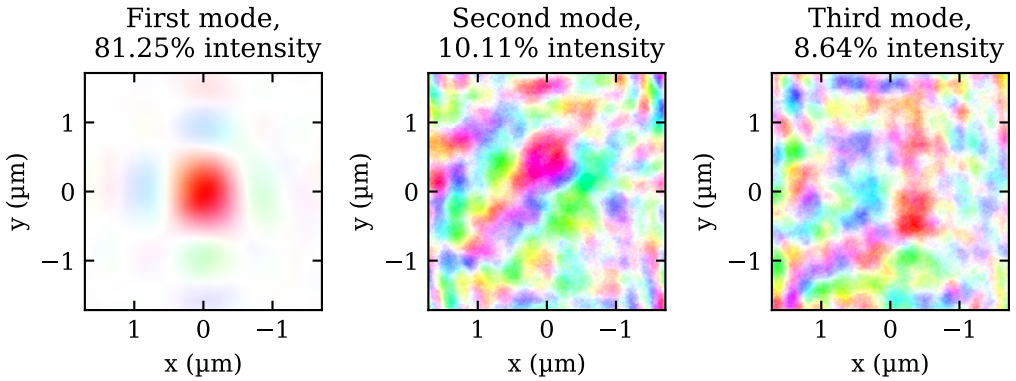

Figure 5.12 – Probe modes decomposition. The beam wavefront has been retrieved from a ptychographic scan on a Siemens star positioned in the focal plane, and decomposed in three coherent modes. Because the first mode accounts for more than 80% of the accumulated intensity, the probe is considered coherent and the FWHM of the central lobe in the two directions can be used as a good approximation of the transverse coherence lengths.

intensity of the beam, the first mode can be used as a good approximation of the beam and the latter is said to be coherent. As an example, Figure 5.12 shows three modes of the probe retrieved from a ptychographic performed in the focal plane. The first mode accounts for 81.25% of the total intensity of the beam, hence high enough to treat the probe as coherent.

Moreover, the probe decomposition into modes enables one to evaluate the transverse coherence lengths of such a coherent beam. In an ideal case, the beam is fully coherent and its first mode accounts for 100% of the intensity, hence the coherence length is then slightly smaller than the beam size. The main question is how to evaluate the beam size. A valid reasoning relies on the integrated intensity of the beam. On experimental retrieved probe of Figure 5.12, the secondary lobes of the first mode account for less than 5% of the total intensity of the beam, concentrated in the central lobe. Hence, the central lobe can be used as an accurate definition of the beam, and its size characterized by its FWHM. As a result, the FWHM of the central peak can be assimilated to the transverse coherence length of the beam.

5.3.2 *Embedded grain alignment and characterization*

After thorough characterization of the probe, the detector was oriented to reach one of the Bragg reflections from one of the indexed grains. Note that the cylinder was put at $\eta = 0°$, *i. e.* angular scans were performed on the φ-angle solely, in order to avoid any of the gravity-related drifts of the sample stage. The fast SXDM

GRAIN	BRAGG REFLECTION	BRAGG ANGLE (°)	PHI (°)	NU (°)	DELTA (°)
#42	(111)	15.08	34.37	31.15	0.52
	(111)	15.05	-78.13	21.09	23.37
	(200)	17.48	2.04	28.0	23.51
#141	(111)	15.08	18.38	31.06	2.90
	(111)	15.08	89.20	31.06	2.92
	(111)	15.08	-33.19	18.46	25.36
	(200)	17.48	67.08	23.11	28.20

Table 5.2 – The two DCT-indexed Zirconia grains, with different Bragg reflections along with the corresponding angular orientation, that have been measured for Bragg CDI. Phi is the in-plane angle of the sample, nu and delta are the in-plane and out-of-plane detector angles. For each reflection, the angular scan consisted in 462 angles with 2 seconds exposure and 0.0026° angular step.

method (see section 4.4.2) was then used to get its precise location over the cylinder, allowing us to align it with the beam and take a closer look at the diffraction pattern on the detector.

The intensity map of a quick scan of the cylinder is shown on the left part of Figure 5.13. A grain is clearly visible on the bottom part of the cylinder. Indeed, the intensity collected by the detector is higher when the beam shines on this grain, as the detector is located closely to the grain's Bragg reflection.

The scanning X-ray diffraction maps of three independent Bragg reflections, namely (111), $(11\bar{1})$ and (200), are represented on the right part of Figure 5.13. Note however that the contours obtained by this method are projections along the given reflections, not the actual shape, and give the maximal - potential - extent of the grain. Hence, it looks like the projection of the grain onto any axis should not exceed 3 µm. This length is already an indication that the beam size will be the limiting factor. As a comment, even if this grain was not the only one identified from the DCT analysis, the others were unfortunately not smaller and their diffraction pattern presented less visibility, leading us to discard them from further measurements. Indeed, we needed to focus on the grains giving rise to the more contrasted diffraction pattern as we knew that the BCDI phase retrieval process was already impinged on by the coherence conditions - beam smaller than the embedded grains. All in all, two grains have been measured thoroughly at multiple reflections that are described in table 5.2.

Once the grain was localized, the detector positioned at a Bragg reflection and the beam adjusted to a suitable size, rocking curves of horizontal scattering diffraction were recorded. By rocking the φ angle of the diffractometer with steps of 0.0026°

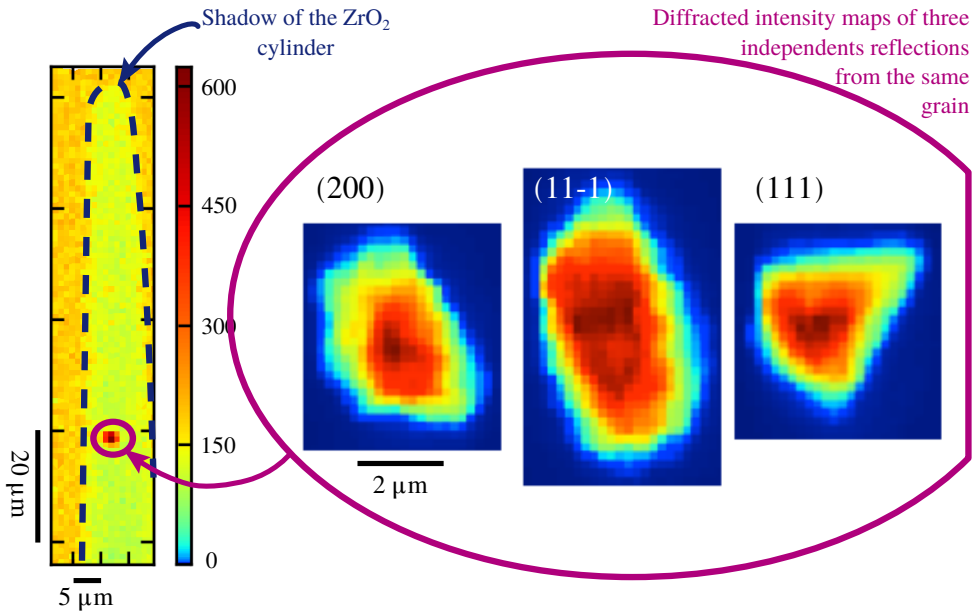

Figure 5.13 – SXDM for grain localization, and higher resolution SXDM on the grain at three different Bragg conditions. On the left hand side, the whole cylinder is visible, with the dotted blue line indicating its shadow. The purple circle signals the grain within the cylinder: as it is positioned in Bragg condition, its scattering recorded by the detector is more intense than from the rest of the sample. On the right hand side is displayed the high-resolution mapping of three independent reflections, namely (111), $(11\bar{1})$ and (200), of the detected grain. Note the scale bar of 2 µm, common to the three maps, given us insight about the projected size of the grain.

and $\Delta\varphi = 0.6^\circ$ around the maximum intensity of the Bragg reflection, we collected 462 frames, each of 2 seconds exposure, for the three independent reflections. Figure 5.14 depicts the sums of all frames for each probed reflection. The total intensity of any Bragg peak accounts for more than 1.5×10^8 photons.

As an example, Figure 5.15 shows a portion of the φ-angle scan from the (111) Bragg reflection in a semilog scale. The geometrical configuration described up to now enables us to know what is the maximal extent of the sample in order to respect the oversampling ratio of at least two (see section 3.7.2). Equation 3.47 relates the detector distance D to the maximal extent of the crystal l in the plane parallel to the one of the detector, hence we have :

$$l \leq \frac{D\lambda}{2p_{det}} = 1.7\,\mu\text{m} \tag{5.3}$$

Moreover, the oversampling requirement also impacts the angular step size $\delta\varphi$. Indeed, it can be derived geometrically, using small angle approximation ($\sin\left(\frac{\delta\varphi}{2}\right) \approx \frac{\delta\varphi}{2}$), that the maximum extent in the scanning direction is defined by :

$$l \leq \frac{1}{2d_{hkl}\delta\varphi} = 3.3\,\mu\text{m}, \tag{5.4}$$

for a $\{111\}$ Bragg reflection, given that $a = 0.5135\,\text{nm}$ is the lattice parameter of Zirconia. From these calculations, it appears that the data we collected are well oversampled for grain of size equivalent to the beam, at least in the plane parallel to the detector. In this plane, the transverse coherence components of the X-ray beam are comparable to the size of the first coherent mode (see Figure 5.12 and the associated subsection), hence the main central spot of the beam will be used as a support for phase retrieval.

Concerning the third dimension, one should now raise the question of the longitudinal coherence length of the X-ray beam. Indeed, the longitudinal coherence length of the X-ray beam at ID01 is of the order of 780 nm (see section 3.9), and depending on the Bragg reflection the optical path length difference (OPLD) between incident X-rays scattered from the extents of the crystal will change. When the OPLD is larger than the longitudinal coherence length, the sample is said to be under partial illumination, and the visibility of the interference fringes will drop, notably along $\vec{q}$ direction S. J. Leake et al., 2009. For a Bragg angle of θ =15.24° ((111) Bragg reflection of Zirconia), the maximum extent is equal to $\text{OPLD}_{\max}/2\sin\theta = 1.48$ µm. This value is smaller than any of the projected length of the grain as measured with SXDM, and hence will complicate the reconstruction process.

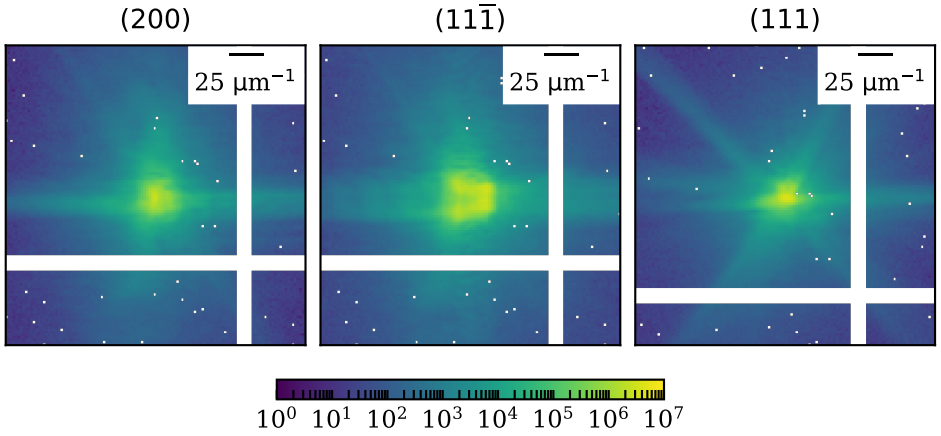

(a)

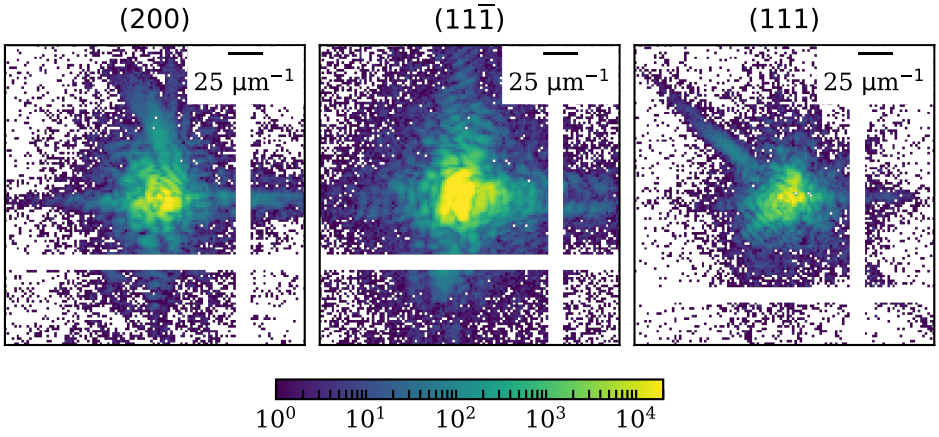

(b)

Figure 5.14 – Diffraction patterns from a unique grain, at different Bragg reflection, namely (111), (11$\bar{1}$) and (200). (a) The displayed intensity is taken from the sum of all 462 detector frames recorded during a rocking curve with a 2 seconds exposure and a 0.0026° angular step. Streaks are visible and are different from one reflection to another, indicating potentially some faceting of the grain. (b) Intensities at the maximum of each rocking curve, where fringes are clearly visible along certain streaks, a signature of the coherent interferences between the scattered X-ray from the grain at a given reflection. Note that for each row, the colorbar is the same for the three subplots, and the scale bar is given in reciprocal units (resolution in reciprocal space is $\frac{2\pi p_{det}}{\lambda D} = 1.8 \times 10^{-3}$Å$^{-1} = 0.18$ µm^{-1}).

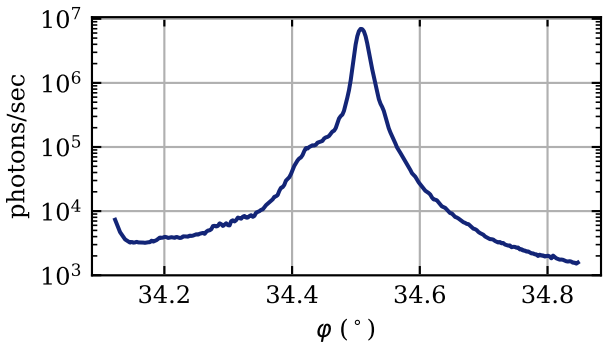

Figure 5.15 – Rocking curve from the (111) Bragg reflection of a given ZrO_2 grain, zoomed on a 0.6° portion, displaying the integrated intensity recorded on the detector.

5.3.3 *Phase retrieval process*

The phase retrieval procedure for this dataset was performed entirely using the open-source software library PyNX, using Graphical Processing Units, which also provides tools to easily compute scattering maps around a Bragg reflection Favre-Nicolin, Coraux, et al., 2011. PyNX lies at the heart of this work as it now also enables to perform fast Bragg Coherent Diffraction Imaging reconstruction algorithms, in 2D or 3D, for small-angle or Bragg diffraction data.

In order to start a phasing process, the first step is to set a support for the object. In the case of the grain presented in Figures 5.13 (direct space) and 5.14 (reciprocal space), we could estimate the real space projections onto the (111), (11$\bar{1}$) and (200) reflections to be at least 2 µm. However, the probe we used was characterized *via* forward ptychography on a reference Siemens Star object, and its FWHM is found to be around 500 x 500 nm^2, as depicted in Figure 5.8. Hence, the complete grain is very likely to be under partial illumination. For instance for a given Bragg reflection, Figure 5.16 shows the comparison between the shape obtained from the relative 0.1 threshold of the intensity auto-correlation and the beam size, in the detector plane. Nevertheless, as it was mentioned above (from the coherent modes probe decomposition, see section 5.3.1.3), the slits being small enough (30 x 30 µm^2) before the focusing optics and the retrieved probe wavefront being at its focus position, one can legitimately assume that the FWHM of the central lobe of the probe is equivalent to the coherence length in the two vertical and horizontal directions: it will thus be used as an initial support for the phase retrieval.

Then, the phase retrieval procedure consisted in performing 200 cycles of ER and 600 cycles of RAAR, and run this 1000 times from random initial phases to generate 1000 independent reconstructions. Obviously the number of cycles indicated are

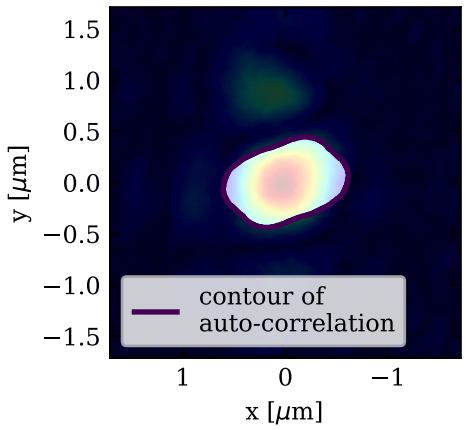

Figure 5.16 – Intensity auto-correlation from (200) Bragg reflection superimposed onto the beam profile. The beam appears in the background, while the auto-correlation is translucent. This depicts that the shape of the central lobe of the probe is comparable with the shape defined by the 10% threshold of the intensity auto-correlation, strengthening the use of the central lobe as an initial support for the phase retrieval.

the total number of iterations performed for each algorithm, but the actual chain of algorithms is described in 5.1. The algorithm are represented by operators (as introduced in section 3.7.4), as it is the most convenient way to use them in a readable script. During the complete process, the cycles were interrupted by updates of the support (operator SupportUpdate). In order to avoid any twinned solution, where two symmetrical solutions get superimposed, we used a temporarily halved support Guizar-Sicairos and Fienup, 2008 (operator DetwinRAAR). In addition, partial coherence refinement (see section 3.7.5.2, denoted as the EstimatePSF operator) is applied when the solution comes close to convergence. Finally, the chain is ended with some Error Reduction (operator ER) as it is the best converging method, as long as possible local minima have been avoided on the way.

In order to keep the object in a volume similar to the initial support, we enforce the following condition for the support update: the only pixels affected by the support update lie within ± 5 pixels around the outer border of the support, and this for each update so the support can slowly grow. For each independent reconstruction, the fixed relative threshold for the support update was randomly chosen in the interval $[0.2, 0.4]$. As a result, 1000 reconstructions were carried out from the same chain of algorithms, each starting with random phases, in order to collect the 50 reconstructions with the best metric. The choice of the metric will be discussed in 5.3.3.1.

In order to tackle the limitations of partial coherence, the principles described in section 3.7.5.2 are applied in PyNX. Let us remind that partial coherence correc-

Algorithm 5.1 Example of python code for BCDI reconstruction using PyNX operator-based API.

```
from pynx.cdi.cl_operator import ER, SupportUpdate, RAAR, DetwinRAAR,\
EstimatePSF, ShowCDI, ScaleObj
from pynx.cdi.cdi import CDI
# Load diffraction patterns, detector mask, wavelength..
# diffraction_pattern = np.load('file')...
# Set an initial support from auto-correlation of the object
tmp = np.abs(fftshift(fftn(diffraction_pattern.astype(np.complex64))))
thres = tmp.max() * 0.1
_support = (tmp > thres).astype(np.int8)

# Create a CDI python object
cdi = CDI(fftshift(diffraction_pattern), obj=None, support=fftshift(_support),
    mask=None,
          detector_distance=1,
          wavelength=wavelength,
          pixel_size_detector=55e-6)
# Initial scaling, required by mask
cdi = ScaleObj(method='F') * cdi

# Apply chains of algorithms to the CDI object
# Do 50 cycles of RAAR, followed by support update, repeated 3 times
cdi = (SupportUpdate(threshold_relative=0.25, force_shrink=False) * RAAR() **
    50) ** 3 * cdi

# Do 10 cycles of DetwinRAAR (ie RAAR with a temporary halved support)
cdi = DetwinRAAR() ** 10 * cdi

# Do 50 cycles of RAAR, followed by support update, repeated 5 times
cdi = (SupportUpdate(threshold_relative=0.25, force_shrink=False) * RAAR() **
    50) ** 5 * cdi

# Do 50 cycles of RAAR, followed by support update, then
# calculate partial coherence point-spread function
# with 100 cycles of Richardson-Lucy, repeat this 4 times
cdi = (EstimatePSF() ** 100 * SupportUpdate(threshold_relative=0.25,
    force_shrink=False) * RAAR() ** 50) ** 4 * cdi

# Do 50 cycles of ER, followed by support update, then
# calculate partial coherence point-spread function
# with 100 cycles of Richardson-Lucy, repeat this 3 times
cdi = (EstimatePSF() ** 100 * SupportUpdate(threshold_relative=0.25,
    force_shrink=False) * ER() ** 50) ** 3 * cdi

# Finish with 50 cycles of ER, followed by support update
cdi = SupportUpdate(threshold_relative=0.25, force_shrink=False) * ER() ** 50 *
     cdi
```

Listing 5.1 Example of python code for BCDI reconstruction using PyNX operator-based API.

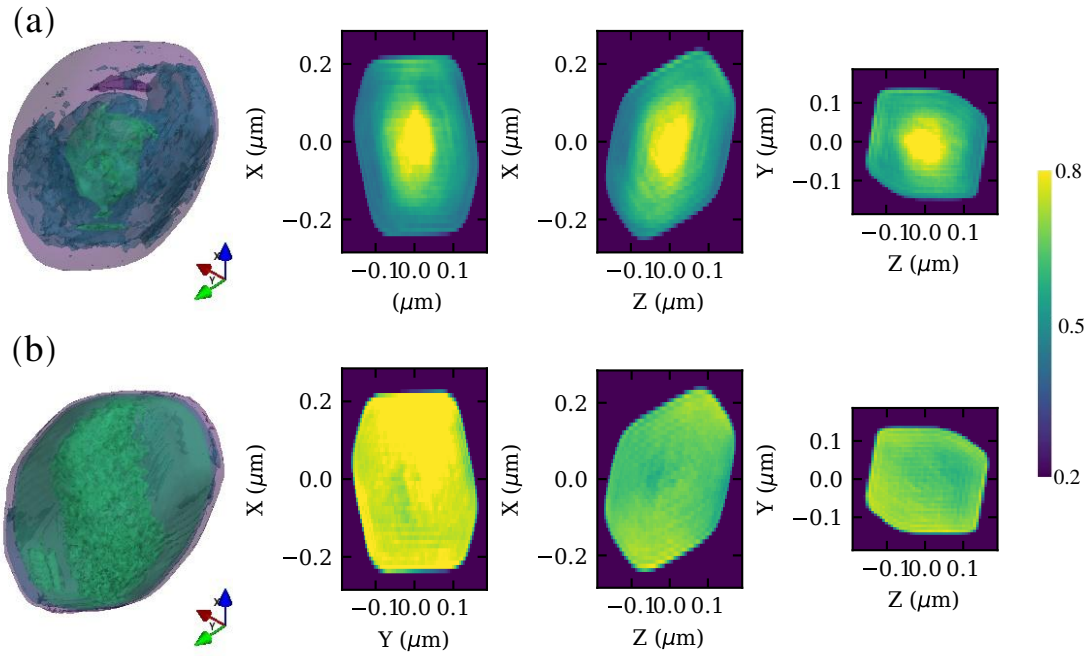

Figure 5.17 – Isosurfaces and cross-sections of a reconstructed gold nanocrystal with different considerations on coherence, from data collected at the 34-ID-C beamline, APS. On the left, transparent isosurfaces (20-60% of the maximum) of the reconstructed nanocrystal, and related cross-sections in the three laboratory frame orthogonal planes, taken from the center of the nanocrystal. (a) Images from the reconstruction assuming full coherence and (b) using the partially coherent modulus constraint.

tion relies on the introduction of a blurring kernel in a blind deconvolution step. To demonstrate the robustness of the partial coherence correction implemented in PyNX, Figure 5.17 shows a typical reconstructed image of a single gold nanocrystal, of few micrometers in size, from an angular scan performed in the Bragg geometry on 34-ID-C at the Advanced Photon Source in Chicago Energy Office of Science User Facility, n.d., comparing the amplitude without (a) and with (b) the accommodation of partial coherence.

5.3.3.1 *Free Log-Likelihood as an unbiased metric*

As discussed in section 3.7.5, several figures of merit for CDI analysis can be used. However, Favre-Nicolin *et al.* Favre-Nicolin, S. Leake, et al., 2019 proposed recently a new metric in order to evaluate the validity of solutions. Indeed, they showed that most figures of merit strongly rely on *a priori* knowledge of the object, and that some of them can even get worse while approaching a better solution (from a known sample). For instance, the Poisson Log-Likelihood (see section 3.7.5.4 for definition) gets worse when the support is tightened around the true solution.

To tackle this issue, they proposed to set aside a small percentage of diffraction data - the 'free' set - and refine the structure against the remaining set of diffraction data. Then the Poisson log-likelihood is evaluated by comparing the calculated diffraction data against the 'free' set, hence producing an unbiased figure of merit, LLK_{free}. This method was inspired from the jack-knifing approach, that was originally developed for unbiased statistical evaluation Quenouille, 1949; Efron and Stein, 1981. Note that this approach is even more appealing in the case of CDI, as the uncertainty in the support area can be large, contrary to refinement in crystallography that relies on a known atomic sequence or chemical formula.

The LLK_{free} metric has been implemented in the PyNX toolkit, in the following way. Firstly, approximately 5% of the observed diffraction dataset is set aside to constitute the 'free' set. In order to get ride of the correlations between neighbouring pixels that would create a strong relationship between the working set and the 'free' set, the latter is made of groups of islands of radius 3 pixels. Then, the 'free' pixels are randomly scattered around the dataset, with the only constraint that the area within 5% of the maximum radius, at the center of the diffraction pattern, must remain unaffected. Indeed, this area generally contains a large number of photons and needs to stay unmasked to generate a good initial estimate of the object. Finally, through the projection algorithms, during the application of the reciprocal space constraints, pixels belonging to the 'free' set are considered masked and keep their calculated complex value, with no update on the amplitude.

During the experiment, we followed the strategy of Favre-Nicolin *et al.* to focus on the Poisson Log-Likelihood LLK_{free} as the photon counting properties of the Maxipix detector theoretically make Poisson distribution the natural choice (see section 3.7.5.4 for comparison of Gaussian and Poisson distributions). Therefore, from the 1000 reconstructions performed, the 50 with the lowest Poisson LLK_{free} were kept, after subpixel alignment Guizar-Sicairos, Thurman, et al., 2008 and phase matching of the solutions. They had up to 778100 points in the support, *i. e.* 0.89% of the total volume generated from the number of pixels in the reciprocal space, and a LLK_{free} up to 0.156. However, note that the LLK_{free} is not an *absolute* figure of merit, hence its single value from one reconstruction does not indicate its validity, but it is the generation of a number high enough (typically 50-100) of reconstructions and their combination that make the metric robust. Here, 1000 reconstructions were used due to the low coherence of this experiment.

5.3.3.2 *Orthonormal mode decomposition*

The usual way to deal with a set of best solutions is to average them and then compare the average against the diffraction data, *e. g.* by plotting the Phase Retrieval Transfer Function (PRTF) Chapman et al., 2006; Shapiro et al., 2005; Chushkin et al.,

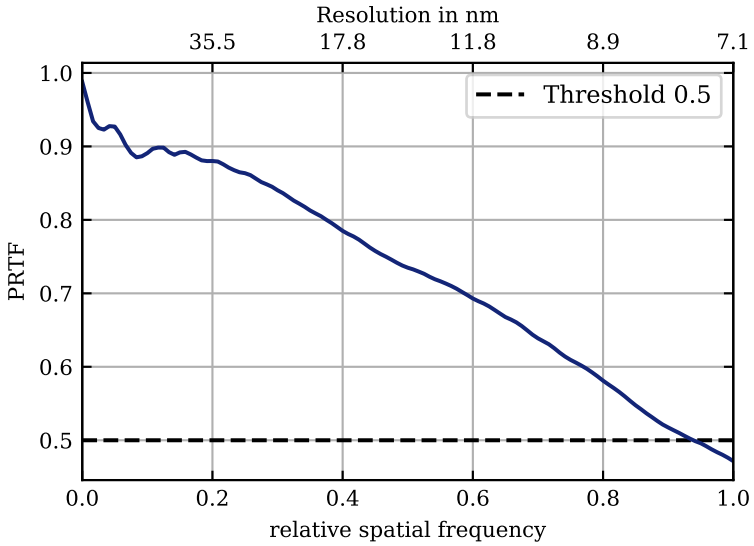

Figure 5.18 – Phase Retrieval Transfer Function of the reconstructed gold nanocrystal, using the partial coherence correction (blue line). The dotted horizontal line corresponds to PRTF = 0.5. From the intersection between the PRTF line and the dotted line, one can estimate the resolution to be around 7.6 nm.

2014. The PRTF is the ratio of the calculated amplitude to the measured amplitude as a function of the resolution ring, which is a fraction of the sampling frequency of the dataset. The relative frequency at which the PRTF is equal to 0.5, or to $1/e$, can be used as an estimate resolution of the reconstruction. Figure 5.18 shows the PRTF calculated for the gold nanocrystal reconstruction from Figure 5.17, with taking into account the partial coherence correction.

Another solution proposed in Favre-Nicolin, S. Leake, et al., 2019 is to compute eigenvectors for the selected best solutions, yielding a set of orthonormal eigen-solution. This method offers two advantages compared to averaging: firstly, the outlier solutions will only contribute to secondary modes of the eigenvector decomposition, and secondly, the overall squared amplitude of each eigen-solution yields a weight that can be used as a gauge of the correlation between solutions, with the ideal case being that the first - in terms of weight - eigen-solution be as close to 100% as possible.

5.3.4 *Results*

Reconstruction from most of the angular scans performed on different grains, different reflections were only partially successful. As well, scans were performed on three parts of a unique grain with the idea of stitching the results in order to get a full grain reconstruction, but unfortunately it was not possible to evaluate the

precision of the distance between the center of two scans, as no features between the reconstructions were easily identifiable.

However, the most intense mode from the reconstructions from one scan (#271, reflection (200)) looks consistent enough to be presented. The first mode of the orthonormal eigen-solutions represents 81.5% of the 50 solutions. The phase ramp of the final data is then removed by subtracting the mean value of the phase gradient along each direction. Indeed, a slight mis-centering of the diffraction dataset prior phase retrieval leads to a linear phase ramp. This comes from the basic properties of modulation of the FT that for any real number ξ_0, if $h(x) = e^{2\pi i x \xi_0} f(x)$, then $\mathcal{F}(h)(\xi) = \mathcal{F}(f)(\xi - \xi_0)$.

In order to get a first look on the solution, one can consider checking its shape in comparison to the one of the probe. Figure 5.19 gives this comparison by displaying a cross-section of the normalized amplitude of the reconstructed grain in the plane transverse to the beam's propagation. The cross-section of the solution (left hand side) is divided by the probe (right-hand side) and a semi translucent mask, taken from the central lobe of the probe, is superimposed on the solution for visualization purpose. That way, it is clear that the normalization by the probe tends to homogenize the reconstructed amplitude, consolidating the idea that the solution is actually a fraction of the total volume of the grain.

Figure 5.20 depicts the 3D representation of the final solution, both in the laboratory reference frame, and within a frame relative to the grain itself, with the Z-axis being aligned with the $\vec{q}$ Bragg vector. The volume is taken from a 50% threshold of the amplitude and mapped with the retrieved phase. On the facets of the cube axis are displayed 2D normalized amplitude cuts from the center of the grain, with white contours depicting the 50% threshold. From the laboratory frame, the probe's profile is quite recognizable (see Figure 5.8) on the (ZY) plane, and its secondary lobes also looks to appear on the (XY) and (XZ) planes, along the propagation direction. This suggests that the probe is indeed limiting the reconstruction and only the illuminated volume of the grain is potentially retrieved. From the grain frame, one has a better understanding of the displacement field along the $\vec{q}$ vector, as it is aligned with the Z axis.

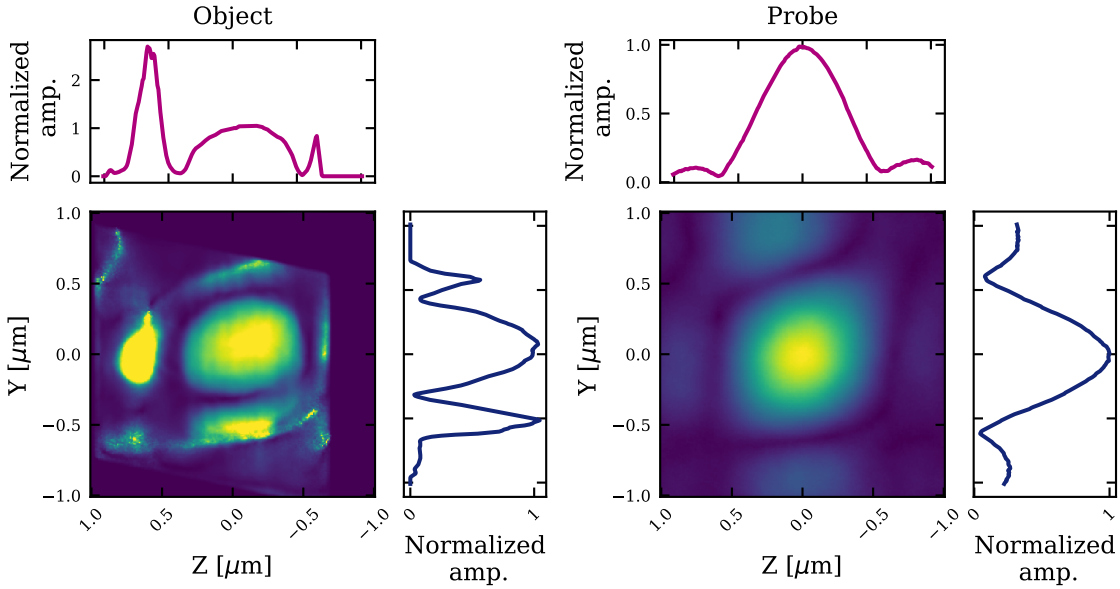

Figure 5.19 – Comparison of the first mode solution versus the probe, in the plane transverse to the beam propagation ((YZ) in the 3D figure 5.20). On the left hand side, the square subplot is a cut of the amplitude at the center of the grain, averaged over 10 pixels in the X-axis direction, and normalized by the probe. This probe being represented on the right-hand side square subplot. For both amplitude cuts, the 1D lines represent extracted profiles from the Y=0 (top, magenta) and Z=0 (right, dark blue). Note that the side lobes from the probe create artifacts in the normalized grain amplitude.

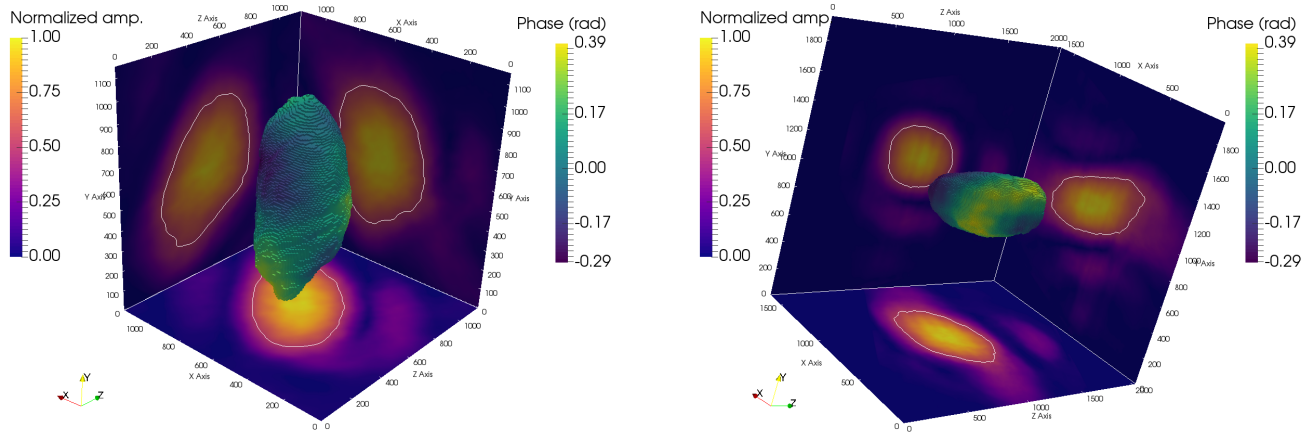

(a) Orthogonal Grain frame: $\vec{q}$ is aligned with the Z-axis

(b) Orthogonal laboratory frame: X downstream, Y vertical and Z inboard

Figure 5.20 – 3D reconstruction from the (200) Bragg reflection of a ZrO_2 grain, in the orthogonal frames of both (a) the grain and (b) the laboratory. The grain's frame is as $\vec{q}$ is along the Z-axis. Note the convention of the laboratory axes: X downstream, Y vertical and Z inboard. For both subplots the grain is represented by an isosurface of 50% of the amplitude's maximum, mapped with the phase. The displacement along the Bragg vector behaves as the phase, as they are both proportional. The projections depict the normalized amplitude of the reconstruction, taken from the center of the volume.

This gives a good confidence that the reconstructions are correct, even if the partial coherence introduces severe limitations on the resolution of the reconstruction.

In order to extract quantitative information from the reconstruction, the displacement field along $\vec{q}$ is calculated from the phase ϕ and the norm of $\vec{q}$:

$$u_{hkl} = \frac{\phi}{\|\vec{q}\|}, \tag{5.5}$$

with $\vec{q}$ being evaluated from the center of mass of the 3D diffraction pattern, taking into account the exact location of the "direct beam" onto the detector :

$$\vec{q} = \frac{2\pi}{\lambda} \begin{pmatrix} \cos(\delta')\cos(\nu') - 1 \\ \sin(\delta') \\ -\sin(\nu')\cos(\delta') \end{pmatrix}, \quad \text{with} \begin{cases} \delta' = & \delta - (y_{com} - y_0)/\text{pixperdeg} \\ \nu' = & \nu - (x_{com} - x_0)/\text{pixperdeg} \end{cases} \tag{5.6}$$

where δ' and ν' are the corrected angles of the diffraction pattern. They take into account the robot arm angles δ and ν, the "central pixel" position (x_0, y_0) of the "direct beam", *i. e.* the position of the center of mass of the beam onto the detector

while all the diffractometer & robot arm angles are set to zero, and the position of the center of mass of the diffraction pattern (x_{com}, y_{com}).

From the displacement field, the strain inside the grain can be evaluated by calculating the displacement gradient :

$$\epsilon_{hkl} = \partial_{hkl} u_{hkl} \tag{5.7}$$

The grain frame from Figure 5.20 provides an insight into how the projected displacement u_{200} (being directly proportional to the phase) behaves. Some corners are in tension while others in compression. However, the displacement remains extremely small, from $-d_{200}/20$ to $+d_{200}/20$ Å. Figure 5.21 shows cross-sections of the grain displacement and strain fields along the X-axis of the grain frame. Note that the contours are defined by setting a threshold on the amplitude of the reconstruction, equals to 35% of the maximum amplitude. The strain field appears to be close to the limits of sensitivity of BCDI, varying between -10^{-4} and 10^{-4}, with some modulations clearly visible, probable artifacts of the reconstruction. Thus, the solution holds little information about the inhomogeneous strain.

Furthermore, having collected full rocking curves from different grains allows to get an idea of the inter-grain mean deformation. From the knowledge of the direct beam, that gives us precise calibration of the detector positioning, the center of mass of each of the collected Bragg peak onto the detector can be transformed into an absolute value of the inter-planar distance of the lattice planes in Bragg condition. Relative to $a_{ZrO_2} = 5.135$ Å, the lattice parameter of Zirconia, the different measured grains present between -0.25% and +0.05% strain (extrapolated with respect to any of the probed Bragg reflections). Figure 5.22 shows the average strain measured on each grain, for each Bragg reflection. A trend is visible: the grains located at the bottom of the cylinder exhibit an averaged strain around -0.2% whereas the grain located at the top of the sample is almost unstrained, reaching some kind of relaxation. For more details, Table 5.3 gathers the strain collected on a given grain, from three distinct locations on this one grain. At each of the three Bragg reflection, the grain was illuminated at three distinct location by translating the beam of ± 500 nm along the direction transverse to the scattering plane. That way, the center of mass of the averaged diffraction pattern (along the angular scan) gives insight into the strain at each of the locations. As depicted in Table 5.3, the strain does not vary more than 0.23% within this grain, and even more particularly the strain along the (111) and (200) present negligible variations (below 0.05%). Overall, these results show that the small strain present at the bottom of the cylinder tends to vanish along the height of the sample, whereas within a grain the intrinsic strain variations are at a very low scale.

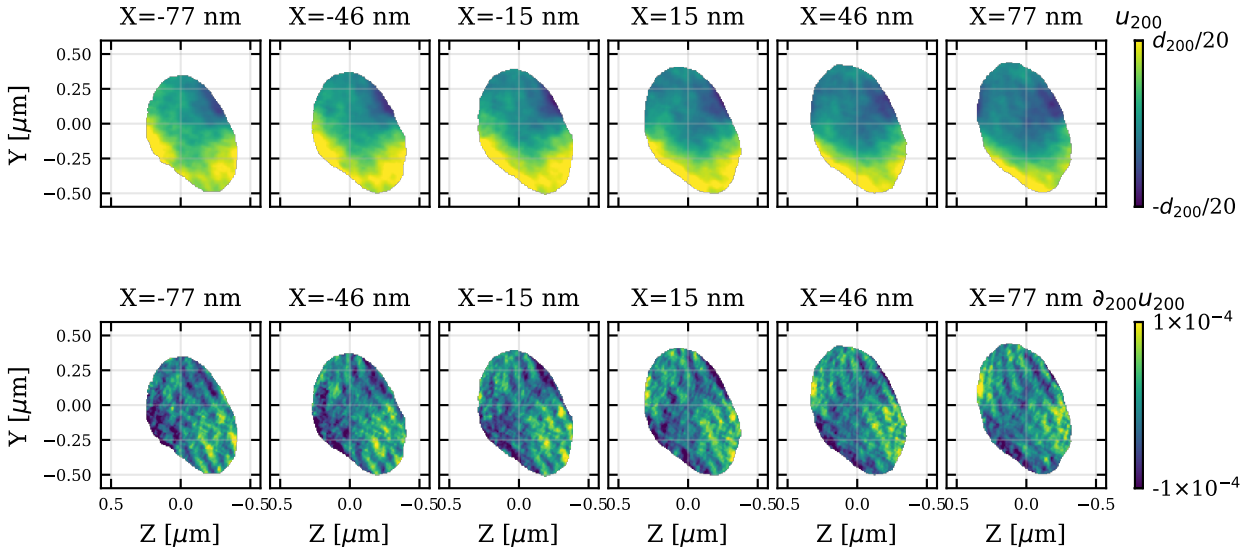

Figure 5.21 – Local displacement and strain fields at different cross-sections of a ZrO_2 grain along the X-axis (See Figure 5.20 for frame reference). The [200] direction is along the Z-axis. On the top row, the evolution of the u_{200} local displacement field for selected cross-sections. On the bottom row, the change in the $\partial_{200}u_{200}$ local strain field for the same cross-sections. Note that the strain is defined relative to the average lattice constant measured on this same Bragg reflection. The scale of the local displacement is within $-d_{200}/20$ to $+d_{200}/20$ i. e., between -0.013 and 0.013 Å and the scale of the strain is between -10^{-4} and 10^{-4}, showing the very small deformation inside the portion of the illuminated grain. However, it is worth pointing out that 10^{-4} is usually the limit of strain sensitivity for BCDI, hence these results have to considered with great care. Moreover, the fluctuations in the strain cross-sections are likely due to phase retrieval artifacts.

strain on a grain	along (111)	along (200)	along $(1\bar{1}1)$
Left-side	-0.256%	-0.205%	-0.185%
Center	-0.256%	-0.21%	-0.162%
Right-side	-0.256%	-0.21%	-0.168%

Table 5.3 – Average strain evaluated from the center of mass of the diffraction pattern at different Bragg reflection, from the same grain but at different location (by moving the beam for $\pm$500 nm along the direction transverse to the scattering plane).

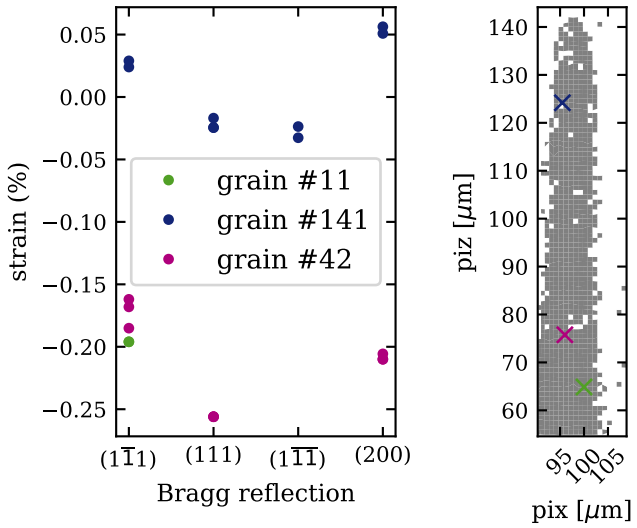

Figure 5.22 – Average strain measured on three different grains, from different Bragg reflections, with different probe position onto the grain (for grain #42 and #141, the beam has been translated by $\pm$500 nm from a central position, along the direction transverse to the scattering plane). Note that grain #42 and grain #141 are separated by approximately 50 µm in the vertical direction, while grain #11 is 10 µm below grain #42, as it is depicted by the right-hand side of the figure (the shadow of the cylinder is in gray, while the colored markers match the colors of the left-hand side plot).

5.3.5 *Discussion and outlook*

We used a combination of two X-ray imaging techniques that has never been tested before in order to observe strain fields at a nanometer scale in non-isolated grains, embedded in a polycrystalline sample volume. The non-coherent Diffraction Contrast Tomography technique was found to be easily implemented on a setup which would then require small changes to meet the requirements of Bragg Coherent Diffraction Imaging. These two techniques are quite mature, thanks to a decade of developments, so there is strong belief that they will be used again in more successful way. Indeed, even if the DCT was quite prolific in term of reliable orientation matrices for different grains, we did not succeed to find grain of satisfactory sizes (below 500 nm of diameter). Several probe sizes have been studied, by defocusing the sample and tweaking the coherent slits aperture, but the identified grains all remained partially illuminated, either because of transverse or longitudinal coherence lengths of the probe.

Longitudinal coherence length is a limit that could be overcome after the upgrade of the ESRF. With a 100 times more brilliant source, the efficiency of the monochromator will not be the first concern and the use of Diamond(400) could be taken into consideration. Experimental measurements Khounsary et al., 1993

have shown that the Darwin widths of Diamond(400) and Silicon(111) are similar (around 5 arcsec at 12.6 keV) but as the Bragg angle of Diamond(400) is a factor 3.6 larger than the one of Silicon (111), the energy resolution $\frac{\Delta E}{E} \propto \frac{\Delta\theta}{\theta}$ of such a monochromator would be improved by the same factor. Thus, the gain in the longitudinal coherence length $\frac{\lambda^2}{2\Delta\lambda}$ would also be increased. Moreover, not only the gain from the ESRF EBS upgrade will be a more parallel beam, but also coherent slits are, until the upgrade, limited by the divergence of the beam which prevents from opening them wider. Indeed, before the EBS upgrade, the electron beam within the storage ring presents a strong asymmetry with, for the low-β straight sections presenting a size of σ_e =114.4 × 8.24 µm^2 (FWHM, H × V) and a divergence of σ'_e =251.7 × 2.82 µrad^2 (FWHM, H × V). The undulator natural photon source size and divergence are given by Onuki and Elleaume, 2003:

$$\begin{aligned} \sigma_u &= \tfrac{2.74}{4\pi}(\lambda L)^{1/2} \approx \tfrac{1}{2\pi}(\lambda L)^{1/2} \\ \sigma'_u &= 0.69(\lambda/L)^{1/2} \approx (\lambda/2L)^{1/2} \end{aligned} \tag{5.8}$$

where λ is the emitted wavelength, $L = N\Lambda_u$ is the undulator length with Λ_u the magnetic period and N the number of magnetic periods. Then, the photon source size and divergence are approximately given by the convolution of the electron beam sizes and the undulator natural sizes. For the ID01 U35 undulator, this leads to photon source sizes (in µm) and divergences (in µrad) of:

$$\Sigma_{H,V} = \left[\sigma^2_{e(H,V)} + \sigma^2_u\right]^{1/2} = (114.4,\ 8.25), \quad \Sigma'_{H,V} = \left[\sigma'^2_{e(H,V)} + \sigma'^2_u\right]^{1/2} = (255.85,\ 45.97) \tag{5.9}$$

The EBS upgrade of the storage will impact the electron beam source size and divergence, leading to a change of the photon source size and divergence. The new values will be of (in µm and µrad):

$$\Sigma_{H,V} = (71.4,\ 8.5), \Sigma'_{H,V} = (47,\ 46) \tag{5.10}$$

Hence, a more symmetrical divergence of the photon beam. These are promising prospects for developing BCDI on a wider range of sample size.

5.4 STRAIN SENSITIVITY IN BCDI RECONSTRUCTIONS

5.4.1 *Resolution from BCDI dataset*

Bragg Coherent Diffraction Imaging yields information about two different scale: on the one hand, spatial resolution and on the other hand, strain sensitivity. Indeed, if the spatial resolution can often be given a rough estimate, as it will depend

on the maximal extent in reciprocal space of the recorded diffraction pattern, the reconstructed strain arises from the retrieved phases hence its resolution is not obvious. The principal asset of Coherent Diffraction Imaging techniques is the ability to reach high-resolution imaging. The theoretical spatial resolution is given from four parameters of the experiment, namely the energy of the X-ray beam, the detector-to-sample distance, the number of pixels in each direction of the diffraction pattern and the detector pixel size. However, as mentioned in Chapter 3, the actual spatial resolution is limited by the quality of the recorded diffraction patterns, uncertainties in the dataset, or the data analysis, and has to be quantified by mathematical tools. That way, two criterion are mostly used: the phase-retrieval transfer function (PRTF) Chapman et al., 2006 and the Fourier Shell Correlation (FSC) Heel and Schatz, 2005; Harauz and Heel, 1986. While the PRTF relies on the Fourier amplitude of the final solution, the FSC measures the normalized cross-correlation coefficient between two 3D volumes and hence depends on two reconstructions that has to be the result of independent datasets. Both methods are widely used in the literature when it comes to give the spatial resolution of the reconstruction Vila-Comamala et al., 2011; Ulvestad et al., 2015, but the scientific community still lacks a common criterion to assess the strain precision of the reconstruction.

5.4.2 *"Strain shell correlation" for strain sensitivity*

5.4.2.1 *Models*

In order to cope with strain precision from a Bragg CDI dataset, we proposed to discuss two methods. For both of them, strain sensitivity is evaluated from the comparison between two reconstructions of the same object, but from two independent datasets. Then, the reconstructed objects have to be aligned and with similar shape, so that they can be mapped on a common regular grid of N voxels. The main feature, common to both methods, is the 'strain difference' matrix. Evaluated for each reconstruction, this N^2 symmetric matrix is constructed as follows : for each voxel, the absolute difference of strain is computed with all other voxels in the same object :

$$D_{ij} = \left|\varepsilon_i - \varepsilon_j\right|, \quad \forall (i,j) \in [0, N-1]^2 \tag{5.11}$$

where ε_i is the strain evaluated at the i^{th} voxel of either reconstruction.

Next, the first method is inspired from the Fourier Shell Correlation, as it relies on the computation of the correlation between the two strain difference matrices, as a function of the difference shell. Hence, it becomes a "strain shell correlation"

method, where for a set of n shells $\{s_1, \ldots, s_i, \ldots, s_n\}$ of strain interval, the strain shell correlation value v is calculated as:

$$v_i = \frac{\sum D_1 D_2}{\sqrt{\sum D_1^2 D_2^2}} \tag{5.12}$$

where the D_1 and D_2 are the "strain difference" matrices, taken at the indices (j, k) so that $\left|\varepsilon_j - \varepsilon_k\right| \in s_i$, the strain shell where v_i is evaluated. The precision of the strain can then be evaluated as the value for which the correlation is of 0.5.

For the second method, more straightforward, the per-voxel standard deviation between the two strain difference matrices is computed. It yields a map of the noise level at each voxels, and should be more sensitive to surface issues, *e. g.* when the support is slightly incorrect and induces errors near its borders, and could also be computed from more than two datasets.

5.4.2.2 *Numerical validation*

In order to evaluate these methods, simulations were performed to generate datasets from a simple 2D model. It illustrates the effect of the integrated intensity on the level of correlation, assuming that the model (*i. e.* the phases) are known with Poisson noise.

Starting from a 80×80 array simulating a cross section into a layer of Si, two standard BCDI datasets are generated by adding phase ripples to the array, calculating its FT, applying Poisson noise to produce two different datasets with altered amplitudes and then calculating the inverse FT of the two datasets. Figure 5.23 shows the result of the correlation curve with respect to the absolute strain difference range contained in the datasets, while varying the total number of photons. This Strain Shell Correlation method shows that for very high number of photons, *e. g.* 10^8, the strain precision can be as fine as 1.5×10^{-6}, whereas this value drops to around 10^{-4} when the total photons count drops to 10^3. Note that this 10^{-4} value for the strain sensitivity is used as a reference from the community, but rarely mentioned.

5.4.2.3 *Application to real datasets*

To test the analysis method, works were carried on in collaboration with the F. Hofmann group (University of Oxford) on real datasets acquired at 34-ID-C of the Advance Photon Source Energy Office of Science User Facility, n.d., Argonne National Lab, USA in August 2014, consisting of multi-reflection BCDI on gold microcrystals with varying Focussed Ion Beam (FIB) doses for imaging or sample preparation Hofmann, Tarleton, et al., 2017. The aim of the experiment was to spatially-resolve the full lattice strain tensor and hence examine the defects caused by FIB in initially

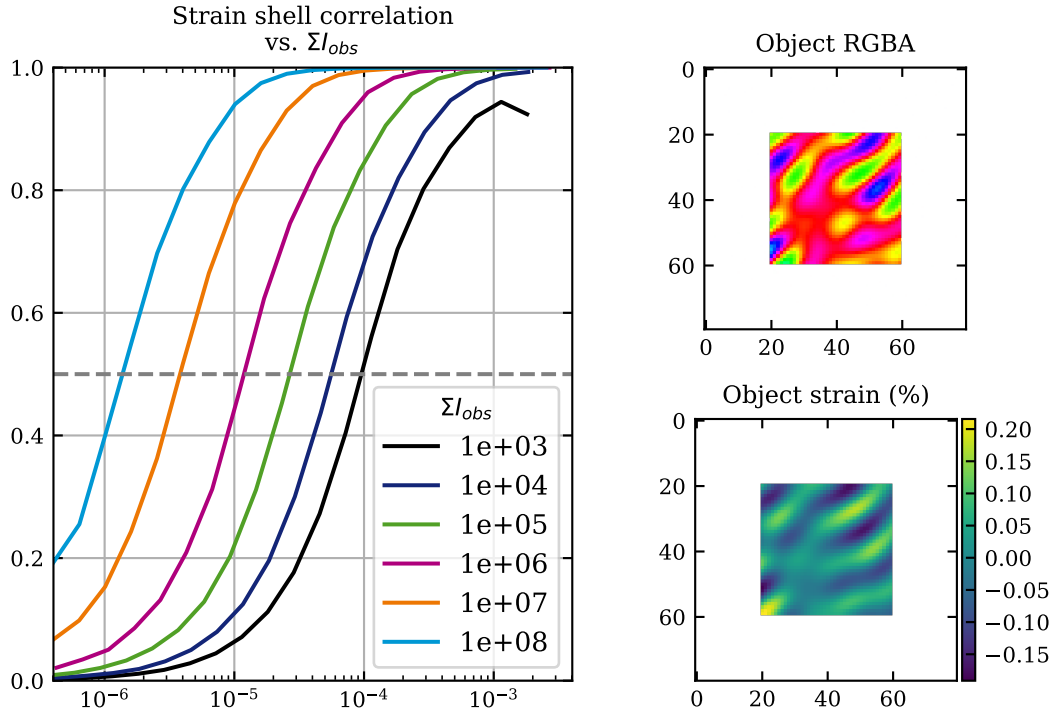

Figure 5.23 – Simulation of the Strain Shell Correlation for varying number of photons. Starting from one 2D array with phase ripples, two different datasets are produced by performing FT, then adding random Poisson noise, and finally applying an inverse FT, this for different levels of total number of photons. On the left hand is plotted the strain shell correlation between those two datasets, for total intensity varying between 10^3 and 10^8 photons. On the right hand side, the initial test array with its phase (top), and the corresponding strain map (bottom). From this, one can clearly see that the strain precision drops from 1.5×10^{-6} at 10^8 photons, to 10^{-4} at 10^3 photons.

pristine objects. Prior to coherent X-ray diffraction measurements, the gold crystals lattice orientations were determined by Synchrotron X-ray micro-beam Laue diffraction at beamline 34-ID-E at the APS Hofmann, Phillips, et al., 2017.

The full dataset that was shared with us consists in data from two different crystals. On the one hand, a crystal which was exposed to a Ga^+ dose just sufficient to image the sample (30 keV, 50 pA, 4.5×10^4 ions/μm^2), and on the other, a crystal into which a central hole was FIB-machined. For each crystal, a maximum of six reflections have been measured, with roughly twenty angular scans performed for each reflection. Each set of scans was divided in two, taking either the odd or the even scans, and in order to evaluate the Strain Shell Correlation as a function of the total intensity, we also aligned and summed 2, 4, 8 and up to 15 scans.

Then, 100 reconstructions starting from different random phases, and random threshold for the support update (between 0.2 and 0.3) were computed using PyNX. The same recipe was applied, with a total of 1000 cycles of RAAR and 40 cycles of ER, using the partial coherence modulus constraint when the number of scans summed up was larger than 2. Similarly to what was carried out in section 5.3.3, only the 20 reconstructions with the lowest LLK_{free} were kept, and the eigensolution with the highest relative intensity was selected as the final solution. As an example, Figure 5.24 shows the reconstruction result for the (200) reflection of the crystal exposed to low-dose FIB, with a 3D rendering colored by the retrieved lattice displacement magnitude. The reconstruction is in excellent agreement with the one presented in Figure 2 of Hofmann, Tarleton, et al., 2017, giving us good confidence to apply our strain sensitivity tools on our reconstructed datasets.

From two independent solutions, retrieved by phasing a dataset made of either the even or the odd indexes of a scan, or a sum of scans, we were able to test the Strain Shell Correlation method. Figure 5.25 shows cross-sections of the phase (first column), the strain (second column) together with the standard deviation map (top right) of the strain differences and the Strain Shell Correlation curve. A maximum standard deviation of 10^{-4} is found, and the correlation curve is of 0.5 at $|\Delta\varepsilon| \simeq 2.5\times10^{-5}$, showing quite good strain sensitivity.

This Strain Shell Correlation curve was obtained from the comparison of two reconstructions coming from the sum of 8 scans, hence with the total intensity of about 1.5×10^7 photons. Figure 5.26 depicts the evolution of the Strain Shell Correlation with respect to the total intensity in the diffraction pattern. One can see that there is no clear shift of the strain correlation curve to higher $|\Delta\varepsilon|$ when increasing the number of photons. This is most likely due either to the lower effective resolution achieved with less scans summed, washing out details, or to the fact that even the smallest total intensity in our dataset is already comparable with the level at which significant strain precision is reached.

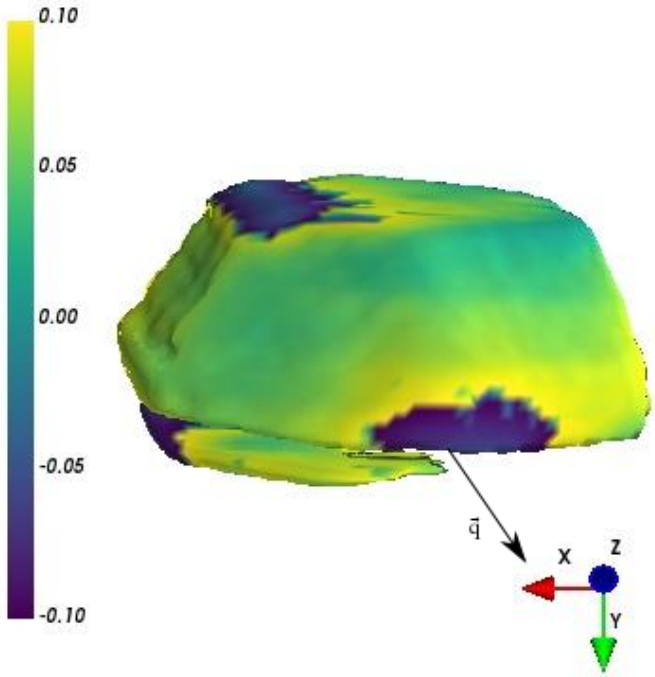

Figure 5.24 – 3D rendering of a crystal after low-dose FIB exposure, colored by lattice displacement magnitude. Note that the displacement scale is in nm, while the crystal is around 900 nm large. The (200) $\vec{q}$ vector direction is shown by a black arrow.

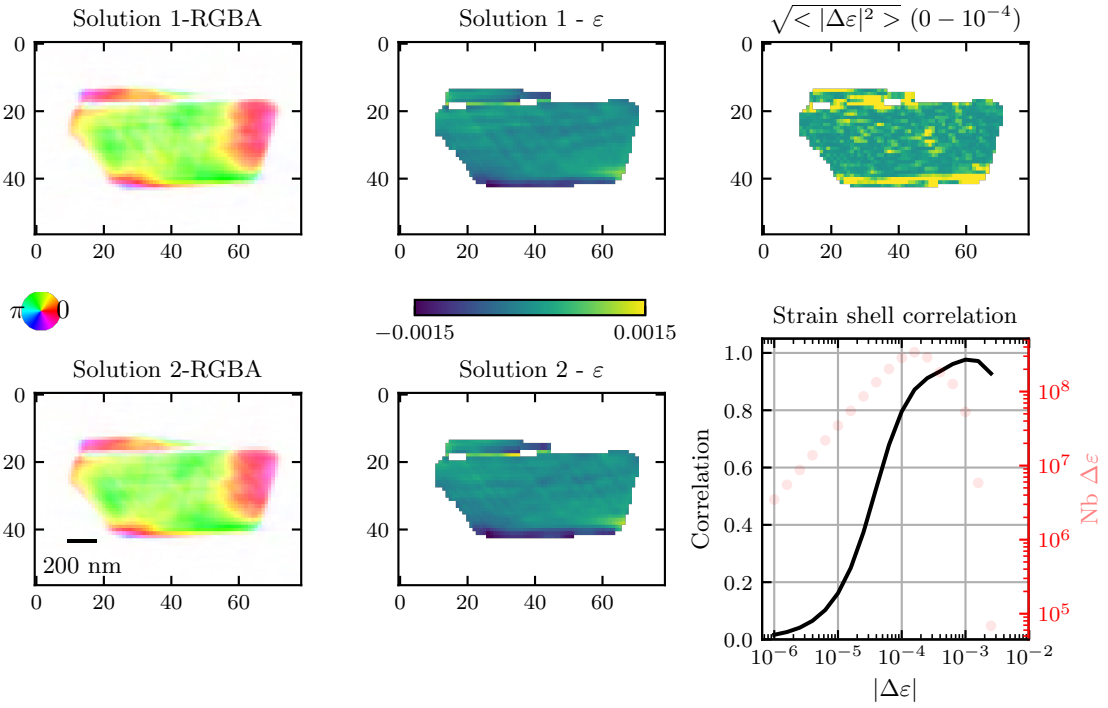

Figure 5.25 – Strain Shell Correlation measurement on reconstructions from the (200) reflection of a low-dose FIB exposed gold nanocrystal. 8 angular scans were aligned in reciprocal space and summed up prior to phase retrieval, leading to approximately 1.5×10^7 photons in the raw diffraction data. The first column shows cross-sections of the RGBA solutions, while the second column depicts cross-sections of the strain, ranging from -0.15% to +0.15%. On the top right is displayed the standard deviation of the absolute strain differences between each dataset, reaching maximal value of 10^{-4} in the neighborhood of some borders. On the bottom right, the Strain Shell Correlation curve (black line), together with the number of $|\Delta\varepsilon|$ pairs (red dots), are shown. From this, a strain precision of 2.5×10^{-5} is demonstrated.

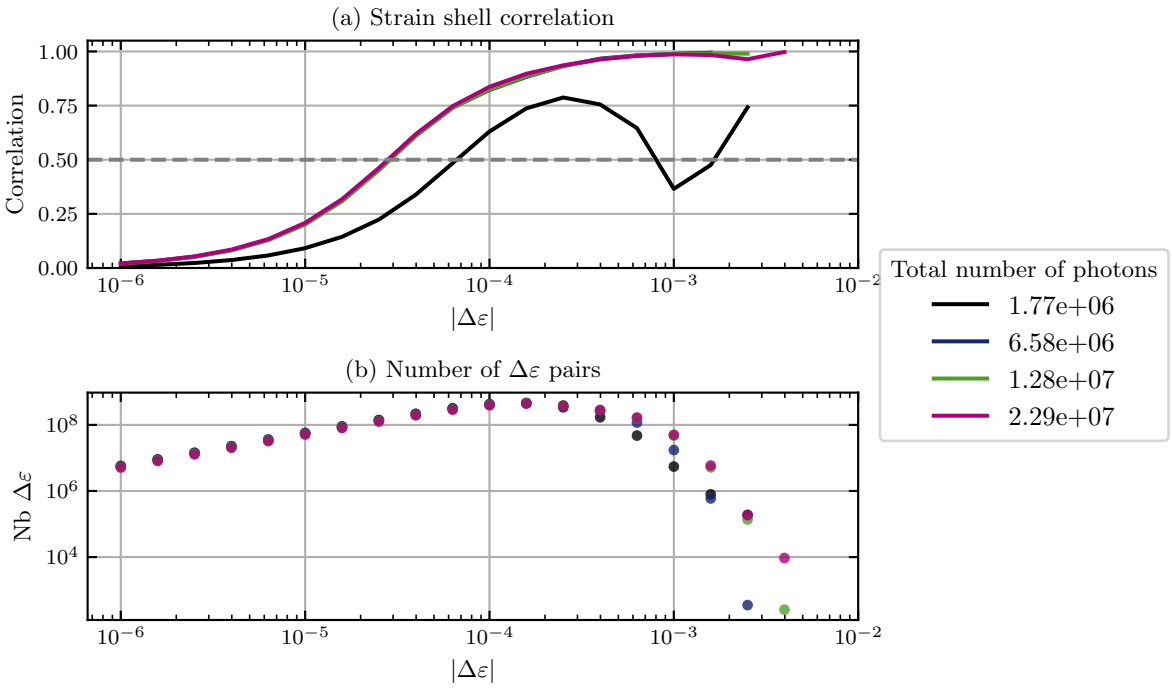

Figure 5.26 – Evolution of the Strain Shell Correlation curves with respect to the total number of photons in the diffraction pattern used for phasing. From several angular scans performed on the (002) reflection of a low-dose FIB exposed gold nanocrystal, four different datasets were created. The Strain Shell Correlation was then evaluated for four different total number of photons, coming from the sum of either 2, 4, 8 or 15 angular scans.

Nonetheless, a last comment can be made on the way strain is calculated. Indeed, in the results presented so far, we used an arbitrary direction along which the gradient of the retrieved phase was calculated, so that it did not thoroughly correspond to the direction of the scattering vector. Actually, in order to calculate the phase gradient along the scattering direction, a rotation of the 3D solution is needed, and this implies interpolation. Figure 5.27 shows the Strain Shell Correlation versus the total number of photons, when the phase gradient is calculated after rotation of the 3D solution so that the scattering vector is aligned with the first axis of the array. The interpolation was performed with the regular grid interpolate class from the SciPy Python library Virtanen et al., 2019, using a linear method Wikipedia, n.d. Interpolating the data will necessarily lead to a degradation of the quality of the data, and this might be the reason why the strain precision decreases from approximately 2×10^{-5} to 5×10^{-5}, for a same total number of photons, when evaluating the strain along the scattering direction. Note also that the interpolation also accentuates the unexplained behaviors of the Strain Shell Correlation curves around higher $|\Delta\varepsilon|$*i. e.*, low-strain sensitivity, where a sharp decrease can be observed.

5.4.3 *Outlook*

Note that in the case where multiple independent reflections have been probed, the back calculation of the expected strain from the experimentally retrieved full strain tensor should not only be more complete, but also would not depend on systematic errors, *e. g.* angular position, crystal centering, detector non-uniformity... Nonetheless, the Strain Shell Correlation method presents the advantage of requiring only two "independently" measured dataset, while giving a good quantitative evaluation of the strain precision.

5.5 CONCLUSION

In this chapter, we first demonstrated that the Diffraction Contrast Tomography method proves to be a strong support for conducting Bragg Coherent X-ray Diffraction Imaging on embedded samples. The combination of these two techniques is robust enough to be considered on a wider scale of samples, especially when it is possible to tweak the X-ray beam size in order to make it match with the sample's grains size. Using forward ptychography is undoubtedly an asset for this task, and allows for a good characterization of the coherence properties of the X-ray beam. Note however that great care should be given to alignment of the DCT setup, as the resulting grains orientation matrix are crucial for the ability to navigate quickly between the embedded grains.

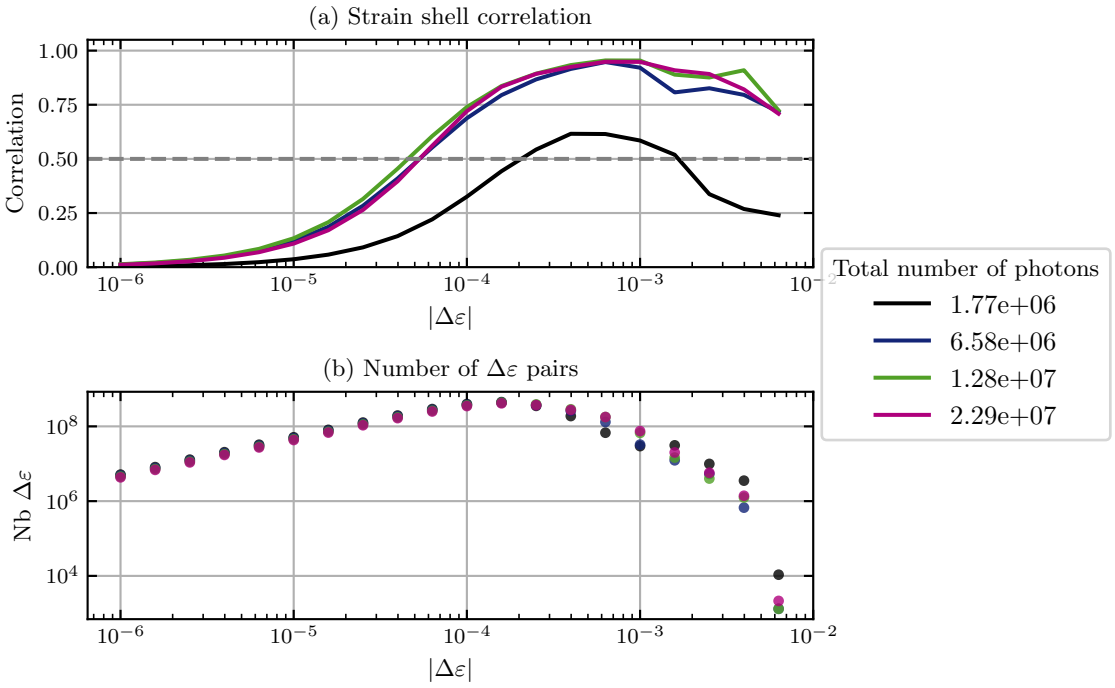

Figure 5.27 – Evolution of the Strain Shell Correlation curves with respect to the total number of photons in the diffraction pattern used for phasing. From several angular scans performed on the (002) reflection of a low-dose FIB exposed gold nanocrystal, four different datasets were created. The solutions were then interpolated so that the scattering vector (whose coordinates are $q_z = -0.92^{-1}$, $q_y = 2.64^{-1}$, $q_x = -1.29^{-1}$ in the laboratory frame) is aligned with the first axis of the 3D solution. The Strain Shell Correlation was then evaluated for four different total number of photons, coming from the sum of either 2, 4, 8 or 15 angular scans.

Even if it was not possible to obtain complete reconstructions of Zirconia embedded grains, due to partial coherence limitations and beam size, not only we could demonstrate that displacements within a one grain remain very small (a twentieth of the interplanar distances) but also we were able to get statistical information about different grains and different Bragg reflections, showing us little discrepancy from one grain to another. Moreover, the upgrade of the ESRF-EBS shows promising capability for these kind of techniques, with the possibility to increase the beam size without being impacted by lateral divergence, or by using the very high flux to replace the silicon (111) monochromator by a Diamond (400) that would lead to a longitudinal coherence length almost 4 times longer.

Finally, we discussed a new tool that enable to evaluate the strain precision of Bragg Coherent X-ray Imaging reconstructions. Despite BCDI becoming a mature technique, detailed understanding of the strain sensitivity remains elusive. We tried to tackle this issue by proposing a method, inspired by Fourier Shell Correlation, relying on two independently measured datasets, that evaluates the correlation between the absolute strain difference of the two datasets. Applied to experimental measurements, the Strain Shell Correlation shows that a strain precision of 10^{-4} might be a bit conservative in certain cases, but remains a good approximation for BCDI.

Reischig, P., A. King, L. Nervo, N. Vigano, Y. Guilhem, W. J. Palenstijn, K. J. Batenburg, M. Preuss, and W. Ludwig (2013). « Advances in X-ray diffraction contrast tomography: flexibility in the setup geometry and application to multiphase materials. » en. In: *Journal of Applied Crystallography* 46.2, pp. 297–311. DOI: 10.1107/S0021889813002604 (cit. on pp. 142–144).

Lyckegaard, Allan, Erik Mejdal Lauridsen, Wolfgang Ludwig, Richard Warren Fonda, and Henning Friis Poulsen (2011). « On the Use of Laguerre Tessellations for Representations of 3D Grain Structures. » en. In: *Advanced Engineering Materials* 13.3, pp. 165–170. DOI: 10.1002/adem.201000258 (cit. on p. 142).

Robinson, I. K., I. A. Vartanyants, G. J. Williams, M. A. Pfeifer, and J. A. Pitney (2001). « Reconstruction of the Shapes of Gold Nanocrystals Using Coherent X-Ray Diffraction. » In: *Physical Review Letters* 87.19, p. 195505. DOI: 10.1103/PhysRevLett.87.195505 (cit. on p. 142).

Mastropietro, F., P. Godard, M. Burghammer, C. Chevallard, J. Daillant, J. Duboisset, M. Allain, P. Guenoun, J. Nouet, and V. Chamard (2017). « Revealing crystalline domains in a mollusc shell single-crystalline prism. » en. In: *Nature Materials* 16.9, pp. 946–952. DOI: 10.1038/nmat4937 (cit. on p. 142).

Gremillard, L., T. Epicier, J. Chevalier, and G. Fantozzi (2000). « Microstructural study of silica-doped zirconia ceramics. » In: *Acta Materialia* 48.18, pp. 4647–4652. DOI: 10.1016/S1359-6454(00)00252-4 (cit. on p. 142).

Deville, Sylvain, Jérôme Chevalier, and Laurent Gremillard (2006). « Influence of surface finish and residual stresses on the ageing sensitivity of biomedical grade zirconia. » In: *Biomaterials* 27.10, pp. 2186–2192. DOI: 10.1016/j.biomaterials.2005.11.021 (cit. on p. 142).

Poulsen, Henning Friis (2004). *Three-Dimensional X-Ray Diffraction Microscopy: Mapping Polycrystals and Their Dynamics*. en. Google-Books-ID: _jzrH20Qu6cC. Springer Science & Business Media (cit. on p. 143).

Ludwig, W., S. Schmidt, E. M. Lauridsen, and H. F. Poulsen (2008). « X-ray diffraction contrast tomography: a novel technique for three-dimensional grain mapping of polycrystals. I. Direct beam case. » en. In: *Journal of Applied Crystallography* 41.2, pp. 302–309. DOI: 10.1107/S0021889808001684 (cit. on p. 143).

Gordon, Richard, Robert Bender, and Gabor T. Herman (1970). « Algebraic Reconstruction Techniques (ART) for three-dimensional electron microscopy and X-ray

photography. » In: *Journal of Theoretical Biology* 29.3, pp. 471–481. DOI: 10.1016/0022-5193(70)90109-8 (cit. on p. 144).

Ludwig, W., P. Reischig, A. King, M. Herbig, E. M. Lauridsen, G. Johnson, T. J. Marrow, and J. Y. Buffière (2009). « Three-dimensional grain mapping by x-ray diffraction contrast tomography and the use of Friedel pairs in diffraction data analysis. » In: *Review of Scientific Instruments* 80.3, p. 033905. DOI: 10.1063/1.3100200 (cit. on pp. 144, 145).

Lowe, David G. (2004). « Distinctive Image Features from Scale-Invariant Keypoints. » In: *International Journal of Computer Vision* 60.2, pp. 91–110. DOI: 10.1023/B:VISI.0000029664.99615.94 (cit. on pp. 145, 146).

VINCENT, Thomas et al. (2019). *silx-kit/silx*. Zenodo. DOI: 10.5281/zenodo.3579228 (cit. on p. 145).

al., Sole et. *SIFT using SILX*. URL: http://www.silx.org/doc/silx/latest/description/sift.html (cit. on p. 145).

Ponchut, C., J. M. Rigal, J. Clément, E. Papillon, A. Homs, and S. Petitdemange (2011). « MAXIPIX, a fast readout photon-counting X-ray area detector for synchrotron applications. » en. In: *Journal of Instrumentation* 6.01, pp. C01069–C01069. DOI: 10.1088/1748-0221/6/01/C01069 (cit. on p. 149).

Favre-Nicolin, V. (2019). *PyNX Python Library*. URL: http://ftp.esrf.fr/pub/scisoft/PyNX/ (visited on 08/2019) (cit. on p. 150).

Mandula, O., M. Elzo Aizarna, J. Eymery, M. Burghammer, and V. Favre-Nicolin (2016). « PyNX.Ptycho: a computing library for X-ray coherent diffraction imaging of nanostructures. » en. In: *Journal of Applied Crystallography* 49.5, pp. 1842–1848. DOI: 10.1107/S1600576716012279 (cit. on p. 150).

Pfeiffer, Franz (2018). « X-ray ptychography. » In: *Nature Photonics* 12.1, pp. 9–17. DOI: 10.1038/s41566-017-0072-5 (cit. on p. 151).

Chubar, Oleg and P Elleaume (1998). « Accurate and efficient computation of synchrotron radiation in the near field region. » In: *proc. of the EPAC98 Conference*, pp. 1177–1179 (cit. on p. 154).

Thibault, P. and A. Menzel (2013). « Reconstructing state mixtures from diffraction measurements. » In: *Nature* 494.7435, pp. 68–71. DOI: 10.1038/nature11806 (cit. on p. 155).

Leake, Steven J., Marcus C. Newton, Ross Harder, and Ian K. Robinson (2009). « Longitudinal coherence function in X-ray imaging of crystals. » EN. In: *Optics Express* 17.18, pp. 15853–15859. DOI: 10.1364/OE.17.015853 (cit. on p. 161).

Favre-Nicolin, V., J. Coraux, M.-I. Richard, and H. Renevier (2011). « Fast computation of scattering maps of nanostructures using graphical processing units. » en. In: *Journal of Applied Crystallography* 44.3, pp. 635–640. DOI: 10.1107/S0021889811009009 (cit. on p. 163).

Guizar-Sicairos, Manuel and James R. Fienup (2008). « Phase retrieval with transverse translation diversity: a nonlinear optimization approach. » In: *Optics Express* 16.10, pp. 7264–7278. DOI: 10.1364/OE.16.007264 (cit. on p. 164).

Energy Office of Science User Facility, U.S. Department of. *Station 34-ID-C at APS*. URL: https://www.aps.anl.gov/Microscopy/Beamlines/34-ID-C (cit. on pp. 166, 177).

Favre-Nicolin, Vincent, Steven Leake, and Yuriy Chushkin (2019). « Free log-likelihood as an unbiased metric for coherent diffraction imaging. » In: *arXiv preprint arXiv:1904.07056* (cit. on pp. 166, 168).

Quenouille, M. H. (1949). « Problems in Plane Sampling. » In: *The Annals of Mathematical Statistics* 20.3. Zbl: 0035.09103, pp. 355–375. DOI: 10.1214/aoms/1177729989 (cit. on p. 167).

Efron, B. and C. Stein (1981). « The Jackknife Estimate of Variance. » In: *The Annals of Statistics* 9.3. Zbl: 0481.62035, pp. 586–596. DOI: 10.1214/aos/1176345462 (cit. on p. 167).

Guizar-Sicairos, Manuel, Samuel T. Thurman, and James R. Fienup (2008). « Efficient subpixel image registration algorithms. » In: *Optics Letters* 33.2, pp. 156–158. DOI: 10.1364/OL.33.000156 (cit. on p. 167).

Chapman, Henry N. et al. (2006). « High-resolution ab initio three-dimensional x-ray diffraction microscopy. » In: *JOSA A* 23.5, pp. 1179–1200. DOI: 10.1364/JOSAA.23.001179 (cit. on pp. 167, 176).

Shapiro, David et al. (2005). « Biological imaging by soft x-ray diffraction microscopy. » In: *Proceedings of the National Academy of Sciences* 102.43, pp. 15343–15346. DOI: 10.1073/pnas.0503305102 (cit. on p. 167).

Chushkin, Y., F. Zontone, E. Lima, L. De Caro, P. Guardia, L. Manna, and C. Giannini (2014). « Three-dimensional coherent diffractive imaging on non-periodic specimens at the ESRF beamline ID10. » In: *Journal of Synchrotron Radiation* 21.3, pp. 594–599. DOI: 10.1107/S1600577514003440 (cit. on p. 167).

Khounsary, Ali M, Robert K Smither, Steve Davey, and Ankor Purohit (1993). « Diamond monochromator for high heat flux synchrotron x-ray beams. » In: *High Heat Flux Engineering*. Vol. 1739. International Society for Optics and Photonics, pp. 628–642 (cit. on p. 174).

Onuki, Hideo and Pascal Elleaume (2003). *Undulators, wigglers and their applications*. CRC Press (cit. on p. 175).

Heel, Marin van and Michael Schatz (2005). « Fourier shell correlation threshold criteria. » In: *Journal of Structural Biology* 151.3, pp. 250–262. DOI: 10.1016/j.jsb.2005.05.009 (cit. on p. 176).

Harauz, George and Marin van Heel (1986). « Exact filters for general geometry three dimensional reconstruction. » In: *Optik.* 73.4, pp. 146–156 (cit. on p. 176).

Vila-Comamala, Joan, Ana Diaz, Manuel Guizar-Sicairos, Alexandre Mantion, Cameron M. Kewish, Andreas Menzel, Oliver Bunk, and Christian David (2011). « Characterization of high-resolution diffractive X-ray optics by ptychographic coherent diffractive imaging. » In: *Optics Express* 19.22, pp. 21333–21344. DOI: 10.1364/OE.19.021333 (cit. on p. 176).

Ulvestad, Andrew, Jesse N. Clark, Ross Harder, Ian K. Robinson, and Oleg G. Shpyrko (2015). « 3D Imaging of Twin Domain Defects in Gold Nanoparticles. » In: *Nano Letters* 15.6, pp. 4066–4070. DOI: 10.1021/acs.nanolett.5b01104 (cit. on p. 176).

Hofmann, Felix, Edmund Tarleton, Ross J. Harder, Nicholas W. Phillips, Pui-Wai Ma, Jesse N. Clark, Ian K. Robinson, Brian Abbey, Wenjun Liu, and Christian E. Beck (2017). « 3D lattice distortions and defect structures in ion-implanted nanocrystals. » In: *Scientific Reports* 7, p. 45993. DOI: 10.1038/srep45993 (cit. on pp. 177, 179).

Hofmann, F., N. W. Phillips, R. J. Harder, W. Liu, J. N. Clark, I. K. Robinson, and B. Abbey (2017). « Micro-beam Laue alignment of multi-reflection Bragg coherent diffraction imaging measurements. » In: *Journal of Synchrotron Radiation* 24.5, pp. 1048–1055. DOI: 10.1107/S1600577517009183 (cit. on p. 179).

Virtanen, Pauli et al. (2019). « SciPy 1.0–Fundamental Algorithms for Scientific Computing in Python. » In: *arXiv e-prints*, arXiv:1907.10121, arXiv:1907.10121. arXiv: 1907.10121 [cs.MS] (cit. on p. 183).

Wikipedia, The Free Encyclopedia. *Trilinear interpolation. (2013, January 17)*. URL: http://en.wikipedia.org/w/index.php?title=Trilinear_interpolation&oldid=533448871 (cit. on p. 183).

6

BRAGG PTYCHOGRAPHY

6.1 INTRODUCTION

Ptychography is a recent method allowing the reconstruction of an extended object from the measurement of its diffraction pattern at multiple positions of the sample, while ensuring some degree of overlap of the illumination. As a result, Ptychography copes with the main limitation of the CDI lensless techniques, that struggles to reconstruct non-isolated objects, whose size is preferably smaller than the illuminating beam size.

First introduced in the 1970's in order to increase the resolution of electron microscopes Hegerl and Hoppe, 1970, Ptychography is now widely used and developed for both visible light and X-rays, and for both reflection and transmission geometries. From the redundancy introduced by the overlapping in the sample plane, phase retrieval algorithms lead to reconstruction with spatial resolution better than the probe size or even the scanning step size, reaching near-wavelength spatial resolution Maiden and J. M. Rodenburg, 2009.

Besides its ability to retrieve arbitrarily large sample, Ptychography also presents the strong asset of reconstructing not only the sample's complex-valued density function, but also the profile of the incoming wavefield.

6.2 PRINCIPLES OF PTYCHOGRAPHY

Being part of the group of CDI techniques, Ptychography relies on the same coherence properties that have been described earlier. The major difference that prevails is the ability to discard the isolated-object requirement, hence to a certain extent the oversampling requirement in Fourier space. The real space support constraint is replaced by a condition of overlapping of the real space scanning positions, meaning that the probe illumination has to be scanned with a step smaller than the probe's size. In practice, it is usually the sample that is scanned and the beam fixed, for obvious reasons at synchrotron facilities. Indeed, translating the focusing optics instead of the sample is limited by the weight of those optics. The FZP mount at ID01 being around 2.5 kg, it would require a recalibration of the PI motor PID parameters and

will inevitably lead to a lot of vibrations [1]. Moreover, it is crucial for Ptychography that the incident illumination remains constant throughout the entire scan. Figure 6.1 depicts a typical transmission setup for ptychography.

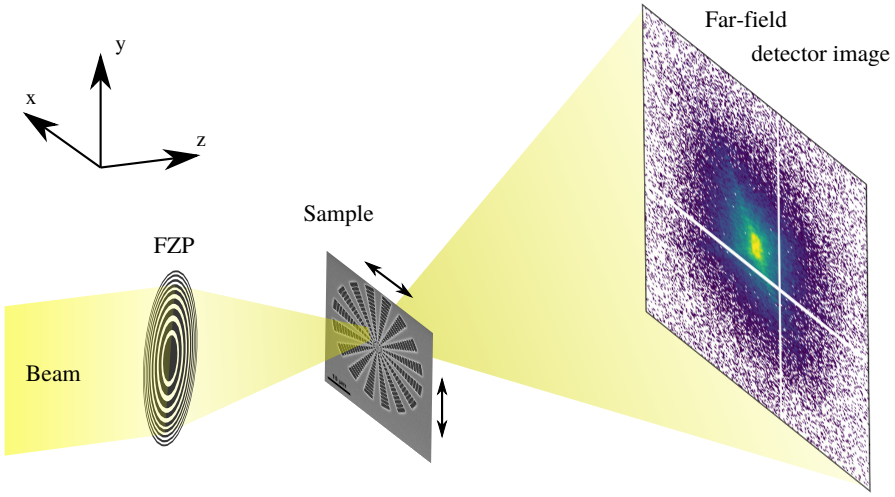

Figure 6.1 – Scheme of Ptychographic data collection setup. The sample is scanned in the vertical plane (xy) with overlapping illumination steps, while the far-field diffraction pattern is collected for each position with a 2D pixel detector.

All in all, Ptychography is a resourceful combination of CDI and Scanning Transmission X-Ray Microscopy (STXM), two methods benefiting from coherence properties of an illumination but have been developed independently. On the one hand, The former brings its promise of very high spatial resolution, together with its limitation to isolated sample, on the other the latter provides a transmission map of an isolated object from a scanned probe, while limited by the extent of the focal spot.

Reconstruction techniques used for Ptychographic dataset have been through three major stages. At the very beginning of the technique, the reconstruction technique allowed a one-step reconstruction called Wigner distribution deconvolution Bates and J. M. Rodenburg, 1989; Chapman, 1996; McCallum and J. M. Rodenburg, 1993; J. M. Rodenburg and Bates, 1992, but required a very tight scanning grid. Then, Faulkner and Rodenburg were the first to introduce a real space implementation of Ptychography using iterative projection-based algorithms Maiden and J. M. Rodenburg, 2009; Faulkner and J. M. Rodenburg, 2004; Thibault, Dierolf, Bunk, et al., 2009, that were significantly less stringent on the measurements. More recently, non-linear optimization algorithms such as maximum-likelihood optimization including noise statistics Thibault and Guizar-Sicairos, 2012; Godard, Allain,

1. Note that the cSAXS beamline, PSI, has recently developed the ability to scan the FZP instead of the sample Odstrcil et al., 2019.

Chamard, and J. Rodenburg, 2012 (see 3.7.5.4) have been including as refinement steps to boost the quality of reconstructions.

At first sight, the reconstruction procedure relying on iterative algorithms is similar to that of all CDI methods, alternating constraints between real and reciprocal space via the use of discrete FT. Actually, the difference lies in the way the update of the object guess is made, *i. e.* taking into account all the diffraction patterns that contain redundant information. In addition to allow studying extended objects, Ptychography intrinsically solves two of the problems commonly associated with phase retrieval : defocus and twin image. Indeed, when a non-negativity constraint on the object cannot be used, both the reconstruction of the true object and a slightly out of focus image can fit inside a slightly larger-than-the-object support and satisfy the far-field intensity constraint Chapman et al., 2006. Otherwise, thanks to the translation diversity, in Ptychography there is only one plane where the translating object and illumination functions can be expressed as a product of one another. The well-known twin image problem of CDI for centrosymmetric supports Fienup and Wackerman, 1986, originating from the fact that both $\psi(\vec{r})$ and $\psi^*(-\vec{r})$ have the same Fourier intensity pattern, is also removed by translational diversity and the knowledge of the transverse shifts imposed on the sample.

6.2.1 *Ptychographic Iterative Engine*

The translation-diverse phase retrieval approach was originally brought up by Rodenburg and Faulkner with the introduction of the Ptychographic Iterative Engine (PIE) J. M. Rodenburg and Faulkner, 2004. In Ptychography, one assumes that the interaction of an object and a probe can be modeled by a complex multiplication, leading the expression of the intensity at the j-th scan position to be :

$$I_j(\vec{q}) = \left| \mathcal{F}\left[O(\vec{r}) P(\vec{r} - \vec{R}_j) \right] \right|^2, \tag{6.1}$$

where $\vec{r}$ and $\vec{q}$ are suitable real-space and reciprocal-space coordinate vectors, and the probe and object two-dimensional wavefronts are denoted by $P(\vec{r})$ and $O(\vec{r})$, respectively. The aim of a ptychographic reconstruction is to retrieve a unique object that agrees with all the measurements, giving the known positions $\vec{R}_j$, the scanning probe $P(\vec{r})$ and the diffraction patterns $I_j(\vec{q})$. The convergence is inevitably favored by the overlapping constrained illumination, because the latter implies multiple updates of the different object realizations within a single iteration.

The PIE process is recalled as the following :

1. A real space function $O_{j,n}(\vec{r})$ is set as a first guess of the object function, where the subscript g, n accounts for a guessed function at the n-th iteration.

2. The guess function is multiplied by the illumination function, shifted at the current position $\vec{R}_j$, producing a guessed exit wave function :

$$\psi_{g,n}(\vec{r},\vec{R}_j) = O_{g,n}(\vec{r})P(\vec{r}-\vec{R}_j) \tag{6.2}$$

3. The exit wave is propagated to the detector by applying a Fourier Transform :

$$\Psi_{g,n}(\vec{q},\vec{R}_j) = \mathcal{F}\left[\psi_{g,n}(\vec{r},\vec{R}_j)\right] = \left|\Psi_{g,n}(\vec{r},\vec{R}_j)\right| e^{i\phi_{n,g}(\vec{q},\vec{R_j})}, \tag{6.3}$$

where $\phi_{n,g}(\vec{q},\vec{R_j})$ is the (guessed-probably incorrect) phase in reciprocal space at iteration n, for position $\vec{R}_j$.

4. Apply the Fourier constraints, from the measured intensities I_j :

$$\Psi_{c,n}(\vec{q},\vec{R}_j) = \sqrt{I_j}e^{i\phi_{n,g}(\vec{q},\vec{R_j})} \tag{6.4}$$

5. Inverse Fourier transform back to real space to obtain an updated guess at the exit wave function :

$$\psi_{c,n}(\vec{r},\vec{R}_j) = \mathcal{F}^{-1}\left[\Psi_{c,n}(\vec{q},\vec{R}_j)\right] \tag{6.5}$$

6. Update the guessed object, in the area covered by the probe, using the update function :

$$\begin{aligned} O_{g,n+1}(\vec{r}) = O_{g,n}(\vec{r}) + \frac{\left|P(\vec{r}-\vec{R}_j)\right|}{\left|P_{max}(\vec{r}-\vec{R}_j)\right|}\frac{P^*(\vec{r}-\vec{R}_j)}{\left(\left|P(\vec{r}-\vec{R}_j)\right|^2+\alpha\right)} \\ \times\beta\left(\psi_{c,n}(\vec{r},\vec{R}_j) - \psi_{g,n}(\vec{r},\vec{R}_j)\right), \end{aligned} \tag{6.6}$$

where α is a term used to avoid division by zero when $P(\vec{r}-\vec{R}_j) \simeq 0$, and β is a feedback parameter, usually between 0.5 and 1.

7. Move to the next position $\vec{R_{j+1}}$.

8. The steps (2)→(7) are repeated over all positions $\vec{R}$ to update the complete object. Completion is achieved after n iterations, where one iteration is defined as one pass over all scan positions.

Convergence of the algorithm is typically monitored computing the sum squared error in the reciprocal space. In 2009, Maiden and Rodenburg developed a revised version of PIE, called extended PIE, so that the requirement for an accurate model of the illumination is not longer required. The algorithm relies on the same steps as described above, until step 6 where the update function is split into an update for the object and an update of the probe. The two update functions are really similar to the one of equation 6.6, as it basically reverses the role of the two unknowns.

However, Guizar-Sicairos and Fienup noticed in 2008 that the PIE algorithm can be expressed as a steepest decent algorithm Guizar-Sicairos and Fienup, 2008. Indeed, the update step of equation 6.6 can be expressed as ;

$$\psi_{g,n+1}(\vec{r},\vec{R}_j) - \psi_{g,n}(\vec{r},\vec{R}_j) = \beta \frac{\left|P(\vec{r}-\vec{R}_j)\right|}{\left|P_{max}(\vec{r}-\vec{R}_j)\right|}\left(\psi_{c,n}(\vec{r},\vec{R}_j) - \psi_{g,n}(\vec{r},\vec{R}_j)\right), \tag{6.7}$$

where we used equation 6.2 and :

$$\frac{P^*(\vec{r}-\vec{R}_j)P(\vec{r}-\vec{R}_j)}{\left(\left|P(\vec{r}-\vec{R}_j)\right|^2+\alpha\right)} = \frac{\left|P(\vec{r}-\vec{R}_j)\right|^2}{\left(\left|P(\vec{r}-\vec{R}_j)\right|^2+\alpha\right)} \simeq 1 \tag{6.8}$$

Then, using the derivation provided by Fienup in his pioneering paper on phase retrieval algorithms Fienup, 1982, the direction of steepest descent for a squared-error metric for $\sqrt{I_j}$ with respect to $\psi_{g,n}(\vec{r},\vec{R}_j)$ is found to be given by :

$$-\frac{\partial}{\partial\psi_{g,n}(\vec{r},\vec{R}_j)}\left\{\sum_{\vec{q}}\left[\left|\Psi_{g,n}(\vec{q},\vec{R}_j)\right| - \sqrt{I_j(\vec{q})}\right]^2\right\} = 2\left(\psi_{c,n}(\vec{r},\vec{R}_j) - \psi_{g,n}(\vec{r},\vec{R}_j)\right) \tag{6.9}$$

As a result, by comparing the right-hand sides of equation 6.7 and 6.9, it becomes clear that the update step of PIE can be seen as a steepest descent algorithm with a spatially variant step size of :

$$\beta\frac{\left|P(\vec{r}-\vec{R}_j)\right|}{\left|P_{max}(\vec{r}-\vec{R}_j)\right|} \tag{6.10}$$

Observing that conjugate-gradient is an other gradient search algorithm superior to the one steepest descent, Guizar-Sicairos suggested the use of a non-linear optimization algorithm to simultaneously optimize the object, the illumination and the translation parameters. The analytical expressions of the algorithm are provided in Guizar-Sicairos and Fienup, 2008; Guizar-Sicairos, 2010 but will not be detailed here. Not only the algorithm proved to be superior to PIE when the system is not accurately known, but also allowed including nonidealities, *e. g.* transverse coherence, detector misalignments, finite pixel size...

6.2.2 *Difference Map*

In parallel to the work of Guizar-Sicairos and Fienup, Thibault *et al.* published a new reconstruction approach that can also extract both the specimen's transmission

function and the illumination profile, but based on the difference map algorithm, intended to solve constraint-based problems Thibault, Dierolf, Bunk, et al., 2009. Difference map is an iterative algorithm originally developed for phase retrieval Elser, 2003, but now has a wide range of applications Elser et al., 2007.

As illustrated by Thibault, the difference map algorithm aims to find the intersection point between two constraint sets. When it comes to Ptychography, all the "views" of the object can be regrouped into a state vector $\mathbf{\Psi} = \{\psi_1(\vec{r}), \psi_2(\vec{r}), \ldots, \psi_N(\vec{r})\}$ that then must comply with two simultaneous constraints: the Fourier constraint for compliance with the measured intensities , and the overlap constraint stating that each view has to be factorized as a multiplication between the probe and object. On the one hand, the Fourier constraint $\mathbf{\Pi_F}$ consists of applying the Fourier projection $\boldsymbol{P}_m$ on each individual view, and can be written, reusing the formalism from section 3.7.4 :

$$\mathbf{\Pi_F}(\mathbf{\Psi}) : \psi_j \rightarrow \psi_j^F = \boldsymbol{P_m}(\psi_j) \tag{6.11}$$

Note that ψ_j^F is the same object as $\psi_{c,n}(\vec{r}, \vec{R}_j)$ in the last section considering PIE, *i. e.* the updated view whose Fourier magnitudes have been replaced by the measurement $\sqrt{I_j}$ of the diffraction at the j-th position corresponding to a $\vec{R}_j$ translation. On the other hand, the overlap projection $\mathbf{\Pi_O}$ can be computed from the minimization of the distance $\|\mathbf{\Psi} - \mathbf{\Pi_O}(\mathbf{\Psi})\|^2$, which results in finding estimates $\hat{P}$ and $\hat{O}$ that minimizes :

$$\|\mathbf{\Psi} - \mathbf{\Pi_O}(\mathbf{\Psi})\| = \sum_j \sum_{\vec{r}} \left| \psi_j(\vec{r}) - \hat{P}(\vec{r} - \vec{R}_j)\hat{O}(\vec{r}) \right|^2, \tag{6.12}$$

Setting to zero the derivative of equation 6.12 with respect to $\hat{P}$ and $\hat{O}$ gives the solution as a system of the following equations :

$$\begin{aligned} \hat{O}(\vec{r}) &= \frac{\sum_j \hat{P}^*(\vec{r} - \vec{R}_j)\psi_j(\vec{r})}{\sum_j \left| \hat{P}(\vec{r} - \vec{R_j}) \right|^2} \\ \hat{P}(\vec{r}) &= \frac{\sum_j \hat{O}^*(\vec{r} + \vec{R}_j)\psi_j(\vec{r} + \vec{R}_j)}{\sum_j \left| \hat{O}(\vec{r} + \vec{R_j}) \right|^2} \end{aligned} \tag{6.13}$$

These equations need to be solved simultaneously in the case $\hat{P}$ is unknown or need refinement, as the system 6.13 can not be decoupled analytically. By introducing the overlap projection $\mathbf{\Pi_O}$ as :

$$\mathbf{\Pi_O}(\mathbf{\Psi}) : \psi_j \rightarrow \psi_j^O(\vec{r}) = \hat{P}(\vec{r} - \vec{R}_j)\hat{O}(\vec{r}), \tag{6.14}$$

the iterative procedure of Difference map can be readily written in a form close to the Hybrid Input Output (HIO) :

$$\mathbf{\Psi_{n+1}} = \left[\boldsymbol{I} + (1 + \beta)\mathbf{\Pi_F} - \mathbf{\Pi_O} - \beta \mathbf{\Pi_F} \right] \mathbf{\Psi_n} \tag{6.15}$$

The evolution of the procedure is monitored by the squared absolute difference between the current and previous updates :

$$\epsilon_{n+1} = \|\mathbf{\Psi_{n+1}} - \mathbf{\Psi_n}\| \tag{6.16}$$

However, the choice of the error metric is not limited to the one of equation 6.16. Firstly because this metric is a good convergence criterion but gives no indication of the fit quality. Secondly, because of noise and experimental limitations, the constraints sets are never perfectly compatible. As a result, the iteration never reaches a stop, rather a steady state regime where the error is small but non-zero. Nonetheless, DM has proven its fast early convergence, and the use of Maximum Likelihood (described in section 3.7.5.4) for refinement as a final step makes the combination of DM and ML an efficient choice for ptychographic reconstructions.

Both DM and ML are implemented as operators in the PyNX library, allowing for efficient and quick resolution of the ptychographic problem. These operators are routinely used, via a very handy script, to solve the probe's profile at the beginning of every experiment performed on the ID01 ESRF beamline. A siemens star pattern, with a very fine "cheesy" structure is used as a reference object to enable switching to update the probe during the algorithms chain. See section 5.3.1.1 for examples of siemens star reconstruction and associated probes. Note that a third algorithm, namely the Alternating Projection (AP) introduced by Marchesini *et al.* Marchesini et al., 2016, can be used with an accurate initial guess.

6.2.3 *Assumptions in ptychographic algorithms and experimental constraints*

There are two major assumptions required for Ptychography. The first one concerns the relationship between the object and probe functions, that needs to be a multiplication providing the exit-wave. The validity of this wave factorization assumption has been investigated by Rodenburg and Bates as a reciprocal space argument J. M. Rodenburg and Bates, 1992, and in real space by Thibault *et al.* in the supplementary material of Thibault, Dierolf, Menzel, et al., 2008. Introducing the resolution R of the imaging system, which has to be replaced by the "intrinsic resolution" as soon as the object is a weak scatterer producing narrower angular range of intensity, Thibault *et al.* gave the maximum depth of the sample, Z, for which the assumption is valid :

$$Z = \frac{Ra}{\lambda}, \tag{6.17}$$

where λ is the wavelength of the illumination, whose spatial extent is defined by a. Z represents the "depth of field" of the method. Moreover, as Ptychography's main feature is the overlapping between the adjacent illuminations, a is typically

much larger than R, hence the depth of focus of the illumination, a^2/λ, is larger than Z and one can legitimately assume that the probe is constant within the depth of the object.

The second assumption of Ptychography is the fact that the illumination function should remain constant over all scanned positions. It is clear for the original PIE algorithm, where no update is performed on the probe and has to be supplied from the very beginning. In the difference map algorithm, even if the probe can be updated, it is still assumed that from one position to another both probe and object are the same, but translated, meaning that if there is a modification of the illumination during the entire scan, it will result in an average of the initial and final probe state.

Then, the quality of a ptychographic reconstruction depends highly on the scanning process. Indeed, very accurate knowledge of the positions of the probe with respect to the sample is required, as any discrepancy can have a severe negative impact on the quality of the reconstruction, lowering resolution and blurring the smallest features Shenfield and J. M. Rodenburg, 2011. As a result, a high accuracy sample stage is needed, such as the PImars piezo stage of the ID01 beamline that is driven in close loop operation. The detector distance needs to be precisely known, as it is directly linked to the pixel size of the object reconstruction (see equation 3.46). In the case where the step size of the ptychographic scan is significantly different from an integer number of pixels, use of subpixel registration algorithms Guizar-Sicairos, Thurman, et al., 2008 can be used to increase the reconstruction's quality.

Last but not least, the symmetries emerging from raster scanning can lead to artefacts in the reconstructed data. Indeed, the factorization of the views into P and O can add an uncontrolled degree of freedom Thibault, Dierolf, Bunk, et al., 2009, as we recall here : if $P(\vec{r})$ and $O(\vec{r})$ are solutions to the ptychographic problem, then so are the functions $O'(\vec{r}) = f(\vec{r})O(\vec{r})$ and $P'(\vec{r}) = f(\vec{r})^{-1}P(\vec{r})$ if and only if $f(\vec{r}) = f(\vec{r} - \vec{R}_j)$ for all positions j. The only solution is the trivial $f = cste$, unless the points $\vec{R}_j$ lie on a lattice, *i. e.*, the scan is on a raster grid, where any periodic function on this lattice would be solution. Therefore, there are an infinity of solutions for the Ptychographic dataset. However, this "raster grid pathology" can be trivially solved by breaking the symmetry of the scan by choosing different probe positions for the measurement, such as a spiral scan (Wikipedia, n.d.).

6.3 PTYCHOGRAPHY IN BRAGG CONDITION

Ptychography has been widely developed for the transmission geometry, together with the use of other techniques such as tomography to generate ultra high resolu-

tion reconstruction of 3D volume Holler et al., 2017. However, when it comes to crystalline material where the interest lies in imaging not only the density but also the displacement fields within the sample, the only solution is to use the Bragg geometry. As a result, scientists of the CDI field started looking into the applicability of ptychography in the Bragg scattering condition since 2011Chamard, Dollé, et al., 2010; Hruszkewycz, Holt, Proffit, et al., 2011; Hruszkewycz, Holt, Tripathi, et al., 2011; Godard, Allain, and Chamard, 2011. Numerous techniques in Bragg geometry have been derived from the basis of ptychography, namely the collection of diffraction patterns from overlapping illumination areas. A review of these techniques together with the main associated limitations are given in the following.

6.3.1 *Bragg Projection Ptychography: a 2D case*

Prior to considering the case of 3D reconstructions, a projection version of Bragg Ptychography is discussed. It relies on a ptychographical scan performed at one Bragg angle, preferentially at the exact Bragg condition. In comparison to the 3D case, no angular scan of the sample is needed, and the inversion process does not need any constraint. All in all, this yields a technique with rapid throughput and high-resolution 2D imaging capabilities, that can be used as a premier structural characterization tool for nanocrystalline samples.

The particularity of this method is that it enables to reconstruct the projection along the exit wave vector. Indeed, the far-field 2D coherent diffraction pattern measured at the Bragg condition from a locally illuminated crystal is the FT of the projection of the crystalline volume along the exit wave vector $\vec{k_f}$. Thus, using standard Ptychography algorithms, the sample projection can be reconstructed by assuming that the illumination is an infinite plane wave, apertured by the complex sample shape function. For instance, the combination of 2D Ptychography algorithms enables one to reconstruct both the projected incident beam and a projection of the sample density and phase.

In 2D Bragg Projection Ptychography (BPP), the retrieved object lies within a plane parallel to the detector, thus a strong assumption needed is that the sample is homogeneous in depth. The projection assumption along the exit wave vector also implies a change in the geometry of the scan, as it has to be seen with respect to this projection unlike in the case of forward Ptychography. Indeed, the final solution is obtained in a plane normal to the exit wave vector, and each illumination position has to be evaluated according to this final geometry.

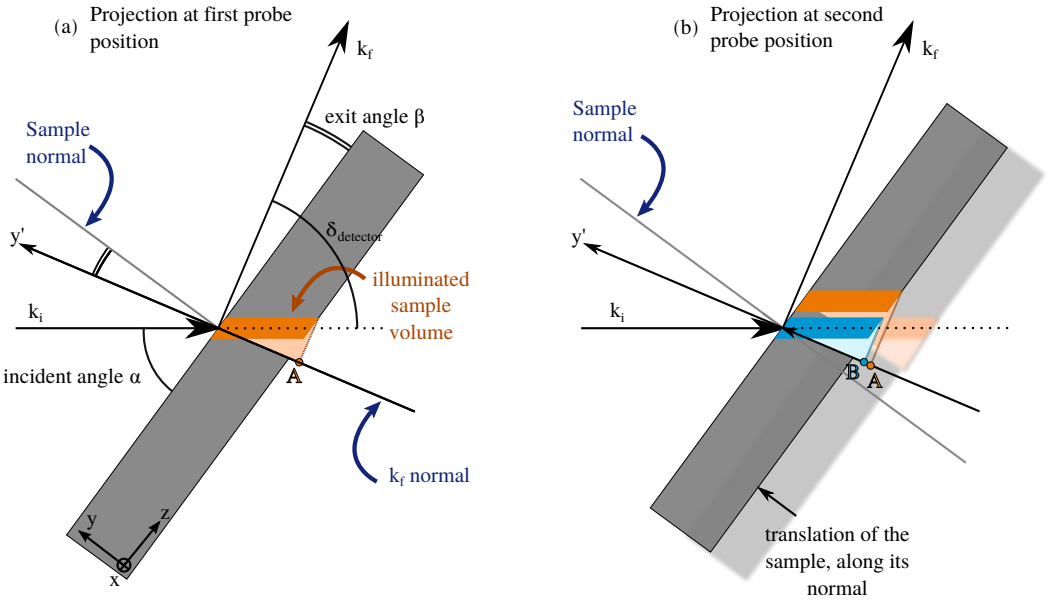

Figure 6.2 – 2D Bragg Projection Ptychography. Relationship between a sample displacement and the related displacement in the projected detector plane. In (a), the orange portion represents the illuminated sample volume, which is then integrated along $\vec{k_f}$. All the angles related to the Bragg scattering geometry are depicted, together with the frame associated to the sample (x, y, z) and the one associated with the detector (x, y'). The light orange area represents the projection of the illuminated sample area onto the $\vec{k_f}$-normal plane (x, y'). In (b), the sample has been translated in the direction along its normal, and the new illuminated sample volume is indicated in blue. Again, the light blue area represents the projection onto the $\vec{k_f}$-normal plane. Finally, the A and B points account for the displacement magnitude of the beam projection. This figure shows that in the case where the exit angle is small compared to the Bragg angle, a large displacement of the sample along its normal derives into a small displacement in the $\vec{k_f}$-normal plane. This results in an anisotropic pixel size, larger in the y' direction. (Inspired from supplementary informations of Hruszkewycz, Holt, Murray, et al., 2012)

Figure 6.2 depicts the relationship between a movement of the sample, along its normal y, and the related displacement projected in the detector plane (x, y'). During an experiment, the beam stays still and the sample is scanned along two orthogonal directions, through a piezo stage mounted beneath it. this way, the usual scanning is performed in the (x, y) plane. Because the x direction vector is common to both the $\vec{k_f}$-normal and $\vec{k_i}$-normal planes in most cases, displacements along this direction are equivalent in both frames. However, the displacement along the y direction vector, normal to the sample, changes the projection position on the $\vec{k_f}$-normal plane in a complicated way. Figure 6.3 shows a more detailed construction

in order to calculate the magnitude of the corresponding displacement along $\vec{y}'$, given a specific translation a along $\vec{y}$:

$$y' = \sin(\beta) \cdot \frac{1}{\tan(\alpha)} \cdot a, \tag{6.18}$$

where β is the exit angle and α the incident angle. When the exit angle becomes shallow, the projection geometry creates an "elongated" solution, where the pixel size in the y' direction can become 10 times bigger than the one in the x direction.

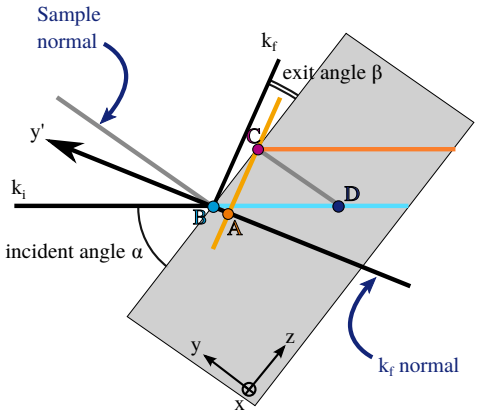

Figure 6.3 – Detailed geometry for the calculation of the displacement in the $\vec{k_f}$-normal plane associated to a translation of the sample along its normal. The blue and orange lines depict the illuminated sample "areas" before and after translation, respectively (see Figure 6.2). The translation of the sample is represented by the $\vec{DC}$ vector and the A and B points depicts the projection of the first point of the illuminated sample "areas", before and after translation respectively. Then, the magnitude of $\vec{AB}$ can be calculated using $\left\|\vec{CB}\right\|$, the exit angle β and the incident angle α, in the two triangles (ABC) and (BCD): $\left\|\vec{AB}\right\| = \left\|\vec{DC}\right\| \sin\beta/\tan\alpha$. Note also that the direction of the two displacements are the same.

In 2012, Hruszkewycz *et al.* published the first paper describing the use of this new 2D BPP method, applied to the quantitative imaging of lattice distortions in epitaxial semiconductor heterostructure Hruszkewycz, Holt, Murray, et al., 2012. At the Hard X-ray Nanoprobe beamline (APS), they focused a 11.2 keV beam to a 85 nm spot onto a rectangular multilayer heterostructure made of a 15 nm etched SOI layer capped with a 65 nm thick epitaxial SiGe stressor layer. In order to collect a ptychographic dataset, the beam was scanned along the sample onto a 101×3 grid, with step size of 25 nm, while the detector, located at 65 cm from the sample, collected the diffraction patterns at the exact (004) Bragg reflection of SiGe. Various numerical simulation were performed in order to compare the measured diffraction dataset to the model of $\vec{k_f}$-projection of the illuminated thin films. Moreover, care was taken in order to establish the very center of the experimental Bragg angular

scan before scanning, as it is a key parameter for the reliability of the CDI reconstruction I. K. Robinson, Vartanyants, et al., 2001; Vartanyants and I. K. Robinson, 2001; I. K. Robinson and Vartanyants, 2001. The 13 µm-width pixels of the 1024 × 1024 detector were binned 2 × 2, as the oversampling factor was high enough to shrink down the size of the diffraction array, which leads to a reduction of the computational time. Hence, the pixel size of the reconstruction was of 2.68 nm. Then, the PIE algorithm was used with a simulated beam in order to reach a first estimation of the sample, which was in turn implemented as an initial guess for the DM algorithm. After 500 iterations, the final solution was conserved. Note that no constraint was needed to achieve an accurate reconstruction. Moreover, they were able to estimate the spatial resolution of the reconstruction using the sharp edge of retrieved density: 16 nm. To conclude, the retrieved phase allowed them to extract the lattice slope evolution approaching the edge of the sample.

In 2014, Holt *et al.* developed further the analysis of 2D BPP reconstruction and presented a method to extract separately the components of lattice strain and rotation from the retrieved object Holt et al., 2014. The investigated sample consisted in a semiconductor device prototype, composed of SOI lithographically etched into parallel 100 µm-long, 60 nm-wide strips separated by 460 nm. SiGe with 20 at. % Ge stressor were deposited into the etched trenches, inducing in-plane compressive stress in the SOI channel regions. The respective thicknesses of SiGe and SOI were 60 nm and 75 nm. At the Hard X-ray Nanoprobe beamline (APS), a FZP was used to focus a 9 keV beam down to 35 nm FWHM. They used the homogeneity of the sample along the stripes direction to perform "unwound" spiral scans, introducing in this direction an offset of 60 nm to each point in addition to the spiral pattern. Hence structural damage were mitigated and the recorded intensity was ≈10 times higher than in a normal scan mode. The "virtual step" of the spiral scans was of 13 nm. However, the spatial variations of strain or morphology of the reconstructed images will only represent an average in the lines direction. The (004) Bragg reflection of both SiGe and SOI structures were recorded and sufficiently separated in reciprocal space to be reconstructed independently. Neither insights on the algorithms used for the 2D BPP reconstruction are given, nor considerations on the spatial resolution achieved, but the reconstruction are in very good agreement with numerical Boundary Element Method models, notably because of the particular geometry of the sample and the experiments.

To conclude this review of 2D BPP, one should note that only three more papers were published at the time of this thesis, namely the work of Takashi *et al.* on nanoscale dislocation strain fields in thick silicon crystal *Takahashi et al., 2013* and those of Hruszkewycz's group of research, on imaging local polarization in ferroelectric thin films Hruszkewycz, Highland, et al., 2013 and on imaging domain

patterns in epitaxial thin films Hruszkewycz, Zhang, et al., 2016. As a result, this shows the wide range of applications of 2D BPP, an imaging that can reach high-resolution reconstruction of spatial variations, such as strain, tilt or polarization. Nonetheless, the technique is limited to well-defined geometries, and assumptions have to be made in order to quantitatively exploit the results.

6.3.2 *3D Bragg Ptychography: numerical and experimental studies in the literature*

NUMERICAL DEMONSTRATION Firstly, 3D X-Ray Bragg Ptychography was introduced by Godard, Allain and Chamard Godard, Allain, and Chamard, 2011 as a technique that would particularly tackle the case of highly non-homogeneous strain fields through a numerical demonstration. Starting from a simulated strained two-dimensional sample, the ptychographical problem is solved for both the known illumination case and the most difficult case of unknown illumination.

In order to do so, the authors developed a constrained PIE (cPIE) algorithm, that introduces a regularization constraint applied on the exit wavefield modulus inside the main loop of PIE. This regularization constraint comes from a very accurate estimate of the strained sample, obtained from the monitoring of the diffraction patterns measured at each beam position. In a first step, the shape of the object is estimated. As in a SXDM experiment, the integrated intensity at each position leads to a good estimate of the object modulus, which then need to be interpolated on a grid whose step matches the inverse of the Fourier space extent, and deconvoluted by the probe distribution to compensate the broadening introduced from the finite beam size. In a second step, the phase of the object is estimated. As the center of mass of the Bragg diffraction pattern is mostly governed by the phase associated with the effective electron density of the sample, mapping the relative shift of the Bragg peak with regard to a reference reciprocal space position gives rise to a first order approximation of the gradient of the phase of the object. Indeed, a peak shift of M pixels along a given direction on the detector is produced by a linear phase with a slope of $2\pi\frac{M}{N}$ radians per pixel, N being the number of pixel on the detector along the considered direction. After an other interpolation of the retrieved phase gradients, integration can be performed and a good estimate of the strained object provided.

Using approximately 2500 inversion steps and a known illumination, the cPIE leads to a much more satisfying solution whereas the PIE is far form converging to the true solution. When introducing noise in the diffraction patterns, the retrieved phase is still satisfactory with cPIE, while the retrieved modulus starts showing voids and irregularities. With an unknown illumination, the cPIE leads to reasonable phase field retrieval, but requires twice the average intensity on the whole

detector at each illumination position. Note that the algorithm was tested for two overlapping ratio $\mathcal{O}$ quantifying the redundancy of the ptychographical dataset, 46% and 35%, with increasing quality observed in the results for larger $\mathcal{O}$. Within the assumption that the probe can be assimilated to a Gaussian of radius r_0, the surface overlapping ratio - preferred over the linear one - is given by the analytical expression :

$$\mathcal{O} = r_0 \left(2r_0 \arccos\left(\frac{R}{2r_0}\right) - R\sqrt{1-\left(\frac{R}{2r_0}\right)^2} \right) / \left(\pi r_0^2\right) \tag{6.19}$$

where R is the step distance. It is worth stressing out that this numerical demonstration has been performed in a simplified case, where the diffraction patterns are acquired at only one Bragg angle, hence no depth information is recovered but only a 2D slice. However, the authors claim that by using the same technique as in Bragg CDI, *i.e.* the angular scanning of the sample to explore a 3D volume of the reciprocal space, the 2D approach can easily be extrapolated to 3D without need for tomographic methods Guizar-Sicairos and Fienup, 2008.

6.3.2.1 *First experimental reconstruction*

After this numerical introduction, a first publication with results from an actual ptychographic dataset was published by Godard *et al.* Godard, Carbone, et al., 2011, dealing with patterned Silicon-on-insulator wafer composed of two 40 nm thick Si <110> lines.

A particular focus is going to be put on the experimental conditions. A one-dimensional line scan with a 300 nm step size was performed along a direction transverse to the parallel lines, and at each scan position a 0.4° wide rocking curve was performed, scanning the incident angle with steps of 0.04°. The acquisition time was set to 50 s by frame with a detector mounted 1.17 m downstream, and the illumination FWHM was of 200 x 600 nm^2 at the focus, impacting on the sample with a 22.35° incident angle at 8 keV. These figures are recalled here to act as a reference point to compared with the ones used during the experiments carried on in the scope of this thesis. Within the experimental conditions of the experiment, the elongated footprint of the illumination onto the sample is evaluated to give rise to a probe of radius 300 nm, hence the overlapping ratio derived from equation 6.19 is of 39%. As the measurement-sampling rate was too small in the rocking curve direction, with only 0.4° explored, the authors increased by a factor of 2 along the corresponding real space direction. All in all, the reciprocal space voxel size resulting from the experimental conditions is of 1.9 x 1.8 x 11 x $(10^{-3})^3$ nm^{-3}. Furthermore, the resolution claimed in the real space direction corresponding to the

rocking curve is of 40 nm, which is actually the expected size of the sample. Hence, the representation of the results may have to be considered with care.

6.3.2.2 *Dealing with undersampled dataset*

Nonetheless, these two first publications paved the way for more trials of 3D Bragg Ptychography experiments. Firstly, Berenguer *et al.* showed that 3D X-ray Bragg Ptychography could also be used to retrieve an elongated sample from undersampled dataset in the rocking curve direction Berenguer et al., 2013. Introducing a penalization on the reconstructed density through the addition of a regularization term containing *a priori* information, typically about the object thickness, to the cost function of a scaled gradient algorithm. Interestingly, they stressed that, given the particular framework of a Bragg CDI measurement, a constraint on the thickness of the object actually provides a constraint along the two real-space direction of the scattering plane. This is due to the non-orthogonality of the conjugated frames, depicted in Figure 6.4.

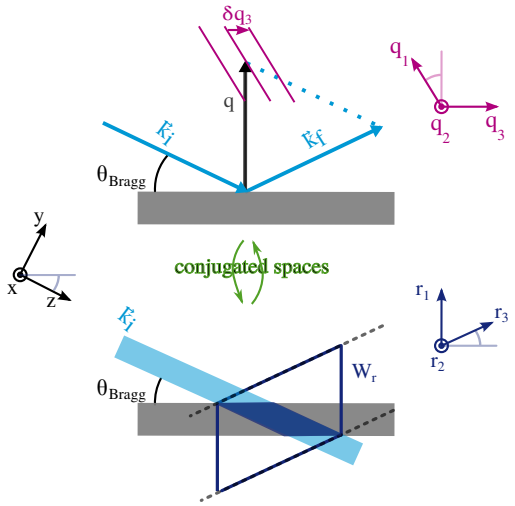

Figure 6.4 – Conjugated spaces involved in Bragg CDI imaging. The $(\vec{x}, \vec{y}, \vec{z})$ basis is the fundamental one of the laboratory, while the sample is rotated with a θ_{Bragg} angle around the x-direction. (Top) Reciprocal space measurement basis is $(\vec{q_1}, \vec{q_2}, \vec{q_3})$ with $(\vec{q_1}, \vec{q_2})$ in the detector plane and $\vec{q_3}$ being the direction probed along the angular scan (rocking curve). (Bottom) The conjugate basis, in real space, where the object is reconstructed, is $(\vec{r_1}, \vec{r_2}, \vec{r_3})$. The blue frame W_r is the smallest numerical window which fully contains the exit field, represented in dark blue. (reused from Berenguer et al., 2013)

Numerical and experimental demonstrations are given in the paper, applied to a set of two parallel silicon lines, of thickness and width of 180 nm and 950 nm respectively, spaced by 2 µm and assumed to be strain free on average. The ptychographical dataset was obtained in the vicinity of the (220) Bragg reflection, by scanning the sample transversely to the lines, with a total of 11 positions separated by

approximately 500 nm. The rocking curve, willingly undersampled, was made of 8 steps of 0.01° and each frame was taken from a 50 s-long exposure. Data acquisition was performed at CRISTAL beamline (Soleil synchrotron), with a monochromatic beam at 8.5 keV, whose central spot at focus reached 3 x 1 μm^2, and an Andor detector (1024 x 1024 pixels of size 13 x 13 μm^2) located 2 m away from the sample. From the regularized ptychographical procedure, the claimed resolution was about 80 nm. Finally, a description of the crystalline properties is lacking, restricting the demonstration to the imaging of the 3D density solely.

6.3.2.3 *Exploitable description of the 3D crystalline properties*

"STRAIN IN A SILICON-ON-INSULATOR NANOSTRUCTURE REVEALED BY 3D X-RAY BRAGG PTYCHOGRAPHY" Then, Chamard *et al.* demonstrated that 3D X-ray Bragg Ptychography could quantify in 3D a displacement field in a lithographically patterned silicon-on-insulator nanostructure Chamard, Allain, et al., 2015. Willing to overcome the limitations of 2D reconstruction and lack of crystalline properties information, the authors developed a highly controlled experimental procedure allowing for higher robustness and better sensitivity of a 3D reconstruction, based on not only an accurate definition of the X-ray illumination but also on an optimized inversion procedure.

The key demonstration of the article is performed on a shot-noise corrupted numerical dataset, created from a meticulous pre-analysis of the experimental diffraction patterns. The experimental conditions are the following. At the ID13 beamline (ESRF), a 12 keV beam was focused down to 0.31 x 0.23 μm^2 (H x V) and characterized with a method inspired by Quiney and detailed in the paper Quiney et al., 2006 [2]. A 180 nm thick silicon-on-insulator, mounted in the horizontal scattering condition, was scanned along the vertical direction, normal to the scattering plane, with 15 illumination-to-sample positions each separated by 50 nm. Using equation 6.19, the overlapping ratio is found to be around 72.5%. The scanning was performed at 21 different incident angles, covering a 0.28° angular range, in the vicinity of the (220) Bragg reflection of silicon (θ_B =15.1°), while the diffraction patterns were recorded on a Maxipix detector (516 x 516 pixels of size 55 μm) at a distance of 2.25 m from the sample. All these experimental conditions lead to a voxel size in the conjugate direct space of 7.9 x 7.9 x 21 nm^3, assuming no cropping nor padding.

The retrieval procedure relied on a conjugate gradient algorithm chosen to optimize the Poissonian likelihood, with the introduction of a regularization term aiming at constraining the object within a film-like support. The initial guess was the

2. Note that this Quiney method leads to probe with phases that are quite continuous, and does not provide a mode decomposition. For these reasons, the probe retrieval with Siemens star reconstruction using forward ptychography could be preferred.

strain-free model, with a shape close to the SOI pattern nominal shape. The final reconstruction yields a good accuracy with the nominal object shape studied by scanning electron microscopy, even if some density fluctuations remain. From the 3D plot of the retrieved density presenting sharp edges in all three direction of space, the authors claim a resolution of 50 x 45 x 15 nm^3. However, the resolution being smaller than voxel size in the last direction, this implicitly suggests that some padding and/or interpolation of the diffracted intensity along the rocking curve direction have been performed. Nonetheless, the specific behavior of the displacement field component u_{220}, notably at the bottom interface and at the in-plane edge, is in good agreement with the model made to fit with the particular behavior of the diffraction patterns.

"NON-DESTRUCTIVE THREE-DIMENSIONAL IMAGING OF CRYSTAL STRAIN AND ROTATIONS IN AN EXTENDED BONDED SEMICONDUCTOR HETEROSTRUCTURE" In Pateras et al., 2015, Pateras *et al.* managed to obtain an accurate reconstruction of bonded semiconductor heterostructure, imaging strain and tilt of the crystalline lattice at the interface of an InP stack and a 40-nm thick InGaAs layer. At the ID13 beamline at the ESRF, they performed a 180-frames rocking curve (of 0.54° angular range) at the (004) Bragg reflection, repeating it at each position of a 11 x 9 steps scan of the sample. In order to avoid saturating the detector and to increase signal-to-noise ratio, the same ptychographical scan was performed 3 times, and summed up prior to the reconstruction. From a 2D Maxipix detector mounted at 1.38 m from the sample, the author claims a voxel size in the orthogonal direct space of 15.5 x 16.5 x 9 nm^3 (in x,y,z, see Figure 6.5 for axes reference) which accounts for a 3D window in reciprocal space of 130 x 120 x 180 pixels. In order to characterize the X-ray illumination, the Quiney method was used, based on the simple and fast measurement of the overfocused direct beam intensity pattern performed with a high-resolution camera.

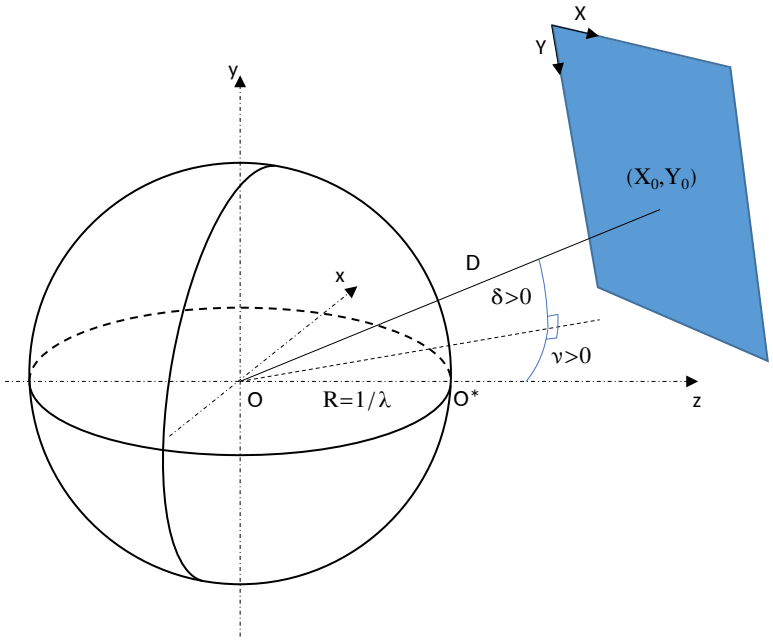

Figure 6.5 – Bragg diffraction geometry. The detector orientation depicted here follows the default CXI convention with a 'top, left' origin as seen from the sample. Note the inversion of the x and y axis between the 'laboratory' reference frame (O, x, y, z) and the detector reference frame (which points towards the detector and follows the 'top, left' origin for pixels).

Then, the retrieval process of the object relied heavily on a very accurate pre-modeling of the sample, which was used as an initial guess of the iterative algorithm plus as a regularization term throughout both of the 1000 iterations of ordered-subset and 1000 iterations conjugated scaled-gradient, applied in that order. Moreover, a finite-thickness planar support (353 nm thick along the out-of-plane direction of the sample) was key for the algorithm to converge. Finally, prior to a detailed discussion about crystal plane tilts, the author estimates the resolution to be about 9 nm in the (001) direction from the broadening of the out-of-plane strain at the InP/InGaAs interface. One could also stress that the computing time to perform the whole inversion, rarely given in publications, was about 117 hours.

"REVEALING CRYSTALLINE DOMAINS IN A MOLLUSC SHELL SINGLE-CRYSTALLINE PRISM." Finally, the example of crystalline domains in a mollusc shell single-crystalline prism retrieved by 3D X-ray Bragg Ptychography was published by Mastropietro *et al.* Mastropietro, Godard, et al., 2017. Prior to the Bragg Ptychography experiment at the ID13 beamline, the authors investigated the structure of the sample by means of Coherent Anti-Stokes Raman Scattering microscopy Cheng and Xie, 2004. This gave them additional insight, notably about the fluctuations in carbonate density. An analysis of the speckle patterns allowed the authors to estimate the presence of several domains and their shape within the elongated sample, hence to

build a numerical sample as close as possible to the real object, which is key for the iterative cPIE to converge.

For the Ptychography experiment, a 15 keV probe was focused down to 80 x 100 nm^2 (H x V, FWHM) and characterized with an approach derived from the Quiney method Chamard, Allain, et al., 2015. The longitudinal coherence of the beam was found to be large enough to ensure full illumination of a sample of thickness up to 1.9 µm, at the (110) Bragg reflection. As the calcite prism thickness has been estimated to 1.75 µm, the sample was considered under coherent illumination along its width. The diffraction dataset was recorded at a Bragg angle of 9.6° on a 2D detector located 2.6 m from the sample while scanning the sample across the beam with steps of 45 nm, over a 9 x 9 point mesh. Using equation 6.19, and a beam radius defined as half of the FWHM characteristic size, one gets an overlapping ratio of 45% (resp. 32%) in the horizontal direction (resp. vertical). The step size of the angular scan was set to 0.007° with an exposure time of 30 s by frame. In order to reduce the computing time, the 3D volume of reciprocal space was reduce to 286 x 286 x 94 pixels, *i. e.* cropping the detector array and dividing the number of points in the rocking curve by 3. This results in a direct space pixel size of 13.7 x 13.7 x 7.2 nm^3.

As in the previous paper from Chamard *et al.* ibid., the inversion was then performed with an optimized procedure, extensively tested on numerical data simulating as closely as possible the experimental conditions and sample. In order to constrain the thickness of the solution, a regularization term was introduced in the criterion. A serie of reconstructions was performed with different thicknesses in the regularization term while monitoring the error-metric. When the regularization thickness was too thin, the error-metric was found to diverge, whereas when the regularization thickness was too thick, the error-metric would shrink up to a point where the regularization would not impact the reconstruction anymore. That way, the inflection point of the L-curve (monitoring the error-metric versus the thickness) gave the authors the optimal thickness according to the dataset. The final reconstruction was obtained after 100 cycles of ordered-subset algorithm, which was then followed by 100 cycles of conjugated gradient algorithm.

A relevant discussion on the spatial resolution of the solution is given in the supplementary information of the paper. Obviously, the voxel size of the reconstructed object in direct space does not account for an estimation of the spatial resolution. Three different approaches are given to estimate the latter. First, the extent of the diffraction patterns in the three directions of the dataset volume gives an upper limit of the spatial resolution, estimated to 35 nm in this case from a 2-photon threshold. However, this does not take into account the quality of the inversion process. To do so, the authors proposed to calculate the extent of the ratio of the square of the reconstructed diffracted amplitude and the experimental intensity recorded on the

detector and integrated along all ptychographical positions. From a threshold of 10%, the 3D spatial resolution is estimated to 48 x 62 x 54 nm^3. Finally, the thicknesses of the boundaries between two adjacent mis-oriented domains can give a third estimation of the resolution, estimated here at 40 $\pm$ 10 nm along the three directions. Note that this last method requires the presence of sharp interfaces, and that the Fourier Shell Correlation approach is out-of-reach from the narrowness of the data, which prevents from extracting two still-converging sub-data sets, as it will be the case in most of ptychographical datasets.

6.3.3 *3D Bragg Ptychography: limitations*

The previous section investigated the development of the 3D Bragg Ptychography technique, but although the success of several experiments, one has to stress out that the technique suffers from many limitations, which can even corrupt an entire dataset.

To begin with, it is the quality of the dataset that will define the success of a 3D Bragg Ptychography reconstruction. As for a Bragg CDI experiment, visibility and extent of fringes in the diffraction patterns are key to consider phasing a dataset. Diffuse scattering, from *e. g.*, a substrate, can also be a source of struggles for the algorithms to converge, no matter the size of the beam and the overlapping ratio of the scan. As a result, all the reconstructions that have been published so far emanate from high SNR Bragg peak with very small background scattering. During the coherence diffraction experiments conducted on the ultra-thin sSiGe nanostructures, the thickness of the sample was another source of limitations, both for a numerical point-of-view (pixelation of a 2-voxels thick object that will be discussed in section 6.4) and regarding the scattered intensity. Moreover, it is important to evaluate how that the nanofocused beam, carrying a high flux density, can damage the sample throughout time.

One can divide in two categories the usual difficulties that arise during a nanoprobe experiment involving scanning and diffraction: setup instabilities and beam-to-sample misalignment. The setup instabilities are of two kinds: short-time-scale vibrations and long-time-scale drifts. The former can be assessed from the variations of the low count intensity pixels, when comparing two adjacent beam-to-sample positions, at the same Bragg angle. A knowledge of the sample is then vital to be able to differentiate structural variations from setup vibrations impacting the diffraction pattern. Long-time-scale drifts are more difficult to assess in case of extended sample. Mainly, temperature fluctuations or mechanical drifts will fall within this category. In a typical synchrotron experimental hutch, thermal isolation is present to avoid temperature fluctuations, but sometimes a continuous air flow

at a particular frequency is enough to create visible drifts of the sample. On the other hand, mechanical drifts are a result of the accuracy of the translation stage. Indeed, in order to ensure redundancy in the dataset, translation steps smaller than about a fraction of the beam size have to be chosen. This becomes delicate as soon as the beam reaches characteristic sizes below a few tens of nanometers. Besides, while piezoelectrical translation stages are able to provide such specifications in an horizontal setup, vertical scattering geometry requires the stage to be tilted. As a result, mechanical stresses arise and decrease the translation performance. One has to stress that a 3D Bragg Ptychography experiment can lead to measurement time of several hours (a typical process composed of $\approx$100 scan positions, repeated at up to 200 incident angles, with 0.8 s exposure time, can last more than 4 h without considering the dead times) whereas the scan positions have to remain the same while rocking the incident angle.

The second category relates to the impact of beam-to-sample misalignment. Firstly, it has been showed that the shrinkage of the beam footprint during the rocking curve can be neglected. Indeed, the reduced extent of the angular scan, of less than a degree Pfeifer et al., 2006, leads to a footprint shrinkage that is smaller than the typical size of one voxel (10 nm). Hence, the illuminated volume throughout the angular scan can be considered constant. However, the main issue is the alignment of the beam-to-sample position with respect to the center of rotation of the experimental stage. In practice, because of the sphere of confusion of the diffractometer, this condition is never fully fulfilled. As a result, any shift of the illuminated volume from the center of rotation of the stage will lead to the illumination of different volumes during the rocking curve. This can be analytically derived. For a shift l_{COR}, an angular scan of amplitude $\Delta\theta$ around an incidence angle α, the corresponding motion of the illuminated volume will be :

$$\Delta x = \frac{l_{\mathrm{COR}}\Delta\theta}{\tan\alpha} \tag{6.20}$$

For an angular extent of less than a degree, at incident angle above 20°, a discrepancy between the center of rotation and the beam-to-sample position of up to 500 nm is bearable as it will induce a shift of less than 15 nm, comparable with the typical voxel sizes.

In conclusion, the use of 3D Bragg Ptychography is appealing as it allows imaging structural variations within an extended sample, but the necessity of a nanofocused beam together with rotation stages prevents the technique from being robust enough to be use routinely. The mechanical difficulties and the extensive acquisition time that arise from the particular geometry make of 3D Bragg Ptychography a technique limited by sample positional drifts and radiation damage. The latter

limitation is common to all techniques involving X-ray scanning as was addressed by Howells *et al.* Howells et al., 2009. For instance, a too long exposure under X-rays at 8 keV can bend and tilt 60 nm-thick SOI lines as illustrated in Figure 6.6. After a full 3D Bragg ptychographical scanning was performed, with 256 positions at 14 different incident angles, with 2 seconds exposure by scanning point (beam size of 450 nm (H) $\times$ 75 nm (V)), the diffraction from the SOI lines (004) Bragg peak is diverted on the sides of the detector, as a result of tilting of the lattice. This can be due to a volume expansion of the thin oxide layer below the Si lines, as already discussed in Mastropietro, Eymery, et al., 2013.

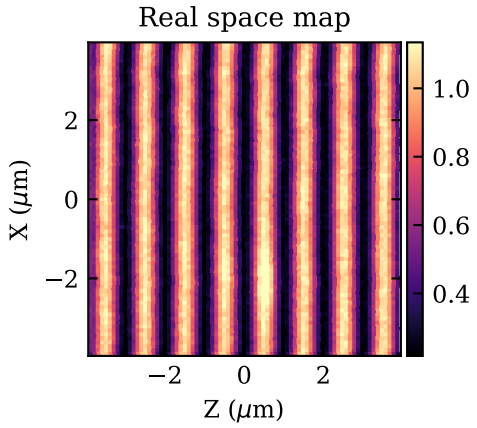

(a) Integrated diffracted intensity map before X-ray exposure.

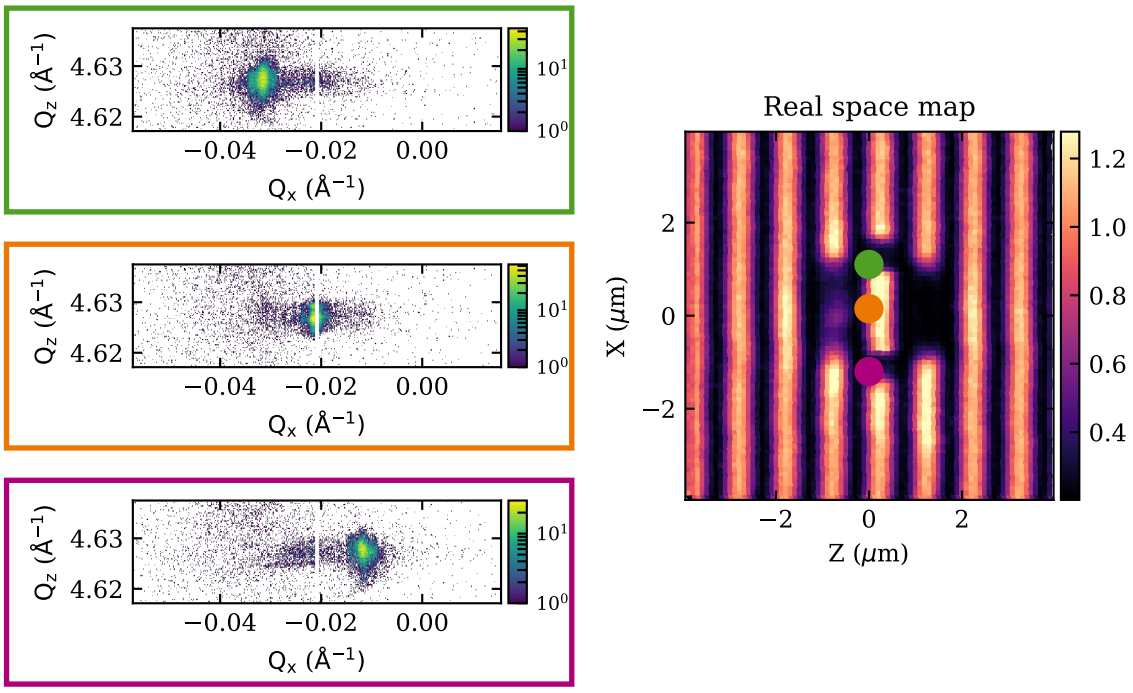

(b) Integrated diffracted intensity and diffraction patterns at selected locations, after X-ray exposure.

Figure 6.6 – X-ray radiation damage on SOI sample. A 60 nm thick SOI layer made of regularly spaced 500 nm-width lines is damaged by a 12 hours-long exposure to X-rays. 6.6a Integrated diffracted intensity space map before performing spiral scan of 256 points, 2 s exposure per point at 14 incident angles. 6.6b The same region of the sample, after performing a spiral scan, with the diffraction patterns at different locations on the sample. The colored frame (green, orange, purple) around the diffraction patterns are related to the corresponding colored points on the real space map, where the lines are clearly modified by the radiation damage. The footprint of the spiral scan is visible on the real space map. The diffraction is shifted to the edges of the detector depending on the beam-to-sample position.

6.3.4 *3D Bragg Projection Ptychography*

6.3.4.1 *Single-angle*

In order to cope with the main limitations of 3D Bragg Ptychography, the idea was to reduce the full Bragg ptychographical dataset, *i. e.*, a set of diffraction patterns recorded at each position of a spiral scan for different incident angles describing an angular scan, to the same as in 2D BPP, with diffraction patterns recorded at solely the exact Bragg angle. Then, as demonstrated by Hruszkewycz *et al.*, while two dimensions of the problem are encoded in reciprocal space by the diffraction in the detector, the information about the third dimension is actually encoded in real space, by the displacement of the beam towards the detector Hruszkewycz, Allain, et al., 2017. Indeed, translating the beam in real space in two directions (into/out of the page, towards/away from the detector) actually results in diffraction patterns that yield structure profiles within different columns of the 3D object.

After gathering a ptychographical dataset collected at a given HKL-index Bragg reflection, the major operator that lies at the heart of single-angle 3D BPP is the back-projection operator. At this Bragg condition and at a given beam-to-sample position j, the diffracted wave $\tilde{\Psi}_j$ is related to the 3D diffracting object O and the probe P_j according to:

$$\tilde{\Psi}_j = \mathcal{F}\mathcal{R}P_jO \tag{6.21}$$

where $\mathcal{R}$ is the 3D X-ray projection operator along the exit beam direction. This projection operator is borrowed from computed tomography. Then, its adjoint $\mathcal{R}^\dagger$ is the back-projection operator that allows converting the 2D diffracted wave back to the 3D object. The main question is then how to calculate the back-projection.

Mathematical explanations of the "beam deconvolution" approach for single-angle Bragg Projection Ptychography can be found in the Supplementary information of ibid. In the PyNX library, three different approaches were implemented. In order to present them, one can recall the algebraic problem of BPP. In order to obtain the two-dimensional wavefront Ψ_j, the product of the probe times the object has to be summed along the propagation direction, for all the volume that falls within the object-probe domain (see Figure 6.7). This domain is discretized into N layers along the Z direction, leading to the expression:

$$\Psi_j(\vec{r}) = \sum_{Z=z_1}^{Z_N} P(\vec{r} - \vec{r}_j)O(\vec{r}) \tag{6.22}$$

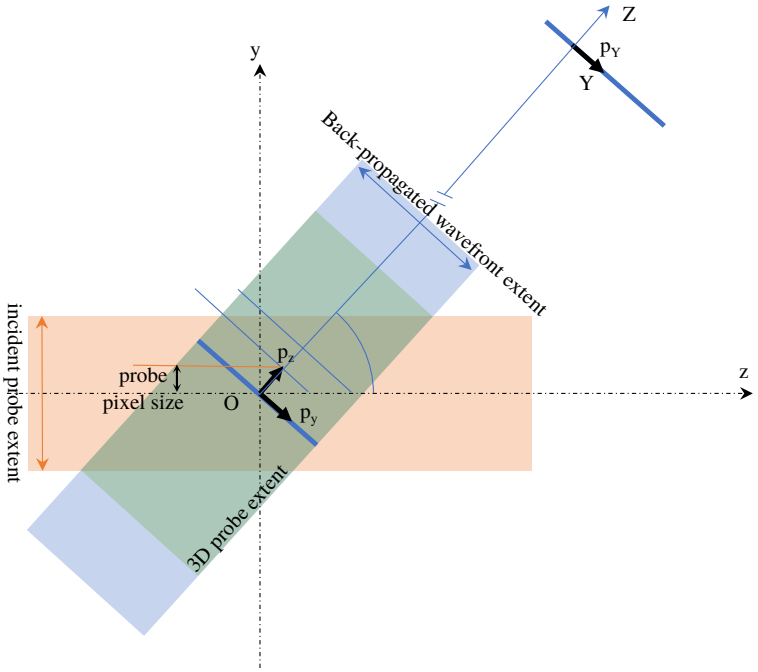

Figure 6.7 – Bragg projection geometry, with the back-propagated wavefront and the incident wavefront of the illumination. The 'laboratory' orthonormal reference frame is (O, x, y, z), whereas the 'detector' reference frame is the laboratory one, after a rotation to point towards the detector, and inversion of both x and y axis (because in the laboratory reference frame y points upwards, whereas on the detector the origin is at the 'top, left', so Y is oriented downwards).

Note that this expression is equivalent to $\mathcal{R}P_jO$, *i. e.*, the wavefront is a 2D object, in the real space and still needs to be Fourier transformed in order to be in reciprocal space. Then, similarly to forward Ptychography, once an updated Ψ_j wavefront has been obtained, updated values for object and probe must satisfy:

$$\min \sum_j \left| \Psi_j(\vec{r}) - \sum_z P(\vec{r} - \vec{r_j}) O(\vec{r}) \right|^2$$

Generally speaking, this is an ill-posed problem, similar to tomography. It follows that for a unique minimum to exist, there must be more (linearly-independent) illuminations than the number N of Z-layers in the probed object. Then, searching for an optimal value for the object, three approaches were considered: object update via replication, object update via incremental update and object update via gradient minimization.

OBJECT UPDATE VIA REPLICATION: Once the Ψ_j wavefront has been back-propagated to object space, the simplest way to spread this wavefront along the Z-layers of the object is to replicate the wavefront along Z (taking into account the support), and

then normalize. In the case of a single illumination j, a trivial solution can be written:

$$O(\vec{r_Z}) = \frac{P^*(\vec{r_z} - \vec{r_j})\Psi_j(\vec{r})}{\sum_Z \left|P(\vec{r_z} - \vec{r_j})\right|^2} \tag{6.23}$$

However, since for a given object voxel the illumination is not the same for all probe positions, equation 6.23 can be weighted depending on the probe amplitude, *e. g.*, minimizing:

$$\sum_j \left|P(\vec{r_z} - \vec{r_j})\right|^2 \left| O(\vec{r_Z}) - \frac{P^*(\vec{r_z} - \vec{r_j})\Psi_j(\vec{r})}{\sum_Z \left|P(\vec{r_z} - \vec{r_j})\right|^2} \right|^2 \tag{6.24}$$

thus:

$$\begin{aligned} \sum_j \left\{ \left|P(\vec{r_z} - \vec{r_j})\right|^2 O^*(\vec{r_Z}) - \left|P(\vec{r_z} - \vec{r_j})\right|^2 \frac{P(\vec{r_z} - \vec{r_j})\Psi_j^*(\vec{r})}{\sum_Z \left|P(\vec{r_z} - \vec{r_j})\right|^2} \right\} = 0 \\ \implies O(\vec{r_Z}) = \frac{1}{\sum_j \left|P(\vec{r_z} - \vec{r_j})\right|^2} \sum_j \left|P(\vec{r_z} - \vec{r_j})\right|^2 \frac{P^*(\vec{r_z} - \vec{r_j})\Psi_j(\vec{r})}{\sum_Z \left|P(\vec{r_z} - \vec{r_j})\right|^2} \end{aligned} \tag{6.25}$$

However, this weight is not unique, and one could for instance weight by the sum of the probe intensity along the entire stack of layers.

OBJECT UPDATE VIA INCREMENTAL UPDATE: Two major issues arise while calculating the 3D object at each iteration when performing object update via replication. Firstly, the uncertainty of the breakdown of Ψ into the contribution from all individual layers makes it impossible to reconstruct the object in a single projection, even in the case where all the computed phases are correct. Secondly, as the update recomputes the entire object at each iteration, there is little chance to learn from the previous iteration: the phases will get better, but there is no clear way to improve the partitioning of Ψ into the contribution from all individual layers. One way to improve this is to only perform incremental updates of the object, by considering the difference between the calculated and back-propagated Ψ:

$$\Delta\Psi_j = (\mathcal{P}_m - 1)\sum_Z P(\vec{r} - \vec{r_j})O(\vec{r}) = (\mathcal{P}_m - 1)\Psi_{j,calc} \tag{6.26}$$

where $\mathcal{P}_m$ is the modulus projection operator, consisting of a propagation to the detector (Fourier transform and quadratic phase factor), applying the amplitudes from the observed diffracted intensity and back-propagating to object space. Then,

the object can be updated in a similar way to what was derived earlier. The quantity to minimize is:

$$\sum_j \left| \Delta\Psi_j(\vec{r}) - \sum_Z P(\vec{r}-\vec{r}_j)\Delta O(\vec{r}) - \sum_Z \Delta P(\vec{r}-\vec{r}_j)O(\vec{r}) \right|^2 \tag{6.27}$$

Ignoring ΔP, the incremental probe, one can get the same relationship as in the object update via replication, but on the incremental update of the object.

OBJECT UPDATE VIA GRADIENT MINIMIZATION: The object derivative can be used as a search direction, and then a gradient minimization algorithm (single-step or full conjugate gradient) can be used. Starting from the derivative versus the object:

$$\frac{\partial}{\partial O_{r,z_0}} \sum_j \left| \Psi_j(\vec{r}) - \sum_Z P(\vec{r}-\vec{r}_j)O(\vec{r}) \right|^2 = -\sum_j P(\vec{r_{z_0}}-\vec{r}_j)\left(\Psi_j^*(\vec{r}) - \sum_Z P^*(\vec{r}-\vec{r}_j)O^*(\vec{r}) \right) \tag{6.28}$$

If the search direction ΔO is known, the optimal value for the object is $O + \gamma\Delta O$, which can easily be minimized against γ (see Appendix C).

The tests carried on with the PyNX library tend to show that the gradient minimization is the method that is leading to the best results, however it is also the more computationally demanding method, as both the object gradient and the γ-determination require looping over all calculated and observed frames.

6.3.4.2 *Multi-angle*

Not only the single-angle BPP suffers from the complexity of the object update, but also requires high-diffraction angles ($>\sim 60°$) as the effectiveness of localizing sample structure along the beam propagation direction is maximized for $2\theta = 90°$ and vanishes when $2\theta = 180°$ or $0°$. In order to cope with the limitations of single-angle BPP without falling back into those of 3D Bragg Ptychography, Hill *et al.* developed a generalized 3D multiangle BPP approach (maBPP) Hill et al., 2018. This approach is based on the measurement of far-field diffracted intensities at a set of angles about a given Bragg peak of the crystalline sample. According to the authors, it allows relaxing experimental constraints as incommensurate positions from one angle to the other can be incorporated into the phase retrieval. As a result, position and angle are two degrees of freedom that maBPP enables to introduce. The main difference with respect to single-angle BPP lies in the expression of the small angular deviations from the Bragg condition as $\vec{Q} = \vec{q} - \vec{G_{HKL}}$, where $\vec{q}$ is the scattering vector and $\vec{G_{HKL}}$ is the Bragg reciprocal lattice vector. This vector $\vec{Q}$ encodes changes in a coherent diffraction pattern due to angular variations along a

Bragg rocking curve. Then, the diffracted waves at the detector can be expressed in a similar fashion as in equation 6.21, using the same notations:

$$\tilde{\Psi}_j = \mathcal{F}\mathcal{R}Q_{\theta_j}PO \tag{6.29}$$

where the term $Q_{\theta_j} = \exp\left(i\vec{r}\cdot\vec{Q}_{\theta_j}\right)$ is a 3D real-space complex-valued phase term that encodes spatial frequencies corresponding to angular deviations from the exact Bragg angle. Introduced in equation 6.22, this factor allows decoupling the object values along the same Z-layers, which will have different coefficients for different angles. Authors used equation 6.29 to derive a gradient minimizing the sum squared error and introduced it into the PIE algorithm. Note that only strongly scattering angles were used, for a total of 8 angles, and 25 iterations were enough to reach a satisfying solution. The implementation of maBPP into the PyNX library is still under development, hence no examples will be presented, but this technique is essential in solving the uniqueness problem of the distribution of amplitude along Z-layers of the object.

6.4 NUMERICAL TESTS OF PYNX BRAGG PTYCHOGRAPHY LIBRARY

Orthonormalization matrix

Before looking at numerical simulation and trial on real dataset, it is important to stress out that the particular geometry of 3D Bragg Ptychography, whether single-angle or not, implies to deal with the conjugated spaces very carefully. Indeed, multiple frames are interacting and rigorous definitions are needed. This is done by following the NeXus convention Könnecke et al., 2015, which defines that the basis frame should be the one of the laboratory with $\vec{z}$ along the direct X-ray beam propagation, $\vec{y}$ up and $\vec{x}$ horizontal, going left as seen from the X-ray source, as depicted in Figure 6.5. Then, the detector is characterized by two rotation angles, the out-of-plane angle, denoted δ and rotating around $\vec{x}$, and the in-plane angle ν rotating around $\vec{y}$. Moreover, note that the default convention of the detector, with a 'top, left' origin as seen from the sample, is such that its frame $(\vec{X}, \vec{Y})$ has opposite sign than the laboratory frame. From this, one is able to define an orthonormalization matrix, that will be used for converting back and forth the object (or probe) coordinates (pixel coordinates in the detector reference frame) to/from orthonormal ones in the reference laboratory frame. A thorough derivation is given in Appendix B

6.4.1 *Strained Si layer, simple model*

In order to test the algorithms implemented in the PyNX library, this section describes a numerical demonstration of 3D BPP. To begin with, a basic check of all the orientations involved in a complete experiment, from the motion of the sample onto the stage to the reconstructed object, through the reciprocal space, was performed via a controlled numerical simulation. A parallelepidic object, 300 nm wide (along x and z) and 60 nm thick (along y), was created with a limited resolution, *i. e.*, a discrete grid with a step being an integer multiple of the basic lattice parameter of Si (here, the step was 5 times a_{Si} =5.4309 Å), resulting in 37632 scatterers. A strain bump was added within the layer through the modification of the vertical coordinate. A displacement $u(y)$ was implemented such as :

$$u(y) = \frac{y}{1000} \exp\left(-\left(\frac{x}{300e-9}\right)^2\right) \tag{6.30}$$

A simple wavefront at 8 keV propagating trough a FZP of 300 µm diameter an 9.8 cm focal length, was used as the illuminating probe. The spiral scan consisted in 320 positions, calculated from an Archimedes spiral with a step size of 20 nm. In order to simulate a (004) Bragg reflection geometry, the coordinates of both the spiral scan positions and the 3D object were rotated around the x-axis of the laboratory frame, with an angle of $\theta_B = 33.53°$, corresponding to the Bragg angle of Silicon at this X-ray energy. The detector located 1 m away from the sample was modeled with a shape of 256 × 256 pixels, of size 55 µm, and its pixels position at a $\delta = 2\theta_B = 67.06°$ angle were converted to scattering vector coordinates in the reference frame. Based on the FWHM of the beam, the overlaping ratio for this setup is of 66% in the horizontal direction, and of 81.1% in the vertical direction because of the beam footprint. Figure 6.8 shows a top view of the sample and the related scan positions, along with a projection of the FZP focused beam on the sample surface.

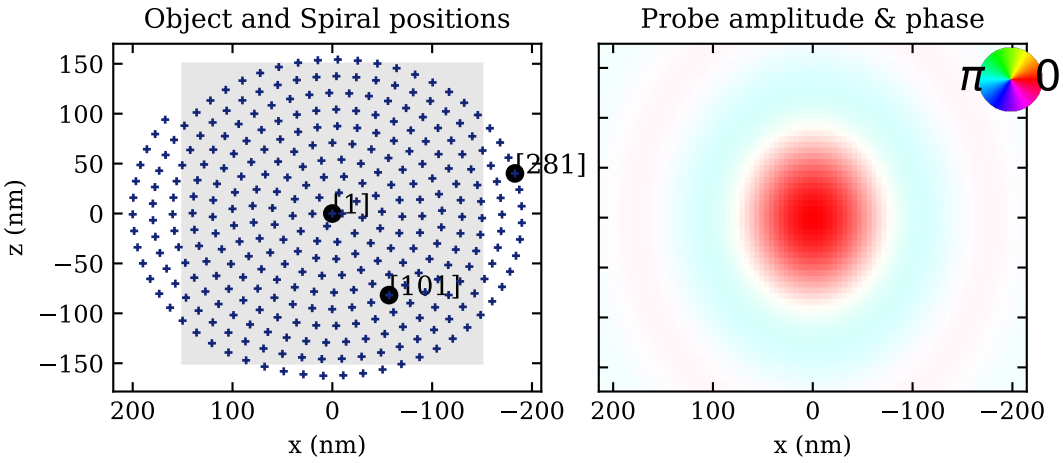

Figure 6.8 – Geometry and beam of numerical 3D BPP simulation. Both subplots are top views, within the sample frame (*i. e.*, the z-axis is rotated by $\theta_B = 33.53°$ around the laboratory z-axis). On the left hand side, the gray area indicates the extent of the SiGe layer, while the blue crosses indicate the 320 beam-to-sample positions. Three distinct positions are highlighted as they will serve as reference for diffraction patterns. Illumination wavefront focused from a FZP of 300 µm diameter and 9.8 cm, at 8 keV. On the right hand side, the projection of the beam onto the sample is depicted. A FZP is considered to be fully illuminated by a plane wavefront originating from a source located 90 m upstream, and an OSA of radius 30 µm is placed 0.2 mm before the focal plane. Both amplitude and phase are represented, described by the HSV colorwheel on the right.

Then, the 320 diffraction patterns were computed numerically using the kinematical sum from each scatterer, after interpolation of the illuminating probe on the scattering positions, assuming the width of the object was small enough to neglect the probe propagation. This was done on a GTX 1060 graphic card, reducing the computational time down to approximately 13 s. A Poisson noise was added to the dataset, assuming a total number of photons of 10^8 over all the frames. Figure 6.9 shows three diffraction patterns, recorded at three different spiral scan positions depicted in Figure 6.8. At the center of the Si layer, the diffraction pattern is centered and symmetric about the q_x, q_y origin of the detector (H, K reciprocal lattice directions). As the beam approaches the edges of the sample, the diffraction pattern gets completely modified, notably the tilt present at the edges elongates the diffraction along H. As a result, the beam samples the lattice distortions within the layer, leading to a modification of the shape and position of the diffraction patterns during the ptychographical scan.

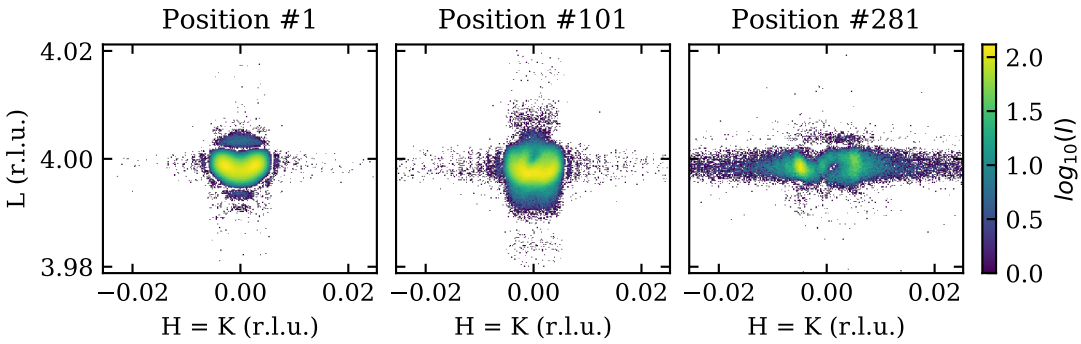

Figure 6.9 – Representative nanofocused coherent X-ray diffraction patterns from a strained Si layer. The position number relates to the ones of Figure 6.8, and differences are evident in the intensity distribution of diffraction images taken from the edge of the square island (position #281) compared to the center of the island (position #1). The effect of out-of-plane strain is also visible as soon as the beam illuminates a volume shifted from the center (such as position #101).

Next, the 3D Bragg Projection module of the PyNX library comes into play. Firstly, one has to create a python class Bragg2DPtychoData for the two-dimensional ptychographic dataset, including the observed diffraction, probe positions, wavelength of the illumination and detector parameters (distance, number of pixels, size of pixels and angles). Secondly, the main class Bragg2DPtycho is initialized, with both the information about the probe, in the reference frame, and from the Bragg2DPtychoData class. One of the attributes of this main class is to calculate the voxel size of the object in the orthonormal frame. In the case of this simulation, it is found to be of 10.65 nm in all directions. This comes from the fact that the detector window is symmetric and the voxel size in the back-projection direction is set to be equal to the smallest voxel size in the two other directions. The following step is to define a support for the 3D object. Indeed, it is crucial to constrain the object reconstruction within a support that confines the extent of the object along the surface-normal direction. This step can be done using a simple equation (*e. g.*, $(\text{abs}(x) < 200e-9) \times (\text{abs}(y) < 200e-9) \times (\text{abs}(z) < 30e-9)$) and a Monte-Carlo integration. In the resulting array, a value of 0 indicates a voxel completely outside the support, while 100 means that the voxel is fully inside, and any value in between is partially inside the support. This floating-point support has been defined in order to avoid step-like issues for the initial object when modeling thin layers that are only a few pixels thick. In the case of the Si layer, a parallelepiped object, slightly larger than the initial object in the horizontal plane and 60 nm thick was used and is shown in Figure 6.10. For the numerical study, the initial object of the 3D BPP was chosen to be strictly equal to its support.

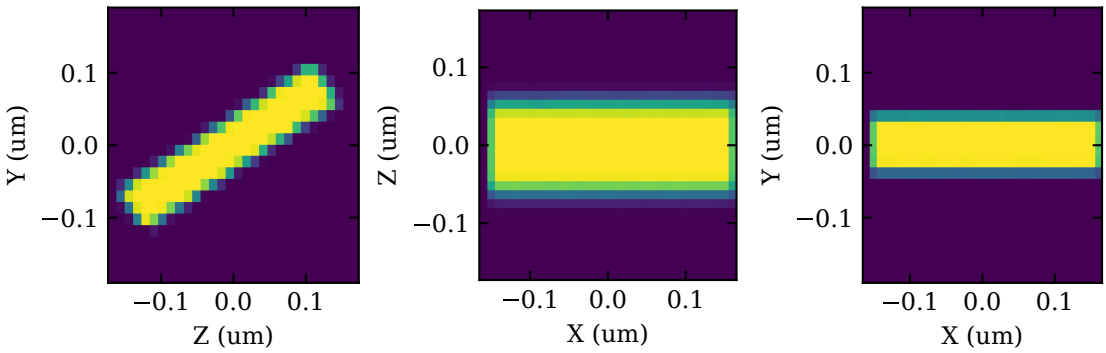

Figure 6.10 – Cross-sections of the support for a thin layer. The (X, Y, Z) frame is the one of the laboratory, following the NeXuS convention, hence the support appears rotated around the X-axis. Note that the cross-sections are taken at the center of the volume. Only the density of the support is displayed, as it has no phase. Moreover, the choice was made to set the initial object strictly equal to the support.

It is of interest to stress out that the set of diffraction patterns of this simulation could also have been calculated using a classical FT approach. Figure 6.11 describes the processes for the two methods, with the advantages that they present. Indeed, using the Bragg2DPtycho class, one can create a support that has the same dimensions as the reference object, and then add the strain to the object, using the relation between phase and displacement (equation 3.23) :

$$Obj_{strained} = Obj_{unstrained} \times \exp\left[2i\pi \frac{y}{1000} \frac{1}{4a_{Si}} \exp\left(-\left(\frac{x}{300\text{e}-9}\right)^2\right)\right] \tag{6.31}$$

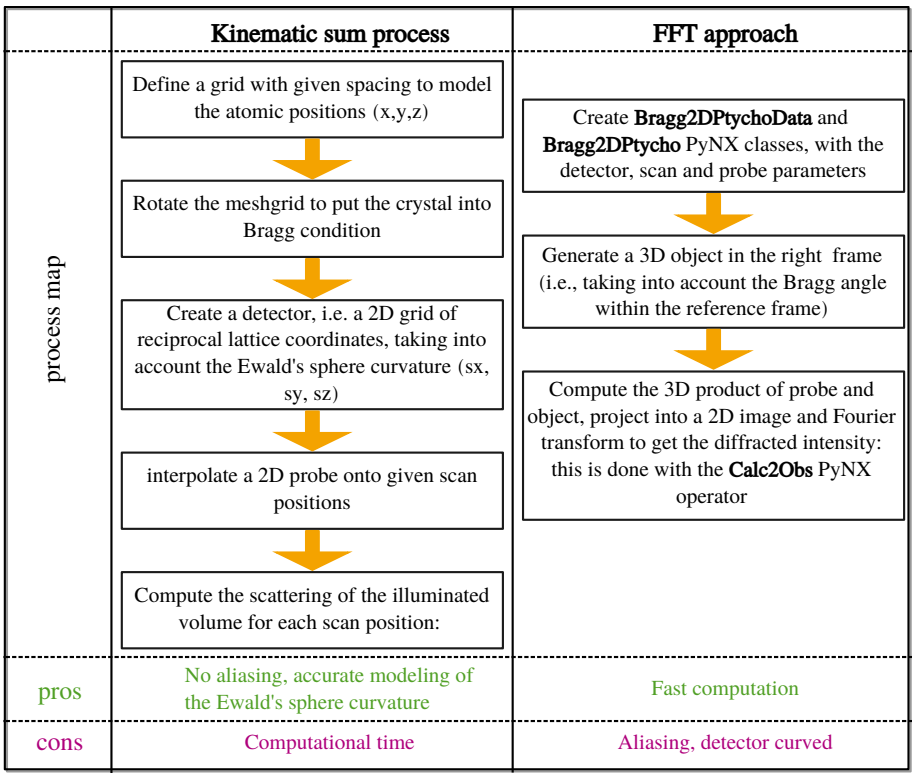

Figure 6.11 – Route for kinematic simulation versus Bragg Ptycho class, using the PyNX library.

Then, the PyNX operator Calc2Obs computes diffraction pattern for given object, probe and beam-to-sample positions, using a FT of the product of the beam with the object, and a Poissonian distribution to add noise. Figure 6.12 shows the comparison between two diffraction patterns calculated at the exact same beam-to-sample position, from the kinematical method and the direct FT method. Obviously, the difference between the two methods can only arise from the difference in the step of the grid used to compute scatterers in the kinematical method, compared to the voxel size of the 3D BPP object. However, in the case described here, there is a factor 2 between the two steps, and no noticeable differences arise. This strengthen the reliability of the FT method, which is in this example 100 times faster.

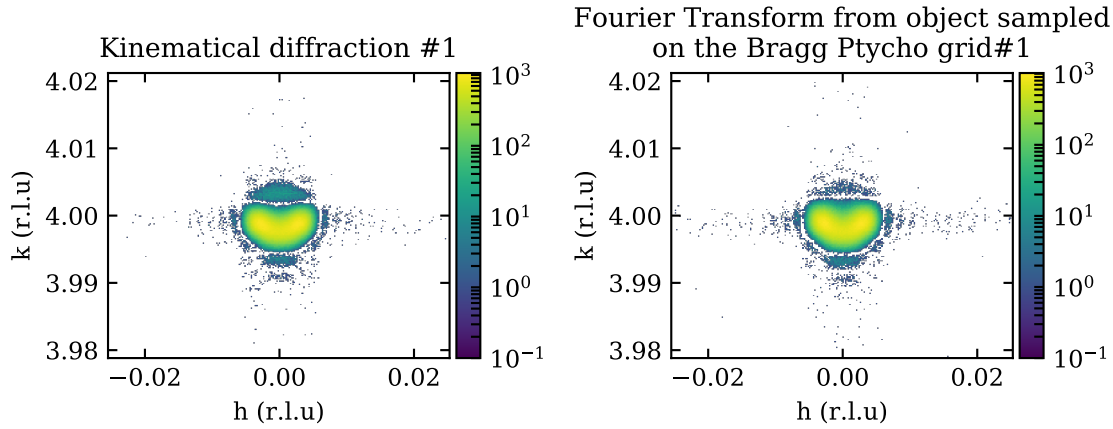

(a)

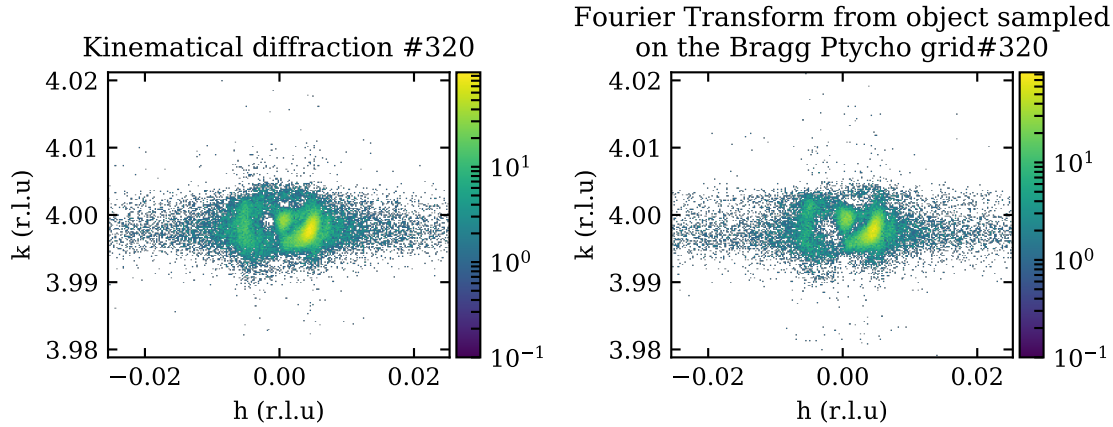

(b)

Figure 6.12 – Comparison of two methods of computation of diffraction pattern from a partially illuminated object. On the left column, the computation was performed using a kinematical sum from all the scatterers within the object, whereas the right column shows the results from a FT of the illuminated object created from a 3D BPP experiment, *i. e.*, limited by the voxel size obtained from the particular Bragg geometry. (a) Diffraction patterns from the central position of the scan, (b) Diffraction patterns from the last position of the spiral scan.

Once the initial object and corresponding support are initialized, a key step is to scale the object with respect to the probe. This is performed through the operator, so that the 3D arrays of object and probe have the same magnitude, and that the product of object times the probe matches the observed intensity (*i. e.*, $\sum \text{abs}(O \times P)^2 = \sum I_{obs}$) . This step is crucial as it will prevent the algorithms from diverging in the early steps. Then, the adapted DM and AP algorithm are used in order to retrieve a solution. 40 iterations of DM are followed by 40 iterations of AP to give the result described in Figure 6.13.

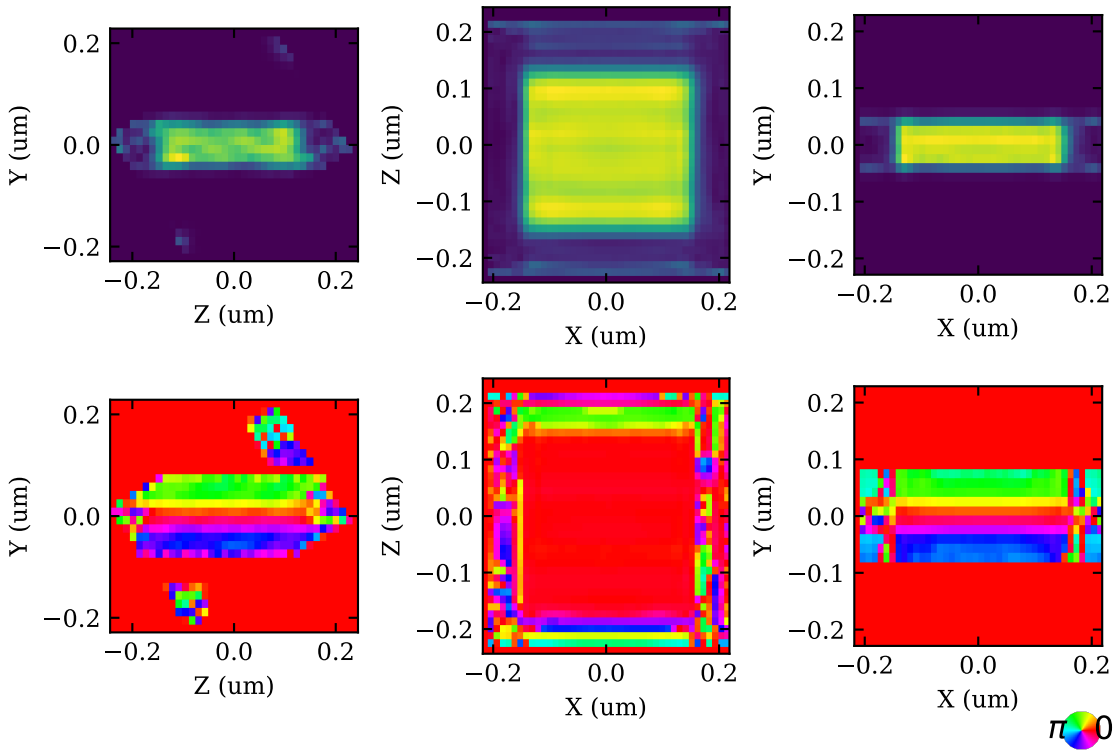

Figure 6.13 – Cross-sections of the reconstructed object using DM and AP on simulated diffraction patterns with a support constraint in real space. The (X, Y, Z) frame is the one of the laboratory with a rotation around the X-axis so that the object appears square. Note that the cross-sections are taken at the center of the volume. (Top) Density and (bottom) phase of the retrieved object. The shape of the object has been retrieved and the phase displays a gradient in the vertical directions, but remains flat in the horizontal plane. This is expected as the numerical phase introduced in the diffracting object, from equation 6.30, is strictly proportional to y, hence the (XZ) cross-section at $Y = 0$ has no phase variations.

In order to evaluate the quality of the reconstruction, one compares the calculated diffraction patterns from the retrieved object to the observed ones. Figure 6.14 shows the comparison between these two sets, at the first and the last beam-to-sample position. The good agreement between the retrieved diffraction patterns and the observed ones strengthens the retrieval process.

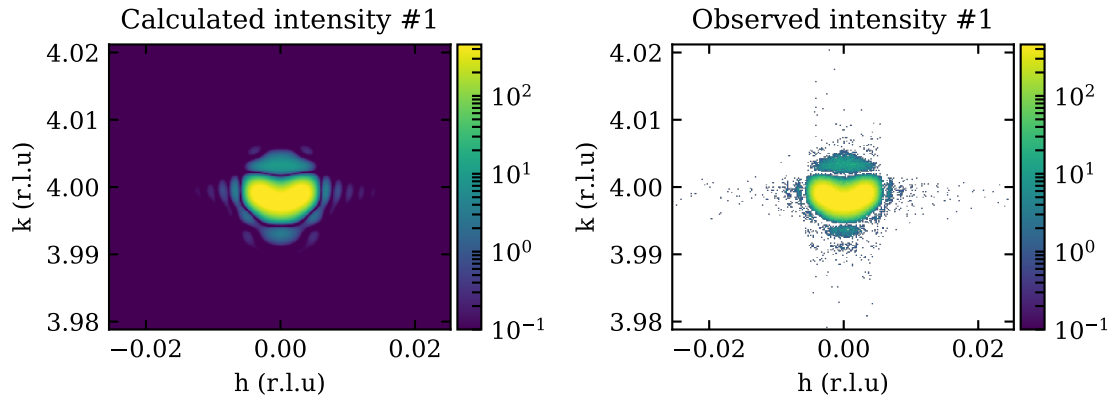

(a)

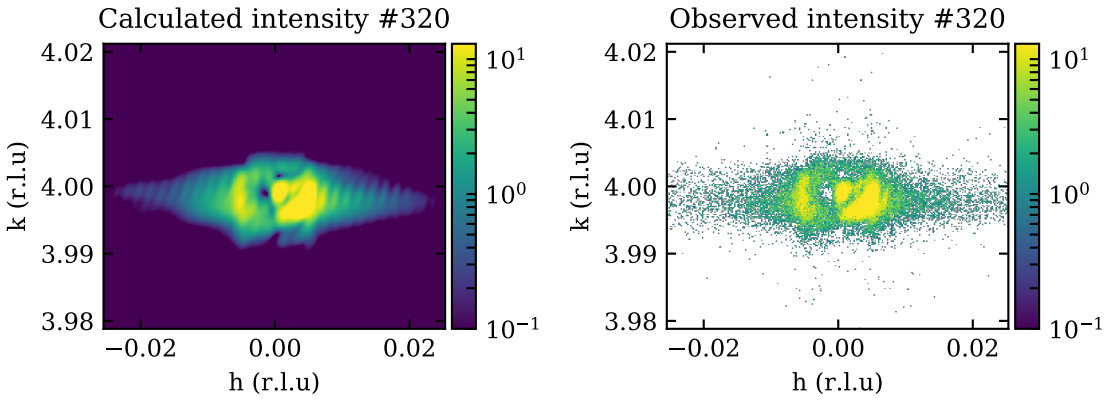

(b)

Figure 6.14 – Comparison of the retrieved diffraction patterns with the observed/simulated ones. On the left column, the diffraction patterns result from a FT of product of the retrieved object time the beam, while the right column depicts the kinematical diffraction patterns with Poisson noise. (a) Diffraction patterns from the central position of the scan, (b) Diffraction patterns from the last position of the spiral scan.

Lastly, a finer analysis on the reconstructed density and phase can be performed. First, the object is rotated around the X-axis of the laboratory reference frame by θ_B so that its sides are parallel to the reference axes. Figure 6.15a shows a cross-section of the retrieved object in the (XY) plane, at $Z = 0$. Corresponding profiles along the Y-axis, at $X = 0$, are depicted in Figure 6.15b. In this direction, the numerical sample is very thin (60 nm) and one can see that the algorithm struggles to determine clear edges, as the pixel size of 10.6 nm limits the resolution. From the profile of Figure 6.15b, the spatial resolution using the edge sharpness is estimated to be ± 1 pixel. Moreover, the phase shows only slight variations, which can be transposed to a corresponding displacement field along the (001) direction. This is

depicted in Figure 6.15c, along with the equivalent strain with respect to an undeformed Si lattice. The input value of 0.12%, homogeneous along the thickness of the object, is quite comparable with the retrieved strain.

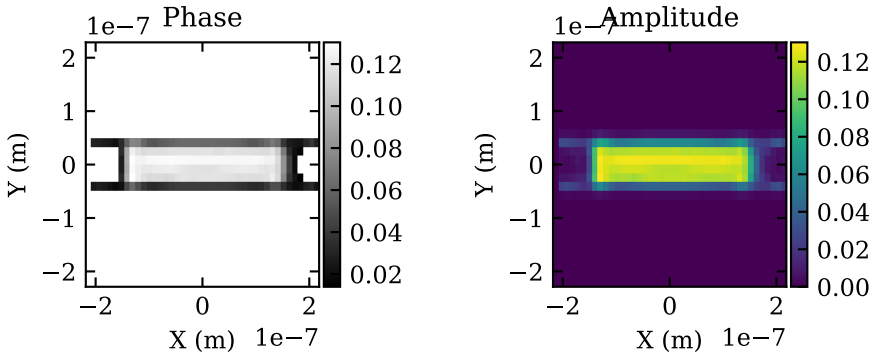

(a)

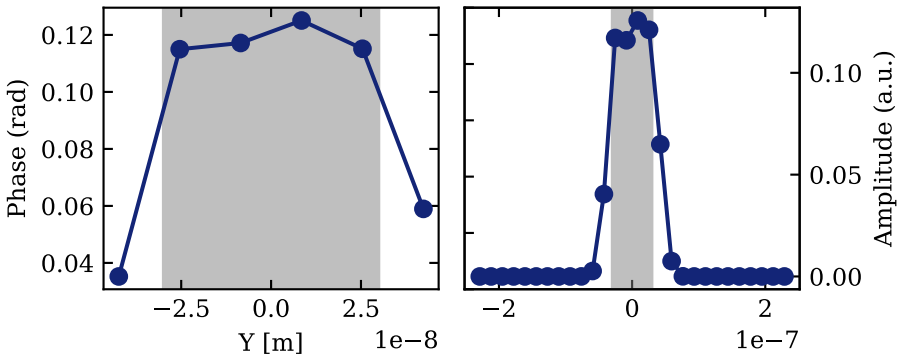

(b)

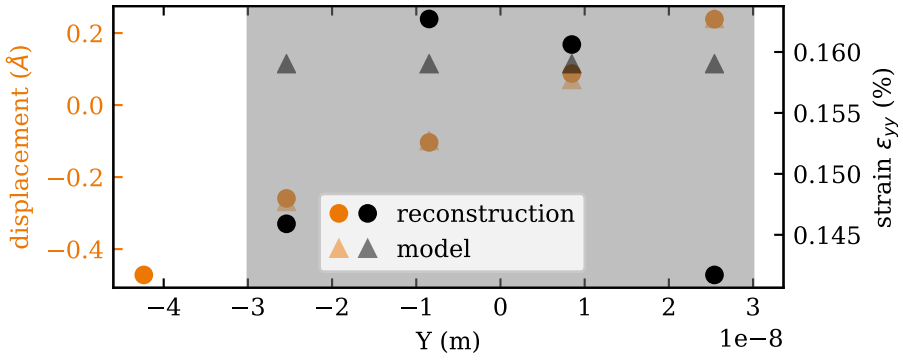

(c)

Figure 6.15 – Vertical cross-sections of the retrieved Si thin layer. 6.15a (XY) cross sections of (right) density and (left) phase of the retrieved object, 6.15b profiles of phase and density along the Y-axis, 6.15c corresponding displacement and strain. In 6.15a, the phase is plotted with a mask hiding the pixels where the density is less than 10% of the maximum density within the cross-section. One can see from the density that the edges have been well retrieved along X, starting from a support that was 1.3 times longer than the true object. In 6.15b & 6.15c, the gray vertical spans serve as visual support to locate the extent of the true object (60 nm thick). The quasi-linear trend of the displacement is expected from the input 6.30. Indeed, in 6.16c, the retrieved values of displacement and strain (circles) are compared to the model (triangles), and there is a strong agreement of the retrieved displacement with the model. Note that the retrieved strain is the real strain ε_{yy}, the out-of-plane strain.

The same analysis is then performed in the horizontal (XZ) plane, where the displacement should be of the form of $\exp\left(-\left(\frac{x}{300e-9}\right)^2\right)$. Figure 6.16a shows a cross-section of the retrieved object in the (XZ) plane, at $Y = 10$ nm, phase and density separated, and the corresponding profiles along the X-axis, at $Z = 0$, are depicted in Figure 6.16b. Figure 6.16b represents the corresponding displacement field and strain. What strikes out is that the expected behavior of the displacement is retrieved, and that except for some oscillations along the Z-axis, the density of the retrieved object is in very good agreement with the numerical sample. From the edge sharpness, one can estimate the spatial resolution to be around ± 1 pixel again. This numerical example demonstrates the ability of the PyNX's version of the 3D BPP algorithm to be efficient and extremely fast. Indeed, the mean time elapsed during one cycle (AP and DM) is ≈ 0.11 s, accounting for a total time of less than 10 seconds to perform the 80 cycles.

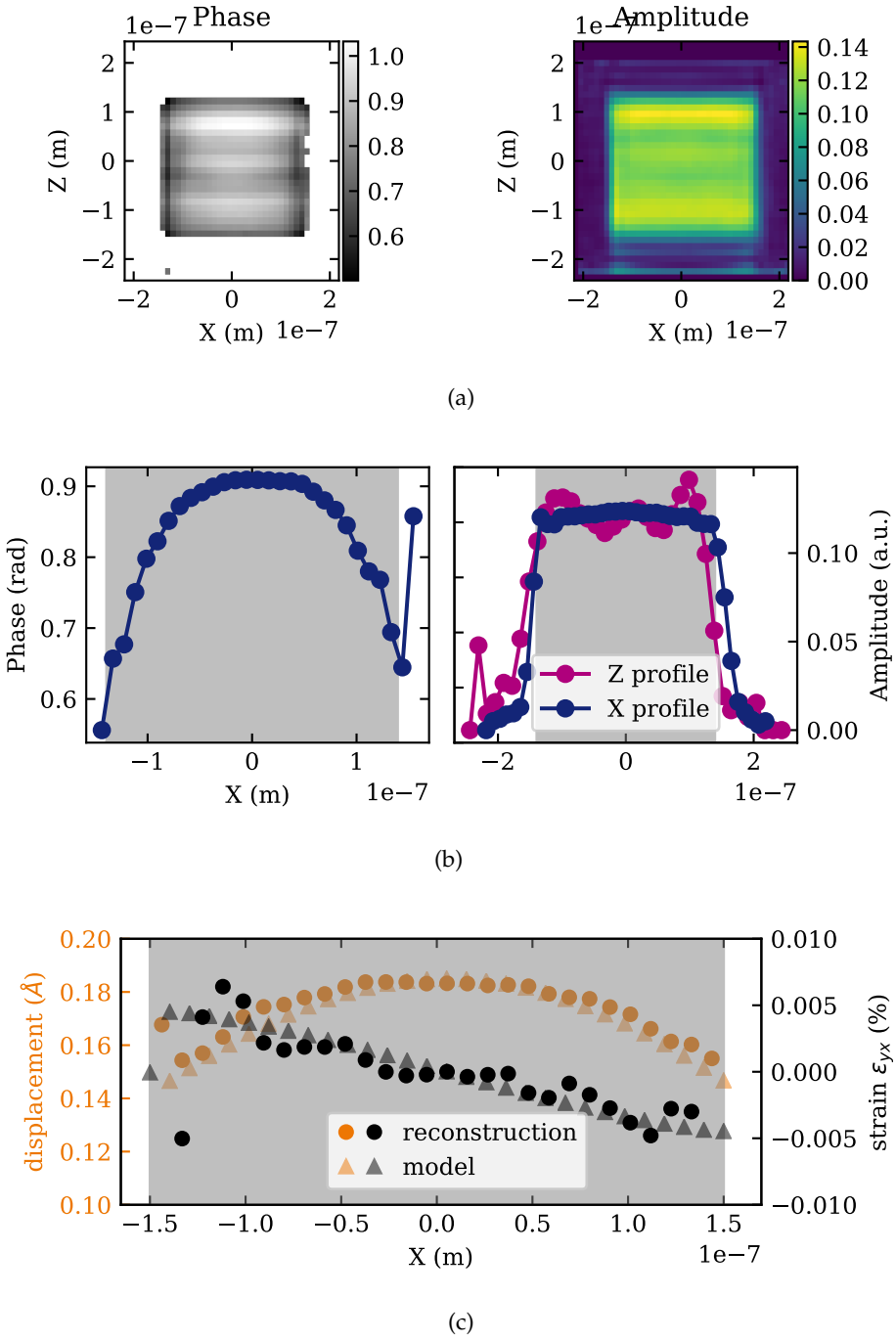

Figure 6.16 – Horizontal cross-sections of the retrieved Si thin layer. 6.16a(XZ) cross sections of (right) density and (left) phase of the retrieved object, 6.16b profiles of phase and density along the X-axis, 6.16c corresponding displacement and strain. In 6.16b, the phase is plotted with a mask hiding the pixels where the density is less than 50% of the maximum density within the cross-section. One can see from the density that the edges have been well retrieved along X, starting from a support that was 1.3 times longer than the true object. In 6.16b & 6.16c, the gray vertical spans serve as visual support to locate the extent of the true object (300 nm wide). In 6.16c, the retrieved values of displacement and strain (circles) are compared to the model (triangles). Note that the strain ε_{yx} is a shear strain.

To conclude, the PyNX process to deal with 3D Bragg Projection ptychographical dataset has proved to be working reliably with simulated dataset, where the input strain is manually controlled. The listing 6.1 shows a simplified route for using the PyNX library and reconstructing a 3D object from a scanning diffraction dataset at the Bragg angle of the sample.

Algorithm 6.1 Building the 3D BPP analysis with the PyNX library.

```
from pynx.wavefront import Wavefront
from pynx.ptycho.bragg2d import *
# Load experiment parameters
wavelength, angles, pixel_size_detector, ny, nx, detector_distance = ...
nb = ...   # number of spiralscan positions
xs, ys, zs = ...# piezo motors! have to comply with the laboratory frame
Iobs = ... # observed intensities
# take care of the signs ! reference frame follows nexus convention i.e., z //
    beam direction, y vertical and x outboard
detector = {'rotation_axes':(('x', -delta), ('y', nu)),'pixel_size':
    pixel_size_detector,'distance': detector_distance}

# Create Bragg 2D Ptycho data object
data = Bragg2DPtychoData(iobs=Iobs, positions=(xs, ys, zs), mask=...,wavelength
    =wavelength, detector=detector)

# Load or create a probe
pr = Wavefront(d=np.fft.fftshift(d['probe'],axes=(-2,-1)), z=0, pixel_size=d['
    pixelsize'], wavelength=wavelength)

# Create main Bragg Ptycho object
p = Bragg2DPtycho(probe=pr, data=data, support=None)

# Init the support
x0, x1, y0, y1, z0, z1 = ... # Base parallelepiped object
rs = 1.0  # Create a support. Larger than the object, or not...
# Equation for GPU init of support using Monte-Carlo integration
eq = "(x >= %g) * (x <= %g) * (y >= %g) * (y <= %g) * (z >= %g) * (z
     <= %g)" %(rs * x0, rs * x1, rs * y0, rs * y1, rs * z0, rs * z1)
s = InitSupport(eq, rotation_axes=[('x', eta)], shrink_object_around_support=
    True)
p = s * p

# Set object starting point, equals to the support
p.set_obj(p.support/100 * np.random.uniform(.2,1.0, p.support.shape))
# Need to recompute optimal centering of frames
p = CalcCenterObjProbe() * p
# Scale object and probe with observed intensity before any optimisation
p = ScaleObjProbe() * p

# Solve !
p = DM(update_object=True, update_probe=False, calc_llk=5, show_obj_probe=0,
    reg_fac_obj_a=0, reg_fac_obj_c=0) ** 40 * p
p = AP(update_object=True, update_probe=False, calc_llk=5, show_obj_probe=0,
    reg_fac_obj_a=0, reg_fac_obj_c=0) ** 40 * p

p = ShowObj() * p
```

Listing 6.1 Building the 3D Bragg Projection Ptychography analysis with the PyNX library.

6.4.2 *Strained SiGe layer, from Comsol modeling of 4.3.1*

After a successful first trial with a 60 nm-thick Si layer, the sample studied in Chapter 4, 20 nm-thick strained SiGe on Insulator, is used as a new test object. The Comsol elastic simulations of 4.3.1 were used to implement an accurate model of displacement fields within the 3D object. A grid of $3 \times 3 \times 2$ nm^3 was used to model a 250 nm square SiGe island, resulting in the creation of 77616 scattering points. In order to create the beam of the ptychographical scan, a FZP of 300 µm diameter and 14 cm focal length was illuminated with a single 8 keV monochromatic point source located 90 m upstream. Coherence slits of 200 $\times$ 200 µm^2 were implemented to create the final probe, depicted in Figure 6.17. The FWHM at the focal plane is of 153 $\times$ 130 nm^2 (H$\times$V).

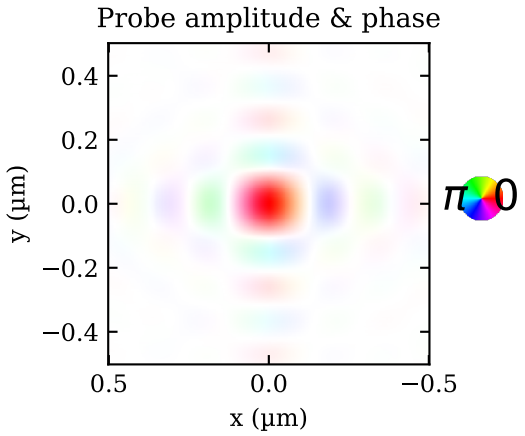

Figure 6.17 – Simulated probe for numerical 3D BPP simulation. The illumination wavefront is focused from a FZP of 300 µm diameter and 9.8 cm focal length, at 8 keV, with coherent slits of 200 $\times$ 200 µm^2. Moreover, an OSA of radius 30 µm is placed 0.2 mm before the focal plane. Both amplitude and phase are represented, described by the HSV colorwheel on the right.

Then, a spiral scan with a step size of 40 nm and 43 positions was used to calculate the kinematic diffraction patterns of the ptychographical dataset, at the (004) Bragg reflection of the theoretical lattice of $Si_{0.76}Ge_{0.24}$. The detector was simulated with 516 pixels of 55 µm size, positioned 1.2 m away from the sample, at an angle $\delta = 2\theta_B^{SiGe} = 66.38^\circ$ in the vertical scattering plane. Figure 6.18 depicts the geometry of the simulation in the laboratory reference frame, with the beam-to-sample positions on a 3D object represented with one scatterer every 50 ones. The incident and exit wavevectors are also shown, together with the projection of the beam onto the sample, at the first scan position.

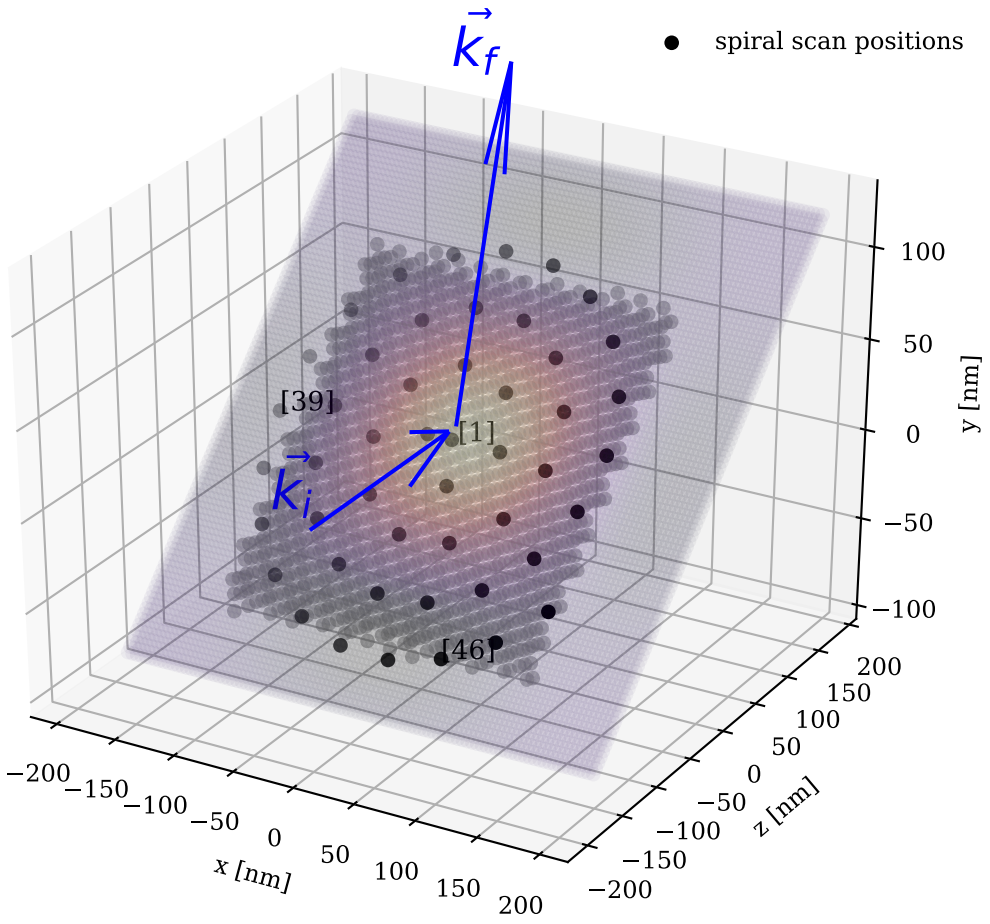

Figure 6.18 – 3D view of the geometry, including the tilted sample and the positions of the scan. The projection of the FZP focused beam onto the sample is also represented, at the first scan position. Note that the sample and the beam are at the same scale. Some positions are highlited as they will be used as references later. The incident and exit wavevectors of the geometry are shown, to remind the reader that the reference frame is the one of the laboratory, with the direct beam propagating along z and the detector, positioned in the vertical scattering geometry, has an angle of 66.38° with the x-axis.

Next, the same process as in the previous subsection 6.4.1 is used to compute numerically the diffraction patterns at each beam-to-sample position. The resulting detector image are shown for three distinct positions in Figure 6.19. Note that the corresponding locations of the beam during the scan are indicated in Figure 6.18. From the first spiral scan position, at the very center of the ultra-thin layer, one can clearly evidence the effect of the layer thickness, whereas in the two side positions, the diffraction patterns extend on the side of the detector, as a result of tilt in the sample. This is expected from the strain analysis performed either from the Comsol modeling or evidenced through SXDM experiments (see chapter 4). All the diffraction patterns are then centered on the center of mass of the diffraction from the first scan position, and cropped. The final window size has to match two rules:

first the window has to be symmetrical and its width must be so that its largest prime divider is lower than 13, as it is required for the GPU computations. As a result, the 3D size of the diffraction data set is of 48 × 440× 440.

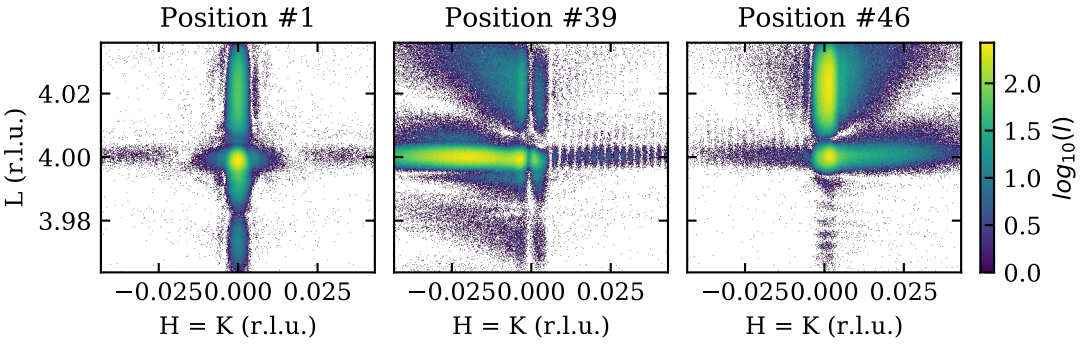

Figure 6.19 – Simulated diffraction patterns from the strained SiGeOI comsol model, with respect to the beam-to-sample position on the layer. Locations of the different probe positions are depicted in Figure 6.18. The probe used for the simulation is smaller than the square SiGe pattern, hence different behaviors can be observed. At the central position (#1), the diffraction patterns encodes the information from the thickness of the layer, and the extension of the central lobe towards lower L values indicate that strain is affecting the layer. At position #39, the probe impinges on the very edge of the square island, thus the diffraction pattern is shifted to the left of the detector as a result of the high tilt coming from the strain relaxation. At position #46, the probe illuminates both the edge and a central part of the layer, hence a combination of the effects described previously are visible.

Then, following the same point-by-point process described in , a support is built to initialize the 3D BPP object. Within the simulated geometrical conditions, the voxel size of the 3D array is a cube of size $7.3 \times 7.3 \times 7.3$ nm^3. The support is initialized as a parallelepipedic object of width 500 nm and thickness 20 nm. As a result, in the layer thickness direction, less than 3 voxels have to be used, leading to step-like effect as the sample is rotated in the reference frame. Figure 6.20 shows the cross-sections of the support in the laboratory frame, with the clear pixelisation effect in the (ZY) plane.

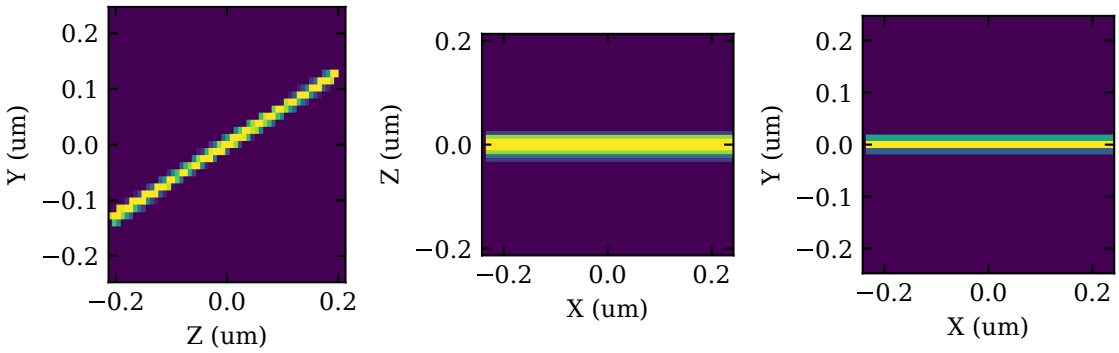

Figure 6.20 – Support initialization for an ultra thin SiGeOI layer. The support's density is displayed in the reference frame, hence appears tilted, and the cross-sections are taken at $X = 0$, $Y = 0$, $Z = 0$.

Next, 40 cycles of DM are performed in order to reach an accurate guess that is then used to perform 40 cycles of AP. In order to reduce the Poissonian LogLikelihood figure of merit, another 40 cycles of DM and 40 cycles of AP are performed [3]. The reconstruction is finished with 40 cycles of ML. Figure 6.21 shows the cross-sections in the laboratory frame of the rotated retrieved object, both in density and in phase. Fluctuations in the density are noticeable, particularly along the Z-axis, which is the projection direction, normal to the detector, for which only the deconvolution by the probe gives spatial resolution. Morevoer, it is clear that the algorithm struggles to define the thickness of the layer, as it supposed to be only 3 pixels thick. Nonetheless, the edges along the X-axis are well retrieved, and phase variations can be observed, that are yet to be compared with the model.

3. When the support is tight, *i. e.*, has the same shape as the initial object, a regularization term can then be introduced in order to enforce continuity of the object density inside the support area.

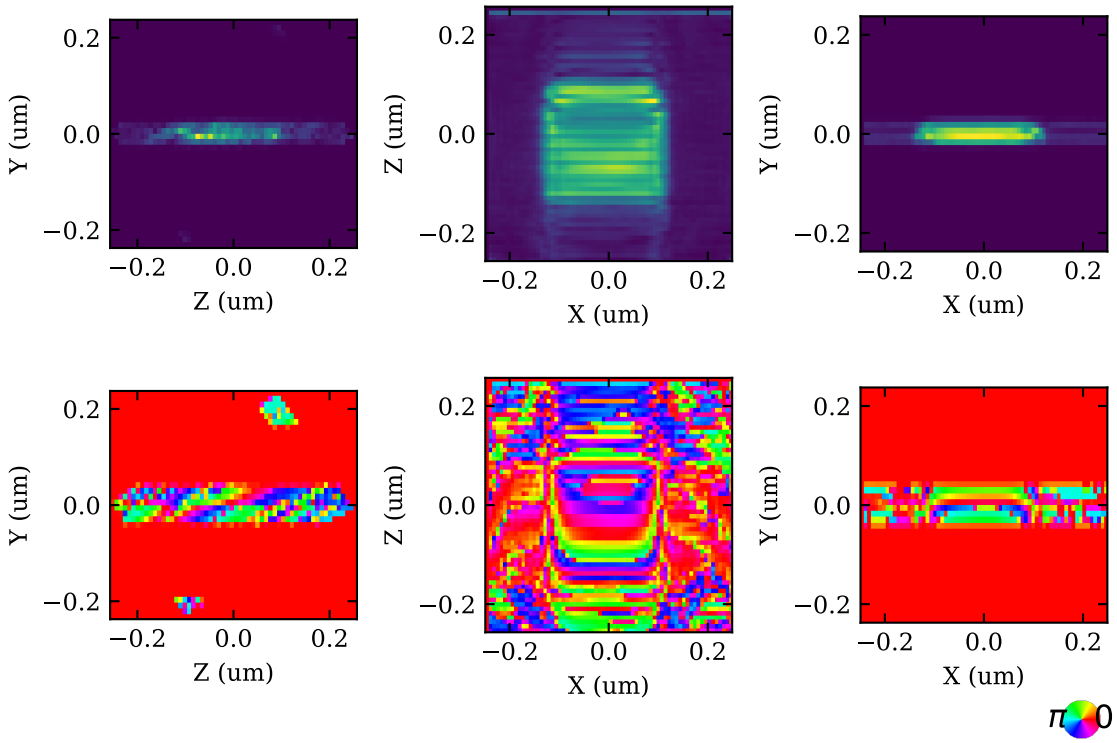

Figure 6.21 – Retrieved object from numerical simulation of 3D BPP. Cross-sections of (top row) object density and (bottom row) object phase. The voxel size if 7.3 nm in every direction, which shows that in the thickness direction (Y-axis) the object is constraint with difficulty. Along the Z-axis, one can note the struggles of the algorithm that result in fluctuations from one line of pixels to another. Nonetheless, the size along the X-axis is retrieved even with a wider initial support (500 nm wide support), and phase gradients can be observed, that most likely are true representations of the tilt and strain within the initial object.

In order to extract more quantitative information from the reconstruction, Figure 6.23 shows an analysis of density, phase, associated displacement and strain in the (XY) plane, at $Z = 0$ nm. In this vertical plane, only two pixels are falling entirely inside the object, which makes the extraction of strain less reliable. No strong variations of phase are visible, and the scale of the associated displacement fields along the (001) direction slightly diverges from the Comsol simulation, with a retrieved value at the interface of around 0.3 Å compared to 1 Å from the model. Moreover, the retrieved out-of-plane strain ε_{yy} (according to the notation of the frame), obtained from the derivative of the phase, is also different from the expected one (0.25% compared to 0.5%). These discrepancies can be imputed to the ultra small thickness of the object, which forces the reconstruction to have only two pixels in this direction, thus increasing the uncertainty.

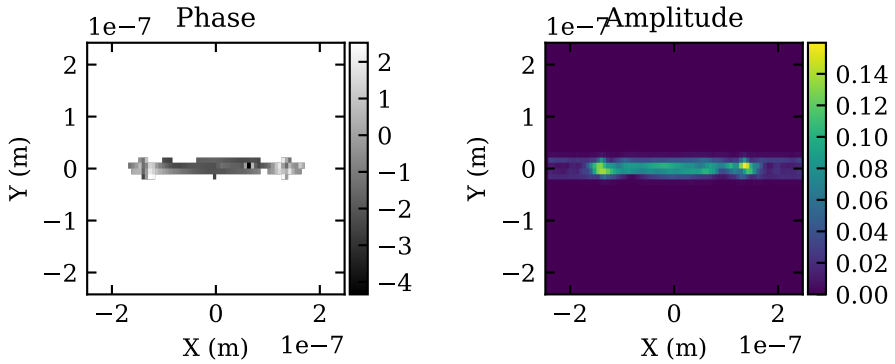

(a)

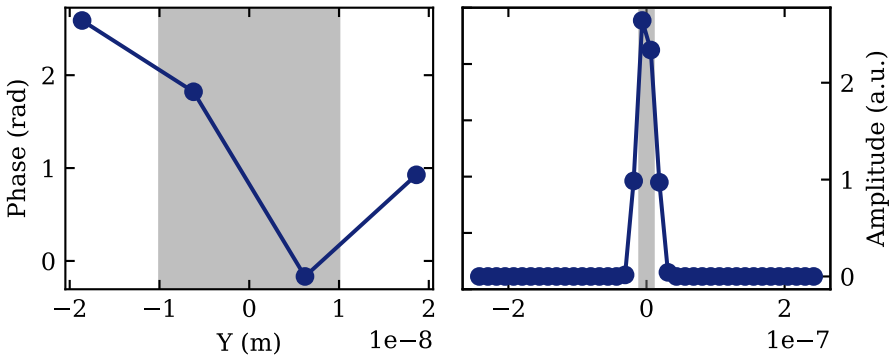

(b)

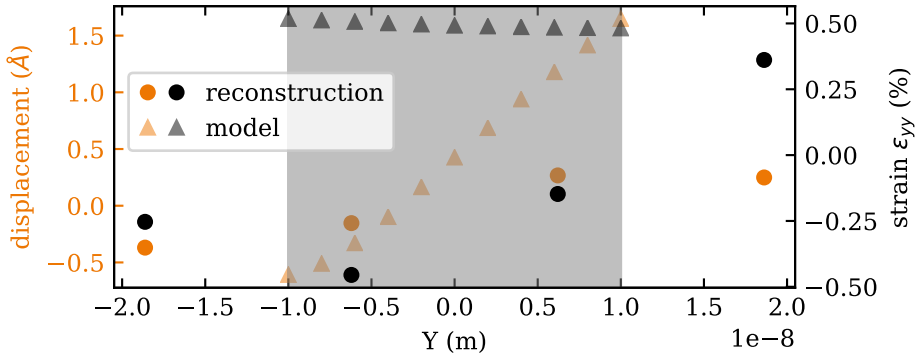

(c)

Figure 6.22 – Analysis of the out-of-plane components of the retrieved SiGe ultra-thin layer. 6.22a(XY) cross sections of (right) density and (left) phase of the retrieved object, 6.22b profiles of phase and density along the Y-axis, 6.22c corresponding displacement and strain. In 6.22b, the phase (in radians) is plotted with a mask hiding the pixels where the density is less than 10% of the maximum density within the cross-section. One can see from the density that the edges have been well retrieved along X, starting from a support that was twice wider than the true object. However, along the Y-axis, the reconstruction is impinged on by the limited voxel size, which is very close to the actual thickness of the sample. In 6.15b & 6.22c, the gray vertical spans serve as visual support to locate the extent of the true object (250 nm wide). This way, only two pixels are really inside the true object, and two straddle the edges. Hence, it is difficult to estimate the quality of the displacement field along this direction.

The same analysis is performed in the (XZ) plane, at $Y = 10$ nm. Figure 6.23 presents the different cross-sections and profiles. In Figure 6.23a, the density of the retrieved object in the (XZ) plane presents a lot of fluctuations along the Z-axis, but a clear square is still visible, with sharp edges along the X-axis. However, the size of the pattern looks to have shrank from the expected width. The phase of Figure 6.23a has been unwrapped, but there are still some residuals of what looks like wrapped phase in the displayed profiles of Figure 6.23b. As a result, a seemingly parabolic profile of the phase is observed, with sharp increases when approaching the edges of the structure. This is in good agreement with the expected deformation of the strained SiGe island. The (004) probed Bragg reflection gives insight into the projection of the displacement field onto the out-of-plane direction, which is in this case along the thickness of the object (Y-axis). Hence, here one retrieved the shear strain ε_{yx}, with respect to the lattice parameter of SiGe, which is in very good agreement with the extracted gradient of the u_y displacement along the X direction from Comsol. However, the corresponding displacement could not be extracted from Comsol hence no comparison can be made for the retrieved displacement.

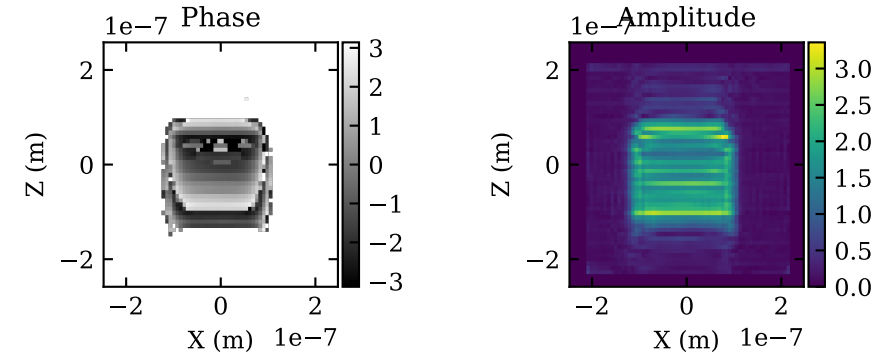

(a)

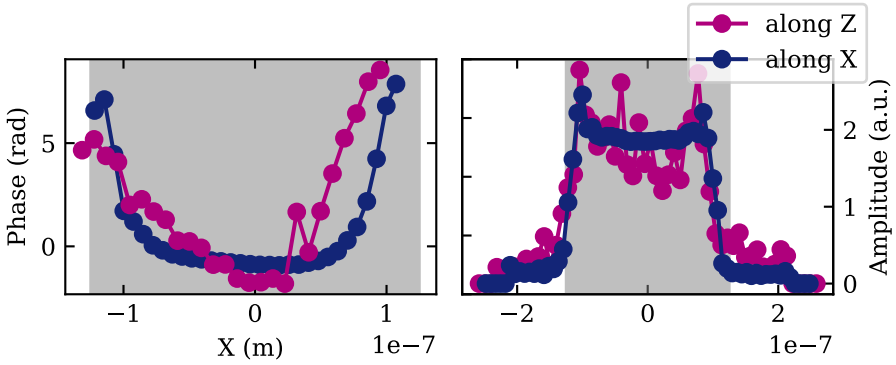

(b)

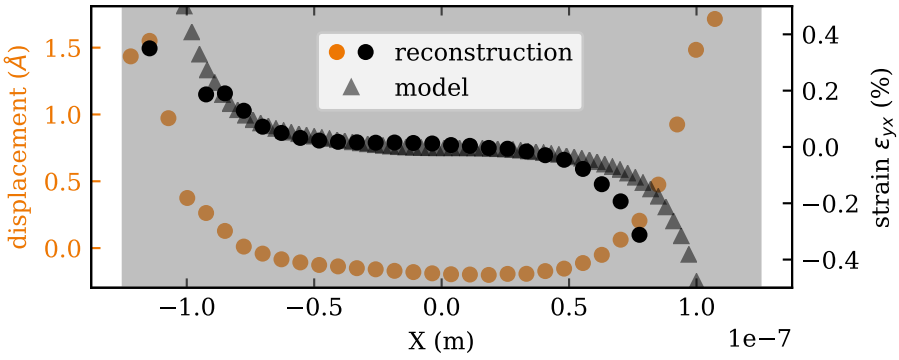

(c)

Figure 6.23 – Analysis of the in-plane components of the retrieved SiGe ultra-thin layer. 6.23a(XZ) cross sections of (right) density and (left) phase of the retrieved object, 6.23b profiles of phase and density along the X-axis, 6.23c corresponding displacement and strain. In 6.23b, the phase (in radians) is plotted with a mask hiding the pixels where the density is less than 25% of the maximum density within the cross-section. One can see from the density that the edges have been well retrieved along X, starting from a support that was twice wider than the true object. In 6.15b & 6.23c, the gray vertical spans serve as visual support to locate the extent of the true object (250 nm wide). From the amplitude profiles, one can see that the quality is poorer along the Z-axis than along the X-axis. The phase profiles seem to exhibit a symmetrical behavior with strong variations towards the edge, however the calculation of corresponding displacement fields and strain is deteriorated by the small-scale fluctuations.

In conclusion, the simulations performed in order to test the reliability and the robustness of the 3D BPP algorithm have shown the actual limitations of the method. Indeed, strain and characteristic sizes of the object are the two major issues. When the strain field is small enough to keep the diffraction patterns well contrasted and confined, the algorithms retrieve quickly and quantitatively the diffracting object whereas the phasing of distorted diffraction patterns that expand on most of the detector results in poor reconstruction. This is strongly coupled with the size of the object, as the algorithm is inherently limited by a certain voxel size, itself defined by the particular Bragg geometry parameters. For this reason, it may be better to treat the ultra-thin objects as 2D layer, and hence use the 2D Bragg Projection Ptychography, putting aside strain resolution in the thickness dimension for the moment.

6.5 EXPERIMENTAL RESULTS

6.5.1 *2D Bragg Projection Ptychography on sSiGeOI*

Experiments have been performed at the NanoMax beamline of the Max IV synchrotron, Lund, Sweden, in order to further characterize the ultra-thin strained SiGe sample of chapter 4. The ability of focusing X-ray beam down to 100 × 100 nm^2 was used to map the strain variation with a theoretical spatial resolution of a few nanometers. Figure 6.24 depicts a view of the experimental hutch of the NanoMax beamline, including the particular robot arm for the detector, which is independent from the sample diffractometer.

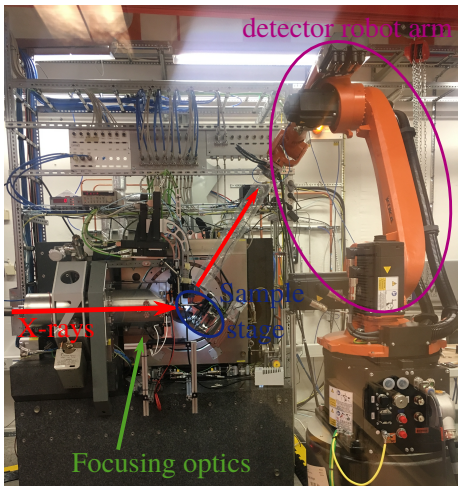

Figure 6.24 – NanoMax (Max IV synchrotron, Lund, Sweden) experimental hutch.

Using a pair of KB mirrors, an 8 keV X-ray beam was focused down, and its wavefront retrieved using the standard beam characterization *i. e.*, a forward ptychographic scan on a reference Siemens star object. The object was placed 500 µm before the estimated focal plane (upstream) and a Pilatus detector was located 4.01 m after the sample stage (downstream). The result of the probe retrieval from the ptychographical scan is shown in Figure 6.25, where both the beam caustic in the horizontal plane and the beam wavefront at the retrieved focal plane are depicted. Note that the FWHM of the beam is found to be of 102 × 109 nm^2 (H×V) at focus.

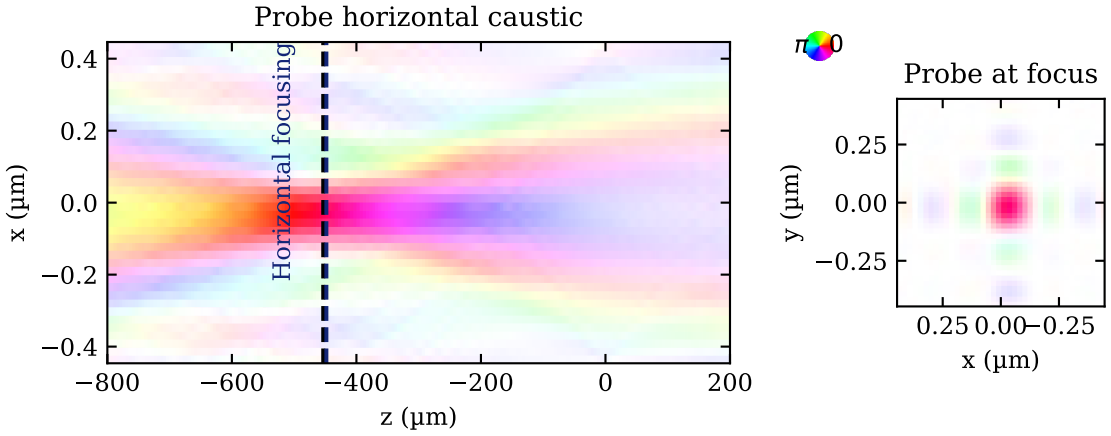

Figure 6.25 – Retrieved X-ray beam wavefront at the NanoMax beamline. (Left) Probe caustic in the horizontal propagation plane, where the horizontal focusing plane is found to be around 500 µm upstream. (Right) Probe wavefront at the focal plane, where it reaches a FWHM size of 102 × 109 nm^2 (H×V). Note that both plots are related to the same HSV colorwheel, depicting the phase with colors and the amplitude in brightness.

A Merlin detector was mounted on the robot arm in order to reach Bragg reflections of the sample. The radius of the arm was set to 0.89 m and the (113) Bragg reflections of both Si and SiGe were investigated. Firstly, angular scan were performed around the Bragg angle of the silicon substrate, *i. e.*, $\theta_{Si}^{113} = 28.24°$, in order to calibrate the experiment. From an analysis similar to 4.4.3, a lattice parameter of Si was found to be of 5.428 Å, which is only 0.05% lower than the tabulated Si lattice parameter at room temperature (300 K). After noticing strong spatial drifts of the sample while in vertical scattering geometry from SXDM maps, the decision was taken to put the sample vertically and use an horizontal scattering geometry. Another angular scan was performed around an incident angle of $\alpha = 54.57°$ while the detector was rotated in-plane to an angle of $2\theta_{Si}^{113} = 56.5°$. This time the measured lattice parameter of Si was 5.431 Å. Next, the detector angle was lowered to 55.5° and the incident angle to 52.4° in order to catch the (113) Bragg peak of the strained

SiGe layer. Optimization of the Bragg angle was performed through the search of the angle leading to the maximum integrated intensity in the detector.

Then, the beam was scanned over several sample areas in order to acquire ptychography datasets. At the time of the experiment, the scanning was performed in the following way : a combination of classic scan, at low velocity in one direction, with fly-scan at high velocity in the other direction. This enabled 2D map of up to $3 \times 3\ \mu m^2$ area with step sizes of 20 nm in the fast direction and 40 nm in the other direction, with exposure time varying between 0.1 and 0.01 s. Figure 6.26 shows the integrated intensity over an entire set of scan positions over a 20 nm-thick $2 \times 2\ \mu m^2$ SiGe island, together with the frame of maximum intensity. The very low count by frame strikes out, as well as the impact of the truncation rod of the silicon substrate.

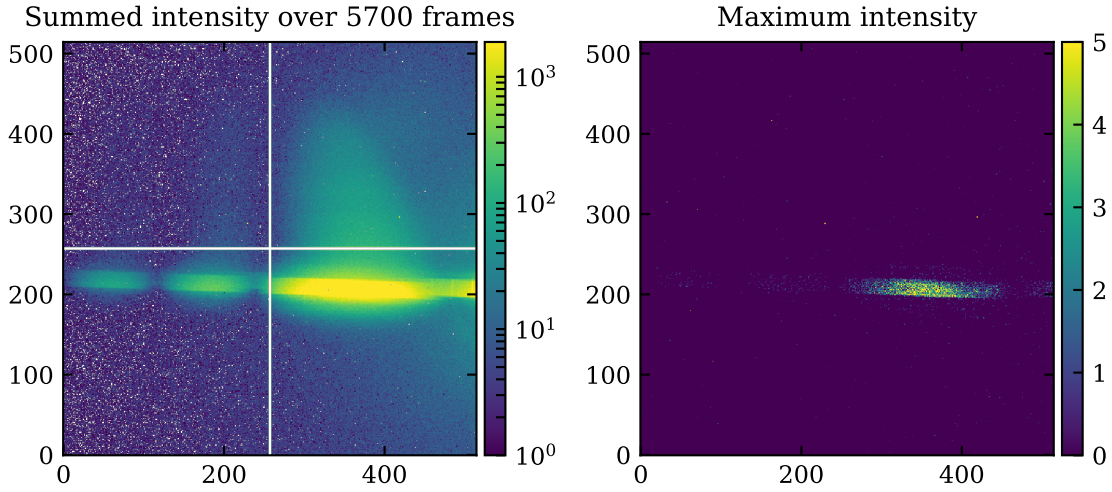

Figure 6.26 – Diffraction patterns from coherent highly focused beam from a SiGe (113) Bragg reflection. (Left) Sum of all the frames acquired during a scan over a 20 nm-thick sSiGe sample, with 0.01 s exposure. (Right) Frame with maximum integrated intensity from the same scan. Note that the scale is in number of counts, and that the chosen geometry is the horizontal scattering, contrarily to the previous experiments. Hence, the high 2θ values are located on the right-hand side of the detector.

Another interesting feature that arises from a ptychographical dataset is the ability to perform integration of the diffracted intensity within some region of interest in the detector with respect to the beam-to-sample position, and hence access real space map with information about the location of scatterers. Figure 6.27 depicts the results of a 101×100 points scan with 40 nm$\times$ 30 nm step size over a 20 nm-thick $2 \times 2\ \mu m^2$ strained SiGe island, with real space maps obtained from three different regions of interest on the detector. Some interesting analysis can be discussed. Firstly, the shape of the SiGe island is well defined from the integrated map from

the ROI number 1 (See the blue rectangle in Figure 6.27). Secondly, one can see that only the upper edge of the square island gives raise to the intensity integrated from the ROI number 2 (See the purple rectangle in Figure 6.27), which only takes into account half of the vertical extent of the diffraction patterns. This is a clear sign of the tilt of the sample. Finally, selecting only the part of the diffraction patterns that is located in between fringes, such as ROI number 3 (See the orange rectangle in Figure 6.27), gives raise to some strange real space map. Indeed, stripes appear as well as extinctions of intensity along vertical (along y) lines, on both side of the island.

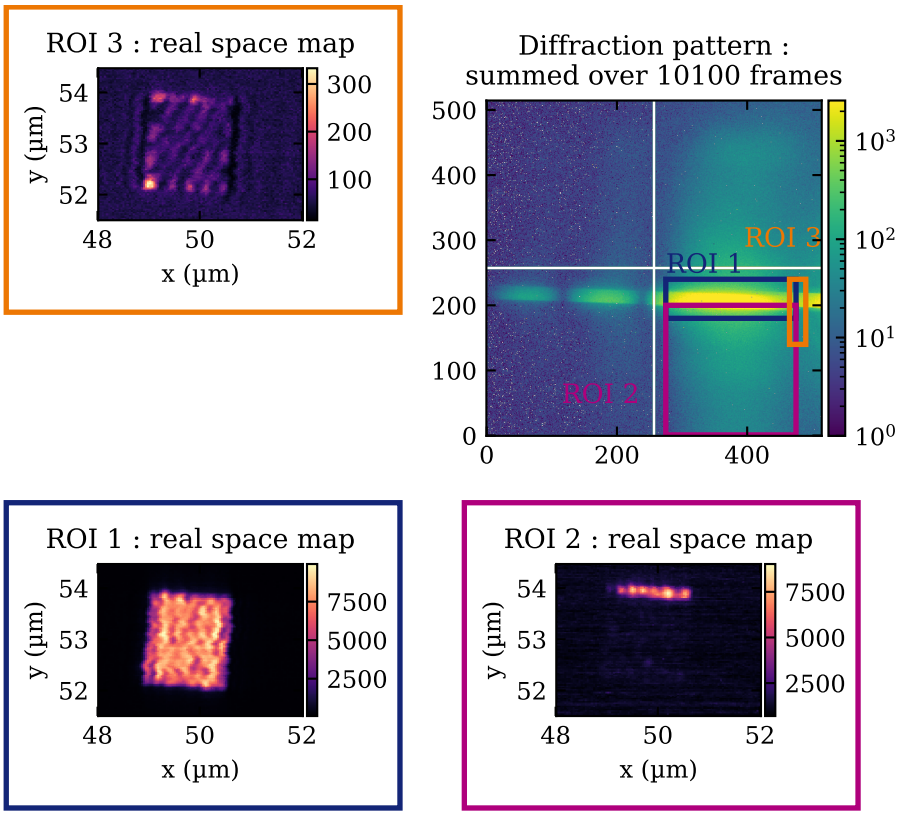

Figure 6.27 – SXDM analysis from Bragg diffraction patterns of a 20 nm-thick strained SiGe island, with a highly-focused beam. On the upper right side, detector image of the summed diffraction patterns over the 10100 positions of a 101 × 100 points scan with 40 nm× 30 nm step size over a 20 nm-thick 2 × 2 µm^2 strained SiGe island. The Bragg angle was optimized from an angular scan around the (113) Bragg reflection of $Si_{0.76}Ge_{0.24}$. On the same plot are depicted three ROIs that are used to perform an integration of the diffraction patterns at each scan position, leading to three real space maps of the sample. ROI #2 shows the impact of the tilted edges on the diffraction, while ROI #3 demonstrates an interesting behavior that is yet to be explained.

Then, the diffraction patterns recorded at one Bragg angle from this previous scan are implemented in a 2D BPP routine, while taking care of the coordinate system as derived in section 6.3.1. In the geometry of the experiment, the exit angle β is

extremely shallow *i. e.*, 3.1° hence the resolution along the horizontal axis will be increased, from 9.8 nm to 235 nm. Indeed, the coordinate of the scan along the horizontal direction has to be corrected by the factor $\frac{\sin(\beta)}{\tan(\alpha)} = 0.0416$. Nonetheless, the algorithm chain composed of 800 cycles of AP converges to a good solution depicted in Figure 6.28. Note that the spatial resolution, obviously degraded along the projection direction *i. e.*, along the x-axis, is high in the y-axis direction as indicated from the step-like shape of the amplitude profile. The width of the retrieved object, taken at 20% of the maximum amplitude, is estimated to be of 1.95 µm.

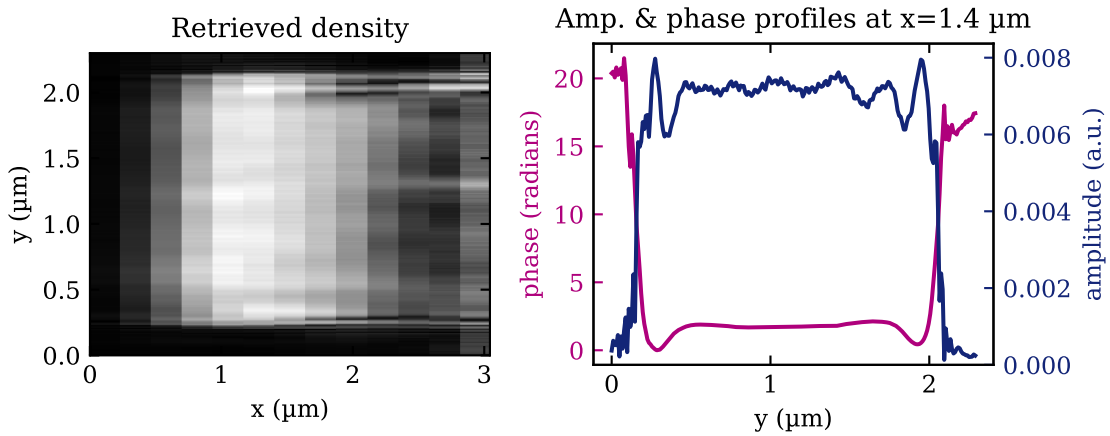

Figure 6.28 – 2D results of forward ptychography applied to a scan of the sample in Bragg condition. (Left) Retrieved density, where the resolution is clearly affected along x, with a pixel size of 235 nm, whereas in the other direction the edges of the structure are retrieved with sharpness. (Right) 1D profiles of both phase and amplitude of the retrieved 2D complex object.

From the reconstructed 2D object, one can also extract the displacement fields. Note that the retrieved displacement fields are projections onto the (113) direction, which still exhibits a particular behavior as the sample relaxes its out-of-plane strain by expanding its in-plane lattice parameter, leading to strong edge effects that the (113) Bragg reflection has sensitivity to. Figure 6.29 shows the vertical profiles of displacement and strain, extracted at $x = 1.1$ µm. Here, the retrieved strain is the real (113) shear strain (see 2.2.4), defined as the deformation of the layer along the horizontal direction :

$$\varepsilon_{113,y} = \frac{\partial u_{[113]}}{\partial y_{[1\bar{1}0]}} \tag{6.32}$$

It is extremely interesting to stress out that the bounce effect on the displacement near the edges clearly agrees with the elastic simulations. Indeed, Figures 6.29a and 6.29b show a close agreement of the strain profile behavior towards the edge of the structure, which reaches a minimal value of around -0.05% just before increasing right before the edge. Moreover, one can evidence that the layer is relaxed on its

central area, but that strain comes into play around 250 nm from the edges. That is in good agreement with the results from the SXDM analysis of chapter 4. This demonstrates the ability of the technique to image low-scale variations of strain, even when the geometry is not favorable (shallow exit angle).

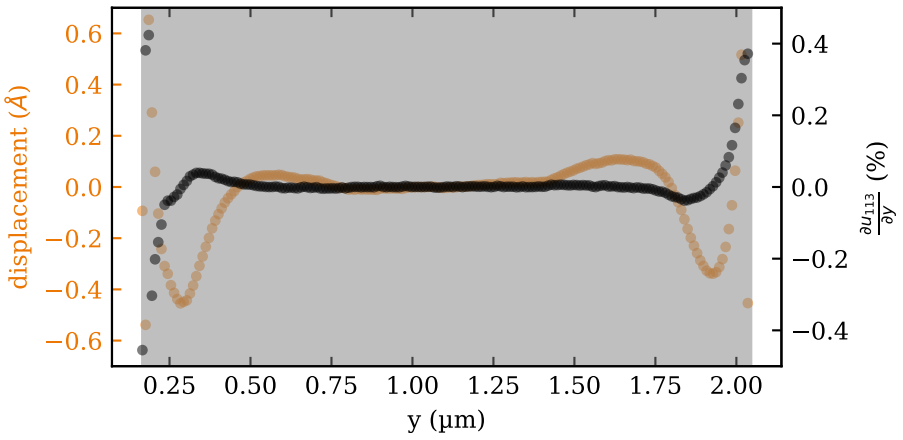

(a)

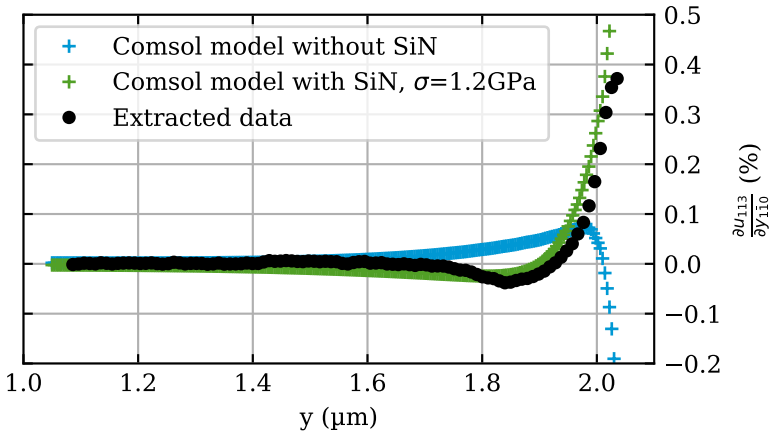

(b)

Figure 6.29 – 6.29a 2D BPP on a 20 nm-thick sSiGe: vertical profiles of displacement and strain. The gray horizonal span delimits the extent of the reconstructed density. 6.29b Extracted (113) shear strain from Comsol modeling in the presence of SiN on top of the sSiGe layer or not. The (113) real shear strain is defined as $\frac{\partial u_{[113]}}{\partial y_{[\bar{1}10]}}$. The strain profile of 6.29a follows the same trend as the corresponding case of 6.29b, *i. e.*, a strained SiGe island with a tensely stressed SiN capping layer.

6.5.2 *2D Bragg Projection Ptychography on GeSn micro-disks*

The 2D Bragg Projection Ptychography code was further tested on suspended Germanium (Ge) Tin (Sn) micro-disks. This section describes the sample realization and the context of the study, then the experimental setup is introduced, and finally a new approach is presented in order to use the 2D BPP method on these strongly strained microsized disks.

The microelectronics industry is actively looking for a CMOS-compatible material with a direct bandgap that could be used to fabricate an efficient monolithic laser source integrated on a Si platform, as an alternative to the transfer of III-V based structures. $Ge_{1-x}Sn_x$ has been identified as a novel, viable candidate, with properties somewhere between its pure components : the direct bandgap of Ge is only slightly higher than its indirect bandgap, while the direct bandgap of α-Sn (lattice parameter 6.4892 Å) is zero. High Sn concentrations in Ge that were initially difficult to achieve due to the low Sn solubility in Ge (<1%), large lattice mismatch (15%) and surface segregation of Sn, can now be reached thanks to the recent progress in Chemical Vapor Deposition (CVD) growth Aubin et al., 2017. Laser operation has subsequently been demonstrated in GeSn structures Wirths et al., 2015; Al-Kabi et al., 2016, highlighting the attractiveness of this CMOS-compatible material for Si photonics. Yet, at that time the laser regime was only observed at cryogenic temperature.

Strain engineering is used to modify the material's properties and thus raise the operating temperature. The initial epitaxial growth of $Ge_{1-x}Sn_x$ layer on Ge substrates usually results in a compressive strain in the layer. This is detrimental since larger Sn concentrations are required to achieve a direct bandgap if the layer is compressed: a direct bandgap $Ge_{1-x}Sn_x$ layer under -0.5% compressive strain (relaxed) requires $x > 0.11$ ($x > 0.08$). The development of etching recipes selective against Ge and GeSn, even at low Sn contents (few %) Al-Kabi et al., 2016; Milord et al., 2017, has allowed to consider suspended structures, that can relax the epitaxial strain. Laser effect with lower Sn content were thus recently achieved in suspended $Ge_{0.915}Sn_{0.085}$ micro-disks Stange et al., 2016 and in micro-disks made by collaborators at the CEA.

An important question that is still open is the relationship between the actual anisotropic strain distribution in the micro-disk and its optical properties. The strain distribution has so far only been estimated using FEM, using mechanical parameters that are linearly interpolated between Ge and Sn, and Raman spectroscopy with Raman strain shift coefficients which are only known for biaxial stress in GeSn, and a known composition Gassenq, Milord, Aubin, Pauc, et al., 2017. However, deviations from linearity are expected in GeSn, as was already observed for the largely

non-linear dependence of the bandgap (bowing of 2.4 eV) Gassenq, Milord, Aubin, Guilloy, et al., 2016. Since the optical properties are highly dependent on the electronic band structure which in turn is dictated by the strain state, an accurate strain measurement is necessary to achieve a complete understanding of the properties of this very promising new material. To this end, an experiment was performed at the ID01 beamline of the ESRF in order to map the strain using coherent X-ray Bragg Ptychography imaging, together with SXDM.

Figure 6.30 shows a typical sample: from top to bottom, it consists of a 8 µm diameter disk made of a 480 nm-thick GeSn bilayer (decomposed in a 225 nm-thick layer with 13% Sn, a transition layer of 90 nm thickness, and a 120 nm-thick layer with 11% Sn), a Ge pillar of 3 µm diameter, 2.5 µm height, and a Si substrate.

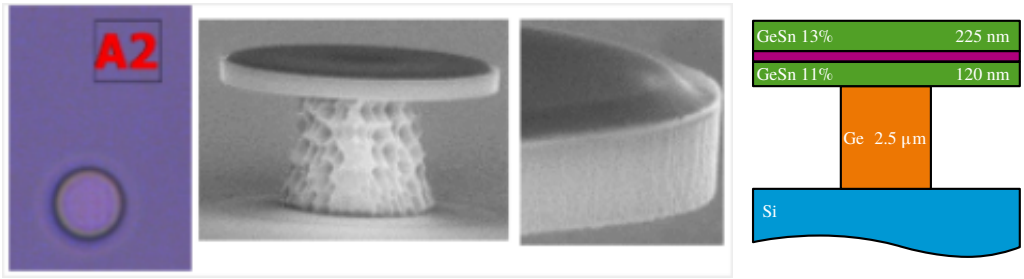

Figure 6.30 – GeSn micro-disk, optical microscope top view, SEM images and schematic of the layers. The disk is 8 µm in diameter and made of a 480 nm-thick GeSn bilayer (decomposed in a 120 nm-thick layer with 11% Sn, a transition layer of 90 nm thickness, and a 225 nm-thick layer with 13% Sn). The Ge pilar is 3 µm in diameter, and 2.5 µm in height. Strong bending of the top layer is clearly visible from the SEM images.

With a focused 8 keV beam (360 × 180 nm^2 FWHM H × V), spiral scans were performed on such a sample with an incident angle around $\alpha = 31.5° \approx \theta_B^{GeSn\,(004)}$ and a 516 × 516 pixels detector located 1 m away recorded the (004) diffraction patterns. Figure 6.31 shows the beam-to-sample positions during a 283 points long spiral scan, with steps of 0.1 µm and exposure time of 1 s. The colorbar is taken from the integrated intensity over the entire detector, normalized by the maximum over the scan. As a result, one can see that even by scanning a 2 × 2 µm^2 area, strong variation of diffracted intensity are visible. This indicates that the strong bending of the micro-disk lead to the creation of isostrain areas, over which the diffraction of the layer remains within the detector area for the same sample and detector orientations. In the example of Figure 6.31, one can highlight a 500 nm-width "horizontal band" that is in Bragg condition, whereas the diffraction coming from the surrounding parts of the micro-disk is not caught by the detector.

This can be interpreted using an isostrain description Kegel et al., 2001; I. Robinson and Harder, 2009: as the disc is curved and can be approximated to a portion

of a sphere of radius, *e. g.*, $R = 100$ µm, when illuminated, only a small layer will be in Bragg diffraction condition. If the natural FWHM of the diffraction from GeSn is *e. g.* $\Delta\omega = 0.01° = 1.8 \times 10^{-3}$ rad, this corresponds to a diffracting thickness of $R \times \Delta\omega = 17$ nm, effectively making the beam see a quasi 2D isostrain layer. Note however that the geometry of the layer is not strictly plane, due to the spherical curvature.

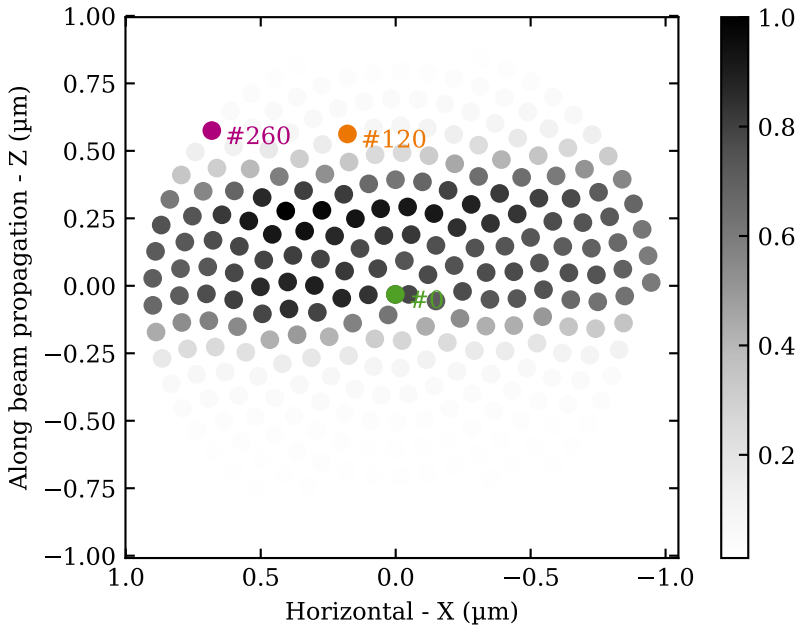

Figure 6.31 – Integrated intensity map from a spiral scan on a GeSn micro-disk. A 283 points spiral scan is performed with steps of 100 nm on a 8 µm diameter GeSn disk, in (004) Bragg reflection condition. The diffraction patterns of each beam-to-sample position are integrated to create a real-space map of the sample, according to its diffraction. Three specific locations are highlighted as they will be used as reference for Figure 6.32. Note that an "horizontal band" is in diffraction condition whereas the remaining of the disk does not diffract onto the detector: this is a clear indication of the bending of the micro-disk, that leads to have only portion of the micro-disk in diffraction condition for a specific incident angle.

The corresponding diffraction patterns are shown in Figure 6.32, for three different locations on the micro-disk. Firstly, it is clear that the diffraction gets deviated while moving on the surface of the micro-disk, with a maximum intensity reached on the central part of the scan, that was preferentially aligned prior to scanning. Secondly, the diffraction from the central area exhibits two spatially separated behaviors: it is split between a clear line-spread diffraction around $q_Z = 4.33$ Å^{-1} and a more disturbed spot with many speckles around $q_Z = 4.35$ Å^{-1}. These lower spot is coming from the top GeSn @13% Sn layer, that has a larger lattice parameter, whereas the upper spot comes from the bottom GeSn @11% Sn layer. Moreover, the

fact that the upper diffraction pattern looks more disturbed is in good agreement with the expectation, as the bottom GeSn layer is more strained and contains more defects than the upper layer.

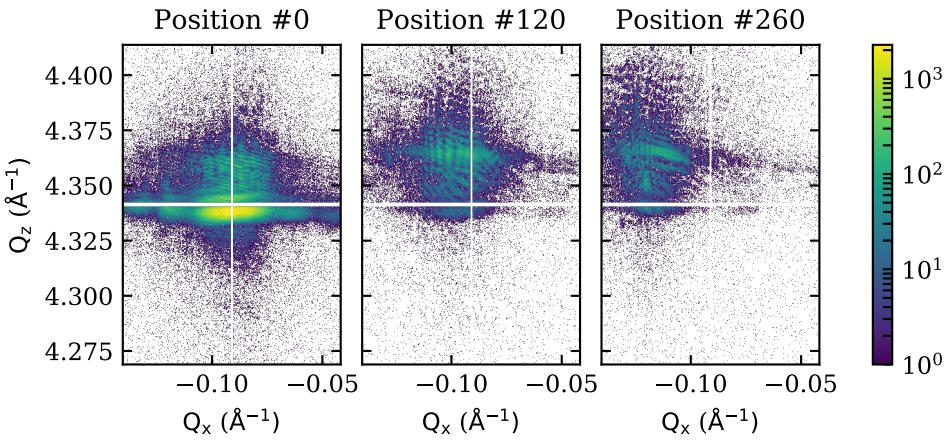

Figure 6.32 – Diffraction patterns from a step-graded GeSn micro-disk, at different beam-to-sample from a spiral scan performed with the central part of the sample being carefully aligned in Bragg condition. By illuminating areas away from the central position (#0), a completely different behavior of the diffracted intensity is recorded. The total intensity decreases and gets shifted on the side of the detector. This indicates that, away from the central position, the micro-disk is bent and no longer in Bragg condition.

The 3D BPP reconstructions on such sample were not satisfactory, mainly due to the wide extension of the diffraction patterns, that actually spread from one side of the detector to another during scanning. The low contrast between diffracted intensities inside and outside the "isostrain band" is also preventing the algorithm from reaching accurate results. Last but not least, because of the huge bending of the micro-disk, precise alignment of the center of rotation of the sample stage with the micro disk was extremely difficult, leading angular scans to span over several degrees. As a result, the decision to perform 2D BPP on a single-angle dataset was taken. Using the fact that the "isostrain band" enables to have only a width-limited part of the micro-disk that is actually in diffraction condition, the 2D BPP should be able to retrieve an in-depth slice of such an "isostrain band". As discussed in section 6.3.1, the algorithm just needs an adjustment of the coordinates system, which in this case amounts to a correction of the vertical coordinates by a factor of $\frac{\sin(\delta-\alpha)}{\tan(\alpha)} = 0.907$. The process was found to be successful with the same recipe as in the previous section, *i. e.*, 800 iterations of AP, combined with a simultaneous optimization on the probe. Figure 6.33 depicts the 2D solution in both amplitude and phase of the solution, together with 1D vertical profiles. Not only the solution retrieves a total thickness of approximately 500 nm, that is in good agreement with

the expectation, but also it seems that the interface at the transit layer is retrieved. Indeed, a gap in the amplitude is associated with a clear change of slope sign of the phase's vertical profile, suggesting a strongly deformed interface as it is the case between the two GeSn layers of the micro-disk. Moreover, the retrieved thickness of both layer is around 200 nm, matching with the nominal characteristic widths. The fact that the amplitude of the lower layer is more disturbed than the top one is likely to be a sign of a larger defect density, due to several defects coming from the growth that are attenuated by the step-graded buffer. Indeed, the idea of the step buffer is to decrease this density, although the composition is increased, a necessary condition to tune the optoelectronic properties. Then, a detailed analysis of phase along both direction can be made.

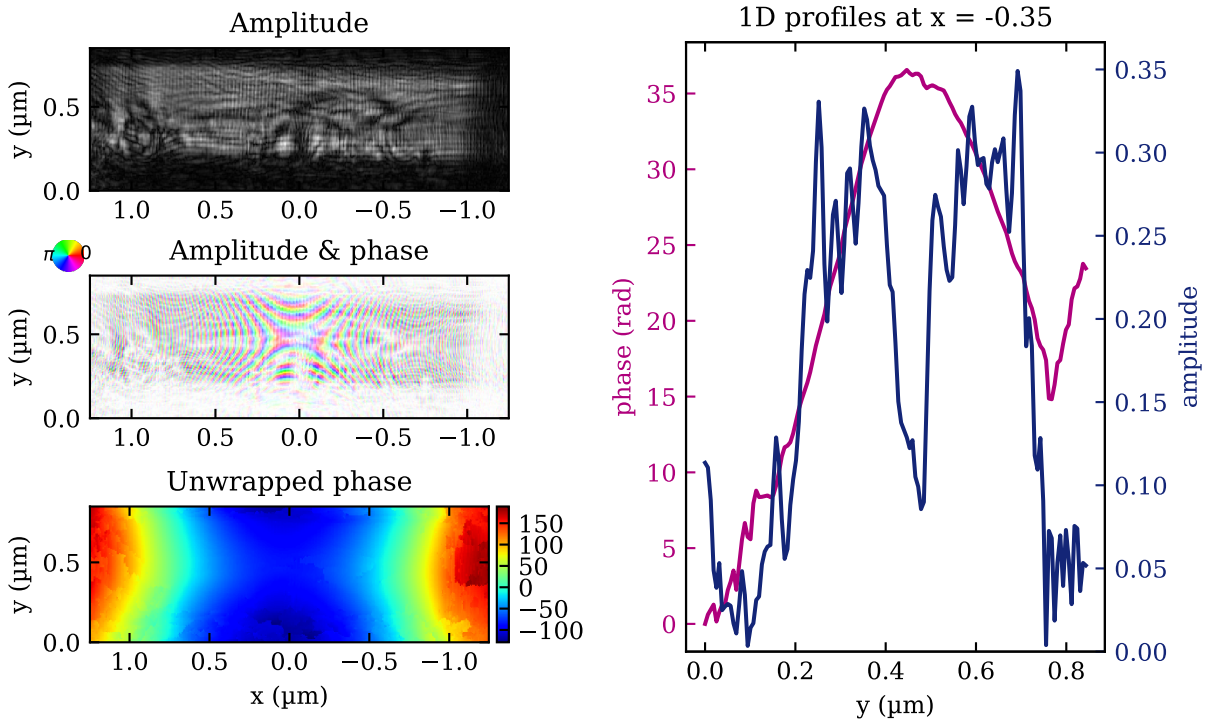

Figure 6.33 – 2D BPP reconstruction on a micro-disk "isostrain band". On the left-hand side, the 2D solution is displayed, in amplitude and in phase, while the bottom subplot depicts the unwrapped phase. It is interesting to stress that the unwrapped phase is parabolic along x. On the right-hand side, 1D vertical profiles of phase (purple) and amplitude (blue) obtained at $x = -0.35$ µm. After 800 iterations of AP, the solution raises a 500 nm-thick layer that is marked by a clear interface around $y = 0.5$ µm. The sharp decrease in amplitude goes along with a change of sign in the phase's slope, delimiting two areas that would correspond to the two GeSn layer with different Sn concentration and different purity. Moreover, the lower layer looks to hold more defects than the top one, which is in good agreement with the expectations.

Firstly, Figure 6.34 presents the derivation of displacement fields and strain from the 1D vertical profile of retrieved phase. Two distinct area, depicted as gray spans, can be differentiated from the slope of the phase or equivalently from the averaged strain value. Indeed, the first area, with an average strain of -0.26%±0.04% (standard deviation) can be assimilated to the lower $Ge_{0.89}Sn_{0.11}$ layer, whereas the second area, with an average strain of 0.13%±0.06%, is likely to be the upper $Ge_{0.87}Sn_{0.13}$ layer. Note that the strain is calculated from the lattice parameter corresponding to the maximum diffraction peak over the scan ($\sim$ 5.78 Å), which was used to center the reciprocal space window during the reconstruction.

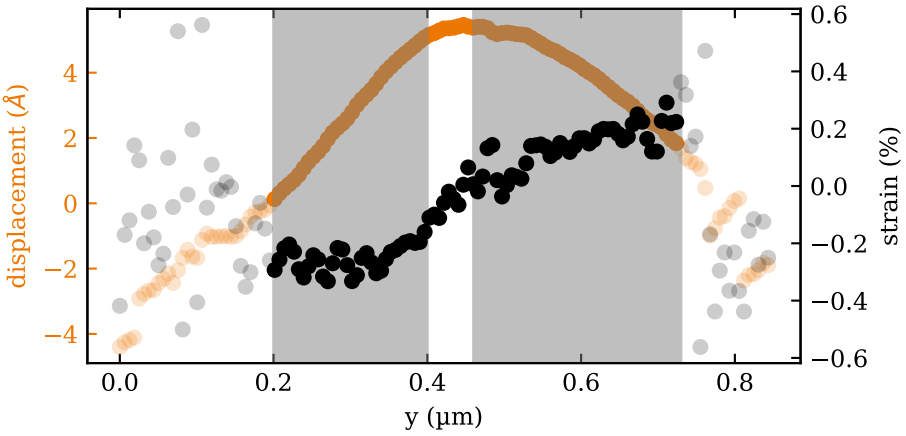

Figure 6.34 – Extracted displacement and strain from vertical cut on the retrieved phase.

Secondly, another interesting feature that can be extracted from the 2D BPP result is the curvature of the dome-like micro-disk. Indeed, as it can be seen directly from the SEM images (Figure 6.30) or from the behavior of the rocking curve, that spans other $\sim 6°$ around the Bragg angle, the micro-disk is so bent that it can be assimilated to a portion of a sphere. As the unwrapped phase along x is a parabola, it sounds reasonable to fit the radius of the sphere which would approximates the parabola around the apex position. In order to do so, a linear regression of the strain $\varepsilon_{yx} = \frac{d_{hkl}}{2\pi}\frac{\partial\varphi}{\partial x}$ is performed. By assuming a parametric relation of the displacement $u_{yx} = R\cos(\omega(x))$, where R is the radius of curvature, with $\omega = \frac{x}{R}$ one has:

$$u_{yx} = R\cos\frac{x}{R} \approx R\left(1 - \frac{x^2}{2R^2}\right) \tag{6.33}$$

Hence, the strain ε_{yx} reads:

$$\varepsilon_{yx} = \frac{\partial u_{yx}}{\partial x} = -\frac{x}{R} \tag{6.34}$$

Figure 6.35 shows the unwrapped phase of the 2D solution, along with an horizontal profile of strain. It is remarkable how linear the strain is over a wide area, with a slope of -9599 m^{-1} and a correlation coefficient of more than 99%. This leads to a radius of curvature of approximately 104 µm for the GeSn micro-disk, which is well in agreement with what one can expect: for a radius of 100 µm, an arc length of 8 µm is seen with an angle of 5.7°.

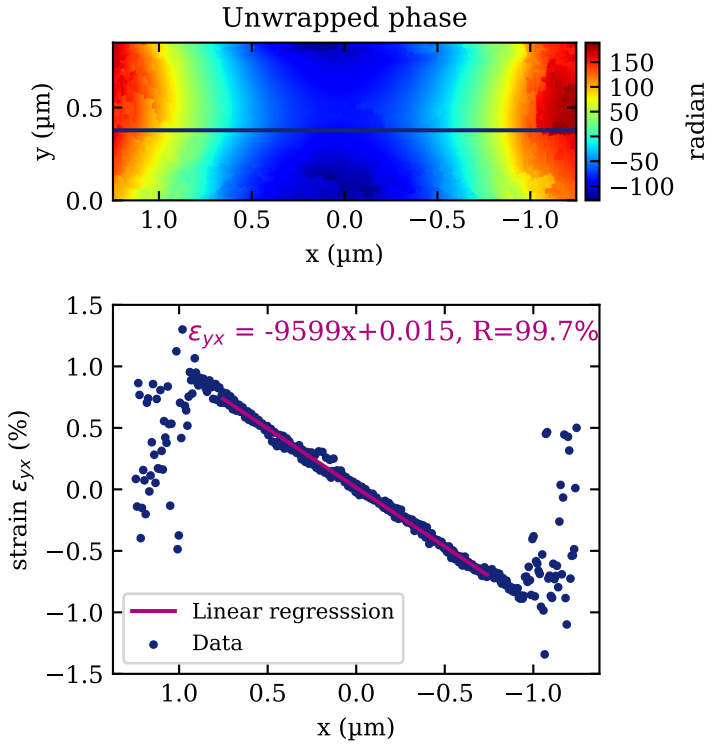

Figure 6.35 – (top) 2D BPP unwrapped phase, (bottom) horizontal cut of the associated strain ε_{yx} (at the location of the blue line above) and corresponding linear regression. The unwrapped phase exhibits a clear parabolic shape horizontally, and the analysis of the extracted strain confirms this behavior. Indeed, the linear regression yields a slope of $s = -9.59 \times 10^3$ m^{-1} with a coefficient of determination of more than 99%. This allow to estimate the radius of curvature of the micro-disk at $x = 0$, which is equals to $\frac{-1}{s} = 104$ µm.

6.6 CONCLUSION

In this chapter focused on Ptychography, the method itself was first detailed, in the usual transmission geometry. This technique, first introduced in the 1970's, has benefited from major improvements in the early 2000. Thanks to the combined efforts of the coherent diffraction imaging community, Ptychography in forward

geometry has reached a mature state and demonstrated to be extremely robust. Setups enhancements allowed to reach just a few nanometers of spatial resolution, and the combination of Ptychography with other imaging technique, *e. g.*, tomography, allowed to image 3D volume to unprecedented levels of resolution.

Then, the two main algorithms that has proven to converge towards satisfying solutions, namely the PIE and the Difference Map (DM) algorithm, have been thoroughly recalled, in order to set the nomenclature and symbols of a typical Ptychographical experiment. However, the assumptions required in order to apply the classical ptychographical algorithm have not to be forgotten: the validity of the wave factorization of object and probe and the fact that the illumination should remain constant over all scanned positions.

The highlight of this chapter is the ability to implement the Bragg geometry into Ptychography. Indeed, accessing the Bragg condition for a crystalline material allows getting insight into the crystalline properties of the sample, such as displacement fields. This high sensitivity to 3D crystalline displacement fields is key for the ongoing development of nanoscience, that relies on the new material properties arising when the dimensions of the structure reach the nanometer scale. Adapting Ptychography to the Bragg case was first considered ten years ago, with a straightforward use of the classical ptychographic algorithm to dataset acquired in the vicinity of a crystal Bragg reflection, leading to 2D solutions with strain sensitivity. Mathematically speaking, the only modification is related to the scan coordinates, that have to be expressed in the frame parallel to the detector. However, as the solutions are back-projection of the detector within the actual sample, strong assumptions on the homogeneity of the sample have to be introduced.

In the early 2010s, 3D Bragg Ptychography was developed, as illustrated by the literature review of section 6.3.2. A few papers were published, but the limitations introduced by mechanical drift and radiation damage over the long-lasting scans make most of the datasets really difficult to reconstruct. Next, the 3D Bragg Projection Ptychography was introduced: a method aiming at coping with these limitations while getting 3D information on crystalline properties. In theory, the information about the "third dimension", *i. e.*, along the direction normal to the detector, that is usually acquired by rocking the sample slightly around its Bragg condition (in 3D Bragg CDI and 3D Bragg Ptychography), is actually encoded in the real-space scanning of the sample. The challenge is thus to deconvolve this information from the set of 2D diffraction patterns at the Bragg angle. Section 6.3.4 describes several ways to achieve this decomposition.

One of the aim of this PhD thesis was to develop and test Bragg Ptychography algorithms within the ESRF python library, PyNX. In 6.4, several numerical simulation and experimental reconstructions are presented, along with some typical

roadmap for using the PyNX library. The latter is consistent for simulated datasets, however the experimental datasets gathered during this work presented intrinsic limitations. On the one hand, the ultra-thin sSiGeOI layers are actually so thin that a 2D-layer approximation is more meaningful. This way, the 2D BPP approach was tested and led to accurate results. On the other hand, the GeSn samples diffraction patterns were so disturbed because of strain and tilt that the 3D algorithms failed to retrieve a good solution. For this case, the 2D BPP approach was actually found to be applicable to GeSn micro-disk. Indeed, this micro-disk are bent to such an extent that an isostrain approximation can be made on thin volume within the sample, leading to accurate reconstruction of the step-graded layers.

In conclusion, improvements are still needed for the single-angle 3D BPP implemented in the PyNX library, but the implementation of multi-angle BPP holds promising insights. Indeed, introducing angular diversity will help the algorithm to converge, while overcoming mechanical issues as the Back-projection operator allows incorporating incommensurate positions from one angle to the other.

BIBLIOGRAPHY

Hegerl, R. and W. Hoppe (1970). « Dynamische Theorie der Kristallstrukturanalyse durch Elektronenbeugung im inhomogenen Primärstrahlwellenfeld. » In: *Berichte der Bunsengesellschaft für physikalische Chemie* 74.11, pp. 1148–1154. DOI: 10.1002/bbpc.19700741112 (cit. on p. 191).

Maiden, Andrew M. and John M. Rodenburg (2009). « An improved ptychographical phase retrieval algorithm for diffractive imaging. » In: *Ultramicroscopy* 109.10, pp. 1256–1262. DOI: 10.1016/j.ultramic.2009.05.012 (cit. on pp. 191, 192).

Odstrcil, Michal, Maxime Lebugle, Manuel Guizar-Sicairos, Christian David, and Mirko Holler (2019). « Towards optimized illumination for high-resolution ptychography. » In: *Optics Express* 27.10, pp. 14981–14997. DOI: 10.1364/OE.27.014981 (cit. on p. 192).

Bates, R. H. T. and J. M. Rodenburg (1989). « Sub-angstrom transmission microscopy: A fourier transform algorithm for microdiffraction plane intensity information. » In: *Ultramicroscopy* 31.3, pp. 303–307. DOI: 10.1016/0304-3991(89)90052-1 (cit. on p. 192).

Chapman, Henry N. (1996). « Phase-retrieval X-ray microscopy by Wigner-distribution deconvolution. » In: *Ultramicroscopy* 66.3, pp. 153–172. DOI: 10.1016/S0304-3991(96)00084-8 (cit. on p. 192).

McCallum, B. C. and J. M. Rodenburg (1993). « Simultaneous reconstruction of object and aperture functions from multiple far-field intensity measurements. » In: *JOSA A* 10.2, pp. 231–239. DOI: 10.1364/JOSAA.10.000231 (cit. on p. 192).

Rodenburg, J. M. and R. H. T. Bates (1992). « The theory of super-resolution electron microscopy via Wigner-distribution deconvolution. » In: *Philosophical Transactions of the Royal Society of London. Series A: Physical and Engineering Sciences* 339.1655, pp. 521–553. DOI: 10.1098/rsta.1992.0050 (cit. on pp. 192, 197).

Faulkner, H. M. L. and J. M. Rodenburg (2004). « Movable Aperture Lensless Transmission Microscopy: A Novel Phase Retrieval Algorithm. » In: *Physical Review Letters* 93.2, p. 023903. DOI: 10.1103/PhysRevLett.93.023903 (cit. on p. 192).

Thibault, Pierre, Martin Dierolf, Oliver Bunk, Andreas Menzel, and Franz Pfeiffer (2009). « Probe retrieval in ptychographic coherent diffractive imaging. » In: *Ultramicroscopy* 109.4, pp. 338–343. DOI: 10.1016/j.ultramic.2008.12.011 (cit. on pp. 192, 196, 198).

Thibault, P. and M. Guizar-Sicairos (2012). « Maximum-likelihood refinement for coherent diffractive imaging. » In: *New Journal of Physics* 14.6, p. 063004. DOI: 10.1088/1367-2630/14/6/063004 (cit. on p. 192).

Godard, Pierre, Marc Allain, Virginie Chamard, and John Rodenburg (2012). « Noise models for low counting rate coherent diffraction imaging. » In: *Optics Express* 20.23, pp. 25914–25934. DOI: 10.1364/OE.20.025914 (cit. on p. 192).

Chapman, Henry N. et al. (2006). « High-resolution ab initio three-dimensional x-ray diffraction microscopy. » In: *JOSA A* 23.5, pp. 1179–1200. DOI: 10.1364/JOSAA.23.001179 (cit. on p. 193).

Fienup, J. R. and C. C. Wackerman (1986). « Phase-retrieval stagnation problems and solutions. » In: *JOSA A* 3.11, pp. 1897–1907. DOI: 10.1364/JOSAA.3.001897 (cit. on p. 193).

Rodenburg, J. M. and H. M. L. Faulkner (2004). « A phase retrieval algorithm for shifting illumination. » In: *Applied Physics Letters* 85.20, pp. 4795–4797. DOI: 10.1063/1.1823034 (cit. on p. 193).

Guizar-Sicairos, Manuel and James R. Fienup (2008). « Phase retrieval with transverse translation diversity: a nonlinear optimization approach. » In: *Optics Express* 16.10, pp. 7264–7278. DOI: 10.1364/OE.16.007264 (cit. on pp. 195, 204).

Fienup, James R (1982). « Phase retrieval algorithms: a comparison. » In: *Applied optics* 21.15, pp. 2758–2769 (cit. on p. 195).

Guizar-Sicairos, M. (2010). *Methods for Coherent Lensless Imaging and X-Ray Wavefront Measurement PhD Thesis PQDT Open* (cit. on p. 195).

Elser, Veit (2003). « Phase retrieval by iterated projections. » In: *JOSA A* 20.1, pp. 40–55 (cit. on p. 196).

Elser, V., I. Rankenburg, and P. Thibault (2007). « Searching with iterated maps. » In: *Proceedings of the National Academy of Sciences* 104.2, pp. 418–423. DOI: 10.1073/pnas.0606359104 (cit. on p. 196).

Marchesini, Stefano, Yu-Chao Tu, and Hau-Tieng Wu (2016). « Alternating projection, ptychographic imaging and phase synchronization. » In: *Applied and Computational Harmonic Analysis* 41.3, pp. 815–851. DOI: 10.1016/j.acha.2015.06.005 (cit. on p. 197).

Thibault, Pierre, Martin Dierolf, Andreas Menzel, Oliver Bunk, Christian David, and Franz Pfeiffer (2008). « High-Resolution Scanning X-ray Diffraction Microscopy. » In: *Science* 321.5887, pp. 379–382. DOI: 10.1126/science.1158573 (cit. on p. 197).

Shenfield, Alex and John M. Rodenburg (2011). « Evolutionary determination of experimental parameters for ptychographical imaging. » In: *Journal of Applied Physics* 109.12, p. 124510. DOI: 10.1063/1.3600235 (cit. on p. 198).

Guizar-Sicairos, Manuel, Samuel T. Thurman, and James R. Fienup (2008). « Efficient subpixel image registration algorithms. » In: *Optics Letters* 33.2, pp. 156–158. DOI: 10.1364/OL.33.000156 (cit. on p. 198).

Wikipedia, The Free Encyclopedia. *Archimedean spiral. (2019, October 17)*. URL: https://en.wikipedia.org/w/index.php?title=Archimedean_spiral&oldid=921695241 (cit. on p. 198).

Holler, Mirko, Manuel Guizar-Sicairos, Esther H. R. Tsai, Roberto Dinapoli, Elisabeth Müller, Oliver Bunk, Jörg Raabe, and Gabriel Aeppli (2017). « High-resolution non-destructive three-dimensional imaging of integrated circuits. » In: *Nature* 543.7645, pp. 402–406. DOI: 10.1038/nature21698 (cit. on p. 199).

Chamard, V., M. Dollé, G. Baldinozzi, F. Livet, M. de Boissieu, S. Labat, F. Picca, C. Mocuta, P. Donnadieu, and T. H. Metzger (2010). « Strain analysis by inversion of coherent Bragg X-ray diffraction intensity: the illumination problem. » In: *Journal of Modern Optics* 57.9, pp. 816–825. DOI: 10.1080/09500341003746645 (cit. on p. 199).

Hruszkewycz, S. O., M. V. Holt, D. L. Proffit, M. J. Highland, A. Imre, J. Maser, J. A. Eastman, G. R. Bai, and P. H. Fuoss (2011). « Bragg Coherent Diffraction Imaging of Epitaxial Nanostructures Using Focused Hard X-ray Ptychography. » In: *AIP Conference Proceedings* 1365.1, pp. 235–238. DOI: 10.1063/1.3625347 (cit. on p. 199).

Hruszkewycz, Stephan O., Martin V. Holt, Ash Tripathi, Jorg Maser, and Paul H. Fuoss (2011). « Framework for three-dimensional coherent diffraction imaging by focused beam X-ray Bragg Ptychography. » In: *Optics Letters* 36.12, pp. 2227–2229. DOI: 10.1364/OL.36.002227 (cit. on p. 199).

Godard, P., M. Allain, and V. Chamard (2011). « Imaging of highly inhomogeneous strain field in nanocrystals using x-ray Bragg ptychography: A numerical study. » In: *Physical Review B* 84.14, p. 144109. DOI: 10.1103/PhysRevB.84.144109 (cit. on pp. 199, 203).

Hruszkewycz, S. O., M. V. Holt, C. E. Murray, J. Bruley, J. Holt, A. Tripathi, O. G. Shpyrko, I. McNulty, M. J. Highland, and P. H. Fuoss (2012). « Quantitative Nanoscale Imaging of Lattice Distortions in Epitaxial Semiconductor Heterostructures Using Nanofocused X-ray Bragg Projection Ptychography. » In: *Nano Letters* 12.10, pp. 5148–5154. DOI: 10.1021/nl303201w (cit. on pp. 200, 201).

Robinson, I. K., I. A. Vartanyants, G. J. Williams, M. A. Pfeifer, and J. A. Pitney (2001). « Reconstruction of the Shapes of Gold Nanocrystals Using Coherent X-Ray Diffraction. » In: *Physical Review Letters* 87.19, p. 195505. DOI: 10.1103/PhysRevLett.87.195505 (cit. on p. 202).

Vartanyants, I. A. and I. K. Robinson (2001). « Partial coherence effects on the imaging of small crystals using coherent x-ray diffraction. » In: *Journal of Physics: Con-*

densed Matter 13.47, pp. 10593–10611. DOI: 10.1088/0953-8984/13/47/305 (cit. on p. 202).

Robinson, I. K. and I. A. Vartanyants (2001). « Use of coherent X-ray diffraction to map strain fields in nanocrystals. » In: *Applied Surface Science*. Proceedings of the International Workshop on Nanomaterials 182.3, pp. 186–191. DOI: 10.1016/S0169-4332(01)00438-X (cit. on p. 202).

Holt, Martin V., Stephan O. Hruszkewycz, Conal E. Murray, Judson R. Holt, Deborah M. Paskiewicz, and Paul H. Fuoss (2014). « Strain Imaging of Nanoscale Semiconductor Heterostructures with X-Ray Bragg Projection Ptychography. » In: *Physical Review Letters* 112.16, p. 165502. DOI: 10.1103/PhysRevLett.112.165502 (cit. on p. 202).

Takahashi, Yukio, Akihiro Suzuki, Shin Furutaku, Kazuto Yamauchi, Yoshiki Kohmura, and Tetsuya Ishikawa (2013). « Bragg x-ray ptychography of a silicon crystal: Visualization of the dislocation strain field and the production of a vortex beam. » In: *Physical Review B* 87.12, p. 121201. DOI: 10.1103/PhysRevB.87.121201 (cit. on p. 202).

Hruszkewycz, S. O., M. J. Highland, M. V. Holt, Dongjin Kim, C. M. Folkman, Carol Thompson, A. Tripathi, G. B. Stephenson, Seungbum Hong, and P. H. Fuoss (2013). « Imaging Local Polarization in Ferroelectric Thin Films by Coherent X-Ray Bragg Projection Ptychography. » In: *Physical Review Letters* 110.17, p. 177601. DOI: 10.1103/PhysRevLett.110.177601 (cit. on p. 202).

Hruszkewycz, S. O., Q. Zhang, M. V. Holt, M. J. Highland, P. G. Evans, and P. H. Fuoss (2016). « Structural sensitivity of x-ray Bragg projection ptychography to domain patterns in epitaxial thin films. » In: *Physical Review A* 94.4, p. 043803. DOI: 10.1103/PhysRevA.94.043803 (cit. on p. 203).

Godard, P., G. Carbone, M. Allain, F. Mastropietro, G. Chen, L. Capello, A. Diaz, T. H. Metzger, J. Stangl, and V. Chamard (2011). « Three-dimensional high-resolution quantitative microscopy of extended crystals. » In: *Nature Communications* 2, p. 568. DOI: 10.1038/ncomms1569 (cit. on p. 204).

Berenguer, F., P. Godard, M. Allain, J.-M. Belloir, A. Talneau, S. Ravy, and V. Chamard (2013). « X-ray lensless microscopy from undersampled diffraction intensities. » In: *Physical Review B* 88.14, p. 144101. DOI: 10.1103/PhysRevB.88.144101 (cit. on p. 205).

Chamard, V., M. Allain, P. Godard, A. Talneau, G. Patriarche, and M. Burghammer (2015). « Strain in a silicon-on-insulator nanostructure revealed by 3D X-ray Bragg ptychography. » In: *Scientific Reports* 5, p. 9827. DOI: 10.1038/srep09827 (cit. on pp. 206, 209).

Quiney, H. M., A. G. Peele, Z. Cai, D. Paterson, and K. A. Nugent (2006). « Diffractive imaging of highly focused X-ray fields. » In: *Nature Physics* 2.2, pp. 101–104. DOI: 10.1038/nphys218 (cit. on p. 206).

Pateras, A. I., M. Allain, P. Godard, L. Largeau, G. Patriarche, A. Talneau, K. Pantzas, M. Burghammer, A. A. Minkevich, and V. Chamard (2015). « Nondestructive three-dimensional imaging of crystal strain and rotations in an extended bonded semiconductor heterostructure. » In: *Physical Review B* 92.20, p. 205305. DOI: 10.1103/PhysRevB.92.205305 (cit. on p. 207).

Mastropietro, F., P. Godard, M. Burghammer, C. Chevallard, J. Daillant, J. Duboisset, M. Allain, P. Guenoun, J. Nouet, and V. Chamard (2017). « Revealing crystalline domains in a mollusc shell single-crystalline prism. » In: *Nature Materials* 16.9, pp. 946–952. DOI: 10.1038/nmat4937 (cit. on p. 208).

Cheng, Ji Xin and X. Sunney Xie (2004). « Coherent Anti Stokes Raman Scattering Microscopy. » In: *The Journal of Physical Chemistry B* 108.3, pp. 827–840. DOI: 10.1021/jp035693v (cit. on p. 208).

Pfeifer, Mark A., Garth J. Williams, Ivan A. Vartanyants, Ross Harder, and Ian K. Robinson (2006). « Three-dimensional mapping of a deformation field inside a nanocrystal. » In: *Nature* 442.7098, pp. 63–66. DOI: 10.1038/nature04867 (cit. on p. 211).

Howells, M. R. et al. (2009). « An assessment of the resolution limitation due to radiation-damage in X-ray diffraction microscopy. » In: *Journal of Electron Spectroscopy and Related Phenomena*. Radiation Damage 170.1, pp. 4–12. DOI: 10.1016/j.elspec.2008.10.008 (cit. on p. 212).

Mastropietro, F., J. Eymery, G. Carbone, S. Baudot, F. Andrieu, and V. Favre-Nicolin (2013). « Time-Dependent Relaxation of Strained Silicon-on-Insulator Lines Using a Partially Coherent X-Ray Nanobeam. » In: *Physical Review Letters* 111.21, p. 215502. DOI: 10.1103/PhysRevLett.111.215502 (cit. on p. 212).

Hruszkewycz, S. O., M. Allain, M. V. Holt, C. E. Murray, J. R. Holt, P. H. Fuoss, and V. Chamard (2017). « High-resolution three-dimensional structural microscopy by single-angle Bragg ptychography. » In: *Nature Materials* 16.2, pp. 244–251. DOI: 10.1038/nmat4798 (cit. on p. 214).

Hill, Megan O. et al. (2018). « Measuring Three-Dimensional Strain and Structural Defects in a Single InGaAs Nanowire Using Coherent X-ray Multiangle Bragg Projection Ptychography. » In: *Nano Letters* 18.2, pp. 811–819. DOI: 10.1021/acs.nanolett.7b04024 (cit. on p. 217).

Könnecke, M. et al. (2015). « The NeXus data format. » In: *Journal of Applied Crystallography* 48.1, pp. 301–305. DOI: 10.1107/S1600576714027575 (cit. on p. 218).

Aubin, J., J. M. Hartmann, A. Gassenq, J. L. Rouviere, E. Robin, V. Delaye, D. Cooper, N. Mollard, V. Reboud, and V. Calvo (2017). « Growth and structural properties

of step graded, high Sn content GeSn layers on Ge. » In: *Semiconductor Science and Technology* 32.9, p. 094006. DOI: 10.1088/1361-6641/aa8084 (cit. on p. 247).

Wirths, S. et al. (2015). « Lasing in direct bandgap GeSn alloy grown on Si. » In: *Nature Photonics* 9.2, pp. 88–92. DOI: 10.1038/nphoton.2014.321 (cit. on p. 247).

Al-Kabi, Sattar et al. (2016). « An optically pumped 2.5 microns GeSn laser on Si operating at 110K. » In: *Applied Physics Letters* 109.17, p. 171105. DOI: 10.1063/1.4966141 (cit. on p. 247).

Milord, L. et al. (2017). « Inductively coupled plasma etching of germanium tin for the fabrication of photonic components. » In: *Silicon Photonics XII*. Vol. 10108. International Society for Optics and Photonics, p. 101080C. DOI: 10.1117/12.2252280 (cit. on p. 247).

Stange, Daniela et al. (2016). « Optically Pumped GeSn Microdisk Lasers on Si. » In: *ACS Photonics* 3.7, pp. 1279–1285. DOI: 10.1021/acsphotonics.6b00258 (cit. on p. 247).

Gassenq, A., L. Milord, J. Aubin, N. Pauc, et al. (2017). « Raman spectral shift versus strain and composition in GeSn layers with 6%–15% Sn content. » In: *Applied Physics Letters* 110.11, p. 112101. DOI: 10.1063/1.4978512. eprint: https://doi.org/10.1063/1.4978512 (cit. on p. 247).

Gassenq, A., L. Milord, J. Aubin, K. Guilloy, et al. (2016). « Gamma bandgap determination in pseudomorphic GeSn layers grown on Ge with up to 15% Sn content. » In: *Applied Physics Letters* 109.24, p. 242107. DOI: 10.1063/1.4971397. eprint: https://aip.scitation.org/doi/pdf/10.1063/1.4971397 (cit. on p. 248).

Kegel, I., T. H. Metzger, A. Lorke, J. Peisl, J. Stangl, G. Bauer, K. Nordlund, W. V. Schoenfeld, and P. M. Petroff (2001). « Determination of strain fields and composition of self-organized quantum dots using x-ray diffraction. » In: *Physical Review B* 63.3, p. 035318. DOI: 10.1103/PhysRevB.63.035318 (cit. on p. 248).

Robinson, Ian and Ross Harder (2009). « Coherent X-ray diffraction imaging of strain at the nanoscale. » In: *Nature Materials* 8.4, pp. 291–298. DOI: 10.1038/nmat2400 (cit. on p. 248).

Troisième partie

CONCLUSION

7

CONCLUSION

Coherent Diffraction Imaging (CDI) techniques are keys in the exploitation of hard X-rays produced at synchrotron facilities. These techniques, based on lensless microscopy, aim at imaging nanoscale properties of a sample by the means of a highly coherent beam. By using reciprocal space patterns diffracted by the sample, algorithms are used to retrieve the phases that have been lost while reaching high spatial resolution. Even if the majority of the techniques that fall into this category are mature, there is still a lot of room for improvement, notably when the Bragg geometry is incorporated. Users that come to a synchrotron facility often seek the advices and help of scientists of the field, as no standard algorithm is available for techniques such as Bragg CDI (BCDI) and Bragg Ptychography. In this work, we studied the implementation of various X-ray diffraction techniques analysis in order to increase their availability to a wider range of users, notably in the context of the EBS upgrade at the ESRF.

The first part of this manuscript gives a detailed description of the theoretical background necessary for the understanding of the samples and methods carried out. Firstly, strain and its impact on a crystal and its scattering was explained. As strain breaks the crystal symmetry, it modifies the band structure of a material and changes its carrier mobility. In chapter 2, a rapid introduction to the related concepts is given, with a particular focus on the theory of elasticity that is primordial for the understanding of the sample of interest: from strained SiGe on Insulator aimed at becoming the channel for the new transistor mode, to GeSn micro-structures paving the way for new laser applications, strain engineering has to be understood.

In chapter 3, a thorough description of X-rays is done along with the explanation of how synchrotron facilities can produce coherent X-rays. In the case of crystalline materials, shining a coherent X-rays beam onto the sample and collecting the scattered intensity around Bragg peaks allows recording information about the deformation of the crystal. This is the motivation for the development of Bragg Coherent X-ray Imaging, which became an essential tool for the understanding of structural properties. During the last twenty years, coherent X-ray scattering has seen very significant progress, notably through the use of better focusing optics, producing a smaller beam size with a much higher photon flux, allowing the study of objects smaller than 100 nm. Moreover, a particular highlight is made on some recent algorithmic improvements such as taking into account the partial coherence of

the incident beam, and maximum log-likelihood refinement, leading to significant increases in the reconstruction accuracy and resolution.

Then, the second part of this manuscript is devoted to the description of the experiments carried on during this PhD thesis. Firstly, chapter 4 presents a case study of strain mapping on strained sSiGeOI ultra-thin patterns, with the demonstration that 100 nm spatial resolution can be obtained using SXDM. This technique yields high-resolution map with high sensitivity to strain and tilt of a crystalline sample, providing careful analysis of the huge amount of diffraction data. In that perspective, a detailed point-by-point road-map is given in the chapter, aiming at guiding users throughout the entire experiment, from data acquisition to analysis. Moreover, the chapter shows that SXDM can also be used a statistical tool, as the numerous patterns present in the studied sample all hold significant interest and provide a general understanding on how the strain relax with respect to the length of a channel. Indeed, the results show that the recently developed technique of condensation, allowing the growth of ultra-thin (13 to 20 nm thickness) SiGe on SOI, yields layers that have a strain relaxation length higher than predicted by the elasticity theory. These results were confirmed by the recent electron holography experiments Boureau et al., 2019, suggesting gliding at the SOI/SiGe interface. Hence, SXDM was demonstrated to be also compatible with the state-of-the-art electronic materials. Last but no least, the SXDM technique developed at the ID01 beamline will benefit from the EBS upgrade, as a higher flux will *e. g.* allow even reducing the exposure time and speed up the whole measurement.

Next, chapter 5 focuses on an innovative combination of two imaging techniques, namely Bragg CDI and Diffraction Contrast Tomography (DCT). Indeed, the two different length-scale of the two techniques were combined to show the ability to switch from a micrometer-scale imaging of a ZrO_2 sample, yielding information on the average strain, into the fine study of an embedded grain within the volume, with nano-scale spatial resolution. As a result, DCT can be used as a tool to register and index grains within a sample and BCDI then comes into play to give quantitative result at the grain scale. The combination of these two techniques is very promising in the future horizons opened by notably the EBS upgrade, that will enable finer tuning of the beam: defocusing a beam to adapt its size to the one of the observed grain in BCDI is key. Besides, the question of strain sensitivity in BCDI reconstructions was addressed, as it is a topic that has been left aside since the beginning of the technique. A method, inspired by Fourier Shell Correlation, was proposed and evaluated on both simulated and real datasets. As a result, Strain Shell Correlation is believed to be an accurate tool for evaluating the strain sensitivity of a reconstruction.

Finally, a method that holds a lot of promises in the search for high-resolution imaging of extended sample is presented in chapter 6. First, the traditional forward transmission Ptychography method is introduced, along with its associated classical algorithms. Then, the case of Bragg geometry is discussed, as the potential ability of Bragg Ptychography to image lattice distortions within a crystal at nanometer-scale spatial resolution in 3D is particularly attracting. The technique, which relies on the collection of diffraction patterns in the vicinity of Bragg peaks, from spatially overlapping position on the sample, has been first developed in 2D, yielding accurate reconstructions of objects presenting enough homogeneities. 2D Bragg Projection Ptychography (BPP) uses standard ptychographical algorithms, with a correction of the scan positions and the assumption that the illumination is an infinite plane wave apertured by the complex sample shape function, in order to recover the sample projection with phase information. The application of 2D BPP to ultra-thin sample, or to isostrain volume within a highly bent sample, leads to accurate results, able to *e. g.* characterize strain variations with high spatial resolution or estimate the curvature of the sample.

Then, the case of complete 3D reconstructions was tackled, using the Ptychographic Iterative Engine (PIE) algorithm with the incorporation of a crucial regularization term. However, full 3D measurements involve performing long-lasting scan at multiple angles of rotation of the sample, and thus suffer from many limitations, particularly long-time mechanical drifts of the stage or radiation damage of the sample. The back-projection operator was then introduced to overcome these experimental limitations, nonetheless, its implementation is not simple. Multiple ways were tested, but so far reconstructions from real dataset still need improvements (ultra thin layers, strongly strained nano-objects). Adding a small number of angles to the set of diffraction data was found to help the convergence, but further complicates the algorithms. One should also stress that these methods relying on back-projection are heavily dependent on a precise support, at least in the direction normal to the detector. Besides, quantitative metric has still to be defined, as small log-likelihood of squared error values are not necessarily synonym of reaching the true solution.

Despite the apparent robustness of the 3D Bragg Ptychography method, next experiments will require much greater knowledge of the experimental regime, as well as exceptional control and stability. Furthermore, highly strained or tilted objects, that will see their diffraction patterns shift to one edge of the detector to the other while scanning, still cause problem of convergence. Last but not least, ultra-thin samples are yet difficult to reconstruct for the embarrassingly simple reason that the voxel size of the reconstruction is currently limited by the experimental conditions (wavelength, detector distance, size and pixel size, getting below 5 nm is hardly

possible). However, stress can be made on the fact that the 2D BPP approach actually holds much outlooks since it is well suited for ultra-thin objects and strongly strained objects that contain volumes which can be approximated with the isostrain approach. Indeed, it has been shown in chapter 6 that firstly ultra-thin object can be approximated to 2D layers, leading the 2D BPP to yield a strain distribution matching closely the elastic simulations, and secondly that the new approach with isostrain extraction of 2D layers from strongly strained micro-disk allow to recover interfaces and phase gradient.

Quatrième partie

APPENDIX

A

SXDM ON ULTRA-THIN 13 NM-THICK SSIGEOI WITHOUT SIN (SAMPLE C) - DETAILED ANALYSIS

The finer analysis of (113) reciprocal space projections at several points on a specific 500 × 500 nm^2 pattern is presented below. Firstly, Figure A.1 recalls the integrated intensity real-space map of the sample of interest, probed at its (113) Bragg reflection, where 8 different locations of the beam onto the sample are highlighted. Then, the corresponding reciprocal space projections along each direction (Q_x, Q_y, Q_z) are depicted in Figures A.2, A.3 and A.4.

In order to exhibit the strong relation between the Q_z component and the strain, but also to show the variation of strain across the pattern, Figure A.5 displays the 1D evolution of both strain and the center of the Gaussian fit on the Q_z projections. The relaxation of strain, which is maximal around the central part of the square island, is visible on both edges.

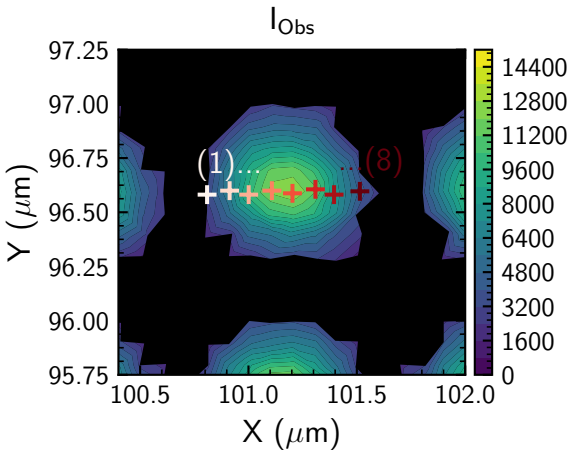

Figure A.1 – Intensity map from (113) Bragg reflection of sample C, centered on a pattern. The crosses depict the location of the reciprocal space projections. Note that the black mask has been set to values below the 65th percentile of the intensity.

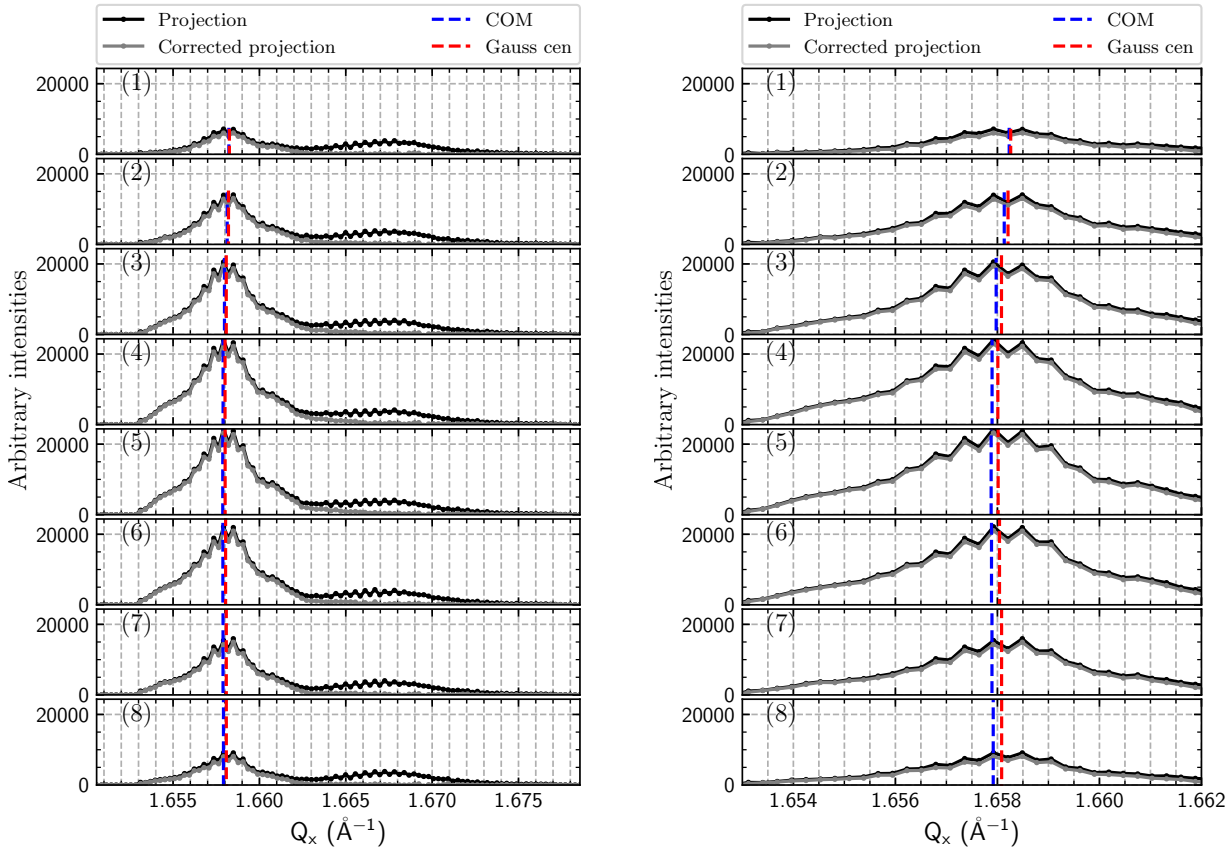

(a) (b)

Figure A.2 – (a) (113) Q_x projections from 8 locations extracted along a given squared pattern (see Figure for locations (1) to (8)). (b) Zoomed views. Black lines depict the scattering integrated over the detector for a full rocking curve on one point of the scan, while gray lines depict the same scattering freed from the Silicon substrate part. Blue dotted lines show the center of mass of the corrected profiles, while the center of the associated Gaussian fit is indicated by vertical dotted red lines. Firstly, one can note that the substrate scattering removal enables to smooth the projections for $Q_x \geq 1.665$ Å^{-1}, as the Si and SiGe peaks are slightly shifted one to each other. Then, from (1) to (8), the center of mass of Q_x hardly varies.

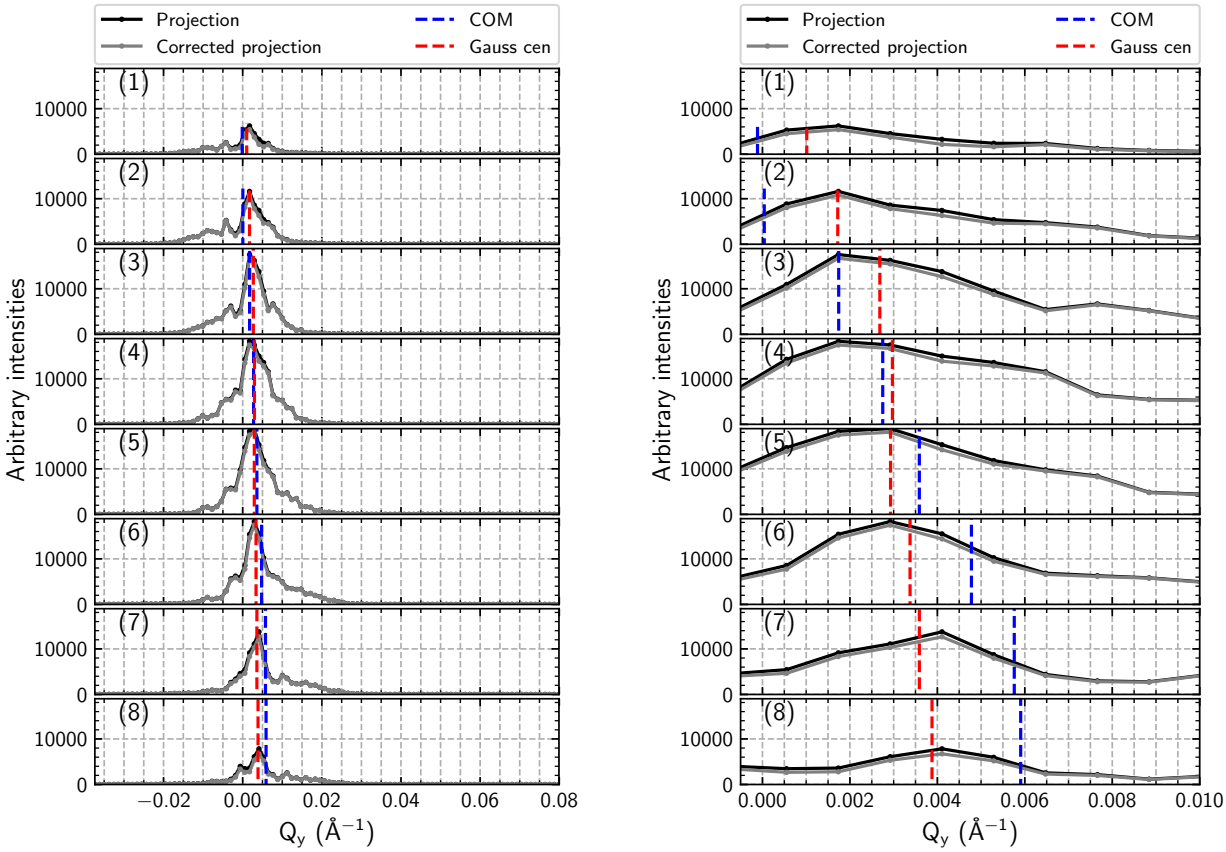

(a) (b)

Figure A.3 – (a) (113) Q_y projections from 8 locations extracted along a given squared pattern (see Figure for locations (1) to (8)). (b) Zoomed views. Black lines depict the scattering integrated over the detector for a full rocking curve on one point of the scan, while gray lines depict the same scattering freed from the Silicon substrate part. Blue dotted lines show the center of mass of the corrected profiles, while the center of the associated Gaussian fit is indicated by vertical dotted red lines. From (1) to (8), one can see that the profiles are not well defined, leading to wider changes in COM than in Gaussian fit. However, the center of mass of Q_y varies within ± 0.006 Å^{-1} which is negligible in term of impact on the strain value.

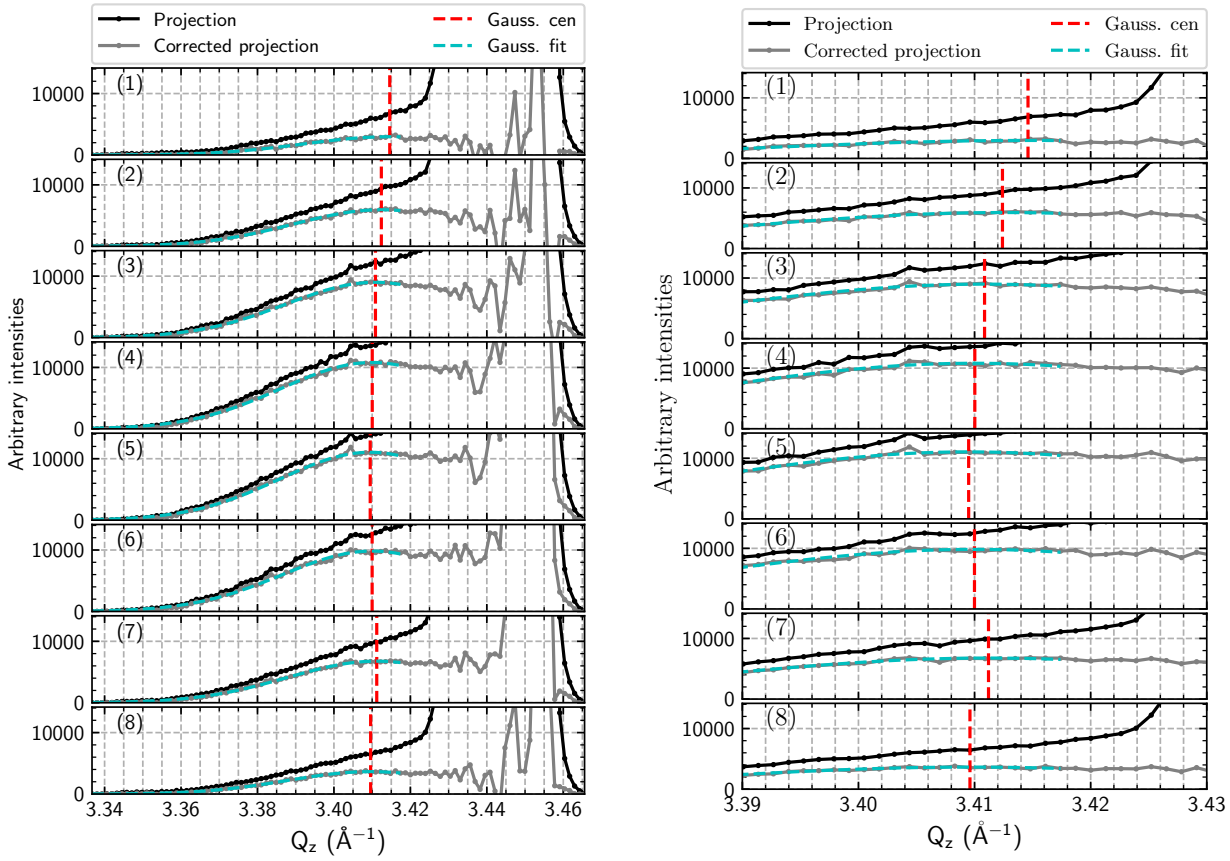

(a) (b)

Figure A.4 – (a) (113) Q_z projections from 8 locations extracted along a given squared pattern (see Figure for locations (1) to (8)). (b) Zoomed views. Black lines depict the scattering integrated over the detector for a full rocking curve on one point of the scan, while gray lines depict the same scattering freed from the Silicon substrate part. Cyan lines depicts the associated Gaussian fit, performed up to a certain limit in Q_z in order to avoid any interference from the Si substrate. The corresponding Gaussian center is indicated by vertical dotted red lines. It is clear that the Si diffusive scattering has a huge contribution to the projection, for $Q_z \geq 3.43$ Å^{-1}. From (1) to (7), one can see that the center of the Gaussian fits follow a trend: from higher values at the edges (*i. e.*, positions (1) and (7)) to a minimum at what could be the center of the nano-island (position (5). These changes are at the origin of strain variations, from 1.14% to 1.21%, as the (113) Bragg reflection is mainly governed by its Q_z component.

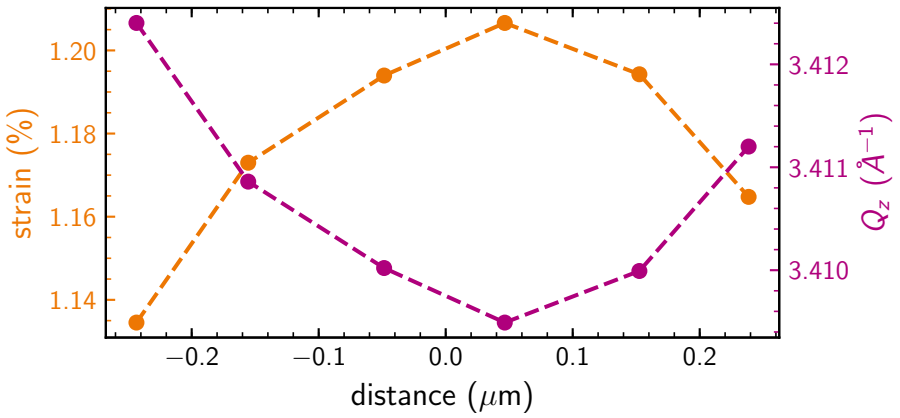

Figure A.5 – Strain and Q_z projections center of Gaussian fit, across one 500 nm width pattern of 13 nm sSiGeOI.

B

ORTHONORMALIZATION MATRIX FOR BRAGG PTYCHOGRAPHY

This appendix details the calculation of the orthonormalization matrix for the particular geometry of Bragg Ptychography, within the NeXuS convention Könnecke et al., 2015, which defines that the basis frame should be the one of the laboratory with $\vec{z}$ along the direct X-ray beam propagation, $\vec{y}$ up and $\vec{x}$ horizontal, going left as seen from the X-ray source. The two separate cases of 3D Bragg Projection Ptychography and complete 3D Bragg Ptychography are given.

B.1 3D BRAGG PROJECTION

For a Bragg Projection experiment, two axes are defined by the back-projection from the detector. These axes are parallel to the detector plane, and with basis vector determined by the inverse FT from the detector pixels. If (x_1, y_1, z_1) are the coordinates after back-projection in the reference frame parallel to the detector frame, the coordinates in the 3D reference frame (x, y, z) are such that :

$$\begin{bmatrix} x \\ y \\ z \end{bmatrix} = R_\nu R_\delta \begin{bmatrix} x_1 \\ y_1 \\ z_1 \end{bmatrix} \tag{B.1}$$

where R_ν and R_δ are rotation matrices respectively of angle ν around $\vec{y}$ and of angle δ around $\vec{x}$. This derives :

$$\begin{bmatrix} x \\ y \\ z \end{bmatrix} = \begin{bmatrix} \cos\nu & \sin\delta\sin\nu & -\sin\nu\cos\delta \\ 0 & \cos\delta & \sin\delta \\ \sin\nu & -\sin\delta\cos\nu & \cos\delta\cos\nu \end{bmatrix} \begin{bmatrix} x_1 \\ y_1 \\ z_1 \end{bmatrix} \tag{B.2}$$

Hence, the 2D basis (for 1 pixel) for the back-projected image is :

$$\left(\frac{-\lambda D}{N_X P_X} \begin{bmatrix} \cos\nu \\ 0 \\ \sin\nu \end{bmatrix}, \frac{-\lambda D}{N_X P_X} \begin{bmatrix} \sin\delta\sin\nu \\ \cos\delta \\ -\sin\delta\cos\nu \end{bmatrix} \right) = \left(p_x \begin{bmatrix} -\cos\nu \\ 0 \\ -\sin\nu \end{bmatrix}, p_y \begin{bmatrix} -\sin\delta\sin\nu \\ -\cos\delta \\ \sin\delta\cos\nu \end{bmatrix} \right) \tag{B.3}$$

with again, λ the wavelength of the incident X-ray beam, D the detector-to-sample distance, N_X and N_Y the number of pixels in the detector along $\vec{X}$ and $\vec{Y}$ of size P_X and P_Y, and p_x, p_y the 2D basis of the reconstructed object.

As for the third axis, since the 2D wavefront which will be propagated to the detector must be summed along the propagation direction, this axis must lie along the sample-detector axis, i.e. perpendicular to the other two axis :

$$\vec{p_z} \parallel R_\nu R_\delta \begin{bmatrix} 0 \\ 0 \\ 1 \end{bmatrix} = \begin{bmatrix} -\sin\nu\cos\delta \\ \sin\delta \\ \cos\delta\cos\nu \end{bmatrix} \tag{B.4}$$

The dimension of p_z can be chosen arbitrarily. A suitable size can be so that its projection on the laboratory z-axis matches the probe's pixel size p_p :

$$p_z = \frac{p_p}{\sin\delta} \tag{B.5}$$

Other size can be chosen for p_z , i.e. to match the displacements of the probe, or an horizontal geometry :

$$p_z = \min\left(\frac{p_y}{\sin\delta}, \frac{p_x}{\sin\nu}\right) \tag{B.6}$$

B.2 3D BRAGG PTYCHOGRAPHY

For a rocking-curve-based 3D Bragg geometry, one has to consider Ψ the rotation angle around the starting diffraction angle. Typically Ψ will vary $\pm 0.5°$. The step along the rotation is ψ, so that :

$$\Psi = I_\Psi \psi \tag{B.7}$$

where $I_\Psi$is the integer index of the rotation along Ψ. In the particular case of a rotation around the x-axis (denoted η in PSIC geometry), the rotation matrix is :

$$R_\Psi = \begin{bmatrix} 1 & 0 & 0 \\ 0 & 1 & \Psi \\ 0 & -\Psi & 1 \end{bmatrix} \tag{B.8}$$

where a linear approximation was used as $\Psi \ll \pi$.

Starting from the coordinates (X, Y) onto the detector, the corresponding coordinates (x^*, y^*, z^*) of the 3D projection to reciprocal space are such that :

$$\begin{bmatrix} x^* \\ y^* \\ z^* \end{bmatrix} = R_\Psi^{-1} \left(\frac{1}{\lambda D} R_\nu R_\delta \begin{bmatrix} -X \\ -Y \\ D \end{bmatrix} - \begin{bmatrix} 0 \\ 0 \\ 1/\lambda \end{bmatrix} \right) \tag{B.9}$$

Indeed, the pixel detector first has to be put into the reference frame and then projected onto the Ewald's sphere of radius $1/\lambda$ under the flat sphere approximation. Next, a translation of the origin to $(0, 0, 1/\lambda)$ is necessary to express the coordinates in the reciprocal space. Finally, as one wants to compute the part of reciprocal space which falls onto the Ewald's sphere, the inverse of the Ψ rotation matrix is applied. One can introduce $\begin{bmatrix} I_X \\ I_Y \\ I_\Psi \end{bmatrix}$ the pixel coordinates onto the detector so that $\begin{bmatrix} X \\ Y \\ \Psi \end{bmatrix} = \begin{bmatrix} I_X P_X \\ I_Y P_Y \\ I_\Psi \Psi \end{bmatrix}$. This way, equation B.9 writes :

$$\begin{bmatrix} x^* \\ y^* \\ z^* \end{bmatrix} = \frac{1}{\lambda D} \begin{bmatrix} -P_X \cos\nu & -P_Y \sin\delta \sin\nu & 0 \\ 0 & -P_Y \cos\delta & -\Psi D(\cos\delta \cos\nu - 1) \\ -P_X \sin\nu & P_Y \sin\delta \cos\nu & \Psi D \sin\delta \end{bmatrix} \begin{bmatrix} I_X \\ I_Y \\ I_\Psi \end{bmatrix} + \frac{1}{\lambda} \begin{bmatrix} -\sin\nu \cos\delta \\ \sin\delta \\ \cos\delta \cos\nu - 1 \end{bmatrix} \tag{B.10}$$

This transformation matrix enables the expression of the three basis vectors of reciprocal space :

$$\begin{bmatrix} \vec{e_1^*} & \vec{e_2^*} & \vec{e_3^*} \end{bmatrix} = \frac{1}{\lambda D} \begin{bmatrix} -P_X \cos\nu & -P_Y \sin\delta \sin\nu & 0 \\ 0 & -P_Y \cos\delta & -\Psi D(\cos\delta \cos\nu - 1) \\ -P_X \sin\nu & P_Y \sin\delta \cos\nu & \Psi D \sin\delta \end{bmatrix} \tag{B.11}$$

and the definition of the center of diffraction $\vec{k_0}$:

$$\vec{k_0} = \frac{1}{\lambda} \begin{bmatrix} -\sin\nu\cos\delta \\ \sin\delta \\ \cos\delta\cos\nu - 1 \end{bmatrix} \tag{B.12}$$

so that :

$$\begin{bmatrix} x^* \\ y^* \\ z^* \end{bmatrix} = I_X\vec{e_1^*} + I_Y\vec{e_2^*} + I_\Psi\vec{e_3^*} + \vec{k_0} \tag{B.13}$$

This derivation is of major importance as it leads to the creation of the orthonormalization matrix and its inverse. After inversion of the 3D array along the (X, Y, Ψ) directions by FFT, the resulting array in real (object) space is non-orthonormal, with basis vectors $\begin{bmatrix} \vec{e_1} & \vec{e_2} & \vec{e_3} \end{bmatrix}$ being reciprocal to $\begin{bmatrix} \vec{e_1^*} & \vec{e_2^*} & \vec{e_3^*} \end{bmatrix}$. For a discrete FT, the dimensions of the basis vectors after transformation are related to the total domain size, *i. e.*, $\begin{bmatrix} \vec{e_1} & \vec{e_2} & \vec{e_3} \end{bmatrix}$ being reciprocal to $\begin{bmatrix} N_X\vec{e_1^*} & N_Y\vec{e_2^*} & N_\Psi\vec{e_3^*} \end{bmatrix}$. This can be solved numerically in matrix form by :

$$\begin{bmatrix} \vec{e_1} & \vec{e_2} & \vec{e_3} \end{bmatrix} = \left(\begin{bmatrix} N_X\vec{e_1^*} & N_Y\vec{e_2^*} & N_\Psi\vec{e_3^*} \end{bmatrix}^{-1} \right)^T \tag{B.14}$$

C

GRADIENT MINIMIZATION FOR THE OBJECT UPDATE IN SINGLE-ANGLE 3D BRAGG PROJECTION PTYCHOGRAPHY

The object derivative can be used as a search direction, and then a gradient minimization algorithm (single-step or full conjugate gradient) can be used. Starting from the derivative versus the object:

$$\frac{\partial}{\partial O_{r,z_0}} \sum_j \left| \Psi_j(\vec{r}) - \sum_Z P(\vec{r} - \vec{r}_j) O(\vec{r}) \right|^2 = - \sum_j P(\vec{r_{z_0}} - \vec{r}_j) \left(\Psi_j^*(\vec{r}) - \sum_Z P^*(\vec{r} - \vec{r}_j) O^*(\vec{r}) \right) \tag{C.1}$$

If the search direction ΔO is known, the optimal value for the object is $O + \gamma \Delta O$, with:

$$\sum_j \left| \Psi_j - \sum_Z P(O + \gamma \Delta O) \right|^2 = \sum_j \left| \Psi_j - \sum_Z PO - \gamma \sum_Z P \Delta O \right|^2 \tag{C.2}$$

$$= \sum_j \left\{ \left| \Psi_j - \sum_Z PO \right|^2 + \gamma^2 \left| \sum_Z P \Delta O \right|^2 - 2\gamma \mathrm{Re} \left[\left(\Psi_j - \sum_Z PO \right)^* \sum_Z P \Delta O \right] \right\} \tag{C.3}$$

For a quadratic expression $A\gamma^2 + B\gamma + C$, the minimum is at the center of the two roots: $\gamma_{\min} = \frac{-B}{2A}$, so that:

$$\gamma_{\min} = \frac{\mathrm{Re} \left[\sum_j \left\{ \left(\Psi_j - \sum_Z PO \right)^* \sum_Z P \Delta O \right\} \right]}{\sum_j \left| \sum_Z P \Delta O \right|^2} \tag{C.4}$$

D

RESUME EN FRANCAIS

D.1 INTRODUCTION

L'ingénierie des contraintes révolutionne actuellement le monde de la nanotechnologie, en ce qu'elle permet d'améliorer les performances de dispositifs tels que les structures semi-conductrices, en manipulant les propriétés physiques des matériaux à travers une déformation élastique. Dans ce contexte, la déformation élastique traduit le déplacement à l'échelle atomique, en prenant comme référence la position d'équilibre d'un arrangement d'atomes d'un réseau cristallin parfait. La déformation peut être le résultat d'une croissance par épitaxie de deux cristaux, ou bien d'une différence de coefficient de dilatation, une contrainte résiduelle ou encore une force extérieure.

Dans le domaine des nanotechnologies, l'introduction de contraintes est utilisée principalement dans le but d'améliorer la mobilité des porteurs de charge dans un canal de transistors, pour des systèmes consistant en une extrêmement fine couche semi-conductrice épitaxiée sur un substrat ou pour ajuster les propriétés optoélectroniques. Cependant, le contrôle et la compréhension de telles modifications à l'échelle atomique sont rendus complexes par l'intéraction directe entre d'une part l'environnement des couches actives d'intérêt pour le procédé complet de fabrication, et d'autre part la réponse du réseau cristallin.

Par conséquent, il est important de développer des techniques de caractérisation précise à l'échelle nanométrique qui introduisent un minimum de perturbations potentielles. Si la Microscopie Electronique en Transmission est la technique pouvant atteindre la plus haute résolution spatiale (sub-nanométrique), elle nécessite en contrepartie une préparation minutieuse de l'échantillon à même d'altérer la contrainte et reste limitée en terme de résolution de contraintes (jusqu'à 10^{-3}): la technique est fondamentalement limitée par la profondeur de pénétration des électrons. A l'inverse, le développement des méthodes dites d'Imagerie par Diffraction Cohérente de rayons X en condition de Bragg a permis d'obtenir une technique de caractérisation ultra-sensible à la déformation cristalline (jusqu'à 10^{-5}) avec une résolution spatiale limitée en théorie uniquement par la longueur d'onde du faisceau sonde. L'utilisation d'un faisceau de rayons X cohérents permet en effet de retrouver numériquement l'information de phase encodée dans l'intensité diffractée. Les reconstructions tridimensionnelles ainsi obtenues sont limitées principalement par

les conditions expérimentales (longueur d'onde, degré de cohérence du faisceau, précision des moteurs, rapport signal sur bruit de l'intensité diffractée, qualité et taille du détecteur) mais aussi par l'échantillon lui-même. En effet, les échantillons présentant des contraintes très inhomogènes ainsi que les échantillons très étendus (ne serait-ce que dans une direction) posent problème. Dans le but de fournir une technique capable de répondre à ces problématiques, la Ptychographie en condition de Bragg a été introduite au début des années 2010.

Ces travaux de thèse sont consacrés à l'étude et au développement de ces méthodes de caractérisation basées sur la diffraction de rayons X en condition de Bragg. Ainsi, la méthodologie est au coeur de ce manuscrit, notamment dans le but de tester et d'implémenter des solutions numériques faciles d'appréhension, efficaces et robustes, notamment via la librairie python PyNX, développée à l'ESRF. Le manuscrit de thèse, rédigé en anglais, se compose de deux parties distinctes. La première est constituée de deux chapitres ayant pour but de présenter les concepts théoriques à propos des notions cristallographiques de contrainte et déformation, ainsi que sur la notion de diffraction cohérente, avec des précisions sur le principe de la géométrie de Bragg. Les techniques et configurations expérimentales sont détaillées, avec un accent particulier sur le formalisme de reconstruction de phase.

La seconde partie du manuscrit se concentre sur la description de l'application des méthodes de caractérisation, à travers trois chapitres. Ainsi, le chapitre 4 est dédié à l'étude de couches gravées de silicium-germanium ultra-minces (de 13 à 20 nm d'épaisseur) et contraintes (sSiGeOI, en anglais strained silicon germanium on insulator), qui sont actuellement développées afin d'être intégrées comme canaux pour la technologie CMOS à base de Silicium complètement déserté sur isolant (FDSOI). L'état de contrainte de ces couches minces revêt un intérêt particulier, d'autant plus que c'est le procédé novateur dit "de condensation" qui a été utilisé pour la croissance du silicium-germanium en une couche ultra-mince avec (quasiment) aucun défaut cristallin. La principale interrogation à élucider réside dans le comportement de la contrainte lorsque des conditions libres sont introduites aux bords des couches par gravure. Une première approche est réalisée par des simulations reposant sur la méthode d'éléments finis (FEM), puis les caractérisations effectuées à l'aide de spectroscopie Raman par le Dr R.Berthelon sont évoqués. Enfin, ce chapitre détaille une description complète de la technique de Microscopie à Balayage par Diffraction de Rayons X (SXDM), ainsi que de la méthode d'analyse associée. Les résultats obtenus grâce à l'utilisation de cette technique sur la ligne de lumière ID01 de l'ESRF sont présentés puis discutés : non seulement il est possible d'extraire une information statistique sur les multiples canaux mesurés, mais encore il est possible d'inférer une longueur moyenne de relaxation de la contrainte.

Le chapitre 5 est dédié la présentation d'une expérience innovante menée à l'ESRF sur la ligne de lumière ID01, couplant la capacité d'indexation de grains microscopiques de la technique d'imagerie de Tomographie par Contraste de Diffraction de rayons X (DCT), avec la résolution spatiale nanoscopique et la sensibilité à la déformation cristalline de la technique d'Imagerie par Diffraction Cohérente en condition de Bragg (BCDI). Un intérêt particulier est porté sur la méthode de caractérisation du faisceau sonde puisqu'il est primordial de faire correspondre la taille transverse du faisceau avec celle du grain étudié. Enfin, la conclusion de ce chapitre sert de proposition pour une nouvelle méthode numérique pour évaluer la sensibilité à la déformation cristalline d'une reconstruction obtenue par BCDI.

Enfin et surtout, le chapitre 6 introduit la méthode dite de ptychographie. D'abord, un court résumé du développement de la technique est introduit, puis les algorithmes principaux utilisés pour reconstruire à la fois l'objet illuminé et le faisceau sonde sont décrit minutieusement. Ensuite, l'étape clé est la transposition de ces algorithmes, originalement crées pour une géométrie dite "directe", où le faisceau, l'objet et le détecteur sont alignés, dans un contexte de géométrie de Bragg. Dans un souci de clarté et d'exhaustivité, le chapitre contient ensuite un portfolio de l'ensemble des publications scientifiques à propos de la ptychographie par diffraction de rayons X en condition de Bragg, depuis les débuts en "Projection 2D" jusqu'aux récentes avancées ayant conduit à la "Projection 3D par angles multiples". De cette façon, le lecteur se voit fournir les outils pour appréhender la complexité des jeux de données produits par une expérience de ptychographie en condition de Bragg. Enfin, les différentes méthodes numériques développées et implémentées dans la libraire Python PyNX sont testées et discutées. En premier lieu, à travers des simulations d'expériences et de reconstructions sur les échantillons de couches ultra-minces de SiGeOI, utilisant notamment les champs de déplacement cristallins obtenus par modélisation d'éléments finis (COMSOL) pour une représentation adéquate des échantillons. En second lieu, ce sont des données provenant d'expériences conduites en synchrotron qui sont analysées à l'aide de ces méthodes numériques. En conclusion, l'efficacité particulière de la ptychographie en condition de Bragg par Projection 2D est démontrée par la reconstruction de la phase d'un micro-disque de multi-couches à gradient de composition en GeSn sous contrainte.

D.2 DÉFORMATION CRISTALLINE - DÉFINITIONS

La déformation est la réponse d'un système à l'application d'une force par unité de surface, appelée contrainte. Par exemple, à cause de la différence de paramètre

de maille entre deux matériaux cristallins, la croissance d'une fine couche sur un substrat conduit inévitablement à une déformation de cette couche.

Depuis l'introduction de la miniaturisation par Richard Feynman comme une science d'avenir, la nanoscience et la nanotechnologie sont en plein essor. En effet, les scientifiques ont découvert qu'en plus d'être plus robustes, du moins à basse température, les nanomatériaux présentent l'avantage d'un contrôle précis de leurs propriétés électronique, optique, magnétique... directement par un ajustement précis de leur déformation élastique. Notamment, les matériaux semi-conducteurs voient leur structure de bande modifiée par l'ajout de déformation élastique, plus précisément une possible levée de dégénérescence de la bande de valence et donc une réduction de la densité d'états. En conclusion, les propriétés électroniques des nanostructures semi-conductrices peuvent être fortement modifiées par l'introduction d'une déformation cristalline, menant à des applications aussi bien dans le domaine des transistors que des systèmes optoélectroniques.

La loi de Hooke définit la relation liant la déformation à la contrainte, en fonction de quantités appelées tenseurs, des constantes élastiques, spécifiques à chaque matériau. Cette relation est à la base de tout calculs de déformation élastique. Elle permet notamment de s'intéresser à la réaction d'un matériau cristallin en croissance par épitaxie sur un substrat cristallin. En particulier, on retiendra que la relation contrainte-déformation d'un matériau peut se simplifier en faisant intervenir le ratio de Poisson : dans la direction de croissance (verticale), la déformation est directement proportionnelle à la déformation moyenne dans le plan horizontal.

D.3 DIFFRACTION COHÉRENTE DE RAYONS X

Dans le cadre de la cristallographie des structures cristallines à trois dimensions, la diffusion de rayons X par des atomes produit des pics bien définis dans les directions déterminées par l'orientation ainsi que les symétries du cristal. Ces pics sont appelés pics de Bragg et proviennent des interférences constructives entre les ensembles discrets de plans atomiques parallèles qui constituent le cristal. Ainsi, ils contiennent des informations directement liées à l'agencement atomique de l'échantillon. Ces considérations sont à la base de la diffraction cohérente, la technique au centre des expériences présentées au long de ce manuscrit. Ce chapitre tend à définir les rayons X et comment ils peuvent être obtenus sous forme de rayonnement synchrotron, puis introduit certaines définitions cristallographiques aidant à la compréhension de la diffusion par un cristal. Enfin, le concept de cohérence est discuté, ainsi que les principes de bases des régimes d'imagerie. Le chapitre se clôt sur une longue présentation de la technique d'imagerie par diffraction cohérente de rayons X (CDI). Pour cela, les algorithmes de reconstruction de la phase sont explicités,

avec des rappels sur les notions de sur-échantillonnage, résolution théorique ainsi que sur les récentes avancées dans le domaine de CDI. Enfin, le cas particulier de CDI en condition de Bragg est introduit, notamment à l'aide de la description d'une expérience typique.

D.3.1 *Rayons X*

Les rayons X furent découverts en 1895 par Wilhelm Conrad Rontgen, et de nombreux progrès ont depuis lors été effectués sur la compréhension dont ils interagissent avec la matière. Ce sont des ondes électromagnétiques dont l'énergie se situe entre 100 keV et 100 eV. Les travaux de cette thèse ont été fait avec des rayons X qualifiés de "dur" dont la longueur d'onde est comprise entre 0.1 et 6 Angström, leur plus grande énergie permettant une meilleure pénétration des radiations. Pour simplifier, trois scénarios peuvent se produire lorsque des rayons X interagissent avec des atomes. Premièrement, le photon X est absorbé par l'atome, ce qui génère une excitation électronique ou phonique de l'atome. Deuxièmement, le photon X est diffusé de manière inélastique, de l'énergie est perdue par le photon et par conséquent le photon diffusé possède une fréquence plus basse que le photon incident. Troisièmement, le photon X est diffusé de manière élastique, l'énergie cinétique est donc conservée. Dans l'approche théorique développée ci-après de la production de rayonnements synchrotron dans les sources de troisième génération, on fera en outre l'approximation dite cinématique, signifiant qu'un photon X ne peut pas subir d'autre diffusion après avoir rencontré un premier électron.

D.3.2 *Rayonnement synchrotron*

Depuis la découverte des rayons X, la principale limitation a toujours été la source de lumière. La première source de rayons X a été réalisée grâce au tube Coolidge, utilisant le principe d'émission thermoïonique. Un filament de tungstène est chauffé, de façon à produire des électrons qui sont accélérés grâce à l'application d'une tension dans le tube, en direction d'une anode refroidie à l'eau. En heurtant l'anode, les électrons subissent une forte décélération et perdent leur excès d'énergie cinématique. Cette perte se traduit majoritairement sous forme de chaleur, mais aussi en partie sous forme d'émission de rayons X. Bien sûr, la différence produite par la création des synchrotrons est phénoménale. Un rayonnement synchrotron décrit un rayonnement émis par des particules chargées et accélérées à une vitesse relativiste le long d'une trajectoire courbe. Cela produit une source d'une intensité et d'une brillance spectrale toutes deux exceptionnelles, particulièrement à très courte longueur d'onde. La particularité des sources synchrotron de

troisième génération, telle que l'ESRF - the European Synchrotron, réside dans l'introduction d'un nouveau genre d'éléments d'insertion, en remplacement des classiques aimants de courbure, les ondulateurs. Ces structures magnétiques multipôle permettent de faire subir aux électrons de nombreuses accélérations successives, conduisant à un rayonnement synchrotron bien plus intense que celui émis par un aimant de courbure. L'intensité de la source augmente et le cône d'émission se rétrécit lorsque le nombre de période du multipôle augmente. A l'ESRF, l'anneau de stockage où circulent des paquets d'électrons fait 844 m de circonférence. Un courant de 200 mA circule à travers 43 aimants de courbure et éléments d'insertion. La majorité des expériences d'imagerie par diffraction cohérente ont lieu sur les lignes de lumière ID01, ID10, ID13 et ID16.

D.3.3 *Définitions cristallographiques*

Un cristal est une structure périodique tri-dimensionnelle, répétant un empilement ordonné ou motif. La périodicité du motif est exprimée par un réseau constitué de nœuds qui représentent les sommets de la maille. Les arêtes de la maille élémentaire définissent les vecteurs de la base. Les plans définis par trois nœuds du réseau, et les directions définies par deux nœuds du réseau sont qualifiés de "nodaux" (plan nodal, direction nodale) ou mieux encore “réticulaires” Les indices de Miller sont utilisés pour désigner l'orientation des plans cristallins dans un cristal. Ainsi, les plans réticulaires (hkl) décrivent l'ensemble de plans parallèles dont les intersections avec le réseau cristallin sont périodiques. Pour un cristal cubique, de largeur de maille a, la distance interréticulaire entre deux plans réticulaires successifs de la famille (hkl) est:

$$d_{hkl} = \frac{a}{\sqrt{h^2 + k^2 + l^2}}$$

Pour n'importe quel cristal, on peut aussi convenablement définir un réseau réciproque, dont la base $(\vec{a^*}, \vec{b^*}, \vec{c^*})$ est défini par:

$$\begin{aligned}
\vec{a^*} &= 2\pi \frac{\vec{b}\times\vec{c}}{\vec{a}\cdot(\vec{b}\times\vec{c})} \\
\vec{b^*} &= 2\pi \frac{\vec{c}\times\vec{a}}{\vec{b}\cdot(\vec{c}\times\vec{a})} \\
\vec{c^*} &= 2\pi \frac{\vec{a}\times\vec{b}}{\vec{c}\cdot(\vec{a}\times\vec{b})}
\end{aligned}$$

Ainsi, la position d'un noeud du réseau réciproque est défini par le vecteur $\vec{G_{hkl}} = h\vec{a^*} + k\vec{b^*} + l\vec{c^*}$ qui est perpendiculaire aux plans réticulaires de la famille (hkl). Il convient alors d'introduire la loi de Bragg, qui dicte que pour une radiation incidente de longueur d'onde lambda, illuminant un ensemble de plans réticulaires

séparés par une distance d_{hkl}, il y aura des pics d'intensité diffractant dans les directions 2θ de l'espace vérifiant:

$$n\lambda = 2d_{hkl}\sin\theta$$

avec: d_{hkl} la distance interréticulaire, θ l'angle de Bragg, ou demi angle de déviation, n l'ordre de diffraction (entier) et λ la longueur d'onde des rayons X incidents. Une compréhension géométrique de la loi de Bragg peut être obtenue grâce à la sphère d'Ewald. La sphère d'Ewald est centrée sur le cristal, son rayon est de $2\pi/\lambda$ dans l'espace réciproque, où les vecteurs d'ondes incidente et diffractée sont de même norme, égal au rayon. L'origine de l'espace réciproque se situe à l'intersection de la sphère et du vecteur d'onde incident. Alors, tout point (h,k,l entiers) du réseau réciproque coïncidant avec l'enveloppe de la sphère d'Ewald se trouve en condition de diffraction de Bragg.

D.3.4 *Diffusion classique*

Cette partie de la thèse reprend les calculs de diffraction par des cristaux, qu'ils soient parfaits ou avec des champs de déplacements. En résumé, l'amplitude diffractée par un cristal est décrit par la somme des facteurs de diffusion atomique de chaque atome constituant le cristal, multipliés par un facteur de phase prenant en compte la différence de phase introduite par la position spatiale de chaque atome. Il est alors possible d'exprimer l'amplitude diffuse comme le produit de deux termes, le facteur de forme et le facteur de structure. Le premier est directement relié à l'enveloppe du cristal, c'est-à-dire sa forme, et définit la forme de la distribution d'intensité résultante. Le second n'est autre que la transformée de Fourier de la densité électronique de la maille élémentaire, et dicte l'intensité relative de chaque réflexion. Lorsqu'un champ de déplacement est présent à l'intérieur du cristal, c'est-à-dire qu'un bloc de matière, atome ou groupe d'atomes, est déplacé de sa position originale par un vecteur $\vec{u}(\vec{r})$, une différence de chemin optique est introduite entre les rayons X diffus, égale à $\vec{q_{hkl}} \cdot \vec{u}(\vec{r})$. L'amplitude diffuse par le cristal en entier est alors réécrite en multipliant par un facteur de phase additionnel l'amplitude diffuse par chaque atome. Le résultat final reste une transformée de Fourier, mais contenant des informations sur les déplacements de chaque atome.

D.3.5 *Cohérence*

Les rayons X ne sont jamais complètement cohérents puisque la relation de phase d'un champ complexe entre deux points différents spatialement et temporellement n'est pas prévisible, c'est-à-dire que le faisceau X ne consiste pas en une onde plane

"parfaite" et possèdera nécessairement un certain degré de cohérence. La manière globale d'évaluer la cohérence d'un champ électromagnétique passe par le calcul de la fonction de cohérence mutuelle (ou degré complexe de cohérence), nécessitant le calcul de la cohérence mutuelle, autocorrélation dans le temps et l'espace du champ électromagnétique. Le degré complexe de cohérence consiste en un jeu de données à 7 dimensions (2×3 coordonnées spatiales et une coordonnée temporelle) qui est difficile à calculer. Cependant, le cadre de l'optique géométrique fournit une autre définition de la cohérence, se divisant en une cohérence longitudinale le long de la direction de propagation, et une cohérence transverse. La cohérence longitudinale dépend de la longueur d'onde, alors que la cohérence transverse dépend de la longueur d'onde, de la taille de la source et de la distance entre la source et l'échantillon. Typiquement, sur la ligne de lumière ID01, lorsque l'ondulateur est réglé pour émettre un faisceau X d'énergie 8 keV, la cohérence longitudinale est de 0.5 µm alors que la cohérence transverse, asymétrique, est de 800 µm x 80 µm. La principale conséquence est que la plupart des échantillons ne sont pas sous une illumination complètement cohérente. En pratique, la portion cohérente du faisceau est sélectionnée à l'aide de fentes puis focalisée sur l'échantillon.

D.3.6 *Note sur les régimes d'imagerie*

La principale information à retenir est que les expériences conduites au cours de cette thèse ont été faites dans le cadre du régime en champ lointain, ou régime de Fraunhofer, où le détecteur est placé suffisamment loin de l'échantillon pour négliger la courbure sphérique des ondes émises par la diffusion atomique, justifiant ainsi l'utilisation de Transformées de Fourier.

D.3.7 *Principes d'imagerie cohérente*

Les techniques d'imagerie par diffraction cohérente (CDI) reposent sur l'utilisation de source possédant une brillance très élevée (nombre de photons par seconde par unité de crosse-section par divergence angulaire par 0.1% de la gamme spectrale) qui peut être produite dans un synchrotron de troisième génération. Le terme CDI regroupe les techniques d'imagerie 3D non-destructive et ne nécessitant pas l'usage d'optique permettant de déterminer la structure de spécimens à une résolution théoriquement limitée uniquement par la longueur d'onde du faisceau incident. En pratique, la résolution se trouvera limitée par le nombre de photons diffusés, l'étendue de la diffraction dans l'espace réciproque captée par le détecteur, mais aussi par les algorithmes de reconstruction eux-mêmes. Après les premières expériences réussies de Miao et al en 1999, le CDI a profité des avancées

en optique des rayons X, qui permettent aujourd'hui d'illuminer des échantillons plus petits que 100 nm, et rendent possible à l'heure actuelle la reconstruction de ces échantillons avec une résolution allant jusqu'à 10 nm. Le principal problème auquel le CDI répond est le problème de Phase, inhérent à la cristallographie sous rayons X : l'intensité enregistrée par le détecteur n'est que le module carré de l'amplitude diffractée par l'échantillon, par conséquent l'information de phase, contenant les informations de champs de déplacement, est perdue. Le CDI utilise des contraintes additionnelles couplées à des algorithmes itératifs pour "retrouver" la phase. Ce manuscrit contient davantage de détails concernant les besoins de suréchantillonnage, les relations entre le champ de vue et les tailles de pixel (detecteur vs reconstruction) ainsi que sur le formalisme général du concept de "récupération de phase" (phase retrieval). En outre, cette partie propose un rapide panorama des dernières avancées réalisées dans ce domaine.

D.3.8 *Imagerie cohérente en condition de Bragg*

L'intérêt du CDI en condition de Bragg est de sonder les champs de déplacement atomiques à l'intérieur de cristaux, qui correspondent à la phase de la densité électronique complexe évoquée plus tôt. En mesurant l'intensité diffractée autour d'un pic de Bragg donné, il est possible de recouvrir l'information de déplacement le long du vecteur de diffraction. Cependant, le cas de la diffraction de Bragg est délicat à traiter, d'autant plus que les cristaux étudiés sont extrêmement petits (nano ou microscopiques) grâce à des configurations expérimentales très sensibles qui doivent être manipulées avec une grande attention. Cette partie du manuscrit présente l'ensemble des calculs nécessaires à la compréhension de la relation entre l'espace réciproque (de détection) à l'espace direct.

D.4 MICROSCOPIE À BALAYAGE PAR DIFFRACTION DE RAYONS X - IMAGERIE DES FLUCTUATIONS DE CONTRAINTES D'UNE NANOSTRUCTURE DE SIGEOI ULTRA MINCE POUR APPLICATION ÉLECTRONIQUE

Ce chapitre fournit une introduction à l'historique des développements de l'ingénierie des contraintes dans les canaux de technologie CMOS (Complementary Metal Oxide Semiconductor) qui permit une amélioration des performances. En particulier, la méthode dite de condensation est détaillée, puisqu'elle a été choisie récemment pour la croissance de couche ultra mince de silicium germanium, structure étant amenée à être intégrée en tant que canal de transistor à FDSOI (silicium pleinement déserté sur isolant, ou en anglais, Fully Depleted Silicon On Insulator). Ensuite la méthode de microscopie à balayage par diffraction de rayons X (SXDM) est présen-

tée en détail, puis utilisée pour évaluer l'état de contrainte dans des couches ultra minces de SiGe directement sur isolant.

D.4.1 *Introduction*

L'ingénierie des contraintes est maintenant perçue comme l'une des meilleures solutions pour continuer à suivre le chemin tracé par la loi de Moore, étant donné que la diminution de la taille des semiconducteurs a atteint ses limites. La technologie retenue dernièrement pour mener à bien l'amélioration continue des performances consiste en l'utilisation de substrats précontraints pour former des canaux ultra minces à très haute mobilité de porteurs. C'est la naissance de la technologie UTTB (Ultra thin Body and Buried Oxide)-FDSOI, combinant un contrôle électrostatique maximal via un oxyde enterré et une réduction des pertes et des courants parasites via une couche ultra mince complètement désertée. Le choix pour cette dernière s'est porté sur l'alliage silicium germanium puisqu'il permet une augmentation significative de mobilité des porteurs. La technique dite de condensation présente trois intérêts : d'abord elle permet d'obtenir une couche de SiGe intrinsèquement sous compression, ensuite elle conduit à des couches à très haute qualité cristalline et enfin elle ne repose que sur des procédés de manufacture déjà conventionnels. La cible de la condensation utilisée pour les échantillons étudiés est une couche de SiGe de 13 (et 20) nm d'épaisseur avec 25 % de germanium.

D.4.2 *Design de l'échantillon - fabrication*

L'empilement des échantillons est le suivant : à partir d'un substrat de silicium sur isolant (SOI, fournisseur : SOITEC) avec une couche d'oxyde enterré (BOX) de 20 nm, une couche de SiGe est crû par épitaxie cohérente par RPCVD. La couche de SiGe sur isolant est ensuite obtenue par condensation, en se servant de l'oxydation préférentielle du silicium. Le résidu de dioxyde de silicium se créant au-dessus du SiGe est supprimé par une gravure mouillée. Ensuite, une gravure est effectuée par lithographie. Pour cela, un masque est déposé par Plasma Enhanced CVD après une protection faite d'une couche d'oxyde de 4 nm d'épaisseur surmontée d'une couche de nitrure de silicium de 55 nm. Pour obtenir un SiGe uniforme en composition de germanium, un réchaud de 30 minutes à 1050 °C sous N2 est effectué. Ensuite, les motifs de SiGe sont obtenus par lithographie ultraviolette après une étape de gravure profonde. Enfin, le SiN est retiré par une gravure sélective au H3PO4. C'est cet empilement qui sert alors de référence. En outre, pour étudier le rôle du masque de SiN, un lot est étudié avant la suppression de la couche de SiN. Un masque spécial a été développé par le CEA-LETI pour comprendre les effets de

géométrie. Ainsi, chaque échantillon contient plusieurs motifs de SiGe, notamment des structures carrées de 500 nm $\times$500 nm, 2 µm $\times$2 µm et 5 µm $\times$5 µm.

D.4.3 *Mesures de déformations, simulations*

Premièrement, la simulation élastique de la couche de SiGe a été réalisée à l'aide du logiciel COMSOL permettant d'utiliser la méthode d'éléments finis. En utilisant une maille de calcul suffisamment fine pour évaluer l'évolution de la déformation aux bords des structures, couplée aux propriétés élastiques correspondant à la géométrie de la maille cristalline (direction principale 110), ces simulations permettent de connaître la déformation théorique de la structure de SiGe, la principale variable étant la largeur de la zone active. Il ressort de ces simulations que, premièrement, quelle que soit la largeur du SiGe, la contrainte se relâche aux bords, et en second lieu, le centre des plus petites structures (500 nm) présente une relaxation. Cette dernière information permet d'inférer que la longueur de relaxation du SiGe est au moins de 250 nm, c'est-à-dire que pour des structures dont la largeur est inférieure à 500 nm, l'état de déformation au centre n'est plus en accord avec l'objectif de compression. Les simulations, réalisées avec et sans SiN, mettent aussi en avant l'effet de cette couche, qui permet donc en théorie de maintenir la contrainte en compression. En effet, les simulations montrent que la déformation hors du plan, à l'approche d'un bord de la structure, est maintenue quasiment identique à celle du centre de la structure, uniquement lorsque la couche de SiN est présente. Ensuite, les résultats de microscopie Raman par R.Berthelon sont synthétisés, avec le rappel qu'ils ont été obtenus avec un faisceau sonde de 500 nm, c'est-à-dire une résolution spatiale d'au mieux 500 nm. Ainsi, les résultats obtenus sont des moyennes des déformations sur une grande plage du matériau, mais ils montrent tout de même que la déformation en compression dans le SiGe diminue lorsque la largeur de la structure diminue, ce qui ne peut être imputé qu'à une relaxation des bords. Enfin, un modèle analytique se basant sur les résultats de mesures par diffraction d'électrons avec nanofaisceau (NBED) obtenus par R.Berthelon, montre que la longueur de relaxation d'une structure de 800 nm de largeur se situe autour de 220 nm.

D.4.4 *Microscopie à Balayage par diffraction de rayons X (SXDM)*

La technique de microscopie à balayage par diffraction de rayons X (SXDM) est une méthode puissante permettant la caractérisation d'échantillons nano et microscopiques, en combinant la résolution dans l'espace réciproque fournie par la diffraction à rayons X durs avec la taille du faisceau sonde dans l'espace direct. La SXDM permet la caractérisation aussi bien d'un point de vue qualitatif que quanti-

tatif des propriétés structurelles de nanostructures individuelles, c'est-à-dire leurs paramètres de maille et orientations. La préparation de l'échantillon est minimaliste, dans le sens où elle ne requiert aucune destruction ou modification de l'état, ce qui ouvre la porte à des études in situ ou bien des structures enterrées. Par conséquent, la technique SXDM peut être considérée non destructive, même s'il convient de garder à l'esprit qu'un nombre trop important de photons interagissant avec l'échantillon peut modifier l'état de contrainte de ce dernier. La technique de SXDM a été développée particulièrement pour la ligne de lumière ID01 à l'ESRF. En effet, les délais des moteurs et du temps de lecture du détecteur ont été optimisés pour fournir des balayages rapides en continu. En bref, une cartographie de 40 000 points de l'échantillon, répétée à 20 angles d'incidence légèrement différents, nécessitait auparavant 9 jours de mesures mais est maintenant faisable en 2 heures et demie. Le principe du SXDM repose sur l'acquisition, en chaque point d'une cartographie, du pic de Bragg 3D en basculant l'échantillon et en enregistrant les images de diffraction avec un détecteur 2D. En rajoutant une troisième dimension aux données 2D du détecteur, il est possible de suivre précisément la position du centre de masse du pic de Bragg, et par conséquent cela donne accès aux variations de la structure locale de l'échantillon. La position du pic de Bragg dans l'espace réciproque est directement liée à la déformation et à l'orientation de la maille sondée. Dans l'espace direct, c'est la taille du faisceau sonde qui définit la résolution, mais dans l'espace réciproque, la résolution est théoriquement limitée par la longueur d'onde des rayons X. Dans le cas d'étude de ces travaux, le flux du faisceau sonde a dû être maximisé (3.5×10^6 photons/sec/nm2) en utilisant 0.4% de la gamme spectrale d'émission de l'ondulateur à 8 keV. En effet, l'épaisseur ultra mince de SiGe nécessite un maximum de photons pour produire suffisamment d'intensité diffractée. Le faisceau X est ensuite focalisé à 220 nm $\times$170 nm. L'angle d'incidence aura bien sûr une influence sur la taille réelle dans le repère de l'échantillon. Une étape cruciale de la technique est l'optimisation des angles de diffraction. L'objectif est donc de fournir une référence fiable pour calibrer les angles de Bragg. Cela est effectué en localisant le pic de Bragg du substrat de silicium, qui est dans son état relaxé et donc dont la valeur du paramètre de maille à température ambiante est bien connue. Cette mesure permet de connaître la correction systématique à appliquer dans les calculs.

D.4.5 *Analyse générique*

Certains problèmes, bien identifiés, s'immiscent régulièrement dans l'analyse d'un jeu de données obtenu par SXDM. Une partie d'entre eux proviennent de la manière dont les intensités diffractées sont acquises, nécessairement limitée par la plage du

balayage angulaire, mais aussi de la qualité et calibrage du détecteur. De plus, les erreurs de mauvais alignement de l'échantillon sont courantes et génèrent des mouvements parasites. Enfin et surtout, la forme de la diffraction dans l'espace réciproque peut s'avérer trompeuse et très compliquée à analyser, puisque par exemple le bruit de fond peut cacher une superposition des pics provenant à la fois de la couche d'intérêt et du substrat. Cette partie s'attarde sur une description de la voie à suivre pour s'affranchir d'une majorité de ces problèmes. Ensuite, il convient d'exposer les grandes étapes de l'analyse typique. Après avoir corrigé un maximum d'artefacts, il faut prendre une vue d'ensemble sur le jeu de données 5D : fusionner et convertir les données brutes en une cartographie 3D de l'espace réciproque pour chaque point du balayage. Dès lors, il est possible de réduire les données à trois jeux de données 2D, en extrayant la position 3D moyenne du pic de diffraction pour chaque point du balayage. En utilisant un repère sphérique de l'espace réciproque, chaque coordonnée peut être facilement interprétée comme une composante significative de la maille cristalline : paramètre de maille, inclinaison et twist. Ainsi, il existe une cartographie 2D de l'échantillon pour chacune de ces composantes. Ces cartographies sont alors suffisantes pour comprendre les variations locales de structure. Toutefois, si trois réflexions de diffraction ont été enregistrées, il est possible de les combiner pour obtenir le tenseur complet des déformations, mais cela nécessite un alignement ou du moins une correction précise de la position de l'échantillon lorsqu'il est basculé pour passer d'une direction de diffraction à une autre.

D.4.6 *Résultats et discussion*

Les échantillons ont été mesurés aux réflexions (004) et (113), pour chacun des différents types de motifs évoqués plus tôt, avec un pas de 100 nm pour le balayage et un champ de vue allant de 6 µm $\times$6 µm jusqu'à 12 µm $\times$12 µm. Cependant, l'intensité diffractée par le substrat de silicium était tellement intense et proche de celle diffractée par la couche de SiGe que l'analyse s'en est retrouvée très compliquée. Les détails de cette superposition se retrouvent dans le corps de ce manuscrit ainsi qu'une présentation détaillée des résultats pour chaque échantillon, chaque motif et chaque réflexion de Bragg. Les résultats se présentent principalement sous deux formes distinctes : d'abord les cartographies de déformation & orientation cristalline, et ensuite une analyse statistique de la déformation dans les zones considérées "centrales" sur chacun des motifs. La première forme des résultats permet de montrer que la relaxation de la déformation sur les bords des différents motifs est visible, et s'accompagne d'une inclinaison de la maille cristalline. L'analyse statistique non seulement montre l'homogénéité entre les motifs d'une même largeur et d'un même échantillon, mais permet aussi de comparer les motifs de différentes

largeurs. La déformation moyenne au centre des motifs est la plus petite pour les motifs les plus étroits. Puisque cette moyenne est extraite au centre des motifs, cela signifie que les motifs les plus étroits sont dans un état que l'on peut considérer relaxé, et non plus pleinement contraint : la longueur de relaxation de la déformation élastique est au moins égale à la moitié de la largeur des plus motifs, soit 250 nm. Enfin, à partir des cartographies il est possible d'extraire les profils de déformation. Cette analyse est réalisée sur les motifs les plus larges, étant donné qu'ils offrent l'avantage d'une part d'une plus grande plage de valeur de déformations et d'autre part de fournir les mesures les moins corrompues par des dérives parasites. Le modèle analytique élaboré à partir des mesures NBED est réutilisé pour évaluer la longueur de relaxation à partir de ces profils de déformations. Le modèle prouve être en bonne adéquation avec les mesures, et conduit à des longueurs de relaxation comprises entre 230 et 380 nm. Même s'il convient de garder à l'esprit que la taille du faisceau produit indéniablement un effet de flou - moyennage de la déformation sur toute la zone illuminée, donc la taille du faisceau est au moins la résolution spatiale des cartographies - ces valeurs de longueurs de relaxation ne sont pas en accord avec les simulations élastiques. Ainsi, ce sont probablement les fluctuations intrinsèques des deux étapes principales du procédé de croissance qui sont incriminables : l'épitaxie cohérente de SiGe sur substrat de SOI et la condensation. Puisque la condensation est un processus cinématique, il est légitime d'émettre des doutes sur l'homogénéité en profondeur et surtout sur la présence potentielle de défaut ou plus probablement de glissement à l'interface SiGe/Si. Il est très intéressant de remarquer que de récentes mesures réalisées par holographie à électron par V.Bourreau produisent des résultats en accord avec un modèle de glissement à l'interface.

D.5 BCDI ET DCT SUR DES GRAINS INCORPORÉS DANS UN CYLINDRE DE ZIRCONE

Ce chapitre fournit la description d'une expérience dont le but est de combiner la technique de Diffraction Contrast Tomography (DCT) avec celle de BCDI, pour caractériser des grains encastrés dans un cylindre de zircone.

D.5.1 *Introduction*

Dans les matériaux céramiques, les propriétés mécaniques sont largement influencées par les contraintes et déformations résiduelles provenant des différences entre les coefficients d'expansion thermique. Bien que les relations macroscopiques et microscopiques entre contrainte et déformation aient longuement été étudiées,

l'étude des champs de déformation à l'échelle microscopique du grain avec une résolution nanoscopique est encore à développer. La technique de DCT permet de localiser les grains présents dans un volume 3D tout en récupérant leur orientation cristalline. Il s'agit ensuite d'utiliser la technique de BCDI sur n'importe lequel de ces grains pour déterminer son tenseur 3D de déformation. Cette capacité à collecter des informations à la fois à l'échelle de l'échantillon - orientation et localisation de grains - et à l'échelle même du grain peut être considérée comme un préalable à toutes investigations sur les interactions complexes entre texture locale et déformation résiduelle. L'échantillon étudié consiste en un cylindre de 10 µm de diamètre et 80 µm de hauteur, préparé à l'aide d'une sonde ionique focalisée (FIB) à partir d'un bloc de zircone stabilisé à l'yttrium ($YZrO_2$, avec 8% d'yttrium). La taille typique des grains dans l'échantillon s'étend de 500 nm à 5 µm. Ce projet d'imagerie a été réalisé en collaboration entre le Dr. Wolfgang Ludwig (INSA Lyon / ESRF), visiteur scientifique sur la ligne de lumière ID11 de l'ESRF, le Dr. Jérôme Chevalier (INSA Lyon) et le Dr. Vincent Favre-Nicolin (ESRF).

D.5.2 *DCT*

La DCT est une technique d'imagerie basée sur la diffraction en champ proche (Fresnel) qui fournit des cartographies à haute résolution de grains dans échantillons polycristallins. Pour chaque grain individuel, la technique peut fournir l'orientation ainsi que le tenseur de déformation élastique avec une précision de quelques 10^{-4}. La technique combine les concepts de reconstruction de volume à partir de projection (tomographie) avec l'imagerie par diffraction de rayons X (topographie). En particulier, la technique s'appuie sur une méthode innovante de paire de Friedel pour analyser les données de diffraction : en indexant les tâches de diffractions il est possible de trouver une base constituée des paires de Friedel et ainsi remonter à la position et orientation du grain donnant lieu à ces paires. Les grains sont ensuite reconstruits individuellement en trois dimensions puis assemblés pour combler les vides à l'intérieur du masque de l'échantillon, lui-même obtenu à partir de l'absorption en géométrie directe. L'installation expérimentale nécessite la possibilité de faire tourner l'échantillon sur lui-même sur 360°, autour d'un axe perpendiculaire à la direction du faisceau incident. Un détecteur dont les pixels font 1.6 µm est placé juste après l'échantillon. Lors de la rotation, les grains constituant l'échantillon se retrouveront en condition de diffraction de Bragg et dévieront une partie du faisceau incident vers une tâche de diffraction, dont la position est enregistrée par le détecteur. Un plan cristallin réticulaire spécifique se retrouvera en condition de diffraction de Bragg un maximum de quatre fois durant une rotation complète, formant ainsi deux paires, séparées par une rotation de 180°

de l'échantillon. Comme les deux tâches d'une seule paire de Friedel définissent le chemin optique du faisceau diffracté qui passe nécessairement à travers le grain, elles permettent de retrouver l'angle de diffraction associé aux plans réticulaires (hkl) et $(h\bar{k}l)$ et ainsi le vecteur de diffraction associé. Sur la ligne de lumière ID01, la technique de DCT a été mise en place après avoir réalisé une LUT (Look Up Table) de l'erreur sur le moteur de rotation autour de l'axe vertical du diffractomètre. L'analyse des données obtenues, par un algorithme MATLAB développé par le Dr. Wolfgang Ludwig, permet d'obtenir rapidement l'orientation précise de 7 différents grains à l'intérieur de l'échantillon. Cela se traduit par la connaissance des angles exacts auxquels orienter l'échantillon pour placer un de ces grains en condition de diffraction de Bragg, information primordiale pour réaliser sans encombres une expérience de BCDI.

D.5.3 *BCDI*

Ces paragraphes présentent l'installation expérimentale utilisée sur la ligne de lumière ID01 pour effectuer la partie imagerie par diffraction cohérente sur le même échantillon. Un détecteur Maxipix est monté à 1.2 m de l'échantillon et le faisceau de rayons X à 8 keV est focalisé à l'aide d'une lentille de Fresnel. Avant de passer en géométrie de Bragg, des contrôles sont effectués en géométrie directe, dans le but de calibrer la taille du faisceau sonde. C'est la technique de ptychographie en transmission, en combinaison avec les algorithmes développés dans la libraire PyNX, qui est utilisée, avec d'abord le sommet de l'échantillon lui-même puis avec un objet de référence, l'étoile de Siemens, dont la granularité et le gradient de motifs permet une reconstruction extrêmement précise du front d'onde des rayons X. Il est aussi possible de procéder à une décomposition orthonormale du front d'onde complexe, qui permet de quantifier l'aspect cohérent du faisceau : plus le mode principal concentre une grande quantité de l'intensité du front d'onde (supérieure à 80%), plus le faisceau peut être considéré comme cohérent. La subtilité consiste à faire correspondre la taille transverse du faisceau avec le plus petit des grains indexés, c'est-à-dire un faisceau gaussien dont le lobe central fait 500 nm de diamètre, tout en concentrant le maximum de front d'onde cohérent dans ce lobe. Les détails relatifs aux considérations de cohérence longitudinale se retrouvent dans le manuscrit. Notons toutefois que l'utilisation de la technique de SXDM dans différentes orientations d'un même grain permet d'obtenir la projection de la forme du grain dans chacune de ces orientations, qui s'avère être parfois plus grande que la cohérence longitudinale. Par conséquent, les conditions d'illumination n'étaient pas idéales vis-à-vis de la taille des grains présents dans l'échantillon.

La méthode de reconstruction des grains est présentée en détail dans le corps du manuscrit, et peut être résumée de la manière suivante. S'appuyant uniquement sur les algorithmes de reconstruction de phase présents dans la librairie PyNX, tournant sur le processeur d'une carte graphique (gpu) NVidia Titan X, le processus fait d'abord intervenir une étape d'initialisation. En effet, il est nécessaire de trouver un support qui délimite les contours de l'objet à reconstruire. Ici, les projections le long de trois réflexions indépendantes ont pu être évaluées grâce à l'utilisation de la technique de SXDM. Cependant, la taille du lobe central du faisceau incident s'avère être légèrement inférieure à ces projections : le grain n'est pas en condition d'illumination complètement cohérente, et seulement la portion du grain illuminée de façon complètement cohérente pourra être reconstruite. C'est donc le lobe central du faisceau qui sert de support à la reconstruction.

Ensuite, 1000 reconstructions différentes, partant de phases aléatoires, sont obtenues en performant, pour chacune d'entre elles, 200 cycles d'Error Reduction (ER) suivis de 600 cycles de RAAR (Relaxed Averaged Alternating Reflectors). Ces deux algorithmes itératifs sont raffinés à l'aide d'un algorithme permettant d'éviter toute "solution double", où deux solutions symétriques se retrouvent superposées en une seule, et d'un algorithme de prise en considération de la cohérence partielle lorsque la solution se rapproche de son point de convergence. Enfin, le Free Log-Likelihood est utilisé comme figure de mérite pour extraire 50 reconstructions, et ces reconstructions servent alors de base pour une décomposition orthonormale en modes propres. Puisque le premier mode représente plus de 80% des 50 solutions, il est conservé comme solution finale au problème. Le volume est alors tronqué au-dessus de 50% de sa valeur en amplitude la plus intense. L'analyse de la phase complexe de ce volume donne directement accès au champ de déformation le long de la direction du vecteur de diffraction. Il en ressort que le champ de déformation à l'intérieur d'un même grain est similaire à la limite de sensibilité de la méthode de BCDI. Cela signifie soit que le champ de déformation ne provient que du bruit dans la reconstruction, soit que le grain est très homogène et ne présente pas de déformation significative. Globalement, cela se comprend puisqu'un tel matériau céramique devrait contenir uniquement des dislocations franches ou bien très peu de déformation à l'échelle microscopique. Il est intéressant de noter en outre que les mesures semblent indiquer qu'un gradient de déformation est présent, non pas à l'échelle d'un grain, mais bien à l'échelle du cylindre lui-même : les grains situés à la base du cylindre sont mesurés avec une déformation moyenne d'environ -0.2% par rapport à la valeur tabulée du paramètre de maille de zircone, alors qu'un grain situé quasiment au sommet du cylindre (soit 50 µm plus haut que les précédents) présente une déformation moyenne quasi nulle par rapport au zircone (inférieure à 0.05%).

D.5.4 *Sensibilité à la contrainte dans les reconstructions de BCDI*

L'imagerie par diffraction cohérente de rayons X en condition de Bragg donne accès à de l'information dans deux domaines bien différents : d'un côté, la reconstruction donne lieu à un objet de l'espace direct, auquel il faut associer une résolution spatiale, de l'autre côté, la résolution du problème de phase permet d'obtenir une caractérisation de la déformation de l'objet, ainsi il convient de définir la sensibilité de la méthode à la déformation. Alors que la résolution spatiale possède maintenant deux techniques bien identifiées et validées par la communauté, c'est-à-dire la PRTF (Phase Retrieval Transfer Function) et La FSC (Fourier Shell Correlation), il n'existe pas de consensus pour ce qui est de la sensibilité de la méthode à la mesure des déformations.

Deux méthodes sont proposées dans ce manuscrit. La méthode la plus détaillée est dérivée de la méthode de FSC, dans le sens où elle reprend le principe de corrélation entre deux reconstructions obtenues à partir de la même chaîne d'algorithmes sur deux jeux de données indépendants du même échantillon, ainsi que le principe de "shells". Les deux reconstructions sont alors réalignées et tronquées à la même taille, pour être cartographiées sur une seule grille commune de N voxels. L'élément central est la matrice des "différences de déformation". Pour chaque reconstruction, une matrice de taille N^2 est construite de la manière suivante : pour chaque voxel, la différence absolue des déformations par rapport à tous les voxels de la reconstruction :

$$D_{ij} = \left|\varepsilon_i - \varepsilon_j\right|, \quad \forall (i,j) \in [0, N-1]^2$$

où ε_i est la déformation évaluée au i-ième voxel d'une reconstruction. Ensuite, pour un ensemble de n coquilles $\{s_1, \ldots, s_k, \ldots, s_n\}$ d'intervalle de déformation, la valeur de "strain shell correlation" est calculée comme :

$$v_k = \frac{\sum D_1 D_2}{\sqrt{\sum D_1^2 D_2^2}}$$

où D_1 et D_2 sont les matrices des "différences de déformation", sommées aux indices (m, l) tels que $|\varepsilon_m - \varepsilon_l| \in s_k$, la coquille de déformation pour laquelle v_k est calculé. Ainsi, la valeur de s_k pour laquelle v_k vaut 0.5 peut être considérée comme la sensibilité à la déformation obtenue par la technique.

Une première validation est réalisée de manière numérique, où un jeu de données de diffraction est simulé en incluant un bruit de poisson. Pour un nombre de photons incidents de l'ordre de 10^3, la méthode de strain shell correlation conduit à une sensibilité à la déformation de l'ordre de 10^{-4}. On retrouve là la valeur par défaut communément utilisée par la communauté comme référence. En outre, cette

simulation montre qu'en augmentant le nombre de photons incidents, la sensibilité à la déformation peut augmenter jusqu'à 1.5×10^{-6}.

Ensuite, cette méthode est testée sur des données expérimentales, obtenues par le groupe de recherche de F.Hofmann (Université d'Oxford) sur la ligne de lumière 34-ID-C de l'Advance Photon Source, USA en août 2014. Les échantillons consistent en plusieurs cristaux d'or après exposition à différentes doses de sonde ionique focalisée. Plusieurs réflexions de Bragg ont été mesurées pour deux cristaux différents, avec environ 20 balayages angulaires pour chacune de ces réflexions. Aussi, en sommant 2, 4, 8 et 15 scans, il est possible de faire varier artificiellement le nombre de photons incidents et ainsi évaluer l'effet du nombre de photons sur la sensibilité à la déformation. Pour 8 scans, la valeur de sensibilité trouvée par la technique de strain shell correlation est de 2.5×10^{-5}. Toutefois, il n'y a pas de signe net d'une amélioration de la sensibilité lorsque le nombre de photons incidents est "artificiellement gonflé". Deux explications potentielles peuvent être apportées : soit la résolution spatiale obtenue avec peu de scans additionnés est trop faible et efface donc des détails, soit le jeu de données avec la plus faible intensité produit une reconstruction qui atteint déjà le niveau de sensibilité signifiant.

D.6 PTYCHOGRAPHIE EN CONDITION DE BRAGG

Ce chapitre se penche sur la technique de ptychographie, depuis ses principes jusqu'à son utilisation en condition de Bragg avec un faisceau cohérent de rayons X. Après une description de la méthodologie, des simulations sont réalisées dans le but de tester le bon fonctionnement des algorithmes implémentés durant la thèse sur la librairie python PyNX. Puis les résultats d'analyses de jeux de données obtenus de manière expérimentale sur les lignes de lumière ID01 à l'ESRF et Nanomax à Max IV, Lund, sont présentés.

D.6.1 *Introduction*

La ptychographie permet la reconstruction d'un objet étendu, c'est-à-dire plus grand que le faisceau qui l'illumine, à partir des images de diffraction obtenues en balayant l'objet avec le faisceau, tout en s'assurant qu'il existe un certain degré de recouvrement entre deux positions d'illuminations successives. Introduite dans les années 1970 dans le domaine de la microscopie électronique, la ptychographie est maintenant largement utilisée et développée pour la lumière visible ainsi que les rayons X, dans les géométries de transmission et de réflexion. De plus, la ptychographie présente deux avantages concrets. Premièrement, grâce à la redondance introduite par le recouvrement, la résolution spatiale d'une reconstruction peut être

meilleure que la taille du faisceau ou le pas du balayage. En second lieu, la ptychographie permet de recouvrir la phase complexe à la fois de l'objet illuminé et aussi du champ d'ondes.

D.6.2 *Principes de la ptychographie*

La ptychographie fait partie des techniques d'imagerie par diffraction cohérente, et s'appuie donc sur les mêmes notions de cohérence que décrites plus haut. La différence majeure réside dans le fait que la condition d'objet isolé est purement abolie, puisque l'objet sera balayé par l'illumination. C'est la condition de recouvrement qui remplace alors la contrainte de support dans l'espace direct. Les dernières avancées en terme de méthodes de reconstruction permettent d'utiliser des algorithmes d'optimisation non-linéaire telle que l'optimisation du maximum de vraisemblance (maximum likelihood, ML) pour améliorer la qualité finale d'une reconstruction. Comme dans les méthodes de CDI, la procédure de reconstruction se base sur des algorithmes itératifs, qui alternent entre des contraintes dans l'espace réciproque et dans l'espace direct grâce à l'utilisation de Transformées de Fourier. Dans les faits, la principale différence se situe dans la façon dont la mise à jour de l'objet est faite, c'est-à-dire que cette mise à jour prend en compte l'ensemble des clichés de diffraction, contenant des redondances. Le premier algorithme mettant en place la reconstruction d'une phase complexe à partir d'une diversité introduite via translation d'une illumination fut introduit par Rodenburg et Faulkner, avec la création du Ptychographic Iterative Engine (PIE) en 2004. En 2008, Guizar-Sicairos et Fienup remarquent que l'algorithme de PIE peut en fait être exprimé comme un algorithme de plus forte pente (steepest descent en anglais), et par conséquent proposent de le réécrire sous la forme d'un algorithme du gradient conjugué, qui s'avère plus efficace et plus robuste tout en permettant aussi de reconstruire le front d'onde incident. En parallèle à ce travail, Thibault et al développent une nouvelle approche permettant aussi de récupérer à la fois l'objet complexe et l'illumination complexe, basée cette fois sur l'utilisation de l'algorithme de Difference Map (DM).

D.6.3 *Ptychographie en condition de Bragg*

Le principal intérêt des matériaux cristallins réside dans la compréhension non seulement de la densité mais surtout des champs de déformation présents à l'intérieur des structures. La géométrie de Bragg apporte la possibilité d'imager de tels champs. Par conséquent, il apparaît évident de transposer les méthodes de ptychographie pour qu'elles soient applicables en condition de Bragg. C'est en 2011 que la communauté scientifique s'est donc intéressée au problème.

Cette partie du manuscrit s'attelle à reprendre de manière exhaustive toutes les publications relevant du domaine, en suivant la chronologie des avancées. Ainsi, les premières tentatives se concentrèrent sur la reconstruction en 2D d'échantillon, transposant directement les algorithmes ptychographiques existant pour la géométrie de transmission directe, avec la particularité que la reconstruction est une projection le long du vecteur d'onde diffracté. En effet, le cliché 2D de diffraction cohérente obtenu à la condition de Bragg d'un objet partiellement illuminé n'est autre que la transformée de Fourier de la projection du volume cristallin illuminé, le long du vecteur d'onde diffractée. Par conséquent, l'objet reconstruit est 2D et dans un plan parallèle au détecteur, c'est-à-dire avec un angle de 2theta par rapport à la normale à l'échantillon. Cela nécessite donc une forte hypothèse concernant l'homogénéité de l'échantillon en profondeur. En outre, un soin particulier doit être apporté à l'évaluation de la nouvelle géométrie qui influe sur la position du faisceau incident vis-à-vis de l'objet, tel qu'il est vu par le détecteur. Il est intéressant de noter que la demi-douzaine d'articles scientifiques publiés, utilisant ou développant la technique, l'éventail d'applications est large : dislocation dans un cristal épais, polarisation locale d'une couche ferroélectrique ou imagerie de domaine dans des couches épitaxiées.

En parallèle, le groupe de P. Godard, V. Chamard et M. Allain entreprenaient de résoudre le problème mathématique de ptychographie 3D en condition de Bragg. Pour cela, ils développent un algorithme dérivé du PIE, y ajoutant une contrainte de régularisation sur le module du front d'onde de sortie. A cette époque, cette contrainte est évaluée à partir d'un modèle de la déformation à l'intérieur du cristal qui lui-même provient de l'analyse des clichés de diffraction. En effet, la position du barycentre du volume de diffraction émis par chaque position de l'illumination sur l'objet est directement liée à la déformation locale de l'objet : il est possible d'obtenir une estimation de l'échantillon. Une publication est dédiée à la présentation de l'algorithme et à des tests numériques, puis une seconde publication propose une reconstruction 3D d'un échantillon réel mesuré expérimentalement. Cependant, les résultats manquent de résolution : elle semble être égale à la taille de l'échantillon le long d'une de ses directions principales, 40 nm. C'est en 2017 qu'une expérience réalisée sur une coquille cristalline de mollusque par F. Mastropietro et al. propose une reconstruction convaincante des domaines 3D de l'échantillon, avec une résolution toujours de l'orde de 40 nm mais sur un objet de 1.75 µm.

Enfin, en 2017 Hruszkewycz et al. montrent que, si deux dimensions sont encodées trivialement dans l'espace réciproque par le détecteur 2D, la troisième dimension quant à elle, est encodée dans le déplacement du couple illumination/objet lorsqu'elle a lieu en direction du détecteur (et non parallèlement au plan du détecteur). Ainsi, en translatant le faisceau dans deux directions pour balayer

l'objet, et en collectant les clichés de diffraction à un seul angle d'incidence, les données contiennent de l'information de l'objet 3D. Pour la récupérer, il faut introduire l'opérateur de rétro-projection, qui transforme un objet 2D en un objet 3D, inspiré de la tomographie assistée par ordinateur. Ceci marque les débuts de la "3D Back-Projection Ptychography" (3D BPP). L'étape complexe est l'implémentation de la rétro-projection dans le processus algorithmique. Trois méthodes sont utilisées dans la librairie PyNX : réplication de l'objet, mise à jour incrémentale de l'objet et minimisation du gradient. Ce manuscrit présente aussi la proposition d'incorporer "quelques" angles au lieu d'un seul, pour aider la convergence de la reconstruction, mais souligne le fait que l'implémentation algorithmique dans PyNX n'est pas encore réalisée.

D.6.4 *Essais numérique de PyNX*

Il est primordial de procéder à des essais numériques des algorithmes développés et implémentés dans la librairie PyNX. Cette librairie visant à faciliter l'usage des techniques de diffraction cohérente telles que présentées jusqu'alors, tout en proposant des calculs rapides effectués sur carte graphique, elle a pour objectif de fournir des outils pratiques et robustes pour analyser directement des clichés de diffraction cohérente.

Tout d'abord, un modèle simple, d'un cristal de silicium contraint, est utilisé pour simuler une expérience de 3D Back-Projection Ptychography. Le cas de la réflexion (004) d'un volume parallélépipédique (300 nm $\times$300 nm $\times$60 nm) est étudié. En prenant en compte une maille de 5.4309 Å, l'angle de Bragg correspondant à cette réflexion (004) vaut $\theta_B = 33.53°$. Un champ de déformation est introduit le long de la direction verticale. L'illumination est simulée à partir d'une Fresnel Zone plate de 300 µm de diamètre, focalisant un faisceau de 8 keV à 9.8 cm de distance focale. Le balayage consiste en un mouvement décrivant une spirale d'Archimède, faite de 320 positions avec un pas de 20 nm. Le détecteur est simulé par une grille de 256 $\times$256 pixels, chacun mesurant 55 µm, et placée à 1 m de l'objet. L'angle entre le faisceau direct et le faisceau diffracté est de $2\theta_B = 67.06°$. Ensuite, les 320 clichés de diffraction sont calculés numériquement en utilisant une somme cinématique de chaque "diffuseur" présent dans le volume de silicium. Grâce au transfert sur gpu, en l'occurrence une carte graphique NVidia GTX 1060, le calcul prend 13 secondes, sachant qu'il y a 37632 diffuseurs (le pas choisi pour simuler l'échantillon par une grille discrète étant de 5 nm). Un bruit de Poisson est ajouté au jeu de données obtenu, en faisant l'hypothèse que la totalité des clichés contient 10^8 photons. Les clichés montrent clairement que la résolution est suffisante pour visualiser l'influence du champ de déformation sur la diffraction par le cristal. La suite du

manuscrit présente en détails comment mettre en place la dreconstruction de l'objet à partir du jeu de données de diffraction en utilisant les classes disponibles dans la librairie PyNX. Après avoir initialisé le support, comme un objet parallélépipédique plus large que l'objet à reconstruire mais de même épaisseur, et l'objet initial, strictement identique à son support, 40 cycles de Difference Map, suivis de 40 cycles d'Alternating Projections sont appliqués pour parvenir à une reconstruction fiable. Notons que cette reconstruction est obtenue extrêmement rapidement, en l'espace d'une dizaine de secondes. En comparant la diffraction simulée à partir de la reconstruction avec celle ayant servi de point de départ, il est clair que les algorithmes ont réussi à reproduire fidèlement la diffraction de l'objet déformé. Ensuite, en terme de densité reconstruite dans l'espace direct, il est aussi visible que les bords francs de la densité reconstruite coïncident avec ceux de l'échantillon. A partir de ces bords francs, la résolution spatiale est estimée à $\pm$ 1 pixel (10 nm). Ces bords francs sont néanmoins présents uniquement dans les directions parallèles au plan du détecteur. En effet, quelques oscillations de densité sont présentes le long de la direction normale au détecteur, c'est-à-dire le long de la direction de rétro-projection. Enfin, le long des directions parallèles au plan du détecteur, la phase complexe, et donc les champs de déformation, est bien reconstruite.

En second lieu, une autre simulation est réalisée, à partir d'un échantillon ayant cette fois la même épaisseur que les couches minces de SiGe expérimentalement étudiées : 20 nm. Les modélisations aux éléments finis provenant de COMSOL sont utilisées pour modéliser l'échantillon et simuler les clichés de diffractions correspondant à 43 illuminations. Les positions d'illumination suivent une spirale d'Archimède, avec un pas de 40 nm. La taille du faisceau simulée est de 153 nm $\times$130 nm (Horizontale $\times$Verticale). Le même procédé de reconstruction est ensuite mis en place, générant un voxel cubique d'arrête 7.3 nm. Il est important de souligner à cet instant que l'épaisseur de la couche étant de 20 nm, le long de l'épaisseur de l'objet à peine 3 voxels sont disponibles pour créer la reconstruction. Cette limitation engendre un effet d'escalier, ou de discrétisation, puisque l'échantillon est reconstruit dans le repère du laboratoire, c'est-à-dire avec une rotation de 2 thetaB autour de l'axe horizontal et perpendiculaire au faisceau incident (axe X). Le résultat obtenu après 40 cycles de DM et 40 cycles d'AP montre de clairs signes de difficultés dans la direction normale au plan du détecteur. Les résultats de phase reconstruite le long de cette direction ne sont pas utilisables puisque seulement 2 voxels sont présents. En outre, dans la direction X, les bords ne sont pas aussi francs que lors de la précédente simulation. Cependant, la phase complexe dans cette direction correspond totalement avec le modèle, ce qui démontre la robustesse de la technique quant à la mesure du champ de déformation (déformation

de la maille le long du vecteur de diffraction de Bragg) le long de la direction parallèle au plan du détecteur.

En conclusion, ces simulations mettent en exergue les limitations de la technique de 3D BPP. En effet, la taille de l'échantillon reste une limite fondamentale de la technique, puisque cette dernière est intrinsèquement liée aux conditions expérimentales, fixant ainsi une taille minimale de voxel de reconstruction : il est compliqué d'envisager une reconstruction complète 3D d'un objet ne faisant que 2 voxels en épaisseur. Cependant, la technique laisse entrevoir qu'une approximation 2D de ces couches ultra minces pourraient déboucher sur des résultats interprétables. En effet, dans la direction parallèle au plan du détecteur, il est possible d'obtenir une reconstruction fidèle de l'évolution du champ de déformation. C'est pourquoi l'approche 2D BPP a été privilégiée pour reconstruire les données expérimentales obtenues durant cette thèse.

D.6.5 *Résultats expérimentaux*

D'abord, les résultats des expériences menées sur les échantillons de SiGeOI ultra mince sont présentés. C'est le jeu de données obtenu sur la ligne de lumière NanoMax du synchrotron Max IV situé à Lund, en Suède, qui a été retenu, car le faisceau utilisé sur NanoMax a l'avantage d'être plus petit (102 nm $\times$109 nm) que celui utilisé lors de nos expériences sur ID01 à l'ESRF. La réflexion étudiée est la (113), nécessitant un angle d'incidence de 28.24°. L'expérience est réalisée dans une géométrie de diffraction horizontale. Le balayage est réalisé sur une zone de 3 µm $\times$3 µm, suivant une grille discrète avec un pas de 20 nm dans la direction rapide des moteurs, et de 40 nm dans la direction orthogonale. Le balayage est centré sur un motif de SiGeOI contraint de 20 nm d'épaisseur et de 2 µm $\times$2 µm de large. Le temps d'exposition par point est de 0.02 seconde, ce qui conduit à un très faible coût de photon diffracté par cliché. Cependant, la diffraction venant du substrat de silicium est tellement intense qu'il est préférable de la limiter par un faible temps d'exposition. Une routine de 800 cycles d'AP est appliquée au jeu de données de diffraction, en prenant en compte la géométrie particulière du scan : l'angle de sortie, entre la surface de l'échantillon et la direction du vecteur d'onde diffracté, est très faible (β= 3.1°) ce qui fait que la résolution spatiale le long de l'axe horizontal est très faible. En effet, il faut corriger la position des illuminations dans cette direction par un facteur 0.0416 (égal à $\sin(\beta)/\tan(\alpha)$ où α est l'angle d'incidence). Comme la résolution dans la direction verticale reste la même que lors d'une expérience de ptychographie en transmission classique, soit $\frac{\lambda D}{nb_{pixel} Taille_{pixel}} = 9.8$ nm, elle est de $^{9.8}/_{0.0416} = 235$ nm dans la direction horizontale. Cependant, le résultat obtenu dans la direction horizontale est largement satisfaisant. On retrouve une largeur de

1.95 µm et les sauts de phase à l'approche des bords de l'échantillon. Cette reconstruction donne accès à la déformation le long du vecteur de diffraction (113) et son évolution le long de l'axe horizontal du cristal de SiGe, c'est donc une mesure de cisaillement. Il est particulièrement intéressant de constater que l'évolution de ce cisaillement correspond parfaitement avec la simulation aux éléments finis, et qu'elle est mesurée pour un échantillon avec une couche protectrice de nitrure de silicium. Ainsi, le rôle de cette couche est à nouveau confirmé : elle permet de maintenir la compression dans le plan.

Dans un second temps, c'est un échantillon d'un micro-disque suspendu d'un alliage de germanium étain qui est étudié. Le GeSn est un candidat viable pour l'industrie microélectronique souhaitant développer un matériau compatible CMOS à gap direct pour fabriquer une source laser monolithique intégrée sur une plateforme de silicium. Cependant, la croissance par épitaxie de GeSn sur substrat de germanium crée nécessairement une contrainte en compression dans la couche de GeSn. Or, plus la déformation est grande et plus la quantité d'étain dans l'alliage doit être grande pour garder un gap direct. C'est grâce au développement d'une technique de gravure sélective de Ge et GeSn, même à basse composition en Sn, qu'il est dorénavant possible de considérer des structures suspendues qui ont l'avantage de relaxer la contrainte épitaxiale. La question qui reste ouverte est celle de la distribution de la déformation anisotropique sur l'ensemble du disque. Cette question est déterminante puisque les propriétés optiques de la couche de GeSn sont intrinsèquement liées à l'état de contrainte. C'est pourquoi une expérience de diffraction cohérente a été réalisée sur la ligne de lumière ID01 à l'ESRF. Le micro-disque étudié consiste en un empilement relativement simple : de haut en bas se trouvent un disque de 8 µm de diamètre, fait d'une bicouche de 480 nm d'épaisseur de GeSn (qui se décompose en une couche de 225 nm d'épaisseur de GeSn à 13 % de Sn, une couche de transition de 90 nm d'épaisseur, et une couche de 120 nm d'épaisseur de GeSn à 11% de Sn), un pilier de Ge de 3 µm de diamètre et 2.5 µm de hauteur, puis un substrat de silicium. Avec un faisceau de rayons X à 8 keV, focalisé à 360 nm x 180 nm (H x V), un balayage, suivant une spirale de 283 points avec un pas de 100 nm, a été réalisé sur l'échantillon incliné à un angle thetaB = 31.5°. Un détecteur de 516 x 516 pixels, situé à 1 m de distance, enregistre les clichés de diffraction de la raie (004) du GeSn. Il est tout de suite remarquable que le centre de masse des clichés de diffraction varie fortement suivant la position de l'illumination, signature de la forte courbure présente sur le disque. Il est ainsi possible d'utiliser une approximation d'iso-contrainte: comme le disque est courbé et peut être approximé par une portion de sphère de rayon, e.g., R = 100 µm, une seule couche mince sera en condition de Bragg. Si la FWHM naturelle de la diffraction du GeSn est DeltaOmega = 0.01° = 1.8 x 10^-3 rad, cela correspond à une épaisseur diffractante de R x Deltaomega =

17 nm, telle que le faisceau ne voit qu'une couche d'iso-contrainte au lieu de toute la surface du disque. Il est donc logique d'essayer de reconstruire cette "tranche" de disque en condition de diffraction, en utilisant directement l'algorithme de 2D BPP. La même méthode de correction que celle évoquée précédemment donne un facteur de 0.907 (on rappelle que la géométrie de diffraction est ici verticale, et l'angle de sortie moins petit). Après 800 cycles d'AP, la reconstruction semble fiable. Premièrement, un saut d'amplitude est clairement visible, signe de la séparation entre les deux couches du bicouche de SiGe. A partir de l'amplitude reconstruite, chacune de ces couches semble être d'une épaisseur de 200 nm, ce qui correspond bien aux spécifications de l'échantillon. En outre, la phase extraite dans la direction verticale permet elle aussi de souligner cette interface. En effet, la phase possède deux pentes bien distinctes le long de la direction verticale. Comme la déformation est directement proportionnel au gradient de la phase, il est clair que la reconstruction fait apparaître deux couches, différenciées spatialement et par leur état de contrainte respectif. Enfin, il est aussi possible d'extraire la phase le long de la direction horizontale pour remonter à la courbure du micro-disque en forme de dôme. En effet, que ce soit par les images SEM de l'échantillon, ou par l'étendue de la courbe de balancement de la diffraction, sur plus de 6° autour de l'angle de Bragg, il est clair que le micro-disque est courbé de telle façon à être assimilable à une portion de sphère. Cela est vérifié par le fait que la phase "déroulée" le long de la direction horizontale suit une parabole. Ainsi, la déformation est remarquablement linéaire sur une étendue de quasiment 2 µm dans cette direction. Le coefficient directeur de la régression linéaire étant proportionnel à la courbure de la parabole, on trouve un rayon de courbure de 104 µm. Cette valeur est en accord avec les attentes : pour un rayon de 100 µm, un arc de longueur 8 µm est vu par un angle de 5.7°.

En conclusion, il a été démontré qu'il est possible d'utiliser la ptychographie en géométrie de Bragg tout en s'appuyant sur des algorithmes robustes et extrêmement rapide, disponibles dans la librairie PyNX. Toutefois, ceci n'est possible qu'à condition de prendre énormément de précautions dans la stabilité de la configuration expérimentale, dans la taille de l'échantillon par rapport aux conditions expérimentales et enfin dans l'état de contrainte de l'échantillon : trop de déformations empêcheront la convergence des algorithmes. La question du nombre d'angles incidents à utiliser reste ouverte puisque, d'abord, pour une courbe de balancement complète (20 à 40 angles) le risque prépondérant est la dérive des moteurs qui corrompt l'ensemble des données, ensuite, pour un seul angle c'est l'opérateur de rétro-projection qui nécessite de nombreuses assistances et reste approximatif dans la direction de rétro-projection, enfin, pour quelques angles, la méthode est trop récente pour être évaluée dans ces travaux de thèse. Cependant, cette méthode aux multiples angles s'avère vraiment prometteuse, puisque la diversité angu-

laire devrait améliorer grandement la convergence des algorithmes tout en profitant de la flexibilité de l'opérateur de rétro-projection qui permet d'incorporer des positions d'illuminations qui varient d'un angle à l'autre. Enfin, par sa simplicité d'approche, la méthode 2D BPP devrait s'imposer comme une méthode intéressante pour réaliser une caractérisation rapide d'un échantillon en 2D, à condition que son homogénéité soit assez grande.

D.7 CONCLUSION

Les techniques d'imagerie par diffraction cohérente sont essentielles pour exploiter pleinement les rayons X durs qui sont générés dans les instruments synchrotrons. Ces techniques, assimilables à de la microscopie sans optique, ont pour but d'imager les propriétés nanoscopiques d'échantillons à l'aide d'un faisceau extrêmement cohérent. Des algorithmes itératifs, naviguant entre l'espace réciproque des intensités diffractées et l'espace direct de l'objet illuminé, permettent de retrouver la phase complexe de l'objet, perdue lors de l'acquisition par le détecteur, et ce avec une résolution spatiale élevée (jusqu'à 10 nm). Même si la majorité des techniques qui sont cataloguées comme des techniques d'imagerie par diffraction cohérente sont considérées comme étant matures, il reste encore beaucoup de place pour des améliorations sur certaines d'entre elles, notamment lorsqu'elles utilisent la géométrie de Bragg, donnant ainsi accès aux déformations cristallines à l'échelle quasi-atomique. Aussi, il n'est pas rare que les utilisateurs des installations synchrotron demandent conseil aux scientifiques travaillant au développement de la technique, puisqu'il n'existe pas encore d'algorithmes standards pour les techniques telles que la Bragg CDI ou la Bragg ptychographie. Dans ce travail de thèse, l'implémentation et la méthodologie de nombreuses techniques de diffraction X ont été étudiées, notamment dans le but de les rendre plus accessibles à un plus vaste éventail d'utilisateurs, encore plus particulièrement dans le contexte du programme ambitieux de modernisation, "l'Upgrade Programme", dans lequel s'est engagé l'ESRF. Le programme de Source de Lumière Extrêmement Brillante (EBS en anglais) est un projet innovant et unique, représentant un investissement de 150 millions d'euros sur la période 2015 - 2022, qui doit dessiner une nouvelle génération de synchrotron : des performances 100 fois supérieures à celles existant dans les synchrotrons actuels. La première partie du manuscrit de thèse fournit une description détaillée du contexte théorique nécessaire à la bonne compréhension des échantillons et des techniques de diffraction utilisées. D'abord, la déformation cristalline, ainsi que son effet sur les propriétés structurelles, est rappelée, ainsi que la diffusion par un cristal, qu'il soit parfait ou déformé. Comme la déformation brise la symétrie d'un cristal, elle modifie aussi la structure de bandes du matériau et par

conséquent influe sur la mobilité des porteurs de charge. Dans le chapitre 2, une introduction relative aux concepts d'élasticité est donnée dans le but de comprendre le fonctionnement des différents échantillons étudiés : depuis le SiGe contraint sur isolant visant à devenir le canal de transistor dernière génération, jusqu'aux micro structures de GeSn ouvrant la voie à de nouvelles applications laser, il est en effet primordial de comprendre l'ingénierie des déformations. Le chapitre 3 fournit une description détaillée des rayons X et de leurs propriétés, ainsi que de la façon dont un synchrotron produit un faisceau cohérent. Dans le cas des matériaux cristallins, en illuminant un échantillon avec une illumination cohérente, il est possible de collecter l'intensité diffractée à différents pics de Bragg et ainsi de remonter à la déformation locale dans l'échantillon. C'est la raison pour laquelle les techniques d'imagerie par diffraction cohérente ont été adaptées en condition de Bragg, permettant alors de sonder les propriétés structurelles d'un échantillon. Pendant les vingt dernières années, de grands progrès dans le champ de la diffraction cohérente ont été réalisés, notablement grâce à l'introduction de meilleures optiques de focalisation, produisant un faisceau de taille plus petite mais avec un flux de photons plus grand : l'étude d'échantillons de taille inférieure à 100 nm est devenu réalisable. En outre, la fin de ce chapitre 3 met l'accent sur les dernières avancées algorithmiques, comme la prise en compte de la cohérence partielle ou l'utilisation du maximum de vraisemblance pour optimiser la qualité d'une reconstruction. Ensuite, la seconde partie du manuscrit est consacrée à l'étude expérimentale réalisée pendant la thèse. En premier lieu, le chapitre 4 présente une étude de cas : la cartographie des déformations cristallines de motifs ultra minces de SiGeOI sous contrainte. En particulier, l'utilisation de la technique SXDM est expliquée en détails. Cette technique apporte une haute résolution spatiale couplée à une haute sensibilité à la déformation et à la désorientation d'un échantillon cristallin, sous réserve que l'analyse soit réalisée avec une attention toute particulière étant donnée d'une part la grande quantité de données brutes générées par la technique, et d'autre part la présence de nombreux obstacles. Dans ce but, le chapitre fournit une feuille de route au point par point pour mener à bien l'analyse des données et guider l'utilisateur potentiel à travers l'entièreté de l'expérience. Par ailleurs, ce chapitre montre que le SXDM peut aussi être utilisé comme un outil statistique, puisque dans le cas étudié le grand nombre de motifs mesurés sert aussi pour la compréhension de la relaxation de la déformation, en fonction de la taille du motif. Ainsi, les résultats montrent que la technique de condensation récemment développée, qui permet de faire croitre des couches ultra minces (13 à 20 nm) de SiGe sur SOI, produit des couches très homogènes mais dont la longueur de relaxation est plus grande que celle prédite par la théorie élastique. Ces résultats sont confirmés par une récente expérience d'holographie à électrons, qui suggère qu'il existe

un glissement à l'interface SiGe/SOI. Par conséquent, il est démontré que la technique de SXDM est compatible avec les matériaux électroniques de pointe. Enfin et surtout, cette technique de SXDM développée particulièrement sur la ligne de lumière ID01 de l'ESRF bénéficiera du programme EBS, tout comme un flux plus important de photons permettra, par exemple, de réduire le temps d'exposition du détecteur et ainsi d'accélérer la vitesse de balayage, réduisant ainsi le temps global d'une expérience. Ensuite, le chapitre 5 se concentre sur un couplage innovant de deux techniques d'imagerie matures, la Bragg CDI et la DCT. En effet, l'intérêt est de combiner les deux échelles proposées par chacune des techniques pour montrer qu'il est possible de passer de l'échelle microscopique d'un échantillon de ZrO_2, où l'information moyenne de la déformation est disponible, à l'échelle fine d'un grain incrusté à l'intérieur de l'échantillon, avec une résolution nanoscopique. Ainsi, la DCT est utilisé comme outil d'indexation des grains à l'intérieur d'un échantillon et la BCDI intervient ensuite pour fournir des résultats quantitatifs à l'échelle du grain. La combinaison de ces deux techniques est prometteuse, particulièrement dans le contexte d'upgrade de l'ESRF qui permettra d'ajuster encore plus finement la taille du faisceau : défocaliser le faisceau pour faire en sorte que sa taille s'ajuste à celle d'un grain est la clé de la réussite de cette technique. Du reste, la fin de ce chapitre propose une méthode pour répondre à la question de la sensibilité à la déformation d'une reconstruction obtenue par BCDI. Ce sujet est souvent mis de côté depuis que la technique existe, à tel point qu'aujourd'hui aucune technique ne permet d'évaluer cette sensibilité. La méthode proposée ici, inspirée de la Fourier Shell Correlation, est testée sur un jeu de données simulé ainsi que sur un jeu de données expérimentales, en collaboration avec le groupe du Dr Felix Hofmann (Oxford). Cette méthode, Strain Shell Correlation, pourrait servir d'outil pour évaluer la sensibilité à la déformation de n'importe quelle reconstruction de BCDI. Enfin, le chapitre 6 présente la méthode de ptychographie et son lot de promesses dans la quête d'une technique d'imagerie haute résolution d'objets étendus. Tout d'abord, la méthode "traditionnelle" de ptychographie en transmission est introduite, avec les algorithmes classiques qui y sont associés. Ensuite, le cas particulier de la géométrie de Bragg est discuté, puisque la capacité potentielle de la Bragg ptychograhie à imager les déformations cristallines avec une résolution de l'ordre du nanomètre en 3 dimensions est particulièrement recherchée. La technique repose sur l'acquisition des clichés de diffraction au voisinage de pics de Bragg, tout en balayant un objet avec des illuminations se recouvrant partiellement d'une position à l'autre. A l'origine, la Bragg ptychographie a été développée en 2D, générant de prometteuses reconstructions à condition que l'échantillon soit suffisamment homogène. Ainsi, la "2D Bragg Projection Ptychography" (BPP) a recours à des algorithmes ptychographiques standards, c'est-à-dire utilisés dans le cadre de transmission directe,

couplés avec d'une part, une correction de la position des illuminations, et d'autre part l'hypothèse que le faisceau incident est une onde plane infinie. La partie 6.5 démontre que l'application de 2D BPP à des échantillons ultra minces, ou à des volumes d'iso-déformation à l'intérieur d'un plus grand échantillon, permet d'obtenir des résultats fiables et robustes, tels que la caractérisation des fluctuations de déformation avec une haute résolution. Dans la continuité, le cas des reconstructions en 3D est abordé. Une revue exhaustive de l'état de l'art est présentée, mettant l'accent sur le fait que la quasi totalité des publications d'alors s'appuient sur l'algorithme du "Ptychographie Iterative Engine" (PIE) enrichi d'un terme crucial de régularisation. Cependant, l'acquisition de données complètes pour une reconstruction 3D nécessite des balayages très précis et très couteux en temps, à de multiples angles d'incidences, et par conséquent souffre de nombreuses limitations. En particulier, les dérives mécaniques lentes et les dommages causés par une exposition prolongée de l'échantillon à un flux intense de rayons X sont les obstacles principaux à la technique. C'est afin de remédier à ces limites que l'opérateur de rétro-projection a été introduit dans le processus algorithmique. Le jeu de données est alors réduit à un seul angle d'incidence, cet opérateur de rétro-projection permet donc de s'affranchir de la nécessité de basculer l'échantillon, réduisant considérablement le temps d'illumination de l'échantillon. Cependant, l'implémentation de cet opérateur n'est pas aisée. Les différentes possibilités d'implémentation sont présentées dans ce manuscrit, mais leur application sur des jeux de données expérimentales n'est, pour l'instant, pas satisfaisante. Considérer quelques (par exemple 5) angles d'incidence pour compléter les données de diffraction (au lieu d'une quarantaine pour un jeu de données 3D complètes), permet en théorie d'augmenter la convergence des algorithmes mais se révèle être une approche difficile à implémenter. En outre, il convient de rappeler que ces méthodes reposant sur un algorithme de rétro-projection dépendent fortement du support de l'objet, au moins dans la direction normale au détecteur. Enfin, ces méthodes nécessitent aussi un consensus en ce qui concerne le choix de la figure de mérite, indispensable à l'évaluation de la convergence. Malgré la robustesse apparente de la méthode de 3D Bragg Ptychography, les prochaines expériences auront besoin d'un maximum de contrôle et stabilité, puisque ce sont au final ces paramètres qui dictent la qualité des données de diffraction. De plus, les objets fortement contraints ou courbés, qui voient leurs clichés de diffraction balancés d'un bord du détecteur à l'autre au cours du balayage, sont encore source de difficulté de convergence. Enfin et surtout, les échantillons ultra minces sont encore aujourd'hui compliqués à reconstruire, pour la simple raison que la taille du voxel de la reconstruction est limitée par les conditions expérimentales (longueur d'onde, distance du détecteur, sa taille et la taille de ses pixels) : il est quasiment impossible de générer des voxels inférieurs à $5 \times 5 \times 5$ nm^3. Toutefois,

il faut souligner que l'approche en 2D BPP est très prometteuse pour l'étude de ces échantillons ultra minces ou très déformés, tant qu'une approche d'iso-contrainte est disponible. En effet, il est montré dans la dernière partie du chapitre 6 que les couches ultra minces peuvent être approximées à des couches 2D, menant à des reconstructions par 2D BPP en accord avec l'holographie par électrons, et que l'approche d'iso-contrainte pour des micro-disques fortement déformés permet de retrouver les interfaces de l'échantillon ainsi que le gradient de phase qui s'y trouve.

DECLARATION

I, Gaétan G. Girard, hereby confirm that the work presented here is my own, and where information has been derived from other source, this has been indicated.

Grenoble, 4/03/2020

Gaétan Girard

Development of Bragg coherent X-ray diffraction and Ptychography methods, application to the study of semiconductor nanostructures

Nanotechnologies rely on the introduction of strain engineering to enhance semiconductor devices performances. As a consequence, non- invasive characterization methods with high spatial resolution and strain sensitivity on low- amount-of-matter samples are required. This PhD work focuses on methodology of X-ray diffraction techniques performed in the Bragg geometry, which allows probing the structural properties of crystalline samples. Firstly, the Scanning X- ray Diffraction Microscopy technique, developed on a fast-timescale at the ESRF ID01 undulator beamline, is described through a thorough analysis of an experiment performed on ultrathin strained SiGe-on-insulator patterns. Secondly, this manuscript focuses on two coherent diffraction imaging techniques, namely Bragg CDI, which yields complex density and strain map of nano-meso crystalline objects, and Ptychography, which use translational diversity to produce quantitative maps of complex transmission function of non-crystalline objects. The motivation developed in this PhD work is to combine these two techniques that both promote highly sensitive phase-contrast properties, in order to provide ultra-high resolution on complex/extended samples. Bragg Ptychography is thus introduced, along with algorithmic descriptions and considerations on the X-ray beam characterization, the latter being still a key component for successful reconstructions.

Keywords : Coherent X-ray diffraction imaging, nanostructures, strain, synchrotron radiation

Développement des méthodes de Ptychographie et diffraction cohérente des rayons X en géométrie de Bragg, application à l'étude de nano-structures

L'ingénierie des contraintes révolutionne actuellement le monde de la nanotechnologie, en ce qu'elle permet d'améliorer les performances de dispositifs tels que les structures semiconductrices, en manipulant les propriétés physiques des matériaux à travers une déformation élastique. La nécessité de méthodes de caractérisation non-invasives, précise à l'échelle nanométrique et ultra-sensible aux déformations, s'en trouve donc accrue. Les nanostructures étudiées servent d'étalons pour le développement d'une méthodologie basée sur la diffraction de rayons X en condition de Bragg. Dans ce travail, la technique de Microscopie par balayage de diffraction X (SXDM) est d'abord détaillée et appliquée à des couches ultra minces de SiGe contraint sur isolant, démontrant être un puissant outil statistique pour évaluer la relaxation de la contrainte après gravure. Ensuite, le manuscrit décrit les techniques d'imagerie par diffraction de rayons X cohérents (CDI) en condition de Bragg, qui permet de reconstruire la densité électronique complexe 3D d'un cristal, et de Ptychographie, qui se base sur l'introduction d'une diversité par translation du faisceau sonde. L'objectif est de combiner ces deux techniques pour développer une technique de haute précision spatiale et ultra- sensible aux déformations, sur des objets pouvant être étendus. Par conséquent, la Ptychographie en condition de Bragg est introduite, ainsi que les algorithmes associés qui permettent de reconstruire à la fois l'échantillon et le faisceau probe, ce dernier étant essentiel pour obtenir des reconstructions concluantes. Il est démontré qu'une approche 2D par projection est suffisante et quantitative dans les cas limites auxquels la thèse se confronte : matériaux ultra- fin approximés par des couches 2D et matériaux ultra-deformés pour lesquels seuls les sous- volumes dans lesquels la déformation varie peu (isostrain) peuvent être reconstruits.

Mots-clés : Imagerie par diffraction X cohérente, nanostructures, contrainte, rayonnement synchrotron